Faculty of Sciences
Department of Analytical Chemistry
X-Ray Microspectroscopy and Imaging Group

THREE DIMENSIONAL QUANTITATIVE X-RAY FLUORESCENCE AT THE MICRO- AND NANOSCOPIC LEVEL: METHODOLOGICAL DEVELOPMENT AND APPLICATIONS

Thesis submitted in fulfillment of the requirements for the degree of
Doctor (Ph.D.) in Sciences: Chemistry

by

Tom Schoonjans

Promotor: Prof. Dr. Laszlo Vincze
Co-Promotor: Prof. Dr. Frank Brenker
Co-Promotor: Dr. Claudio Ferrero

January 5, 2012

Acknowledgements

This work is the result of the successful collaboration between a large number of people. Although I am aware that each of them deserves an explicit mention and expression of gratitude in these acknowledgements, space constraints force me to restrict myself to the main contributors.

By far the most important person in the successful conclusion of this PhD work is Prof. Laszlo Vincze, promoter of this doctoral thesis. It is due to his powers of persuasion, as well as his confidence in my abilities, that I have received the unique opportunity to perform research in his group, working on highly interesting and challenging topics. In particular, I would like to thank him for the most excellent supervision I received over the years, through our personal conversations that were most appreciated and enjoyed. Apart from his scientific support, I am very grateful for his unremitting quest for the funding that was required to finance this work.

I am deeply indebted to the two co-promoters of this work: Dr. Claudio Ferrero of the European Synchrotron Radiation Facility (ESRF) and Prof. Frank Brenker of the University of Frankfurt. I am extremely grateful to the former for giving me the opportunity to spend four months at his research division, which in retrospect have been the most productive of my entire PhD. The new insights that I procured during my stays, through conversations with himself and his colleagues Dr. V. Armando Solé and Dr. Manuel Sanchez del Rio, have turned out to be decisive in the development of the software packages described in this work. His careful examination and correcting of my research papers and this manuscript have greatly added to their overall level of quality.
It is due to Prof. Brenker that I have been able to work on some of the most unique and interesting samples available: cometary dust and interstellar grains obtained from NASA's Stardust mission as well as deep-earth diamonds. Through an intensive collaboration with his post-doctoral researcher Dr. Sylvia Schmitz, we have obtained quantitative results of some truly remarkable datasets. Special thanks goes out to Sylvia, for managing to cope with my very often buggy software, for the privilege of receiving her in our group, as well as for the *Mr. Tom* snacks.

In our research group, I have always been able to rely on the expert advice of our two post-doctoral researchers Dr. Geert Silversmit and Dr. Bart Vekemans. Their help and support

have turned out to be of vital importance during this PhD work. Gratitude goes out to our group's fellow PhD students Björn, Lien, Jan and Eva whose presence in the office and during beamtimes made for a pleasant atmosphere. Their help with the experiments is greatly appreciated!

During my PhD, I have had the pleasure of collaborating with the A&MS and ESA research groups of our department. I would like to thank Deepti, Andrei, Annelies, Hans and Michel for allowing me to get involved in their respective research topics.

Furthermore, I would like to thank the people of the department of Analytical Chemistry and the ESRF, many of whom I consider as dear friends, for the countless lunches, coffee breaks and after-work drinks we enjoyed together. Special gratitude goes out to the ATP members Tine, Chantal, Pieter and Philip who have provided assistance in many ways over the years.

Naast deze mensen uit mijn werkomgeving, wil ik eveneens mijn vrienden en familie bedanken voor hun voortdurende ondersteuning en aanmoediging gedurende de voorbije jaren. Dit werd voornamelijk gewaardeerd op momenten dat het mij soms aan motivatie ontbrak, en het nodig was mij terug op het juiste spoor te brengen. In het bijzonder wil ik hierbij mijn zus, ouders en grootouders bedanken, zonder wie niets van dit alles mogelijk zou geweest zijn.

Last but not least, I would like to thank Niloufer who, although we have only met during the final stages of this work, has had the most profound impact on every aspect of my life, and has improved it in every imaginable way.

Tom Schoonjans
Gent, January 2011

Contents

Chapter 1

Introduction

This work revolves around X-ray fluorescence (XRF), an analytical technique that has been routinely used for several decades in several fields of research such as archaeometry, geology, biology, cosmology, chemistry and more. Essentially, one irradiates a specimen with an intense beam of X-rays, which in turn leads to the production of characteristic radiation from the sample. This secondary radiation carries both qualitative and quantitative information: the former occurs through the energy of the photons which is determined by the electronic configuration of the emitting atoms, enabling identification of the elements present in the sample. The latter is related to the fact that the intensity of the emitted fluorescence is proportional to the amount of atoms that are present in the sample, determined by the elemental weight fractions, sample density and thickness. It is this complex quantitative aspect of XRF that was investigated throughout this work, with a focus on the two main quantification procedures that are being used in the XRF community nowadays: the fundamental parameter method (FPM) and the Monte Carlo simulation of energy dispersive-XRF spectrometers.

The structure of this manuscript reflects the timeline that was followed during the PhD. Chapter 2 contains the required background on XRF that is necessary to fully comprehend the rest of this work: a thorough introduction on the underlying physical aspects of XRF is given, followed by a characterization of the different components of the XRF spectrometers that were used in the framework of this PhD. The second chapter finishes with an introduction to XRF quantification methodology, as well as to the software development that was essential in implementing and using our methodologies.

Chapter 3 covers our work on *xraylib*, a software library providing convenient access to a large number of databases, relevant for X-ray–matter interactions. Initially started as a collaboration between the ESRF (Grenoble, France) and the University of Sassari (Sardinia, Italy), development was taken over in 2008 by ourselves, resulting in over 10 releases containing multiple enhancements, extensions and bugfixes. This open-source software package was subsequently used in all of our quantification tools covered in the following chapters.

Chapter 4 concerns our work on the FPM, with a special focus on the development of a quantification method that can be used when dealing with so-called confocal micro/nano XRF. This unique technique, which distinguishes itself from conventional XRF by the mounting of a polycapillary half-lens in front of the detector, thereby providing depth sensitivity. Our methodology for confocal XRF was applied to a set of cometary dust samples, originating from the Wild 81P/2 comet and captured with the Stardust spacecraft. These unique samples were measured at the ID13 nanoprobe of the ESRF, in collaboration with Prof. Frank Brenker and Dr. Sylvia Schmitz of the University of Frankfurt.

Chapters 5 and 6 concern our work on the Monte Carlo simulations of ED-XRF spectrometers. Chapter 5 covers the complete algorithm that was implemented to allow for the prediction of XRF spectra based on a set of input parameters. It builds further upon the work of Vincze et al. by extending it with a number of new features such as the introduction of M-lines, cascade effects and detector pile-up. In Chapter 6, this algorithm is applied in an iterative, inverse manner in order to have it serve as a quantification tool.

The results obtained throughout this work are summarized in Chapters 7 and 8, along with a number of conclusions and an outlook.

Chapter 2

Quantitative X-ray fluorescence: basic principles

In this chapter, the essential components and underlying principles of XRF quantification methods will be discussed, combined with an overview of the different experimental setups available to acquire XRF data. Since the development of the methodology described in this thesis was intimately connected with the writing of the associated software code, an introduction will also be given to the computational aspects of this work.

2.1 Photon–matter interactions

2.1.1 X-rays

Photons, which are essentially elementary particles representing a quantum of electromagnetic radiation, may interact with matter in a variety of ways. A classification of the different interaction types is usually made based on the energy of the photons, since these will determine the possible interaction types. This work concerns the application of X-rays, a term commonly used to refer to electromagnetic radiation with an energy between 0.1 keV and approximately 100 keV. Their discovery is credited to Wilhelm Conrad Röntgen, who during his experiments with Crookes tubes (discharge tubes) in 1895, noticed that a green glow was emitted by a fluorescent screen painted with $BaPt(CN)_4$, positioned closely to an operational tube. Röntgen referred to the new type of radiation as "X", to highlight that it was an unknown type of radiation. For his discovery, Röntgen was awarded with the

first Nobel Prize in Physics in 1901 [1]. The penetrating power of the X-rays was realized early on, leading to its application in diagnostic medicine, under the form of radiography, which up to this day makes up for the most common use of X-rays. The underlying principle of radiography can be explained by the different X-ray absorption properties of different materials: for a given energy, materials with a higher electron density tend to absorb more X-rays than those with lower electron density. This can be clearly seen in one of the first X-ray pictures (Fig. 2.1) made by Röntgen, in which the hand of his wife Anna Berthe Röntgen is depicted: the darker areas correspond to the bony structures, which are made up primarily of Ca phosphates and will absorb considerably more of the (low energy) X-rays compared to the tissues which contain mostly organic materials composed of C, H, O, S, P and N.

The processes in the relevant X-ray energy range of 1-100 keV causing the attenuation of X-rays can be divided into three separate phenomena: Rayleigh scattering, Compton scattering and the photoelectric effect. The likelihood of occurrence of these processes is expressed using so-called interaction cross-sections, quantities which characterize the probabilities of given interactions between particles and matter.

2.1.2 Rayleigh scattering

Rayleigh scattering refers to the elastic scattering of X-ray photons, referring to elastic scattering by atomic electrons, during which the energy of the scattered photons remains unchanged [2]. The derivation of the expression for the microscopic Rayleigh scattering cross section is based on the Thomson scattering phenomenon, that describes the interaction of photons with free electrons:

$$\sigma_T = \frac{8\pi}{3} r_e^2 = 6.6524586\ldots \times 10^{-25} cm^2 \tag{2.1}$$

with r_e the classical electron radius. Scattering from atoms involves the collective effect of all electrons in the atom. The superposition of all electron contributions is coherent, but not in phase, because not all electrons are located at the same positions in the atom. The influence of the spatial distribution of the electons in the atom is given by the atomic form factor $F(Z, E)$, the Fourier transform of the electron density $\rho(\boldsymbol{r})$ of the atom:

$$F(Z, E) = \int \rho(\boldsymbol{r}) e^{i\boldsymbol{Q}\cdot\boldsymbol{r}} d^3\boldsymbol{r} \tag{2.2}$$

Figure 2.1: X-ray image of the hand of Anna Berthe Röntgen, taken on December 22, 1895. The darker areas correspond to the bony structures of the fingers, and to the ring around the subject's middle finger. Source: `http://science.hq.nasa.gov/kids/imagers/ems/xrays.html`

where $\boldsymbol{Q}$ represents the energy-dependent momentum transfer. Due to the nature of the Fourier transform, the broader the distribution of the electron density, the faster the decay of the atomic form factor. Since the Rayleigh scattering cross section σ_R can be expressed as the product of the Thompson cross section and the square of the atomic form factor:

$$\sigma_R = \sigma_T \cdot F^2(Z, E), \tag{2.3}$$

this decay propagates into this quantity, as can be seen in Fig. 2.2. The angular distribution of the scattering is anisotropic, which is determined by the degree of polarization of the photon and by its energy.

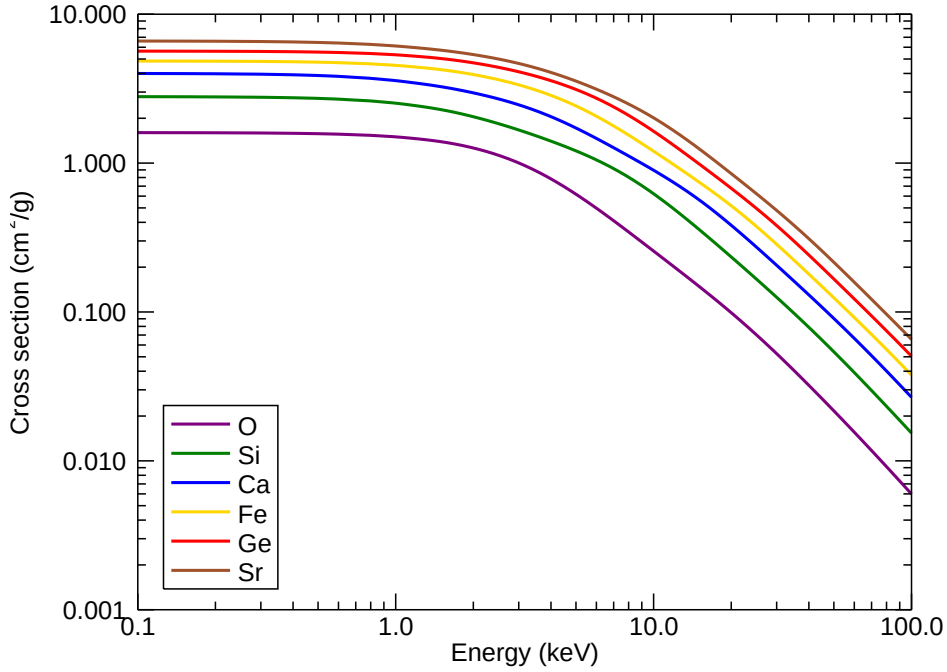

Figure 2.2: Rayleigh scattering cross sections of six elements. It can be seen that at a given energy, the cross section increases with the atomic number. Values were taken from Cullen et al.[3] through the *xraylib* interface.

2.1.3 Compton scattering

The second type of X-ray interaction with matter is Compton scattering. This is a form of inelastic scattering indicating that the photon will have a lower energy after the interaction[2]. This effect, discovered by Arthur Compton in 1923, results in the transfer of part of the energy of the scattered photon to an outer shell electron, which recoils and is subsequently ejected from the atom. The remaining energy is taken by the scattered photon. The energy E_C of the Compton scattered photon can be calculated using the Compton formula:

$$E_C = \frac{E_0}{1 + \frac{E_0}{m_e c^2}(1 - \cos\theta)} \tag{2.4}$$

where E_0, m_e, c and θ correspond to the initial photon energy, electron rest mass, speed

of light and scattering angle, respectively.

An example of Compton scattering cross sections for various chemical elements is shown in Fig. 2.3.

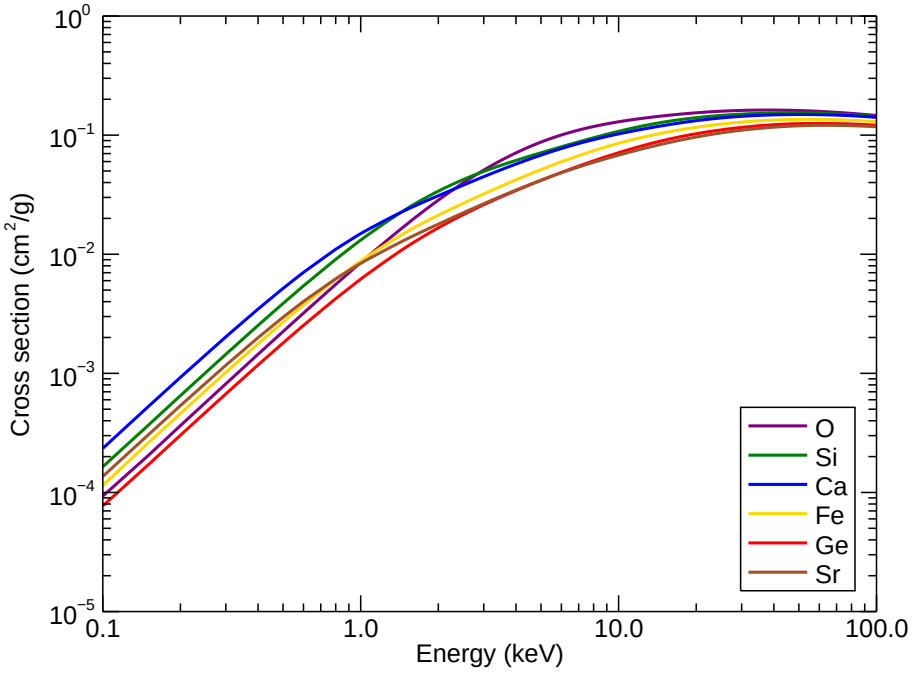

Figure 2.3: Compton scattering cross sections of six elements. Values were taken from Hubbell et al.[4] through the *xraylib* interface.

2.1.4 Photoelectric effect

The third interaction type is the photoelectric effect. This phenomenon, first observed by Heinrich Hertz in 1887 for visible light, concerns the emission of electrons from a material when irradiated with photons. The ejected electrons, called photo-electrons, are produced when an X-ray photon is fully absorbed by the atom, transferring its energy to a bound electron in a given shell of the target atom. For this effect to occur, the photon must possess an energy greater than the binding energy of the electron. After emission, the electron has a kinetic energy equal to the difference of the energy of the incoming photon and the

electron binding energy. The photoelectric effect cross section (also called photoionization cross section) τ is a function of the atomic number Z and the X-ray energy E, which can be approximately expressed as follows[2]:

$$\tau(Z, E) \sim C\frac{Z^4}{E^3} \tag{2.5}$$

Examples of photoelectric effect cross section profiles of various elements are shown in Fig. 2.4.

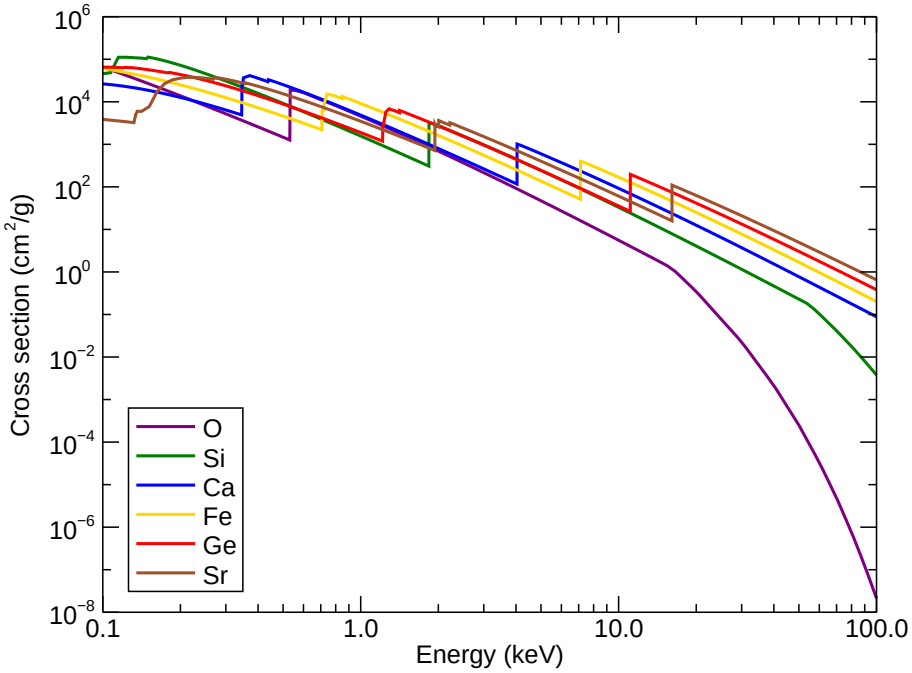

Figure 2.4: Photoionization cross sections of six elements. The discontinuities correspond to the electron binding energies of the (sub) shells. Values were taken from Kissel[5] through the *xraylib* interface.

The discontinuities of these photoelectric cross section curves correspond to the energy dependent contributions of the different occupied shells an atom possesses, each having different electron binding energies. This implies that such a cross section profile must be considered as a superposition of a number of partial photoionization cross section profiles,

one for each occupied shell. An example of the individual contributing photoionization cross sections are shown for Ba in the energy range of 0.1-100 keV in Fig. 2.5.

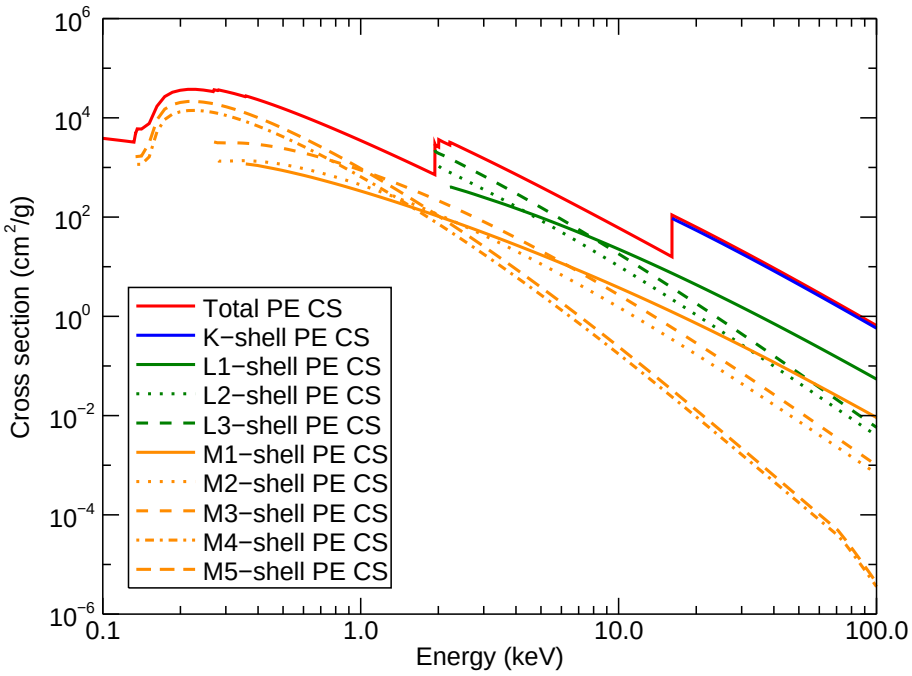

Figure 2.5: Partial photoionization cross sections of Ba. Values were taken from Kissel[5] through the *xraylib* interface.

The partial photoionization cross sections are usually obtained from quantum mechanical calculations[3,5], but are in most cases derived from the total photoionization cross sections through the so-called jump factor approximation. These jump factors are the ratios between the total cross section (mass attenuation coefficient, see Section 2.1.5) just after the edge divided by the value right before the edge[6]. One obtains for the K-shell:

$$J_K = \frac{\sigma_{\text{after}}}{\sigma_{\text{before}}} = \frac{\sigma}{\sigma - \sigma_K} \tag{2.6}$$

The jump factor depends by definition only on the atomic number and shell, and is not a function of the energy. The partial photoionization cross section of the K-shell can be approximated as:

$$\tau_K(E) = \tau(E)\frac{J_K - 1}{J_K} \tag{2.7}$$

Similar expressions may be derived for the other shells and can be found in Brunetti et al [6]. Jump factors produce only reliable results for the partial photoionization cross sections when the incident photons have energies slightly higher than the edge of the element. This is clearly not the case when performing standard XRF experiments, where a large range of elements may be irradiated at energies well above their absorption edges, including the K-edge. A comparison between XRF cross sections obtained using jump factors and (true) partial photoionization cross sections is given in Section 3.2.3.

Strictly speaking, the photoionization cross sections that are obtained from literature and that are shown in the examples, apply only to isolated atoms. In reality, the atoms are part of a material and hence, are influenced by their molecular environment. This influence is apparent when recording absorption data: the absorption edges are shifted by some eV compared to the isolated atom situation, and the absorption profiles display oscillations around the edges. Although this phenomenon forms the basis of techniques such as X-ray Absorption Near Edge Structure (XANES) and Extended X-ray Absorption Fine Structure (EXAFS), it may introduce errors in quantitative XRF since the results depend ultimately upon the reliability of the (partial) photoionization cross sections.

2.1.5 Mass attenuation coefficient

When X-rays pass through matter, then the three effects discussed in the preceding sections will occur simultaneously. The likelihood of each effect will be determined by its cross section. The level of attenuation that the photon beam experience is therefore related to the sum of the three effects:

$$\sigma(Z, E) = \sigma_R(Z, E) + \sigma_C(Z, E) + \tau(Z, E) \tag{2.8}$$

with σ the total absorption coefficient of atom Z at an excitation energy E. If the irradiated sample consists of a number of elements n, each with a weight fraction w_i, then the mass attenuation coefficient is written as:

$$\mu(E) = \sum_{i=1}^{n} w_i \sigma(Z_i, E) \tag{2.9}$$

Given an initial X-ray beam intensity I_0, then the transmitted intensity I after propagation through a material with density ρ and thickness T, is determined by the Lambert-Beer equation:

$$I = I_0 \exp(-\mu(E)\rho T) \tag{2.10}$$

A generalization of this equation can be obtained by considering the case of a sample consisting of m of stacked layers, each with their own composition, thickness and density:

$$I = I_0 \exp\left(-\sum_{j=1}^{m} \mu_j(E)\rho_j T_j\right) \tag{2.11}$$

This equation forms the basis of all absorption calculations related to quantitative XRF, as will be shown in the next chapters.

2.1.6 X-ray fluorescence

The two scattering types that were discussed in Sections 2.1.2 and 2.1.3 only provide limited information about the sample that is being irradiated. Examples include estimates of the thickness and the matrix mean atomic number[7,8]. The photoelectric effect however, has the potential of providing true qualitative and quantitative information about the composition of the sample, through the emission of characteristic photons, called X-ray fluorescence. This occurs through an electron transition from a higher shell to the vacancy created by the photoelectric interaction[1]. The difference between the binding energies of the two shells involved in the transition is released as an X-ray fluorescent photon. It is however possible that this photon is absorbed by another electron in the atom before leaving the atom. This phenomenon is referred to as the Auger effect, causing the emission of a so-called Auger electron, resulting in a situation with two vacancies. A special case of this effect can be observed in shells that have subshells, such as L and M: it is possible that the Auger effect takes place within the subshells[9]. For example, an initial excitation of the L_1 shell may lead to the transition of an electron coming from the L_2 or L_3 subshells. If the transition is non-radiative then the resulting L_1L_2 or L_1L_3 photon may be absorbed in one of the M shells or higher. The vacancy created in the L_2 or L_3 shell may at this point be filled by a radiative transition. This sub-shell transition effect is referred to as a Coster-Kronig transition and is usually quite strong. The likelihood of obtaining a radiative

transition after a photoionization is expressed through the fluorescence yield ω, which is dimensionless and depends on the atom and the excited shell.

The X-ray fluorescence phenomenon is associated with a cross section: the XRF production cross section Q. These cross sections are obtained by multiplying all the quantities that determine the probability of emission of a particular XRF-line: partial photoionization cross section, fluorescence yield and radiative rate. As an example, for the KL_3 line of a particular element, one obtains:

$$Q_{KL3}(Z,E) = \tau_K(Z,E)\omega_K(Z)F_{KL3}(Z) \tag{2.12}$$

with F_{KL3} the radiative rate which is defined as the fraction of radiative transitions that will lead to a particular XRF line (KL_3 in this case). The radiative rates of a number of selected elements are shown in Fig. 2.6.

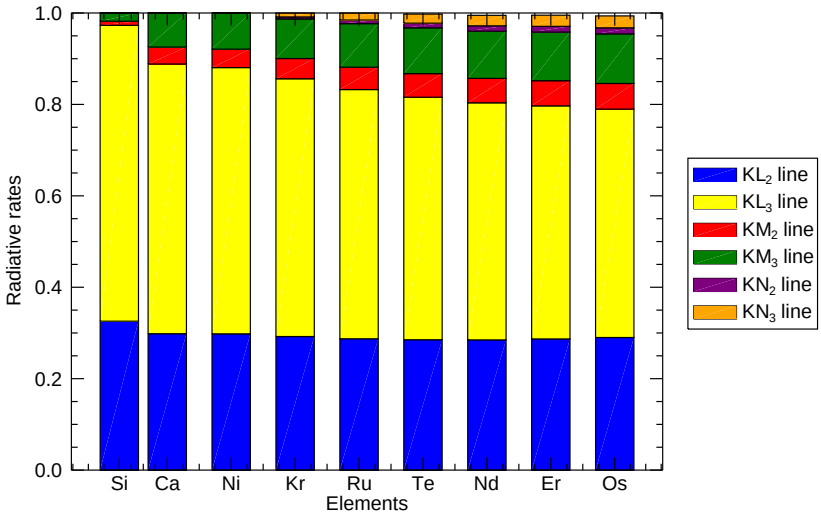

Figure 2.6: Radiative rates of some selected elements. As can be seen from the plot, the number of possible transitions and their intensity depends on the occupation of the different shells. Values are taken from *xraylib* [10].

More complex examples of the XRF production cross sections will be discussed in the next chapter.

2.2 X-ray fluorescence spectrometers

Generally speaking, XRF spectrometers consist of an X-ray source, a sample stage and a detector system. Optionally, the spectrometer may be equipped with monochromatizing and focusing optics, which have the ability to reduce the beam dimensions to (sub-)microscopic levels, allowing for micro- and nano XRF applications. XRF spectrometer systems are divided based on the detection scheme into two categories: energy dispersive (ED) and wavelength dispersive (WD)-XRF. The latter is achieved by having the scattered photons and XRF originating from the sample separated by Bragg diffraction on a single crystal (acting as an analyzer crystal) before being detected. Assuming a fixed detector, with this setup one can scan a wide range of wavelengths by rotating the crystal. Alternatively, simultaneous collection of photons may occur with a fixed-geometry crystal monochromator, if the detector is composed of several individual units or "channels" separated in space.
In this work, only ED-XRF will be considered, therefore throughout the rest of the manuscript the acronym XRF should be considered as an implicit reference to ED-XRF spectroscopy. It should be noted, however, that many of the mathematical derivations are equally valid for WD-XRF spectroscopy, or require only minor modifications. The next sections of this chapter present an overview of the different components that make up an ED-XRF spectrometer.

2.2.1 X-ray sources

Radioisotopes

Certain radioisotopes such as ^{55}Fe and^{109}Cd produce X-rays when decaying through electron capture[11]. In this case, the proton-rich nucleus captures an inner shell electron (typically from the K or L shells), thereby transforming a proton to a neutron, as well as producing a neutrino. The electron vacancy that was created by this process results in an unstable, excited electronic state, which will decay by the transition of an electron from a higher shell. Since the transitions can be either radiative or non-radiative, both characteristic X-ray photons and Auger electrons will be emitted. Although mostly used in medical applications, radioisotopes are also found as a source of X-rays in (portable) XRF spectrometers[12,13]. Their relatively low popularity can be explained by the safety regulations related to radioisotopes, as well as by the time-dependent activity due to the

radioactive decay.

X-ray tubes

A more common source of X-rays are X-ray tubes or X-ray generators. These devices are derivatives of the Crookes tubes, that were instrumental in the discovery of X-rays (see Section 2.1.1), in which the electrons that impact the anode are produced by ionization of the residual air in the tube. In current X-ray tubes (or Coolidge tubes, after their inventor William Coolidge) however, the electrons are produced by the thermionic effect which occurs by heating the cathode filament, usually made from tungsten. The tube current is determined by the temperature of the cathode, thereby becoming the control means for selecting the X-ray tube intensity. The electrons are accelerated towards the anode under the influence of a high voltage electric field, causing them to impact the anode and produce X-rays by two electron–matter interaction types:

Bremsstrahlung electrons are decelerated and deflected as they approach an atomic nucleus. The electron will lose kinetic energy, which is converted into a photon due to the conservation of energy. The energy spectrum that is produced through this phenomenon is continuous, but since the photons may interact with the anode material on their way out through the photoelectric effect, discrete lines will also be produced.

Impact ionization high-energy electrons impacting the anode material may eject electrons from the inner shells of anode atoms, thereby creating vacancies which are filled by transitions from higher shells. If the transition is radiative then an X-ray fluorescence photon, characteristic of the anode material, will be emitted, at a considerably higher intensity than those produced through Bremsstrahlung and subsequent photoionization.

In case of high-power X-ray tubes, the anode is often mounted on a rotor shaft (see Fig. 2.7), allowing it to rotate at high RPM, thereby distributing the electron impact point on a large surface and allowing the anode to cool down. The produced X-rays emanate from the tube through a window (usually made from beryllium), which can be positioned either behind the anode (transmission tube with thin anode) or next to it. The effective source size depends on the area of the anode that was bombarded by electrons, as well as on the angle

under which the anode is seen from the window. The emitted X-ray beam size and divergence is determined by the effective source size and collimation conditions within the tube, as well as by the (optional) focusing optics which will be discussed in Section 2.2.2. The X-ray beam flux is linearly proportional to the temperature of the cathode filament, but it is also influenced by the high voltage since this will determine the extent of the excitation spectrum: the maximum of the Bremsstrahlung will be determined by the voltage, and the discrete lines will only be produced if the voltage is high enough to cause impact ionization. As will be discussed in detail in the next chapters, polychromatic radiation greatly complicates XRF quantification, which is attributed to the required accurate knowledge of the excitation spectrum. This is determined not only by tube current and voltage, but also by the age of the device (degradation through usage). The optional focussing optics usually makes this even more challenging. This can be alleviated to some extent through the use of appropriate absorbers that when placed into the beam, filter out uncertain low-energy spectral components, thereby producing a quasi-monochromatic beam.

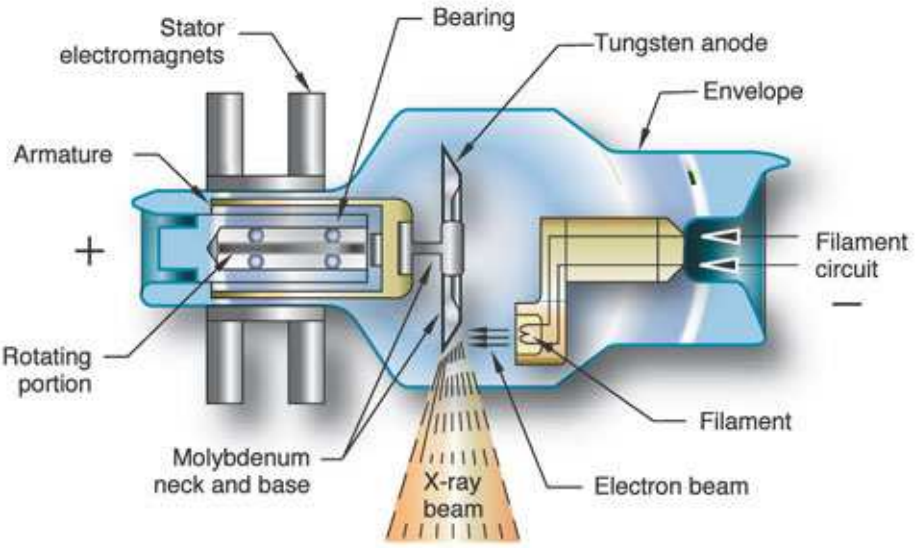

Figure 2.7: Schematic of a typical rotating anode X-ray tube. Source: `http://whs.wsd.wednet.edu/faculty/busse/mathhomepage/busseclasses/radiationphysics/lecturenotes/chapter6/chapter6.html`

Synchrotron radiation

It has been known for over a century that the acceleration of a charged particle will result in the radiation of electromagnetic energy[14]. The development of the betatron and synchrotron electron accelerators led to the first experimental observation of electromagnetic radiation from electrons orbiting in a 70 MeV synchrotron accelerator in 1947 by Elder et al. The emerging electromagnetic radiation, which is called synchrotron radiation (SR) after the source producing it, is generated by the radial acceleration of relativistic electrons (or in some cases positrons) when forced to follow curved tracjectories. The recognition of the unique properties of the synchrotron radiation brought about an explosive development of activity in constructing improved sources for production of the SR and using the radiation in fundamental and applied science.

The original, so-called first generation SR facilities, were designed for use in high energy physics research, such as particle collision experiments. Starting from the 1980s, so-called second generation SR facilities were built with conditions specifically optimized for the production of SR mainly in the X-ray energy range. The unavoidably generated SR was considered a 'nuisance' in these facilities, as it resulted in an energy loss for the accelerated particles. However, due to the unique properties of SR, it was already used for some experiments in a so-called parasitic mode. The so-called third generation facilities were built during the 1990s with radically reduced source sizes and divergencies compared to second generation devices, in which the main sources of SR are insertion devices: periodic magnetic structures, undulators or wigglers, inserted in the straight sections of the synchrotron storage ring. The components of the facilities include a source of electrons or positrons (a so-called positron or electron gun) and an accelerator to produce high-energy beams, usually with a linear accelerator to produce energies up to a few 100 MeV. The accelerated electron/positron beam is subsequently injected into a booster synchrotron and further accelerated to energies in the GeV range. Finally, the electron/positron beam is injected and stored in the actual synchrotron storage ring, as shown in Fig. 2.8. The storage ring houses (electro)magnetic structures for controlling the electron/positron beam during orbiting, so-called radio frequency cavities to supply energy to the beam to compensate for the radiation energy loss, and the actual sources of SR: bending magnets, wigglers and undulators. The SR emitted by the latter sources is guided towards the experimental stations via so-called beamlines, which house a series of X-ray optical elements necessary

to condition the SR beam for specific experiments.

Figure 2.8: Schematic representation of a typical synchrotron, storage ring and associated facilities (pictured is the Soleil synchrotron of Paris, France). An electron gun produces an electron beam which is injected in to a booster ring accelerating the electrons further. Periodically electrons from this booster ring will be inserted into the storage ring that produces the synchrotron radiation at the bending magnets and insertion devices making it available for experiments. Source: `http://www.synchrotron-soleil.fr/`

The synchrotron-produced X-ray beams have unique properties that make them extremely advantageous to use. First of all, SR-beam intensities are many orders of magnitude higher than those produced by conventional X-ray sources. They have a continuous energy distribution so that tunable monoenergetic beams can be produced over a wide range of energies. The photons are highly polarized in the plane of the electron beam orbit, which is extremely important for background reduction in SR X-ray emission-type experiments in particular. SR exhibits very strong natural collimation, it is therefore possible to produce intense beams with little angular divergence. The source size is small and, as a result, the production of intense micro- and nano-beams is feasible. The synchrotron source is

a pulsed source because of the nature of synchrotron-type accelerators. The X-rays are produced in narrow bursts, less than 1 ns in width, and have a time between pulses of around 20 ns or more[14].

In this work, all experimental data was collected at the Hamburg synchrotron radiation laboratory (HASYLAB, Hamburg, Germany) and the European Synchrotron Radiatian Facility (ESRF, Grenoble, France). The former consists of the DORIS (*Doppel Ring Speicher*, double-ring storage) positron storage ring, originally constructed in the 1970s, currently having 31 beamlines in operation. The micro-XRF beamline L, which was used to obtain the XRF spectra shown in Chapters 5 and 6, is equipped with a bending magnet source producing a polychromatic X-ray beam covering the energy range of $\approx$ 3-80 keV, having a size of approximately 1.3 mm by 0.5 mm at the experimental station. The beam size can be reduced to microscopic dimensions by the focusing optics discussed in Section 2.2.2. HASYLAB is only a part of the DESY campus, which includes several synchrotrons as can be seen in Fig. 2.9. Recently the PETRA synchrotron, originally commissioned as a collision particle accelerator, designed for high energy particle physics experiments, has been converted into a high brilliance third generation synchrotron light source, called PETRA III. The associated beamlines are currently being constructed and will be available to users soon.

The ESRF (see Fig. 2.10) currently operates 51 beamlines using synchrotron radiation by insertion devices and bending magnets. Several of its beamlines were used in the scope of this work such as ID13, ID18F and ID22, which provide users with very intense monochromatic micro- and nanoscopic X-ray beams. More profound explanations of these beamlines can be found in Somogyi et al.[16].

2.2.2 X-ray optics

In order to achieve high spatial resolution in microbeam X-ray spectrometers, sophisticated X-ray focusing elements have been developed in order to fulfill the demands to generate intense, highly concentrated X-ray beams. As a result, the methodology of designing and manufacturing X-ray optics has grown in the last decades into a particular branch of physics and technology. Under the title of 'X-ray optics' one can define a wide range of X-ray optical elements exploiting diffraction and refraction phenomena in e.g. crystals, multilayers, Fresnel zone-plates, compound refractive lenses as well as the total external

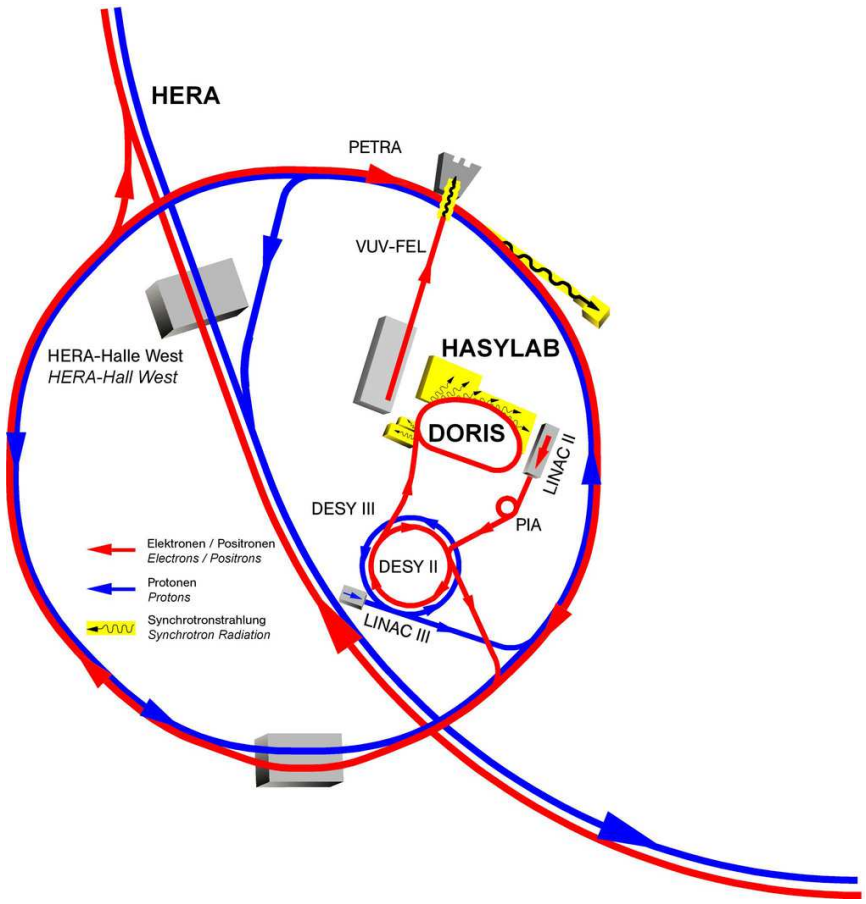

Figure 2.9: Overview of the different accelerators at the *Deutsches Elektronen Synchrotron*, German electron synchrotron. Source: `http://www.lightsources.org`

reflection phenomenon in X-ray mirrors or capillary optics.. These elements are intended to focus, monochromatize or reflect X-rays. Out of the many available options for focusing and monochromatization, only those that where used in the framework of this PhD work will be discussed here.

X-ray monochromatization

The experimental data from synchrotrons found in this work, was acquired at beamlines equipped with a monochromator setup, that allows for the selection of a (narrow) bandwidth from the energy spectrum emitted by bending magnet or insertion device (undulator) sources. Such a setup typically consists of two parallel crystals whose centers are shifted relative to each other. The physical principle that explains the monochromatization is

Figure 2.10: Aerial overview photograph of the European Synchrotron Radiation Facility at Grenoble, Isère, France. Source: `http://www.lightsources.org`

Bragg's law, that yields the angles of diffraction at a given X-ray wavelength from a crystal lattice according to:

$$n\lambda = 2d\sin\theta \tag{2.13}$$

with n an integer corresponding to the various diffraction orders, λ the wavelength of the incident electromagnetic wave, d the spacing between the planes in the crystal lattice, and θ the angle between the incident ray and the scattering planes. When applied to the monochromator setup, this means that when a polychromatic X-ray beam impinges the first monochromator crystal, the diffraction of the different initial wavelengths will occur over wavelength dependent angles. Upon impact on the second crystal under the same angle of incidence, the Bragg condition will be fulfilled again for the wavelength(s) selected by the first crystal (first order and its multiples) as defined by Eq. (2.13). Through variation of the angles of incidence of the two crystals as well as of their relative distances, one can select a given energy band from the original excitation spectrum, whose bandwidth is defined by the properties of crystals or multilayers being used. The use of the second

crystal improves monochromaticity and in a fixed exit configuration it provides a beam position at the sample stage which is independent from the selected monochromator angle (and wavelength). Several types of monochromator materials are in operation at beamlines (in some cases even several types at one beamline) such as Si(111) crystal or multilayers. Each type is characterized by an operational energy range and by the effective bandwidth of the produced monochromatic X-ray beam. An important parameter is also the maximum initial flux they can withstand. Indeed, since the interaction with the crystal generates a considerable amount of heat, one has to be careful not to damage the first crystal of the monochromator setup by the high heat load caused by the polychromatic incident beam. Next to water or cryogenic cooling of the monochromator crystals, filters are being used to remove the lower X-ray energies from the incident spectrum.

Capillaries

Over the past decades, capillary X-ray concentrators have seen increased usage in X-ray spectrometry. These devices operate through repeated total reflection of X-ray photons at the inner wall of the capillary tubes. In micro-XRF, capillaries are used to increase the flux density of the beam of primary radiation impinging on a microscopic spot on the surface of a sample. By scanning the material through the microbeam and recording an XRF spectrum at each position, lateral abundance distributions of major, minor, and sometimes even trace constituents of the sample material may be visualized. Lateral resolutions in the range of 1-100 μm are routinely achieved.
Four major types of capillary X-ray concentrators can be distinguished (see Fig. 2.11):

Straight capillary This is the simplest possible form. During the repeated total reflection of X-rays at the inner walls of the glass tube, the angle of incidence θ_0 remains constant (see Fig. 2.11(a)). They act as mere waveguides and can be used to transport photons from the anode of an X-ray tube to the sample surface, partially eliminating the $\frac{1}{r^2}$ losses that would occur otherwise[17].

Conical capillary This type of capillary operates in a similar manner to straight capillaries but also reduce the X-ray beam down to the dimensions of the end diameter of the taper, as seen in Fig. 2.11(b). Upon each reflection, the angle of incidence θ_i increases by an amount 2γ, i.e. $\theta_i = \theta_0 + (2i - 1)\gamma$. Only those photons for which the angle of

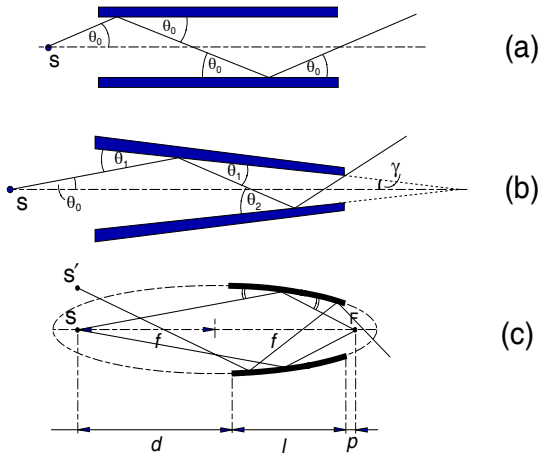

Figure 2.11: Principle of X-ray propagation in (a) straight, (b) tapered and (c) ellipsoidal capillaries. In the last case, the ideal operation occurs when the X-ray source (S) is situated at one focal point of the ellipse and the radiation is focused at the other focal point (F). In the case when the photon originates from a point S' other than the focal point, it is subject to multiple reflections before leaving the device or being absorbed. Figure reproduced from Vincze et al.[17].

incidence of the last reflection ($i = N$) θ_N is smaller than the energy-dependent critical angle of total reflection θ_C will be transmitted by the capillary . Since in the X-ray beam that leaves the capillary the photons may assume all directions $\theta_N \leq \theta_C(E)$ relative to the capillary wall, the emerging beam has a divergence which is of the order of $2\theta_C$. Owing to this considerable divergence (for glass material θ_C, is about 3 mrad at 10 keV) the sample must be placed as close as possible to the exit end of the capillary if the small beam size is to be retained[17].

Ellipsoidal capillary As can be seen in Fig. 2.11(c), photons originating from one focal point S of the ellipse, upon total reflection at the ellipsoidal capillary inner walls, are refocused into the other focal point F. This point may or may not be situated outside the device. The above-described focusing properties apply only to photons that are reflected only once inside the tube. For X-rays that originate from outside the point S, the device behaves in a similar manner to a conical capillary, i.e. these photons are subject to multiple reflections before leaving the tube or being absorbed[17].

Polycapillary Polycapillary X-ray optics are bundles of hollow glass capillary tubes[18]. They differ from single-bore capillaries in that the capillary walls are thin to keep the fractional open area large. For polycapillary optics, focusing or collecting effects come from the overlap of the beams from thousands of capillary channels, rather than from the action within a single tube. As for single-bore capillaries, X-rays can be transmitted down a curved hollow tube as long as the tube is small enough and bent gently enough to keep the angles of incidence less than the critical angle for total reflection, θ_C. A very efficient focusing of X-rays can be achieved by an array of these bent glass tubes (fibres) since they are oriented toward a common focal point. Next to their use as a focusing optics, they are also frequently used as a detector collimator by mounting them in front of a detector as is shown in Fig. 2.12[19]. This so-called confocal XRF spectrometer has been applied successfully in the study of geological, extraterrestrial, biological and artistic samples[19–24]. In this case, a polycapillary half-lens is used which leads to the elimination of single and multiple scattering from outside the microvolume of detection, but due to its high-energy filtering, it further suppresses high-energy scatter peaks, progressively cutting down background intensity above 25 keV. It should be noted however, that this poses a practical limit for the detection of XRF lines as well, limiting the usage of this method. Since the transmission efficiency itself is energy-dependent, this needs to be taken into account when deriving quantification expressions (see Malzer and Kanngiesser[25] and Chapter 4).

Focusing mirrors in Kirkpatrick-Baez geometry

A focusing method based on the principle of total reflection concerns the use of two perpendicularly aligned elliptical total reflection mirrors in a so-called Kirkpatrick-Baez geometry[26]. This system, which is totally achromatic, is very interesting for many microanalytical techniques, and is currently in use at several endstations that focus on nano-imaging applications including the ID13 and ID22 beamlines of the ESRF. Beamspots of a few hundreds of nanometers can be routinely achieved allowing for the retrieval of spatially resolved information at the sub-micrometer level. However, alignment of the two orthogonal mirrors is delicate and needs to be assisted by computer alignment algorithms. Production of these mirrors requires a very high degree of surface smoothness and shape accuracy, rendering them quite expensive. Since they operate based on the total reflection principle, monochromatization is achieved separately by a monochromator setup installed before the total-reflection mirrors. By coating the two mirrors with multilayers, the incident angle

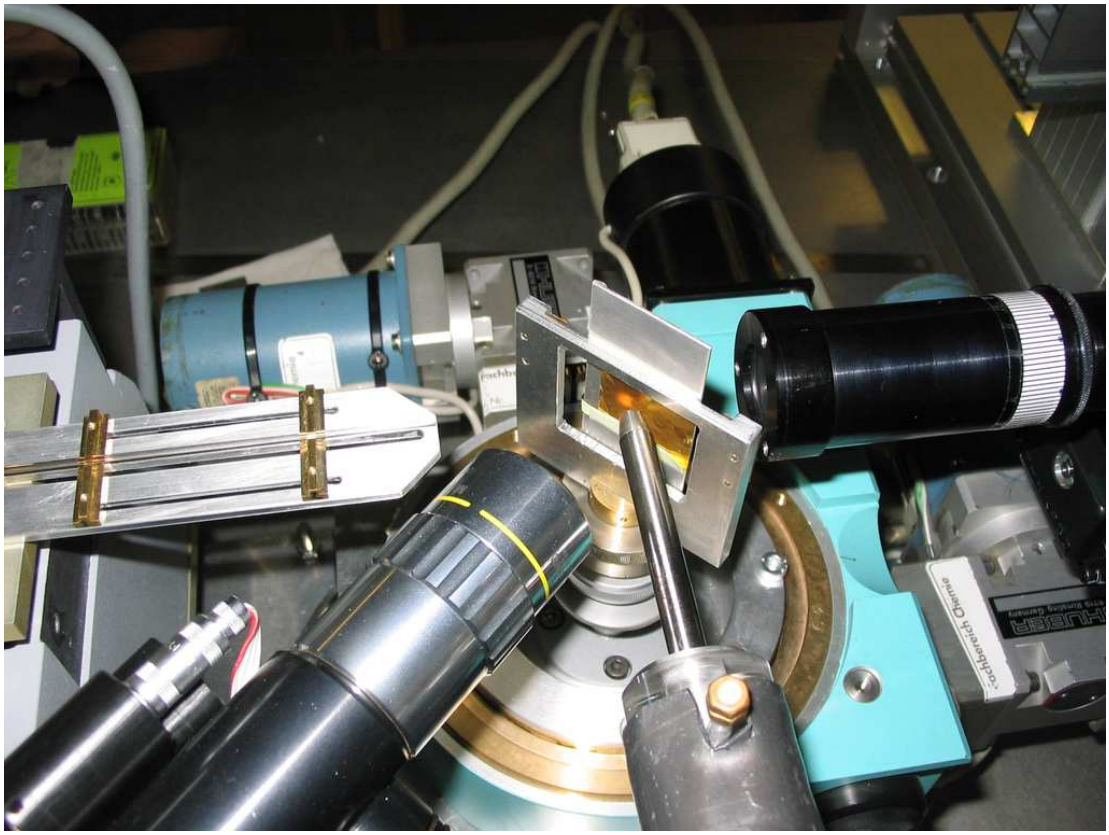

Figure 2.12: Confocal ED-XRF setup as used at HASYLAB beamline L. The polycapillary is mounted in front of the detector collimator while the initial focusing is accomplished with an ellipsoidal (single bounce) capillary on the left.

(defined by Bragg's law) is about ten times larger than the critical angles needed for total reflection on uncoated mirrors. Therefore, the aperture of this kind of optics becomes considerably larger for a given mirror length and in conjunction with the large bandpass of multilayers, and due to the fact that no additional monochromatization is required, the photon flux on the sample can be extremely high. This comes, however at a cost as the achromacity is lost. Usually, there is a double crystal monochromator (e.g. Si-111) positioned in the beam before the Kirkpatrick-Baez system, which may relieve this concern.

Compound refractive lenses

It is also possible to focus X-ray beams using refraction[27]. Since the refractive index is less than one for X-rays, focusing cannot occur when an X-ray beam propagates from

vacuum or air to an optically more dense material having regular (convex) lens shapes. However, the opposite situation yields the required effect: X-ray beams may be focused by refracting on spherical, parabolical or elliptical-shaped holes made inside of solids, i.e. by using concave lenses made of solid materials. A series of holes is necessary in order to obtain a high enough optical phase shift due to the fact that the refractive index is very close to 1. An example can be seen in Fig. 2.13. These so-called compound refractive lenses can be fabricated from a number of low-Z materials. Depending on the photon energy range Be, Al, Si, etc. lenses can be used. Microbeams from several 10 μm down to 0.05 μm can be routinely produced. This setup is in use at several beamlines of the *Angströmquelle Karlsruhe* synchrotron (ANKA, Karlsruhe, Germany) and the ID13 and ID18F beamlines[28] of the ESRF and at the PETRA-III P06 nanoprobe.

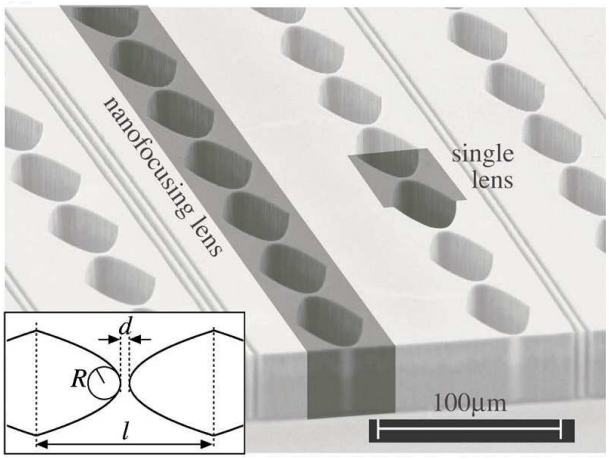

Figure 2.13: Scanning electron micrograph of Si compound refractive nanofocusing lenses. A single lens and a nanofocusing lens are outlined by dark shaded areas. Figure adapted from Schroer et al.

2.2.3 X-ray detection

The detection of X-rays may occur in a number of ways. Historically, X-rays were first detected using a fluorescent screen, which was soon followed by the advent of photographic plates (still widely used in medical applications) and ionization chambers. The latter consists of a gas filled enclosure between two conducting electrodes. When the gas is ionized by incoming radiation, the positively charged ions and the electrons move to the electrodes

of the opposite polarity, thus creating an ionization current which is then subsequently measured by a galvanometer[29]. Both of these detection methods provide no information about the energy of the detected X-rays, but register merely the intensity of the ionizing radiation. The first device designed to enable the measurement of the energy of the ionizing radiation particles is the proportional counter, which has the advantage of being cheap, easy to operate, but comes with a low detection efficiency for (high energy) X-rays, unless it is made rather large. An alternative with much higher detection efficiency for high energy photons is the scintillation detector. These use a scintillating material coupled to photo multipliers, photodiodes or CCDs for the detection of fluorescence light. Their benefits compared to other methods include their small size and efficiency for hard X-rays when using scintillating crystals of higher atomic number elements. The detection speed may be increased when large areas of scintillating material are coupled to a large number of light detectors leading to a high-efficiency imaging detector. Their main disadvantage is their poor energy resolution, which reduces the capability of the system to distinguish photons closely separated in energy.

Semiconductor detectors

A considerably better energy resolution was achieved with the introduction of semiconductor detectors in the early 1960s[29]. The reason behind this is that the mean energy needed to create one primary elementary charge is about 20 to 30 eV for gases while for semiconductors it is only a few eVs, reducing the statistical fluctuations by about a factor of 3. Initially planar Si(Li) and Ge(Li) detectors were developed which are the semiconductor analogue of the ionization chamber, and operate by the ionization of the semiconductor material by incoming photons. The initial interaction can be either through the photoelectric effect or scattering (Rayleigh or Compton), depending on the energy of the photon and the detector material. If ionization occurs, the primary electron (photoelectron of Compton electron), may excite bound electrons from the valence band to the conduction band. These secondary electrons, if sufficiently energetic, may release additional electrons by a cascading process that finally leads to a large number of free electron-hole pairs that can be collected at the electrodes of the device. The collected charge is then converted into an electrical signal which is subsequently stored in a multichannel analyzer. Since the number of generated electron-hole pairs is proportional to the initial photon energy, so will the height of the signal pulse. Usually the semiconductor material is doped with

acceptors (which provide free holes, p-type material) and donors (which introduce free electrons, n-type material) in order to increase the conductivity of the material. This has led to the development of the Si diode detector based on a junction between two p and n semiconductor materials. When this diode is reverse biased, the bulk material is depleted from the free charge and the carriers produced by the interaction of photon in the bulk can be suitably collected at the electrodes by means of the applied field. A continuous flow of charge thermally generated within the bulk material (dark current) is also collected at the detector electrodes, contributing to a statistical spread in the measurement of the signal charge. However, the dark current value can be highly reduced by suitably cooling the detector. The depletion depth that can be achieved by reverse biasing a conventional silicon pn detector is usually limited to 0.3-1 mm. Thicker depletion depths (5-10mm) can be reached by means of the lithium drifting process. In a lithium-drifted silicon detector or Si(Li), lithium ions, which act as donors, are driven through a large volume of a high purity silicon crystal, which tends to be p-type, in order to obtain an "intrinsic"-like bulk material by means of the compensation of the donors and acceptors impurities concentrations. The excess lithium on the surface of deposition on the crystal results in a highly doped n+ layer which acts as an electrical contact, while the uncompensated p region on the opposite is contacted by either a metallic contact or a thin p+ layer. In a Si(Li) detector, the lithium continues to drift significantly at room temperature. Therefore, in order to prevent an undesired redistribution of the lithium dopants, a conventional Si(Li) detector must always be kept cold (usually at liquid nitrogen temperature), even when not operated.
Typically Si(Li) detectors are used in the energy range from a few hundreds eV up to a about 40 keV. Energy resolutions of commercial detectors is of the order of 135 eV at the Mn-K_α line (5.9 keV).

Silicon drift detectors

Although still widely in use, Si(Li) detectors are nowadays being replaced in favor of so-called Silicon Drift Detectors (SDD)[29]. They are characterized by a very low capacitance of the electrode that collects the signal charge, which allows to achieve short shaping times, as well as by a low leakage current, removing the need for the cumbersome liquid nitrogen cooling. Electrical Peltier cooling is used instead, leading to a far more compact device. The semiconductor materials are arranged in a different way compared to the Si(Li) detectors:

a transversal field of ring electrodes causes charge carriers to drift towards the collection electrode. This allows for significantly higher count rates, explaining their popularity for X-ray fluorescence experiments both at synchrotron facilities and in laboratory experiments.

Detection efficiency

The detection efficiency is defined as the fraction of the total number of photons emitted by the source, which effectively interacts in the detector volume and is completely absorbed[29,30]. It comprises several effects:

geometrical efficiency Only a fraction of the photons that are emitted by the sample may actually enter the detector volume. It is given by the ratio of the solid angle under which the detector is seen by the XRF source and 4π.

intrinsic efficiency Depending on the energy of the incoming photons, the composition of the detector crystal and its thickness, one calculates the intrinsic efficiency, expressing the fraction of photons that will interact with the detector material, according to the Lambert-Beer equation (see also Eq. (2.10)):

$$\eta_i = 1 - \exp(-\mu\rho x) \tag{2.14}$$

where μ is the mass attenuation coefficient at the given photon energy, ρ is the density of the detector crystal, and x is the detector crystal thickness.

photopeak efficiency When the photons interact in the detector material either through the photoelectric effect or the Compton effect, it is possible that the respective fluorescence and Compton scattered photons escape from the detector. This leads to the generation of so-called escape peaks in the spectrum, whose energies are equal to the difference between the energy of the primary photon E and the energy of the escape photon E_f. The photopeak efficiency can be defined as the ratio of main peak intensity and the total intensity of the main and its escape peaks.

window efficiency The detector window absorbs a fraction of the incoming photons. In order to minimize this effect, the window is usually made of Be or ultra thin polymers, in order to increase the detection efficiency of the low energy photons. It is determined

through the Lambert-Beer equation Eq. (2.10). The product of the window efficiency and the intrinsic efficiency is referred to as the quantum efficiency.

2.3 X-ray fluorescence quantification methodology

The ultimate goal in quantitative X-ray fluorescence analysis is the conversion of the raw spectral data into concentrations. It consists of a two step procedure. First, one evaluates the spectrum in order to extract the net XRF-line intensities, thereby taking into account the physical processes that occur during detection of the photons. In the second step, the net-line intensities are converted into the elemental concentrations, taking into account the physical processes that take place in the sample material. The necessary procedures will be discussed in this section.

2.3.1 X-ray fluorescence spectrum evaluation

Fundamental aspects

XRF spectral data recorded with a semiconductor detector is always tainted with measurement noise[31]. Two categories can be distinguished: amplitude and energy noise. The former is related to the statistical nature of the counting process, in which random events such as the arrival of X-ray photons at the detector, are observed during a finite time interval. For such a process, the probability of observing N counts when the "true" number of counts is N_0 is given by the Poisson distribution:

$$P(N, N_0) = \frac{N_0^N}{N!} \exp(-N_0) \tag{2.15}$$

Each channel of the recorded spectrum contains a number of counts that obeys this Poisson distribution. The statistical nature of the counting process (Poisson statistics) causes the typical fluctuations which are observed in a spectrum.

The energy noise causes the characteristic lines in ED-XRF spectra much wider than their natural linewidth of 5-10 eV. The broadening is due to the nature of the photon-to-charge conversions that occur in the detector material, as well as due to the electronic noise in the pulse amplification and processing circuit. This will cause X-ray photons with an energy E, which on average corresponds to a pulse height stored in channel i, from time to time to be detected as slightly higher or lower pulses, causing these photons to be scored in channels

above and below i, respectively. Accordingly, characteristic X-ray lines will appear in the spectrum as relatively broad (135-250 eV, the energy resolution), nearly Gaussian-shaped peaks in the spectrum.
Spectrum evaluation would be a trivial exercise in the absence of the two noise contributions, since a spectrum would consists merely of a well-defined continuum on which sharp discrete lines were superimposed. These contributions, however, can never be eliminated entirely. They can be reduced by longer measurement times or more intense beam (amplitude noise) and by using a detector and associated electronics of good quality and by shielding the system from external electronic noise sources (energy noise). It is highly recommended to optimize the experimental parameters using these suggestions since after the data has been recorded it is impossible to extract more information from the spectrum using mathematical procedures than was present originally.
ED-XRF spectra are determined by a number of phenomena that will contribute to their quality. Their understanding is essential when performing quantitative XRF analysis.

Characteristic lines Due to their natural linewidth, X-ray fluorescence lines exhibit a Lorentzian distribution[31,32]. The peak profiles that are observed with a semiconductor detector are subsequently the convolution of this Lorentzian distribution with a nearly Gaussian detector response function. The resulting Voigt profile is usually approximated as a Gaussian since the natural linewidth is small ($\approx$ 10 eV) compared to the much larger width of the detector response function. Only at very high energies (Th and U K-lines) does the Lorentzian contribution become significant and should it be taken into account. The peak shape is sometimes clearly asymmetric: distinct tailing may be seen at the low energy side of the peak and a shelf extending to zero energy, which is due to incomplete charge collection caused by detector imperfections (dead layer and regions of low electric field). The observed emission spectrum of an element is the result of many transitions. All of these lines should be considered when evaluating the spectrum. In this case, it is important not to rely on the natural radiative transition probabilities when considering the line ratios since these will change due to absorption effects in the sample and in the detector crystal.

Spectral continuum The continuum or spectral background is on the one hand determined by the coherent and incoherent scattering of the excitation radiation by the sample,

and on the other hand by detector incomplete charge collection effects. It is therefore governed by the excitation spectrum, the sample composition and detector parameters. In particular the Compton peak is difficult to model due to its broad and non-Gaussian distribution caused by scattering over a range of angles and by the Doppler effect[33]. The incomplete charge collection of intense fluorescence lines in the spectrum complicates the continuum. The cumulative effect of the incomplete charge collection of all lines causes the apparent continuum at lower energies to be significantly higher than expected based on the primary continuum generating processes.

Escape peaks One of the detector artifacts mentioned in a preceding section concerns the occurrence of escape peaks that result from the escape of Si-K (or Ge-K/Ge-L) photons from the detector crystal after photoelectric absorption of the impinging photon near the edges (both the front and the back) of the detector[29,31]. The deposited energy by the incoming photon is in this case reduced by the energy of the escaping fluorescence photon. The escape fraction f may be calculated using the following formula (for the Si K-line)[34]:

$$f = \frac{N_e}{N_p + N_e} = \frac{1}{2}\omega_K \left(1 - \frac{1}{J_K}\right)\left[1 - \frac{\mu_K}{\mu_I}\ln\left(1 + \frac{\mu_K}{\mu_I}\right)\right] \tag{2.16}$$

where μ_I and μ_K are the mass-attenuation coefficients of silicon at the energies of the incident X-ray photon and that of the escaping Si-K$_{\alpha,\beta}$ photon, respectively, ω_K is the K-shell fluorescence yield, and J_K is the K jump ratio of the K-shell of silicon. In Chapter 5, another method is discussed for the calculation of these escape peak ratios, based on the use of Monte Carlo simulations. This method has the extra advantage of simultaneously producing the escape peak ratios of the Compton escape peaks, which become important at high energies and lead to the generation of a continuous band in the low energy region with two maxima, corresponding to the forward and backscattered Compton photons.

Pileup and sum peaks Pileup occurs when two or more photons enter the detector within a time interval smaller than the time required to process one pulse. This results in the emergence of sum peaks at positions in the spectrum that correspond with the sum of the energies of the photons involved in the pileup. They are often found when a few large peaks at lower energies dominate the spectrum. The intensity of the sum peaks is count-rate dependent, therefore they can be reduced by performing the experiment with a lower primary beam intensity.

Discrete nature of a pulse–height spectrum Pulse–height spectra are essentially discrete histograms that represent continuous functions[31]. Considerable systematic errors may be caused when these continuous functions are digitalized into too few channels. If the peak contains less than 2.5 channels at the FWHM, the peak area estimate, for example, obtained by summing the channel contents is largely overestimated[31]. This lower limit of 2.5 channels at FWHM corresponds to a spectrometer gain of 60 eV/channel for a peak width of 150 eV. In practice, 40 eV/channel or lower is recommended, otherwise peak position and width determinations and the results of spectrum fitting become unreliable.

Least-squares fitting using analytical functions

In X-ray fluorescence spectra, the relevant analytical information is found in the net peak areas which can be calculated by eliminating peak overlap and estimating/subtracting the background continuum. Three methods are available that deal with the spectral continuum[31,35]:

1. the continuum can be suppressed or eliminated by a suitable mathematical filter.

2. the continuum can be estimated and subtracted from the spectrum prior to the estimation of the net peak areas.

3. the continuum can be estimated simultaneously with the other features in the spectrum.

Only the last method will be discussed since it was the only one that was used in this work, using the software packages AXIL[36] and PyMca[37]. The net peak areas themselves were fitted by the above mentioned software packages using the least-squares fitting method which is by far the most flexible procedure for evaluating complex X-ray spectra. In this method, an algebraic function, including analytically important parameters such as the net areas of the fluorescence lines, is used as a model for the measured spectrum. The object function (χ^2) is defined as the weighted sum of squares of the differences between this model $y(i)$ and the measured spectrum y_i over a region of the spectrum:

$$\chi^2 = \sum_{i=1}^{n} \frac{1}{\sigma_i^2}[y_i - y(i, a_1, \ldots, a_m)]^2 \tag{2.17}$$

where σ_i^2 is the variance of data point i, normally taken as $\sigma_i^2 = y_i$, and a_j are the parameters of the model function. The goal of this algorithm is to retrieve the optimum values of the parameters, which is accomplished by minimizing χ^2. Mathematically speaking this is equivalent to setting the partial derivatives of χ^2 with respect to the parameters to zero:

$$\frac{\partial \chi^2}{\partial a_j} = 0, j = 1, \ldots, m \tag{2.18}$$

Paramount in solving Eq. (2.18) is the construction of the analytical function that accurately describes the recorded spectrum. This requires an appropriate model for the background, the characteristic lines of the elements and for all other features present in the spectrum such as the escape and sum peaks. Although the response function of the energy-dispersive detector is, to a good approximation, Gaussian, deviation from the Gaussian shape needs to be taken into account. Failure to construct an accurate model will result in systematic errors, which under certain conditions may lead to gross positive or negative errors in the estimated peak areas. On the other hand, the fitting function should remain simple, with as few parameters as possible. In general, the fitting model consists of two parts:

$$y(i) = y_B(i) + \sum_P y_P(i) \tag{2.19}$$

where $y(i)$ refers to the calculated content of channel i and the first part describes the spectral continuum (background) and the second part the contributions of all peak-like structures. Several analytical expressions are available to model the continuum, depending on the excitation conditions and on the width of the fitting region. Since it is virtually impossible to generate an adequate physical model that describes the continuum, due to the large number of processes that contribute to it, very often a polynomial expression is used such as linear polynomials and exponential polynomials[31,36]:

$$Y_B(i) = a_0 + a_1(E_i - E_0) + a_2(E_i - E_0)^2 + \ldots + a_k(E_i - E_0)^k \tag{2.20}$$

$$Y_B(i) = a_0 \exp\left[a_1(E_i - E_0) + a_2(E_i - E_0)^2 + \ldots + a_k(E_i - E_0)^k\right] \tag{2.21}$$

where k is the degree of the polynomial and $(a_0, \ldots, a_K)$ are fitting parameters. The degree of the polynomial is usually adjustable, which is often necessary to obtain a correct fit.

Since the response function of most solid-state detectors is predominantly Gaussian, all mathematical expressions used to describe the fluorescence lines involve this function. The only exception occurs when dealing with K-lines of high Z elements, as was mentioned in an earlier section, in which case a Voigt profile is required. Therefore, a first approximation to the profile of a single peak is given by:

$$\frac{A}{\sigma\sqrt{2\pi}} \exp\left[-\frac{(x_i-\mu)^2}{2\sigma^2}\right] \tag{2.22}$$

where A is the peak area (counts), σ is the width of the Gaussian expressed in channels, and μ is the location of the peak maximum, which correspond to the 3 parameters that characterize a Gaussian peak, and subsequently need to be optimized by the algorithm. Due to the presence of the exponential function in Eq. (2.22), it is clear that a non-linear least-squares procedure is required to find optimum values for the latter two parameters. This implies starting values for these parameters as well as that a solution can only be obtained iteratively. Assuming a spectrum consisting of 10 elements and 2 peaks for each element, then 60 parameters would have to be optimized, which makes it unlikely that the fit would terminate successfully at the global minimum. The number of parameters can be reduced however, by introducing some simplifications. For example, the concept of optimizing the position and width of each peak separately is redundant since the fluorescence line energies are known with a very good accuracy. The peak pattern in the spectrum is directly related to the elements that are present in the irradiated sample. Based on those elements, all X-ray lines that constitute the spectrum can be predicted, as well as their energies. The peak function Eq. (2.22) can therefore be written in function of the energy instead of the channel number. Defining E_0 as the energy of channel 0 and expressing the spectrum gain ΔE in eV/channel, the energy of channel i is given by:

$$E(i) = E_0 + \Delta E \times i \tag{2.23}$$

and the Gaussian peak can be written as

$$G(i, E_j) = \frac{\Delta E}{s\sqrt{2\pi}} \exp\left[-\frac{(E_j - E(i))^2}{2s^2}\right] \tag{2.24}$$

with E_j the energy of the X-ray line and s the peakwidth given by

$$s^2 = \sigma^2_{\text{noise}} + 3.58 F E_j \tag{2.25}$$

where σ_{noise} is the electronic noise contribution to the peak width (standard deviation), F is the Fano factor, and 3.85 is the mean energy required to produce an electron-hole pair in silicon. The four parameters E_0, ΔE, σ_{noise} and F will be refined during the fitting, thereby reducing the dimensionality of the problem. In our example covering the case of 10 elements and 2 peaks, the number of parameter dropped from 60 to 24 parameters. It does require however, that the user supplies additional information: the energies of the different peaks as well as reliable initial guesses for the zero channel energy, gain, Fano factor and the electronic noise. The zero energy and the gain can be obtained using a calibration routine while the Fano factor and electronic noise are system characteristics which are usually known with high precision for a given detector.

The number of fitting parameters may be reduced even further by modeling entire elements, instead of single peaks. Indeed, a number of lines can be considered as linked, such as the KL_2 and KL_3 doublets or all K-lines of an element. The group can be fitted with a single area parameter A representing the total number of counts of all the lines in the group, yielding the equation

$$y_P(i) = A \sum_{j=1}^{N_P} R_j G(i, E_j) \tag{2.26}$$

where G are the Gaussians for the various lines with energy E_j and relative intensities R_j. The summation runs over all lines in the group (N_P) with $\sum R_j = 1$. Although the transition probabilities of all lines that originate from a vacancy in the same (sub)shell are constant, the actual relative intensities are influenced by the absorption and enhancement effects in the sample and in the detector. Therefore, one usually employs the tabulated transition probabilities as starting values in the iterative procedure, but are subsequently allowed to vary. This second modification has the extra advantage of enhancing the resolving capabilities of the procedure in case of considerable peak overlap. Further possible enhancements of the algorithm include the usage of modified peak-shapes that take into account tailing, incomplete charge collection, absorption corrections, sum and escape peaks but these will not be discussed here. Several mathematical algorithms are available to solve the non-linear least-squares problem such as the gradient method, first-order expansion and the Marquardt algorithm.

2.3.2 X-ray fluorescence quantification procedures

The procedures that were described in the previous section allow for the extraction of the net intensities of the X-ray fluorescence lines in a spectrum. In order to obtain the corresponding concentrations, procedures need to be employed that take into account the physical effects that occur in the sample and its environment such as the X-ray fluorescence production probability, the absorption and enhancement effects. The simplest method available is called empirical calibration in which a series of materials is constructed with a known composition that is (very) similar to an unknown sample[9]. Measuring the series of (standard) materials with varying concentration levels of the elements of interest allows for the construction of a calibration curves relating the concentration of particular elements with their corresponding measured net-line intensities. While this method is useful for XRF bulk analysis, it is not suited for the study of heterogeneous samples composed of several phases with varying compositions and densities. To deal with more general situations, a number of different methods have been developed over the years. In this work, focus lies on the so-called fundamental parameter method adapted for confocal XRF analysis and inverse Monte Carlo simulations of X-ray fluorescence spectra. A short description of these methods will be given in this section, while more elaborate explanations are presented in Chapters 4 to 6.

Fundamental parameter method

Initially developed by Sherman[38] during the 1950s, the fundamental parameter method (FPM) exploits the theoretical relation between the net-line intensities and elemental concentrations. In its simplest form, it applies to a situation in which a homogeneous sample is being irradiated by a monochromatic X-ray beam, as is shown in Fig. 2.14.
It is assumed that the X-ray beam consists of photons having an energy E_0 and a flux I_0, directed at a sample defined by a single infinitely wide layer with thickness T and density ρ, and consisting of n elements with weight fractions w_i ($\sum_{i=1}^{n} w_i = 1$). An uncollimated detector is positioned at a distance D from the sample and has an active area A_{DET}. The position of the sample is determined with respect to the incoming beam and the detector with the angles α and β, respectively.
In the following derivations, a coordinate system will be used that is defined according to the X-ray beam (x-axis) and the detector axis (y-axis). A z-axis will be introduced

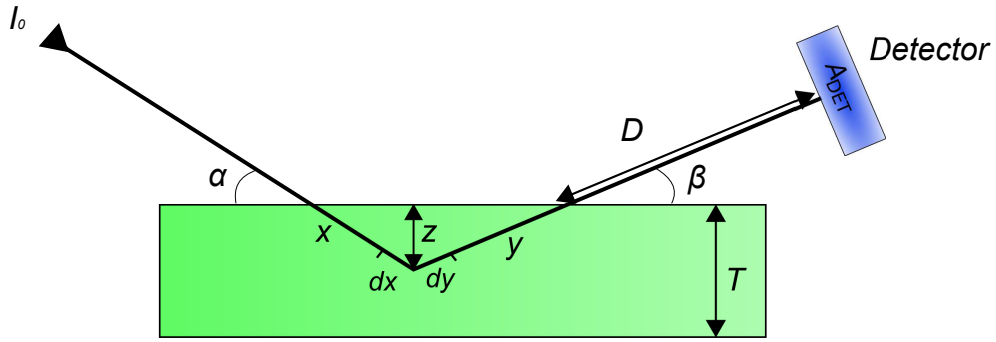

Figure 2.14: Depiction of the model covered by the simplest form of the fundamental parameter method. I_0 stands for the flux of the impinging beam. α and β represent the angles of the incoming and outgoing beams, respectively. T represents the thickness of the sample, D the distance between sample and detector surface and A_{DET} the active detector area.

coinciding with the sample normal. These definitions lead to the following equations:

$$x = \frac{z}{\sin\alpha} \tag{2.27}$$

$$y = \frac{z}{\sin\beta} \tag{2.28}$$

$$\mathrm{d}x = \frac{\mathrm{d}z}{\sin\alpha} \tag{2.29}$$

$$\mathrm{d}y = \frac{\mathrm{d}z}{\sin\beta} \tag{2.30}$$

The derivation of the FPM consists of three steps. Firstly, one determines the K_α (similar equations may be derived for other lines) fluorescence intensity of element i that is generated within the interval $(x, x + \mathrm{d}x)$ using the Lambert-Beer formula:

$$\mathrm{d}I^*_{i,K_\alpha} = I_0 \exp(-\mu_0\rho x)\mu_0\rho\mathrm{d}x\frac{w_i\tau_{i,K}}{\mu_0}p_{K_\alpha}\omega_K \tag{2.31}$$

$$= I_0 \exp(-\mu_0\rho x)w_i Q_{i,K\alpha}\rho\mathrm{d}x \tag{2.32}$$

with:

- w_i = the weight fraction of element i
- $\mu_0 = \mu(E0) = \sum_{j=1}^{n} w_j\mu_{j,0}$ = the attenuation coefficient of the sample at the energy E_0

- $\tau_{i,K}$ = K-shell partial photoionization cross-section of element i
- p_{K_α} = transition probability
- ω_K = fluorescence yield
- $Q_{i,K\alpha} = \tau_{i,K} p_{K_\alpha} \omega_K$ = XRF production cross-section

The second step includes the determination of the *detected* K_α intensity of element i that was generated at a depth $(z, z + \mathrm{d}z)$:

$$\mathrm{d}I_{i,K_\alpha} = \mathrm{d}I^*_{i,K_\alpha} \frac{\Omega_{DET}}{4\pi} \exp(-\mu_1 \rho y) \tag{2.33}$$

$$= I_0 \frac{\Omega_{DET}}{4\pi} \exp\left(-\mu_0 \rho x\right) \exp(-\mu_1 \rho y) w_i Q_{i,K_\alpha} \rho \mathrm{d}x \tag{2.34}$$

$$= I_0 \frac{\Omega_{DET}}{4\pi} \exp\left[-\left(\underbrace{\frac{\mu_0}{\sin\alpha} + \frac{\mu_1}{\sin\beta}}_{\chi} \right) \rho z \right] w_i Q_{i,K_\alpha} \rho \mathrm{d}x \tag{2.35}$$

$$= I_0 \frac{\Omega_{DET}}{4\pi \sin\alpha} w_i Q_{i,K_\alpha} \exp(-\chi \rho z) \rho \mathrm{d}z \tag{2.36}$$

$$= I_0 G w_i Q_{i,K_\alpha} \exp(-\chi \rho z) \rho \mathrm{d}z \tag{2.37}$$

with:

- Ω_{DET} = detector solid angle
- $\mu_1 = \mu(E_{i,K_\alpha}) = \sum_{j=1}^{n} w_j \mu_{j,i,K_\alpha}$ = the attenuation coefficient of the material at energy $E_{i,K\alpha}$
- $G = \frac{\Omega_{DET}}{4\pi \sin\alpha} \approx \frac{A_{DET}}{4\pi D^2 \sin\alpha}$ = geometry factor

Integration over the sample thickness yields the total detected intensity:

$$I_{i,K_\alpha} = \int_0^T \mathrm{d}I_{i,K_\alpha} \tag{2.38}$$

$$= I_0 G w_i Q_{i,K_\alpha} \rho \int_0^T \exp(-\chi\rho z)\mathrm{d}z \tag{2.39}$$

$$= I_0 G w_i Q_{i,K_\alpha} \rho T \left(\frac{1-\exp(-\chi\rho T)}{\chi\rho T}\right) \tag{2.40}$$

$$= I_0 G w_i Q_{i,K_\alpha} \rho T A_{corr} \tag{2.41}$$

A_{corr} stands for the so-called *absorption correction term*, representing the influence of the matrix effects. The value of A_{corr} lies between 0 and 1: for infinitesimally thin samples, A_{corr} can be approximated as 1. Considering the dependence of A_{corr} on w_i, it is clear that this system of equations (one equation for every element i) can only be solved in an iterative manner, with the exception of the case when one assumes A_{corr} equals 1, which corresponds to the case of infinitely thin samples.
The Fundamental Parameter Method, as it was presented in this section, has a few limitations and drawbacks:

- Only first order interactions are being considered. Secondary effects, such as enhancement, are ignored. Extensions exist that take higher order effects into account, but these complicate the equations dramatically.
- The exciting beam is assumed to be monochromatic, suitable for micro-XRF experiments using monochromatic synchrotron radiation
- The detector is assumed to be ideal: the detector efficiency is 100 %, independent of the detected energy.
- The sample is assumed to be homogeneous and to have a flat surface.
- The XRF cross sections Q are often not well known, especially when dealing with L and M-lines.

Some of these issues can be circumvented by using a standard reference material (SRM) based approach. This is accomplished by using Eq. (2.41) for both the unknown sample and an SRM, yielding:

$$\frac{I_{i,K_\alpha}^{(u)}}{I_{i,K_\alpha}^{(s)}} = \frac{I_0^{(u)} G w_i^{(u)} Q_{i,K_\alpha} \rho^{(u)} T^{(u)} A_{corr}^{(u)}}{I_0^{(s)} G w_i^{(s)} Q_{i,K_\alpha} \rho^{(s)} T^{(s)} A_{corr}^{(s)}} \tag{2.42}$$

Since both denominator and numerator share the same geometry factor G (assuming both SRM and unknown were measured under the same circumstances!) and the same XRF production cross section $Q_{i,K\alpha}$, Eq. (2.42) can be simplified into:

$$\frac{I_{i,K_\alpha}^{(u)}}{I_{i,K_\alpha}^{(s)}} = \frac{I_0^{(u)} w_i^{(u)} \rho^{(u)} T^{(u)} A_{corr}^{(u)}}{I_0^{(s)} w_i^{(s)} \rho^{(s)} T^{(s)} A_{corr}^{(s)}} \tag{2.43}$$

Clearly, the equations derived in this section can be modified to accommodate more complex situations, for example, when the sample is composed of several layers (including air layers) or when a confocal setup is being used. However this lies outside of the scope of this section and will be discussed in depth in Chapter 4.

Monte Carlo simulations in quantitative X-ray fluorescence

Superior quantification methods are based on the use of Monte Carlo simulations. These refer to a category of algorithms in which statistical sampling is employed to approximate solutions to quantitative problems that are too complex to solve analytically. The sampling is performed using random numbers from an appropriate probability density function that models the problem. The methods name was chosen by J. von Neumann, S. Ulam and N. Metropolis, in reference of the famous Monte Carlo casino, and was first mentioned in their 1949 publication[39]. Initially the Monte Carlo method was used by these researchers during the Manhattan Project in Los Alamos, as a tool to investigate radiation shielding, necessary for protection against ionizing radiation. The Monte Carlo method was quickly recognized to be a powerful numerical technique and was therefore rapidly adopted by the scientific community. It is used in all fields of science ranging from economy (e.g. simulating the stock market) and mathematics (e.g. solving of multidimensional integrals) to natural sciences (e.g. study of physico-chemical problems such as particle transport)[40]. In this section, some of the components that constitute the Monte Carlo method will be discussed.

Pseudo Random Numbers Initially Monte Carlo simulations were performed using tables of random numbers. With the advent of digital computers however, implementa-

tions migrated quickly to the use of pseudo random number generators (PRNG), which are mathematical algorithms that produce arrays of numbers with a finite period. Many PRNGs are available, but an often encountered algorithm is the 32-bit linear congruential random number generator[40]:

$$X_{n+1} = (aX_n + c) \texttt{ mod } 2^{32} \tag{2.44}$$

with X a pseudo random number, a an integer value referred to as the *magic* multiplier and c and integer constant. The modulo operator `mod` returns the remainder after the long division. These PRNGs take a starting value or seed (X_0), and based on this number a unique array is produced with a cycle length of 2^{32}. It is obvious that great care needs to be taken in the selection of the seed. Often seeds are obtained based on a mathematical formula based on the process identifier and the time. In this work however, superior quality random seeds were used, collected from the `/dev/random` device of a UNIX(-like) system which generates a stream of bits based on the user input peripherals (keyboard, mouse) and network traffic[41]. Such random number generators are cryptographically secure and are often used in the generation of key pairs necessary for authentication. In Chapter 5, more information will be presented on how these seeds are used in the software that was developed in the framework of this PhD.
With the advent of multithreading technologies, specific issues arise when using PRNGs: when each thread has its own PRNG instance, each started with its own (high quality) seed, it becomes likely that after some time the threads will produce identical sequences of random numbers due to the relatively small cycle, leading to unreliable results. The problem was circumvented in this work by relying on a superior PRNG, the Mersenne Twister[42], that has a cycle length of $2^{19937} - 1$, rendering the probability to encounter identical sequences of random numbers produced by different PRNGs in a multithreaded programs negligible. In the case of the most often used implementation of the Mersenne-Twister PRNG (MT19937), one needs 624 iterates before being able to predict all future iterates.

Distribution functions Consider a statistical experiment in which N possible values of a discrete random variable x are observed and f_i corresponds to the frequency (probability mass function) of each possible value x_i. The probability p_i of observing a discrete variable X with a value equal to x_i can be expressed as:

$$p_i = p(X = x_i) = f_i \tag{2.45}$$

with $\sum_{i=1}^{N} f_i = 1$. The cumulative distribution function P determines the probability that X takes on a value less than or equal to x_j:

$$P(X \leq x_j) = \sum_{i=1}^{j} p_i \text{ with } j \leq N \tag{2.46}$$

where $P(x < x_1) = 0$ and $P(x \geq x_N) = 1$. Since P takes on values in the interval $[0, 1]$, it may be used to relate the value of a continuous random variables r, uniformly distributed on $[0, 1]$, to it. This allows for the retrieval of a discrete value x_j corresponding to r:

$$x_j = P^{-1}(r) \tag{2.47}$$

This method is known as random sampling from the inverse cumulative probability distribution and constitutes the basis of the Monte Carlo method.
If the random variable x is continuous and distributed in the interval $[x_{\min}, x_{\max}]$ with the probability density function $p(x)$, then the corresponding cumulative distribution function $P(x)$ is given by:

$$P(x) = \frac{\int_{x_{\min}}^{x} p(z)dz}{\int_{x_{\min}}^{x_{\max}} p(z)dz} \tag{2.48}$$

Inverse sampling by means of a random number r leads to the production of values for x according to $P(x)$:

$$x = P^{-1}(r) \tag{2.49}$$

It will be shown in later chapters that it is not always possible to calculate the inverse P^{-1} analytically due to the complexity of the function. In some cases even the analytical expression of the probability density function $p(x)$ will not be known. This occurs when numerical tables are being used for which it is assumed that $p(x)$ is calculated for sufficient values of x to be considered a continuous function.

Monte Carlo simulations were applied in this work in several distinct ways. A first application will be discussed in Chapter 4 were they were used as a tool to perform error estimation related to our implementation of the fundamental parameter method, yielding

detailed error distributions that would otherwise have been impossible to obtain using the classic error propagation formulas. In Chapter 5, a complete Monte Carlo based algorithm will be described that was developed to simulate the complete spectral response of an ED-XRF spectrometer. Several subroutines within the main algorithm are in their own right Monte Carlo simulations necessary to compute various key components of the spectrum such as the escape peak ratios and the detector pile-up.

2.4 Software development

The earlier sections in this chapter have already indicated the computational nature of this work. Indeed, a considerable amount of time has been spent implementing the different algorithms that will be discussed in the next chapters. In this section, a short overview will be given of the different software tools that were necessary for the development of the software based on this work.

2.4.1 Programming languages

Four different programming languages were used in our software packages: C, Fortran, IDL and Perl. This variety can be attributed to the fact that each of these languages has its own strengths and weaknesses. Their characteristics will be discussed in this section.

The C language

The C programming language was pioneered by Dennis Ritchie at AT&T Bell Laboratories in the early 1970s. It took several years, however, before this programming language began to experience widespread popularity and support, due to a lack of available compilers. Initially, C's growth in popularity was driven in part, by the even faster growth in popularity of the UNIX operating system which was also developed at Bell Laboratories. This operating system had C as its standard programming language and in fact was mostly written in C itself.
With the advent of the IBM PC and MS-DOS era, more and more vendors started developing and selling their own C compilers, mostly according to the appendix found in the first C programming text "The C Programming Language", by Brian Kernighan and Dennis

Ritchie[43]. However, since this appendix did not provide a complete and unambiguous definition of C, the vendors were left to interpret some aspects of the language on their own. This situation was mitigated by a standardization of the C language, carried out by the American National Standards Institute (ANSI) and published in 1990. The standard was adopted by the International Standards Organization (ISO) where it was called ISO/IEC 9899:1990. Since that time, the C language has been augmented, leading to the so-called ANSI C99 standard (ISO/IEC 9899:1999). It should be noted however, that at the time of writing, this standard is not (completely) supported by all implementations, most notably the Microsoft Visual Studio C compiler has no support.
C is usually referred to as a "higher-level language", while at the same time it provides capabilities that enable the user to interact with the hardware and deal with the computer on a much lower level. This is because, although C is a general-purpose structured programming language, it was originally designed with systems programming applications in mind and, as such, provides the user with an enormous amount of power and flexibility[44]. It comes therefore at no surprise that the C language is particularly powerful at all operations involving input and output (I/O), a characteristic that was often exploited in this work[45].
Very often, implementations of more recent programming languages are themselves written in C such as Perl[46], IDL[47], Python, Java, Ruby, Matlab, Lua etc. Such languages allow for the development of software that links directly to C functions (bindings), which is often advantageous since routines compiled in C are usually considerably faster compared to if they would have been implemented in the language itself. This feature was used in this work, when for example data calculated in Fortran was passed to IDL for visualization, before being redirected to Perl for output to XLS (Microsoft Excel) files. In each of these cases, C was used to ensure proper forwarding of the variables.

The Fortran language

Fortran is considered to be the "grandfather" of all scientific computer languages and is one of the first "higher-level languages". Initially developed during the 1950s by IBM, it revolutionized programming and interaction with computers as it allowed programmers to write a desired algorithm as a series of standard algebraic equations, that would be converted by a compiler into machine instructions[48]. Although the first iteration of Fortran had only a limited feature set, it was quickly adopted as it relieved the programmers of

the tedious burden of using assembler language, and were able to concentrate more on the problem at hand. This led to a large influx of scientists and engineers into the world of software development, since they were offered a relatively simple language to tackle their problems without them needing to be computer experts. After the initial release in April 1957, which was followed by two language updates in 1958, Fortran IV was released in 1962 and became the standard for the next 15 years. This version was adopted as an ANSI standard in 1966, and it came to be known as Fortran 66. Updates of the standard were released as Fortran 77, Fortran 90, Fortran 95, Fortran 2003 and recently Fortran 2008[49]. An important feature of Fortran is its backwards compatibility: since over the last decades, millions of lines of have been written using legacy Fortran, the Fortran standard guarantees that these programs are compilable with recent Fortran compilers.
Fortran has dominated the area of scientific programming ever since its first release and has seen continual use in computationally intensive areas such as numerical weather prediction, finite element analysis, computational fluid dynamics, computational physics and computational chemistry. It is one of the most popular languages in the area of high-performance computing and is the language used for programs that benchmark and rank the world's fastest supercomputers[50].
It has been extensively used throughout this work, especially for the subroutines that focus on numeric computations. Two compilers were used in generating our software: Intel Fortran (commercial) and gfortran (open source).

The Perl language

Originally developed by Larry Wall in 1987 as a glue language for UNIX, Perl has long since spread to most other operating systems. Because it runs on nearly every platform, Perl is considered as one of the most portable programming environments available today[51]. Although initially conceived as a simple text-processing language, it has now become a high-level, general-purpose, interpreted, dynamic programming language with object-oriented features[52] and is released under both the Artistic License and the GNU General Public License. Since it is both powerful and accessible, it has become popular in every imaginable field, from aerospace engineering to molecular biology, from mathematics to linguistics, from graphics to document processing, from database manipulation to network management. Perl was used in this work through the `Spreadsheet::WriteExcel` and `Spreadsheet::ParseExcel` modules that are offered through the Comprehensive Perl

Archive Network (CPAN) which hosts over 90000 modules that extend Perl's functionality. As their name suggests, these two modules allow for the creation, reading and modification of Microsoft Excel files. Through these features, it was possible to automatically create reports of FPM based XRF quantification results, including spectra and error estimation distribution histograms.

The IDL language

Virtually all figures used in this work were produced using IDL, short for Interactive Data Language: a commercial closed-source software package distributed by ITT-VIS. It is vectorized, numerical, interpreted and commonly used for the interactive processing of large amounts of data, and is specialized in image processing. These reasons have led to its application in space science, where it is used by the European Space Agency and National Aeronautics and Space Administration (NASA). Open source alternatives are available such as the GNU Data Language project which strives for full syntax compatibility with IDL.

2.4.2 Software dependencies

The different software packages and utilities for the quantification of XRF datasets that were devised in the framework of this PhD have been built around a number of libraries. In addition, a number of standardized file formats were used in order to facilitate input/output operations. With the exception of IDL, all of the employed external libraries are distributed freely and under open source licenses.

xraylib

By far the most used external library in this work concerns the *xraylib* library which provides access to a large number of X-ray related databases such as line energies, edge energies, cross sections etc. The development of *xraylib* was started as a collaboration between the University of Sassari and the ESRF, with the first results published in 2004 discussing the characteristics of the package[6]. This package was chosen over others such as XCOM[53], mucal[54] and Elam's database[55], due to its comprehensive nature and ease of use. Starting in 2008, development was continued by our group in collaboration with the ESRF and the original authors, culminating in an open source project, downloadable

at `http://github.com/tschoonj/xraylib`. Our contributions to the *xraylib* package can be found in Chapter 3.

GNU Scientific Library

The GNU Scientific Library (GSL) consists of a collection of routines dedicated to numerical computing, implemented in C[56]. Although the library covers a wide range of topics, this work uses for the most part only the random number generators (Mersenne Twister) and the random number distribution functions (uniform, exponential, discrete, Gaussian and Lorentzian). These functions were not accessed directly, but through the Fortran bindings FGSL[57].

Hierarchical Data Format Version 5

Our Monte Carlo simulation package that will be discussed in Chapters 5 and 6 makes extensive use of Hierarchical Data Format Version 5 (HDF5) files for storage of the pre-computed scattering inverse cumulative distribution functions, the geometry dependent detector solid angles and the detector dependent escape peak ratios. HDF5 files are particularly suited for this purpose since they were designed to store and organize large amounts of numerical data[58]. The datasets stored within the files can be accessed through either a C, C++, Fortran or Java application programming interface (API) using a POSIX like syntax `/path/to/resource`.

Extensible Markup Language

All our quantification software make use of so-called Extensible Markup Language (XML) files. XML is a standard of the World Wide Web Consortium (W3C) for the syntax of formal markup languages that allows for the representation of structured data in a plain text form[59]. This representation is both machine- and human-readable. XML uses so-called elements and attributes to structure the data, whose syntax is defined by the XML specifications. These specifications, however, do not set the names for these elements and attributes since this determination depends on the goal of the XML-file. It is closely related to the hypertext markup language (HTML), which is used to generate web pages. A large number of software libraries and programming interfaces have been developed that allow for the parsing and creation of XML documents, and have become essential components

for all operating systems. In this work, the handling of XML files was performed using the libxml2 library, which is released under the open source MIT license.

Extensible Stylesheet Language

XML files can be transformed into file formats such as HTML, Portable Document Format (PDF), Scalable Vector Graphics (SVG), plain text or simply other XML files using so-called Extensible Stylesheet Language Transformations (XLST)[60]. This is accomplished through the definition of an XSL file (essentially an XML file) that contains a set of rules that will determine the nature of the transformation. Next, the transformation itself is performed by an XLST processor, producing the required outputfiles. Such transformations have been used extensively throughout this work (in particular related to the Monte Carlo simulations), leading to the creation of HTML, SVG, CSV and SPE files, containing different representations of the acquired simulation results.

OpenMP

With the advent of computer systems equipped with multiple (multicore) CPUs, several programming techniques have been developed that harness this newly acquired computational power. One very frequently used method called multithreading, employs so-called threads, which are the smallest units of processing that can be scheduled by an operating system[45]. By dividing the workload of a particular process over a number of threads, each of which can be assigned to a single CPU, a performance gain can be achieved that is theoretically equal to the number of CPUs in the system. Compilers cannot analyze a computer code to the extent that efficient multithreaded machinecode is produced automatically. Instead, the responsibility is left to the user for inserting the appropriate code segments that arrange the creation and termination of the threads, as well as the synchronization of variables shared by the threads. The API that is required to accomplish this (e.g. POSIX threads for UNIX and UNIX-like operating systems) is often cumbersome, not portable, and requires significant rewrites of existing non-multithreaded code. These issues can be circumvented in many cases through the use of the OpenMP (Open Multi-Processing) API that supports multi-platform multithreaded programming in C, C++ and Fortran, on most processor architectures and operating systems[61]. The API consists of a set of compiler directives, library routines and environment variables that influence run-

time behavior. The directives are used to delimit the sections of the code that are suitable for multithreading and will subsequently be subjected by the compiler to the insertion of the appropriate function calls. Additional directives declare which variables are assumed to be shared by the threads and those that are private to the individual threads. The typical programming model obtained with OpenMP is shown in Fig. 2.15.

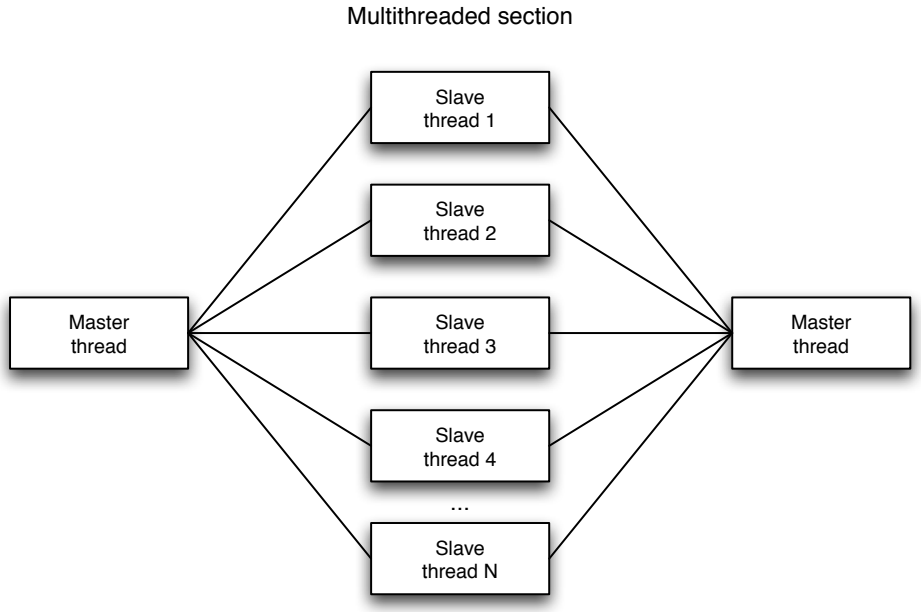

Figure 2.15: Schematic representation of the execution flow of an OpenMP based program. Initially the process is created with a single master thread which executes sequentially until an OpenMP parallel region construct is encountered. At this point a team of N threads is created, which execute blocks of code in parallel. When all threads reach the end of parallel region construct, they synchronize and terminate, leaving only the master thread.

Bibliography

[1] A. Markowicz, X-ray Physics, in: R. Van Grieken, A. Markowicz (Eds.), Handbook of X-ray Spectrometry, CRC Press, 2nd edition, 2001.

[2] C. Raven, Microimaging and Tomography with High Energy Coherent Synchrotron X-Rays, Ph.D. thesis, RWTH Aachen, 1998.

[3] D. Cullen, J. Hubbell, L. Kissel, EPDL97: The Evaluated Photon Library, Technical Report UCRL-50400 Vol. 6 Rev. 5, Lawrence Livermore National Laboratory Report, 1997.

[4] J. Hubbell, W. Veigele, E. Briggs, R. Brown, D. Cromer, R. Howerton, Atomic form factors, incoherent scattering functions and photon scattering cross sections, J. Phys. Chem. Ref. Data 4 (1975) 471–538.

[5] L. Kissel, RTAB: the Rayleigh scattering database, Radiat. Phys. Chem. 59 (2000) 185–200.

[6] A. Brunetti, M. Sanchez del Rio, B. Golosio, A. Simionovici, A. Somogyi, A library for X-ray-matter interaction cross sections for X-ray fluorescence applications, Spectrochim. Acta Part B 59 (2004) 1725–1731.

[7] L. Vincze, K. Janssens, F. Adams, A general Monte-Carlo simulation of Energy-Dispersive X-ray-Fluorescence Spectrometers .1. Unpolarized radiation, Homogeneous samples, Spectrochim. Acta Part B 48 (1993) 553–573.

[8] L. Vincze, K. Janssens, F. Adams, M. Rivers, K. W. Jones, A general Monte Carlo simulation of ED-XRF spectrometers. II: Polarized monochromatic radiation, homegeneous samples, Spectrochim. Acta Part B 50 (1995) 127–147.

[9] M. Mantler, Quantitative Analysis, in: B. Beckhoff, B. Kanngiesser, N. Langhoff, R. Wedell, H. Wolff (Eds.), Handbook of Practical X-Ray Fluorescence Analysis, Springer, 2006.

[10] T. Schoonjans, A. Brunetti, B. Golosio, M. Sanchez del Rio, V. A. Solé, C. Ferrero, L. Vincze, The xraylib library for X-ray—matter interactions. Recent developments, Spectrochim. Acta Part B (2011). In press, doi:10.1016/j.sab.2011.09.011.

[11] N. Langhoff, A. Simionovici, X-Ray Sources, in: B. Beckhoff, B. Kanngiesser, N. Langhoff, R. Wedell, H. Wolff (Eds.), Handbook of Practical X-Ray Fluorescence Analysis, Springer, 2006.

[12] B. Ertugral, G. Apaydin, U. Cevik, M. Ertugrul, A. I. Kobya, K_β/K_α X-ray intensity ratios for elements in the range $16 \leq Z \leq 92$ excited by 5.9, 59.5 and 123.6 keV photons, Radiat. Phys. Chem. 76 (2007) 15–22.

[13] T. He, R. Gardner, K. Verghese, An improved Si(Li) detector response function, Nucl. Instrum. Methods Phys. Res., Sect. A 299 (1990) 354–366.

[14] K. W. Jones, Synchrotron Radiation-Induced X-ray Emission, in: R. Van Grieken, A. Markowicz (Eds.), Handbook of X-ray Spectrometry, CRC Press, 2nd edition, 2001.

[15] F. Elder, A. Gurenwitsch, R. Langmuir, H. Pollock, Radiation from Electrons in a Synchrotron, Phys. Rev. 71 (1947) 829–830.

[16] A. Somogyi, M. Drakopoulos, L. Vincze, B. Vekemans, C. Camerani, K. Janssens, A. Snigirev, F. Adams, ID18F: a new micro-x-ray fluorescence end-station at the European Synchrotron Radiation Facility (ESRF): preliminary results, X-Ray Spectrom. 30 (2001) 242–252.

[17] L. Vincze, K. Janssens, F. Adams, A. Rindby, Detailed ray-tracing code for capillary optics, X-Ray Spectrom. 24 (1995) 27–37.

[18] C. MacDonald, W. Gibson, Applications and advances in polycapillary optics, X-Ray Spectrom. 32 (2003) 258–268.

[19] L. Vincze, B. Vekemans, F. Brenker, G. Falkenberg, K. Rickers, A. Somogyi, M. Kersten, F. Adams, Three-Dimensional Trace Element Analysis by Confocal X-ray Microfluorescence Imaging, Anal. Chem. 76 (2004) 6786–6791.

[20] F. Brenker, L. Vincze, B. Vekemans, L. Nasdala, T. Stachel, C. Vollmer, M. Kersten, A. Somogyi, F. Adams, W. Joswig, J. Harris, Detection of a Ca-rich lithology in the Earth's deep (> 300 km) convecting mantle, Earth Planet. Sci. Lett. 236 (2005) 579–587.

[21] B. De Samber, G. Silversmit, K. De Schamphelaere, R. Evens, T. Schoonjans, B. Vekemans, C. Janssen, B. Masschaele, L. Van Hoorebeke, I. Szaloki, F. Vanhaecke, K. Rickers, G. Falkenberg, L. Vincze, Element-to-tissue correlation in biological samples determined by three-dimensional X-ray imaging methods, J. Anal. At. Spectrom. 25 (2010) 544–553.

[22] V. G. Mihucz, G. Silversmit, I. Szaloki, B. De Samber, T. Schoonjans, E. Tatar, L. Vincze, I. Virag, J. Yao, G. Zaray, Removal of some elements from washed and cooked rice studied by inductively coupled plasma mass spectrometry and synchrotron based confocal micro-X-ray fluorescence, Food Chem. 121 (2010) 290–297.

[23] G. Silversmit, B. Vekemans, S. Nikitenko, S. Schmitz, T. Schoonjans, F. E. Brenker, L. Vincze, Spatially resolved 3D micro-XANES by a confocal detection scheme, Phys. Chem. Chem. Phys. 12 (2010) 5653–5659.

[24] Z. Smit, K. Janssens, K. Proost, I. Langus, Confocal mu-XRF depth analysis of paint layers, Nucl. Instrum. Methods Phys. Res., Sect. B 219 (2004) 35–40.

[25] W. Malzer, B. Kanngiesser, A model for the confocal volume of 3D micro X-ray fluorescence spectrometer, Spectrochim. Acta Part B 60 (2005) 1334–1341.

[26] A. Simionovici, P. Chevallier, Methodological Developments and Applications, in: B. Beckhoff, B. Kanngiesser, N. Langhoff, R. Wedell, H. Wolff (Eds.), Handbook of Practical X-Ray Fluorescence Analysis, Springer, 2006.

[27] A. Snigirev, V. Kohn, I. Snigireva, A. Souvorov, B. Lengeler, Focusing high-energy x rays by compound refractive lenses, Applied Optics 37 (1998) 653–662.

[28] C. Schroer, O. Kurapova, J. Patommel, P. Boye, J. Feldkamp, B. Lengeler, M. Burghammer, C. Riekel, L. Vincze, A. van der Hart, M. Kuchler, Hard x-ray nanoprobe based on refractive x-ray lenses, Appl. Phys. Lett. 87 (2005) 124103.

[29] F. Scholze, A. Longoni, C. Fiorini, X-Ray Detectors and XRF Detection Channels, in: B. Beckhoff, B. Kanngiesser, N. Langhoff, R. Wedell, H. Wolff (Eds.), Handbook of Practical X-Ray Fluorescence Analysis, Springer, 2006.

[30] A. T. Ellis, Energy-Dispersive X-ray Fluorescence Analysis Using X-ray Tube Excitation, in: R. Van Grieken, A. Markowicz (Eds.), Handbook of X-ray Spectrometry, CRC Press, 2nd edition, 2001.

[31] P. Van Espen, Spectrum Evaluation, in: R. Van Grieken, A. Markowicz (Eds.), Handbook of X-ray Spectrometry, CRC Press, 2nd edition, 2001.

[32] J. E. Fernandez, V. Scot, Self-enhancement effects on XRF K-lines due to natural width, X-Ray Spectrom. 38 (2009) 175–181.

[33] M. Van Gysel, P. Lemberge, P. Van Espen, Description of Compton peaks in energy-dispersive x-ray fluorescence spectra, X-Ray Spectrom. 32 (2003) 139–147.

[34] S. Reed, N. Ware, Escape peaks and internal fluorescence in X-ray spectra recorded with lithium drifted silicon detectors, Journal of Physics E-Scientific Instruments 5 (1972) 582–584.

[35] B. Vekemans, K. Janssens, L. Vincze, F. Adams, P. Van Espen, Comparison of several background compensation methods useful for evaluation of energy-dispersive X-ray fluorescence spectra, Spectrochim. Acta Part B 50 (1995) 149–169.

[36] B. Vekemans, K. Janssens, L. Vincze, F. Adams, P. Van Espen, Analysis of X-Ray-Spectra by Iterative Least-Squares (AXIL) - New Developments, X-Ray Spectrom. 23 (1994) 278–285.

[37] V. A. Sole, E. Papillon, M. Cotte, P. Walter, J. Susini, A multiplatform code for the analysis of energy-dispersive X-ray fluorescence spectra, Spectrochim. Acta Part B 62 (2007) 63–68.

[38] J. Sherman, The theoretical derivation of fluorescent X-ray intensities from mixtures, Spectrochim. Acta (1955) 283–306.

[39] N. Metropolis, S. Ulam, The Monte Carlo method, Journal of the American Statistical Association 44 (1949) 335–341.

[40] D. Roet, Monte Carlo simulation of the electron-solid interaction with emphasis on scanning electron microscopy, Ph.D. thesis, Universiteit Antwerpen, 2011.

[41] Linux Programmer's Guide: random, urandom - kernel random number source devices, `http://www.kernel.org/doc/man-pages/online/pages/man4/random.4.html`, 2011.

[42] M. Matsumoto, T. Nishimura, Mersenne twister: a 623-dimensionally equidistributed uniform pseudorandom number generator, ACM Trans. Modelling Comput. Simulation 8 (1998) 3–30.

[43] B. Kernighan, D. M. Ritchie, The C Programming Language, Prentice Hall, second edition, 1988.

[44] S. G. Kochan, Programming in C, Developer's Library, Sams Publishing, third edition, 2004.

[45] W. R. Stevens, S. A. Rago, Advanced Programming in the UNIX Environment, Professional computing series, Addison-Wesley, second edition, 2006.

[46] T. Jenness, S. Cozens, Extending and Embedding Perl, Manning, 2003.

[47] R. Kling, Calling C from IDL, Kling Research and Software, 2nd edition, 2001.

[48] M. Metcalf, J. Reid, M. Cohen, Modern Fortran explained, Numerical Mathematics and Scientific Computation, Oxford University Press, seventh edition, 2011.

[49] S. J. Chapman, Fortran 90/95 for Scientists and Engineers, McGraw-Hill, second edition, 2004.

[50] E. Loh, The Ideal HPC Programming Language, ACM Queue 8 (2010) 30–38.

[51] L. Wall, T. Christiansen, J. Orwant, Programming Perl, O'Reilly, third edition, 2000.

[52] R. L. Schwartz, b. d. foy, T. Phoenix, Intermediate Perl, O'Reilly, 2nd edition, 2006.

[53] M. Berger, J. Hubbell, S. Seltzer, J. Chang, J. Coursey, R. Sukumar, D. Zucker, K. Olsen, XCOM: Photon cross section database, `http://www.nist.gov/pml/data/xcom/index.cfm`, 1987.

[54] P. Bandyopadhyay, C. Segre, MUCAL, `http://www.csrri.iit.edu/mucal.html`, 2005.

[55] W. Elam, B. Ravel, J. Sieber, A new atomic database for X-ray spectroscopic calculations, Radiat. Phys. Chem. 63 (2002) 121–128.

[56] M. Galassi, J. Davies, J. Theiler, B. Gough, G. Jungman, P. Alken, M. Booth, F. Rossi, GNU Scientific Library Reference Manual, Network Theory Ltd., third edition, 2009.

[57] R. Bader, A Fortran binding for the GNU Scientific Library, SIGPLAN Fortran Forum 26 (2007) 4–11.

[58] The HDF Group, Hierarchical data format version 5, `http://www.hdfgroup.org/HDF5`, 2000-2011.

[59] Extensible Markup Language (XML) 1.0, `http://www.w3.org/TR/REC-xml/`, 2008.

[60] Extensible Stylesheet Language (XSL) (Version 1.1), `http://www.w3.org/TR/xsl/`, 2006.

[61] The OpenMP Application Programming Interface Specification, `http://openmp.org/wp/openmp-specifications/`, 1997-2011.

Chapter 3

The *xraylib* library for X-ray–matter interactions

3.1 Introduction

Quantitative X-ray fluorescence (XRF) methods draw extensively from databases of physical parameters for X-ray – matter interactions. Fundamental parameter based methods for example, need access to attenuation and XRF production cross sections and fluorescence line energies. Monte Carlo methods require in addition (un)polarized differential scattering and partial photoionization cross sections, fluorescence yields, (radiative) transition probabilities and more depending on the features implemented in the code. Over the last decades, the acquisition of these parameters has been the subject of extensive research and multiple tabulations can be found throughout the literature. Some published results were obtained from experimental data, while others were derived from quantum mechanical calculations. This situation implies a difficulty for researchers: out of the many different datasets available, which are most reliable? Unfortunately there is no straightforward answer to this question, demonstrated by others[1]. Recently an initiative was started within the framework of the European X-ray Spectrometry Association to measure all relevant fundamental parameters[2]. Several metrology and research institutes such as the Laboratoire National Henri Becquerel/Commissariat à l'Energie Atomique (LNE-LNHB), Physikalisch-Technische Bundesanstalt (PTB) and National Institute of Standards and Technology (NIST) have already pledged their support. Results, however, are not expected to emerge in the near future, considering the comprehensive nature of the task.

Preliminary examinations have already been conducted by the working groups, and have identified some of the issues that are associated with the existing XRF databases. It has been noted for example, that the edge and line energies, line intensities and fluorescence yields of low Z elements are influenced by chemical bonding[3]. A comparison of several photoionization cross section databases has revealed large discrepancies at low Z and high energies due to the high relative uncertainties[4]. In general, very poor agreement was found below 1 keV and around the L- and M-edges.

A second problem encountered with the many existing X-ray databases is their accessibility: only very few have ever ventured into creating a software package that allows for extracting the required data in a convenient manner. Examples include the XCOM[5] package which is distributed by NIST, and MUCAL[6], a library and executable developed at the Illinois Institute of Technology. The former comes in the form of an executable written in Fortran 77 and contains cross sections for scattering[7,8] and photoionization interactions[9]. The latter consists of the McMaster X-ray cross section tables[10] and the fluorescence yields of Krause[11]. Two versions are available from MUCAL: one written in Fortran 77, the other in ANSI C. A more recent and comprehensive example concerns the work of Elam et al.[12] who have compiled several databases of relevant fundamental parameters into a single unstructured ASCII text file. These parameters include atomic weights, densities, edge energies, jump ratios, fluorescence yields, Coster-Kronig transition probabilities, XRF line energies, and various cross sections. In order to access the contents of this file, the authors have developed a computer code written in C++, with bindings for Perl and Fortran. Around 10 years ago, the authors of the present work initiated the development of a software library, called *xraylib*, with the goal of providing convenient access to a large number of different fundamental parameters, important in the field of XRF quantification methodology. A paper was published in 2004, detailing the features of the package at that time[13]. Development, however, never ceased and the library has seen many enhancements and extensions in recent years that will be described in the next sections, along with a short review of the initial features. It is important to note that the included databases were selected by the authors and reflect their personal preferences, based on their experiences. The authors have never aimed to produce datasets of their own, whether through experiments or computational work, and this lies beyond the scope of this work. The work presented in this chapter refers to version 2.15.0 of *xraylib* that was publicly released in June 2011.

3.2 The *xraylib* application programming interface

The functions from the *xraylib* application programming interface (API) provide access to the databases within the library. In this section, the different databases that constitute the library shall be discussed. A full overview of the API is given in Table A.1.

3.2.1 Cross section data (Compton, Rayleigh and photoionization)

The three main photon–matter interaction types in the 0.1-1000 keV energy range are Compton (inelastic) scattering, Rayleigh (elastic) scattering and photoionization. The tabulations of the scattering cross sections found in *xraylib* are taken from Elam et al.[12] The photoionization cross sections are taken from Kissel et al.[14], and are calculated as the weighed sum of individual partial (subshell) photoionization cross sections. The weights in this case correspond to the electronic occupation of the different subshells. Since these databases consist, for each element, of an array of energies with the corresponding cross sections, interpolation is required to determine cross sections at any arbitrary energy. In *xraylib*, this is accomplished using a cubic spline interpolation routine, which requires access to the second derivative values of the cross sections and are also stored in the library. Since the photoionization cross section profiles display discontinuous behaviour at the absorption edges, care has to be taken to avoid erroneous interpolation near these energies. This has been accomplished by setting the second derivatives to zero at the edge energies. Photons may also interact with matter through other processes than the three previously mentioned. An important example concerns the X-ray resonant Raman scattering phenomenon which becomes the dominant inelastic scattering process as the exciting X-ray beam approaches from the lower energy region the absorption threshold of an atomic inner shell[15]. Although such processes may, under certain circumstances, play an important role in analysis, they are not implemented in the current version of *xraylib*.

3.2.2 Differential cross sections

The databases provide access to several differential scattering cross sections. They are available for both unpolarized (U superscript) and polarized radiation (P superscript). In the former case, the functions depend on the polar scattering angle θ and the photon energy

(except for the Thomson cross section), while in the latter case the azimuthal scattering angle ϕ (with regard to the photon electric field vector) is an additional dependency.

Differential Thomson cross section

$$\frac{d\sigma_T^U(\theta)}{d\Omega} = \frac{r_e^2}{2}\left(1+\cos^2\theta\right) \tag{3.1}$$

$$\frac{d\sigma_T^P(\theta,\phi)}{d\Omega} = r_e^2\left(1-\sin^2\theta\cos^2\phi\right) \tag{3.2}$$

with r_e being the classical electron radius.

Differential Klein-Nishina cross section

$$\frac{d\sigma_{KN}^U(\theta,E)}{d\Omega} = \frac{r_e^2}{2}\left(\frac{K}{K_0}\right)^2\left(\frac{K}{K_0}+\frac{K_0}{K}-\sin^2\theta\right) \tag{3.3}$$

$$\frac{d\sigma_{KN}^P(\theta,\phi,E)}{d\Omega} = \frac{r_e^2}{2}\left(\frac{K}{K_0}\right)^2\left(\frac{K}{K_0}+\frac{K_0}{K}-2\sin^2\theta\cos^2\phi\right) \tag{3.4}$$

with:

$$\frac{K_0}{K} = 1+\frac{E_i}{m_e c^2}(1-\cos\theta) \tag{3.5}$$

In Eq. (3.5) $\frac{K}{K_0}$ corresponds to the ratio of the scattered photon energy to the energy of the incident photon E_i, and m_e is the electron mass.

Differential Rayleigh cross section

$$\frac{d\sigma_R^U(\theta,E)}{d\Omega} = \frac{d\sigma_T^U(\theta)}{d\Omega}F^2(x,Z) = \frac{r_e^2}{2}\left(1+\cos^2\theta\right)F^2(x,Z) \tag{3.6}$$

$$\frac{d\sigma_R^P(\theta,\phi,E)}{d\Omega} = \frac{d\sigma_T^P(\theta,\phi)}{d\Omega}F^2(x,Z) = r_e^2\left(1-\sin^2\theta\sin^2\phi\right)F^2(x,Z) \tag{3.7}$$

where x equals $\frac{E}{12.389}\sin\left(\frac{\theta}{2}\right)$ and F is the atomic form factor (taken from Hubbell et al.[7]).

Differential Compton cross section

$$\frac{d\sigma_C^U(\theta,E)}{d\Omega} = \frac{d\sigma_{KN}^U(\theta,E)}{d\Omega}S(x,Z) = \frac{r_e^2}{2}\left(\frac{K}{K_0}\right)^2\left(\frac{K}{K_0}+\frac{K_0}{K}-\sin^2\theta\right)S(x,Z) \tag{3.8}$$

$$\frac{d\sigma_C^P(\theta,\phi,E)}{d\Omega} = \frac{d\sigma_{KN}^P(\theta,\phi,E)}{d\Omega}S(x,Z) = \frac{r_e^2}{2}\left(\frac{K}{K_0}\right)^2\left(\frac{K}{K_0}+\frac{K_0}{K}-2\sin^2\theta\cos^2\phi\right)S(x,Z) \tag{3.9}$$

with S being the incoherent scattering function (taken from Cullen et al.[16]).

3.2.3 XRF cross sections

One of the key features of *xraylib* is the ability to calculate XRF cross sections, which are required for XRF quantification. This can be understood from the Sherman equation[17] that provides a relationship between primary (net) intensities $I_{i,YX}$ of the YX fluorescence line and weight fraction w_i of an element i, assuming that the specimen is irradiated with a monochromatic beam:

$$I_{i,YX} = I_0 G w_i Q_{i,YX} \rho T \left(\frac{1 - \exp(-\chi \rho T)}{\chi \rho T} \right) \tag{3.10}$$

In Eq. (3.10) I_0 is the photon flux, G is a geometry factor determined by the characteristics of the detector and its position with respect to the beam, $Q_{i,YX}$ is the XRF production cross-section and ρ and T are the density and thickness of the specimen, respectively. Of special importance is the factor $\left(\frac{1 - \exp(-\chi \rho T)}{\chi \rho T} \right)$ that corrects for the absorption of both the impinging beam and the produced fluorescence radiation. The factor χ is calculated as:

$$\chi = \frac{\sum_{k=1}^{n} w_k \mu_{k,0}}{\sin \alpha} + \frac{\sum_{k=1}^{n} w_k \mu_{k,1}}{\sin \beta} \tag{3.11}$$

χ is determined both by the experimental setup through the incident and exit angles α and β, and by the mass attenuation coefficients μ of all the elements in a specimen for both the energy of the exciting beam and the fluorescence energy corresponding with the YX transition of element i.

A second used quantification method for XRF involves (inverse) Monte Carlo simulations of photon–matter interactions in a specimen[18–20]. Such algorithms usually include variance reduction techniques, invoked to reduce the computational time. This implies that after each interaction with an element i, the probability $P_{i,YX}$ that a given XRF photon with energy $E_{i,YX}$ would reach the detector can be calculated using the following equation:

$$P_{i,YX} = \frac{\Omega_{det}}{4\pi} w_i \frac{Q_{i,YX}}{\sum_{k=1}^{n} w_k \mu_{k,0}} \exp\left(- \sum_{k=1}^{n} w_k \mu_{k,1} \rho D \right) \tag{3.12}$$

where Ω_{det} denotes the solid angle subtented by the detector, while $\mu_{k,0}$ and $\mu_{k,1}$ are with the attenuation coefficient of element k for the original photon energy and the fluorescence energy E_{YX}, respectively.
The XRF cross sections Q_{YX} (element subscript i dropped for clarity) that were encountered in Eqs. (3.10) and (3.12) can be calculated for the K- and L- lines using the equations:

$$Q_{KX} = P_K(E)\omega_K F_{KX} \tag{3.13}$$
$$Q_{L1X} = P_{L1}(E)\omega_{L1} F_{L1X} \tag{3.14}$$
$$Q_{L2X} = P_{L2}(E)\omega_{L2} F_{L2X} \tag{3.15}$$
$$Q_{L3X} = P_{L3}(E)\omega_{L3} F_{L3X} \tag{3.16}$$

with:

$$P_K(E) = \tau_K(E) \tag{3.17}$$
$$P_{L1}(E) = \tau_{L1}(E) \tag{3.18}$$
$$P_{L2}(E) = \tau_{L2}(E) + P_{L1}(E) f_{L12} \tag{3.19}$$
$$P_{L3}(E) = \tau_{L3}(E) + P_{L2}(E) f_{L23} + P_{L1}(E) f_{L13} \tag{3.20}$$

In these equations τ_Y stands for the partial photoionization cross section for shell Y, ω_Y for the fluorescence yield of shell Y, F_{YX} for the transition probability of XRF line YX and f for the Coster-Kronig transition probabilities. In earlier versions of *xraylib*, the partial photoionization cross sections were approximated using so-called jump factors and the total photoionization cross sections. While these produce reliable results for K-shells, one has to be (very) careful when applying this approximation in the case of the L- and M-shells, as shown in Figs. 3.1 and 3.2.
Recently, the *xraylib* database was extended to encompass the Kissel dataset for partial photoionization cross sections[14]. Using this dataset, a new function `CS_FluorLine_Kissel` was added to the software package, which calculates the XRF cross sections using these partial photoionization cross sections. Since the electron binding energies (edge energies) calculated by Kissel are slightly different from those provided by the `EdgeEnergy` function, the partial photoionization cross sections are extrapolated if the Kissel binding energy is higher than the value returned by `EdgeEnergy`.

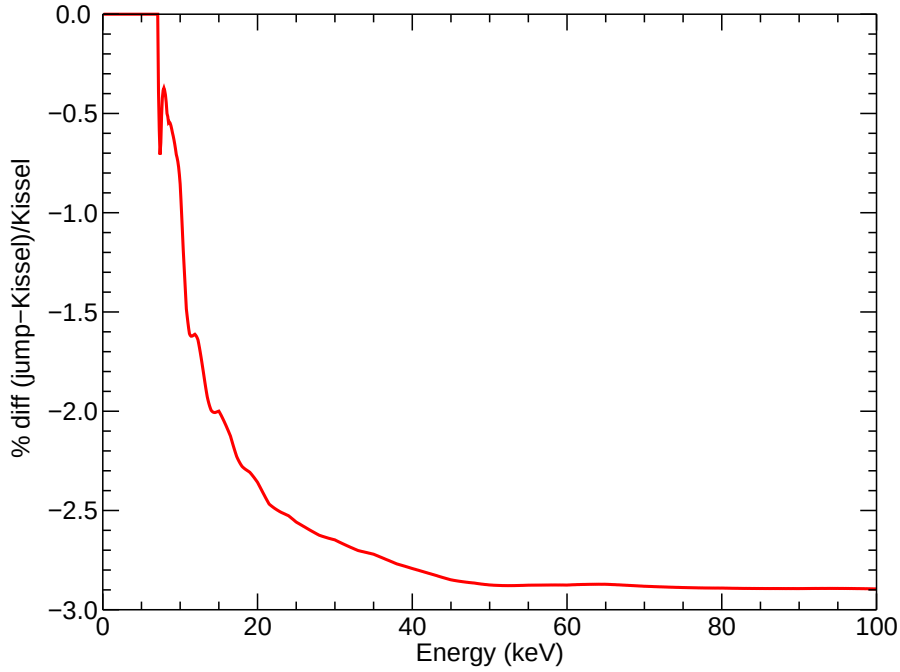

Figure 3.1: Relative differences between the XRF cross sections of the KL_3 line of Fe calculated using the full partial cross section tabulation (Kissel) and the jump approximation.

In recent *xraylib* releases, the M-shells Coster-Kronig transition probability database, provided by Chen et al.[21,22], was incorporated. Using these transition probabilities, in combination with the partial photoionization cross sections database, it is now possible to calculate the XRF cross sections of M-lines. This is accomplished using the following formulas:

$$Q_{M1X} = P_{M1}(E)\omega_{M1}F_{M1X} \tag{3.21}$$

$$Q_{M2X} = P_{M2}(E)\omega_{M2}F_{M2X} \tag{3.22}$$

$$Q_{M3X} = P_{M3}(E)\omega_{M3}F_{M3X} \tag{3.23}$$

$$Q_{M4X} = P_{M4}(E)\omega_{M4}F_{M4X} \tag{3.24}$$

$$Q_{M5X} = P_{M5}(E)\omega_{M5}F_{M5X} \tag{3.25}$$

with:

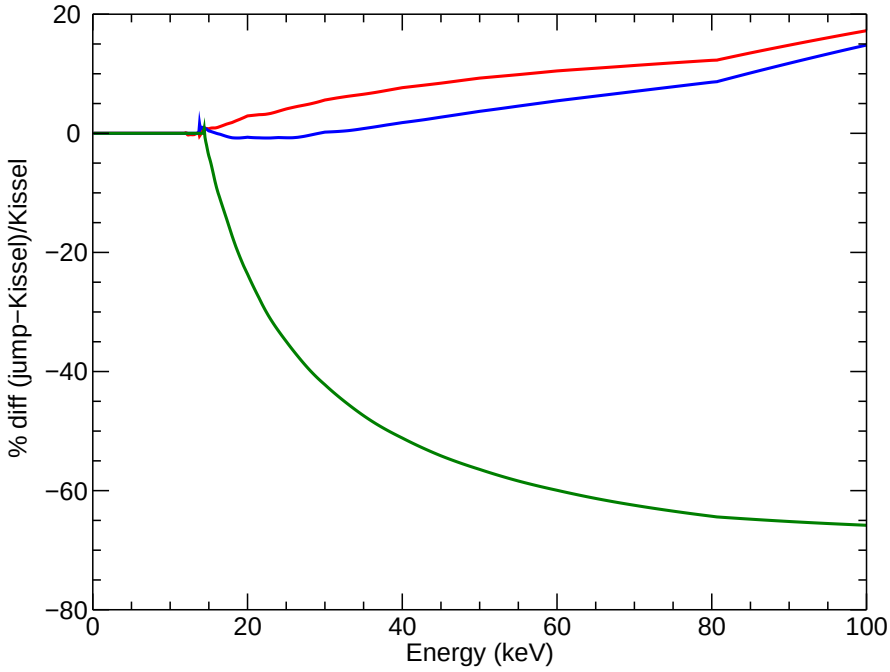

Figure 3.2: Relative differences between the XRF cross sections of the L_3M_5 (red), L_2M_4 (blue) and L_1M_3 (green) lines of Au, calculated using the full partial cross section tabulation (Kissel) and the jump approximation.

$$P_{M1}(E) = \tau_{M1}(E) \tag{3.26}$$

$$P_{M2}(E) = \tau_{M2}(E) + P_{M1}(E) f_{M12} \tag{3.27}$$

$$P_{M3}(E) = \tau_{M3}(E) + P_{M2}(E) f_{M23} + P_{M1}(E) f_{M13} \tag{3.28}$$

$$P_{M4}(E) = \tau_{M4}(E) + P_{M3}(E) f_{M34} + P_{M2}(E) f_{M24} + P_{M1}(E) f_{M14} \tag{3.29}$$

$$P_{M5}(E) = \tau_{M5}(E) + P_{M4}(E) f_{M45} + P_{M3}(E) f_{M35} + P_{M2}(E) f_{M25} + P_{M1}(E) f_{M15} \tag{3.30}$$

The symbols in Eqs. (3.21) to (3.30) have similar meanings as those used in Eqs. (3.13) to (3.20).

3.2.4 Cascade effects

Equations (3.14), (3.15) and (3.16) do not take into account the case when the excitation energy is also sufficiently high to excite the K-shell. If true, these equations must also take into account the contribution from the vacancies generated from the transitions to the K-shell. Two effects can be observed: the radiative transitions produce vacancies in the L_2 and L_3 shells according to the KL_2 and KL_3 transition probabilities, while K-LL and K-LX non-radiative Auger transitions will produce vacancies in the L-shells according to the non-radiative transition ratios. The latter were recently added to the *xraylib* database and were taken from Chen et al.[23] and can be retrieved from the library using the `AugerRate` function.

Based on these considerations, Eqs. (3.18), (3.19) and (3.20) can be rewritten as:

$$P_{L1}(E) = \tau_{L1}(E) + (1-\omega_K)P_K(E)(\sum_{X=L1}^{Q3} a_{K-L1X} + a_{K-XL1}) \tag{3.31}$$

$$\begin{aligned} P_{L2}(E) = {} & \tau_{L2}(E) + P_{L1}(E)f_{L12} + \omega_K P_K(E)F_{KL_2} \\ & + (1-\omega_K)P_K(E)(\sum_{X=L1}^{Q3} a_{K-L1X} + a_{K-XL1}) \\ & + (1-\omega_{L1}-f_{L13}-f_{L12})P_{L1}(E)(\sum_{X=L2}^{Q3} a_{L1-L2X} + a_{L1-XL2}) \end{aligned} \tag{3.32}$$

$$\begin{aligned} P_{L3}(E) = {} & \tau_{L3}(E) + P_{L2}(E)f_{L23} + P_{L1}(E)f_{L13} + \omega_K P_K(E)F_{KL_3} \\ & + (1-\omega_K)P_K(E)(\sum_{X=L1}^{Q3} a_{K-L3X} + a_{K-XL3}) \\ & + (1-\omega_{L1}-f_{L13}-f_{L12})P_{L1}(E)(\sum_{X=L2}^{Q3} a_{L1-L3X} + a_{L1-XL3}) \\ & + (1-\omega_{L2}-f_{L23})P_{L2}(E)(\sum_{X=L3}^{Q3} a_{L2-L3X} + a_{L2-XL3}) \end{aligned} \tag{3.33}$$

In these equations a_{X-YZ} represents the non-radiative transition ratio corresponding to an initial excitation of an X-shell electron, leading to vacancies in the Y- and Z-(sub)shells. The summations run up to the highest occupied (sub)shell, here denoted with the Q_3 shell. The non-radiative cascade contribution is calculated by multiplying the sum of the non-radiative transition rates with the Auger yield A_i^X, that satisfies the relation[24]:

$$\omega_i^X + A_i^X + \sum_{j=i+1}^{k} f_{ij}^X = 1 \tag{3.34}$$

with ω_i^X the fluorescence yield of subshell X_i and f_{ij}^X the Coster-Kronig transition probabilities.

Similar equations can be derived for the M-line XRF cross sections, which may receive contributions contributions due to excitation in the K and L-shells, depending on the excitation energy:

$$\begin{aligned}
P_{M1}(E) = &\tau_{M1}(E) + (1-\omega_K)P_K(E)\left(\sum_{X=L1}^{Q3} a_{K-M1X} + a_{K-XM1}\right) \\
&+ \omega_{L1}P_{L1}(E)F_{L_1M_1} \\
&+ (1-\omega_{L1}-f_{L13}-f_{L12})P_{L1}(E)\left(\sum_{X=L2}^{Q3} a_{L1-M1X} + a_{L1-XM1}\right) \\
&+ \omega_{L2}P_{L2}(E)F_{L_2M_1} \\
&+ (1-\omega_{L2}-f_{L23})P_{L2}(E)\left(\sum_{X=L3}^{Q3} a_{L2-M1X} + a_{L2-XM1}\right) \\
&+ \omega_{L3}P_{L3}(E)F_{L_3M_1} \\
&+ (1-\omega_{L3})P_{L3}(E)\left(\sum_{X=M1}^{Q3} a_{L3-M1X} + a_{L3-XM1}\right)
\end{aligned} \tag{3.35}$$

$$\begin{aligned}
P_{M2}(E) = &\tau_{M2}(E) + P_{M1}(E)f_{M12} + \omega_K P_K(E)F_{KM_2} \\
&+ (1-\omega_K)P_K(E)\left(\sum_{X=L1}^{Q3} a_{K-M2X} + a_{K-XM2}\right) \\
&+ \omega_{L1}P_{L1}(E)F_{L_1M_2} \\
&+ (1-\omega_{L1}-f_{L13}-f_{L12})P_{L1}(E)\left(\sum_{X=L2}^{Q3} a_{L1-M2X} + a_{L1-XM2}\right) \\
&+ \omega_{L2}P_{L2}(E)F_{L_2M_2} \\
&+ (1-\omega_{L2}-f_{L23})P_{L2}(E)\left(\sum_{X=L3}^{Q3} a_{L2-M2X} + a_{L2-XM2}\right) \\
&+ \omega_{L3}P_{L3}(E)F_{L_3M_2}
\end{aligned} \tag{3.36}$$

$$
\begin{aligned}
&+ (1-\omega_{L3})P_{L3}(E)\left(\sum_{X=M1}^{Q3} a_{L3-M2} + a_{L3-XM2}\right)\\
&+ (1-\omega_{M1}-f_{M15}-f_{M14}-f_{M13}-f_{M12})P_{M1}(E)\left(\sum_{X=L2}^{Q3} a_{M1-M2X} + a_{M1-XM2}\right)
\end{aligned}
$$

$$
\begin{aligned}
P_{M3}(E) =& \tau_{M3}(E) + P_{M1}(E)f_{M13} + P_{M2}(E)f_{M23} + \omega_K P_K(E) F_{KM_3}\\
&+ (1-\omega_K)P_K(E)\left(\sum_{X=L1}^{Q3} a_{K-M3X} + a_{K-XM3}\right)\\
&+ \omega_{L1}P_{L1}(E)F_{L_1M_3}\\
&+ (1-\omega_{L1}-f_{L13}-f_{L12})P_{L1}(E)\left(\sum_{X=L2}^{Q3} a_{L1-M3X} + a_{L1-XM3}\right)\\
&+ \omega_{L2}P_{L2}(E)F_{L_2M_3}\\
&+ (1-\omega_{L2}-f_{L23})P_{L2}(E)\left(\sum_{X=L3}^{Q3} a_{L2-M3X} + a_{L2-XM3}\right)\\
&+ \omega_{L3}P_{L3}(E)F_{L_3M_3}\\
&+ (1-\omega_{L3})P_{L3}(E)\left(\sum_{X=M1}^{Q3} a_{L3-M3} + a_{L3-XM3}\right)\\
&+ (1-\omega_{M1}-f_{M15}-f_{M14}-f_{M13}-f_{M12})P_{M1}(E)\left(\sum_{X=M2}^{Q3} a_{M1-M3X} + a_{M1-XM3}\right)\\
&+ (1-\omega_{M2}-f_{M25}-f_{M24}-f_{M23})P_{M2}(E)\left(\sum_{X=M3}^{Q3} a_{M2-M3X} + a_{M2-XM3}\right)
\end{aligned}
\tag{3.37}
$$

$$
\begin{aligned}
P_{M4}(E) =& \tau_{M4}(E) + P_{M1}(E)f_{M14} + P_{M2}(E)f_{M24} + P_{M3}(E)f_{M34}\\
&+ (1-\omega_K)P_K(E)\left(\sum_{X=L1}^{Q3} a_{K-M4X} + a_{K-XM4}\right)\\
&+ \omega_{L1}P_{L1}(E)F_{L_1M_4}\\
&+ (1-\omega_{L1}-f_{L13}-f_{L12})P_{L1}(E)\left(\sum_{X=L2}^{Q3} a_{L1-M4X} + a_{L1-XM4}\right)\\
&+ \omega_{L2}P_{L2}(E)F_{L_2M_4}
\end{aligned}
$$

$$
\begin{aligned}
&+ (1-\omega_{L2}-f_{L23})P_{L2}(E)\left(\sum_{X=L3}^{Q3} a_{L2-M4X} + a_{L2-XM4}\right) \\
&+ \omega_{L3}P_{L3}(E)F_{L_3M_4} \\
&+ (1-\omega_{L3})P_{L3}(E)\left(\sum_{X=M1}^{Q3} a_{L3-M4X} + a_{L3-XM4}\right) \\
&+ (1-\omega_{M1}-f_{M15}-f_{M14}-f_{M13}-f_{M12})P_{M1}(E)\left(\sum_{X=M2}^{Q3} a_{M1-M4X} + a_{M1-XM4}\right) \\
&+ (1-\omega_{M2}-f_{M25}-f_{M24}-f_{M23})P_{M2}(E)\left(\sum_{X=M3}^{Q3} a_{M2-M4X} + a_{M2-XM4}\right) \\
&+ (1-\omega_{M3}-f_{M35}-f_{M34})P_{M3}(E)\left(\sum_{X=M3}^{Q3} a_{M3-M4X} + a_{M3-XM4}\right)
\end{aligned} \tag{3.38}
$$

$$
\begin{aligned}
P_{M5}(E) =& \tau_{M5}(E) + P_{M1}(E)f_{M15} + P_{M2}(E)f_{M25} + P_{M3}(E)f_{M35} + P_{M4}(E)f_{M45} \\
&+ (1-\omega_K)P_K(E)\left(\sum_{X=L1}^{Q3} a_{K-M5X} + a_{K-XM5}\right) \\
&+ \omega_{L1}P_{L1}(E)F_{L_1M_5} \\
&+ (1-\omega_{L1}-f_{L13}-f_{L12})P_{L1}(E)\left(\sum_{X=L2}^{Q3} a_{L1-M5X} + a_{L1-XM5}\right) \\
&+ \omega_{L2}P_{L2}(E)F_{L_2M_5} \\
&+ (1-\omega_{L2}-f_{L23})P_{L2}(E)\left(\sum_{X=L3}^{Q3} a_{L2-M5X} + a_{L2-XM5}\right) \\
&+ \omega_{L3}P_{L3}(E)F_{L_3M_5} \\
&+ (1-\omega_{L3})P_{L3}(E)\left(\sum_{X=M1}^{Q3} a_{L3-M5X} + a_{L3-XM5}\right) \\
&+ (1-\omega_{M1}-f_{M15}-f_{M14}-f_{M13}-f_{M12})P_{M1}(E)\left(\sum_{X=M2}^{Q3} a_{M1-M5X} + a_{M1-XM5}\right) \\
&+ (1-\omega_{M2}-f_{M25}-f_{M24}-f_{M23})P_{M2}(E)\left(\sum_{X=M3}^{Q3} a_{M2-M5X} + a_{M2-XM5}\right)
\end{aligned} \tag{3.39}
$$

$$+ (1 - \omega_{M3} - f_{M35} - f_{M34}) P_{M3}(E) \left(\sum_{X=M3}^{Q3} a_{M3-M5X} + a_{M3-XM5} \right)$$
$$+ (1 - \omega_{M4} - f_{M45}) P_{M4}(E) \left(\sum_{X=M4}^{Q3} a_{M4-M5X} + a_{M4-XM5} \right)$$

These equations were implemented in the library as `CS_FluorLine_Kissel_Cascade` that returns values in $\frac{cm^2}{g}$ and as `CSb_FluorLine_Kissel_Cascade` that returns values in $\frac{barn}{atom}$. In addition, three other functions have been added that calculate either just the radiative cascade contribution (`CS_FluorLine_Kissel_Radiative_Cascade`), either just the non-radiative cascade contribution (`CS_FluorLine_Kissel_Nonradiative_Cascade`) or the cross sections without the cascade contributions (`CS_FluorLine_Kissel_no_Cascade`), enabling the user to investigate the contributions of the cascade effect in detail.
The magnitude of the cascade effect can be seen in Fig. 3.3, which shows the spectra of pure Ba, obtained using a Monte Carlo simulation code for XRF energy-dispersive spectrometers[19]. From this example, it can be clearly seen that the cascade effect not only increases the line intensity, but also changes the ratio between the individual lines. This observation can be attributed to the strong cascade effect coming from the radiative transitions (ω_K of Ba is 0.92) which will only increase the intensity of the L_2 and L_3 lines since the KL_1 transition is of multipole type and is consequently extremely weak. The XRF cross sections for several L-lines of Ba are presented in Table 3.1, and the XRF cross section profiles for the L_3M_5 line are drawn in Fig. 3.4.

Table 3.1: XRF cross sections ($\frac{cm^2}{g}$) of selected Ba lines, excited at 40.0 keV and obtained with or without the contribution of radiative and/or non-radiative cascades

XRF-line	No cascade	Radiative cascade	Non-radiative cascade	Full cascade
$L_3M_5(L_{\alpha 1})$	0.106551	0.857583	0.209919	0.960951
$L_2M_4(L_{\beta 1})$	0.0741785	0.491372	0.139335	0.556528
$L_3N_5(L_{\beta 2})$	0.0168431	0.135562	0.0331830	0.151902
$L_1M_3(L_{\beta 3})$	0.0426127	0.0426127	0.0600876	0.0600876

A different situation can be found in Fig. 3.5, depicting the (partial) spectra of Pb, obtained using the same Monte Carlo simulation code. In this case, one observes a strong

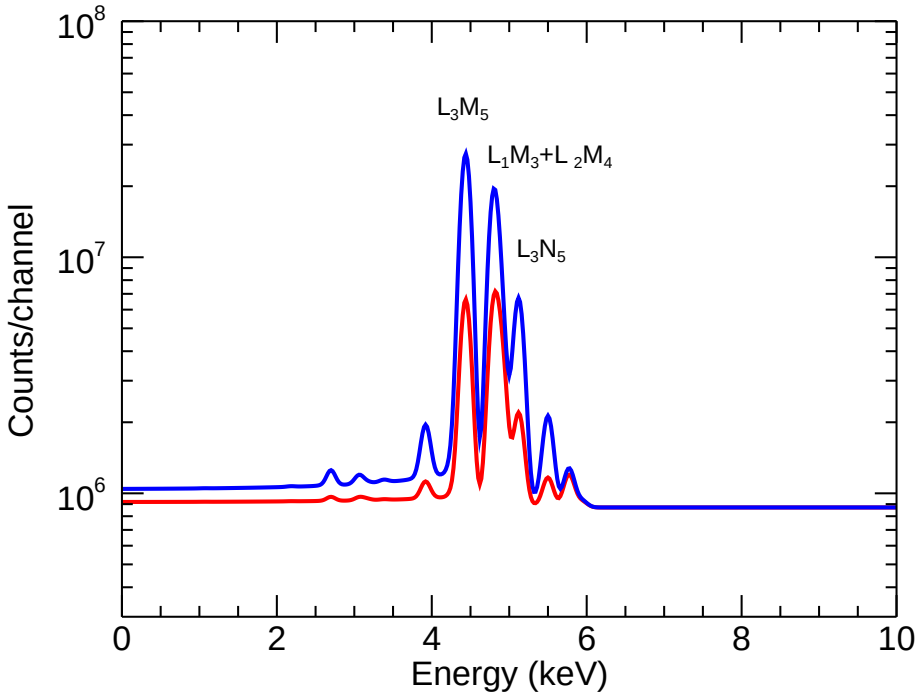

Figure 3.3: Partial spectrum of pure Ba, excited using a 40.0 keV beam. The red curve was obtained ignoring the cascade contributions while the blue spectrum was generated enabling both radiative and non-radiative cascades. The most intense L-lines are indicated.

contribution coming from the non-radiative cascades, which can be explained by the rather low fluorescence yields of the Pb L-shells. In the particular case of the M_1N_2 line of Pb one can observe that the cascade effect has a very large contribution from the non-radiative cascades, which can be attributed to the fact that all the L_XM_1 lines of Pb have very low XRF production cross sections. The XRF cross sections for several L- and M-lines of Pb are represented in Table 3.2, and the XRF cross section profiles for the M_5N_7 line are drawn in Fig. 3.6.

3.2.5 Atomic parameters

The edge energies (electron binding energies) are taken from the tabulation by Larkins et al[25]. The line energies are calculated by the way of the difference of the binding ener-

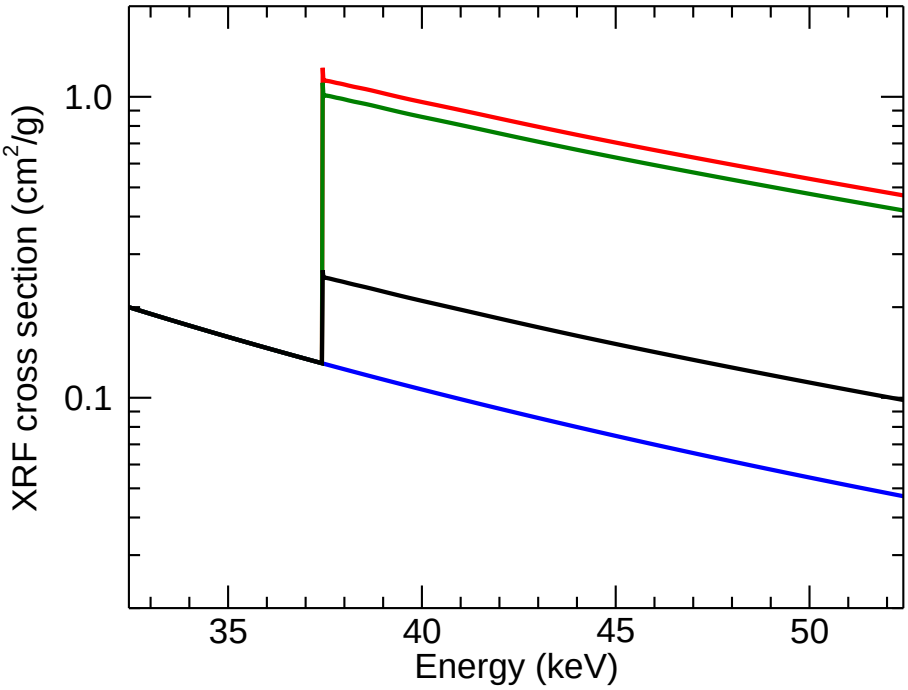

Figure 3.4: L_3M_5 cross section profiles of Ba, in the energy region around the K-edge. The blue curve was obtained disabling the cascade contributions, while the black and green curves refer to cases in which the radiative and non-radiative contributions were alternatingly left out. In the red curve both the radiative and non-radiative contributions are included.

gies of the electrons involved in the transition. The X-ray emission rates are taken from Scofield[26,27] and Bhalla[28], while the fluorescence yields are taken from the compilation of Elam et al.[12]. Atomic level widths are taken from the work of Campbell and Papp[29]. These parameters enables, for example, the calculation of the half-width at half-maximum (HWHM) of the Lorentzian distribution ℓ centered at E_0 and describing the characteristic line shape of an XRF line, a fact that is usually ignored in XRF quantification procedures[30]:

$$\ell(E, E_0; \gamma_{E_0}) = \frac{1}{\pi} \frac{\gamma_{E_0}}{\left((E - E_0)^2 + \gamma_{E_O}^2\right)} \tag{3.40}$$

where γ_{E_0} is equal to half of the sum of the atomic level widths of the participating shells.

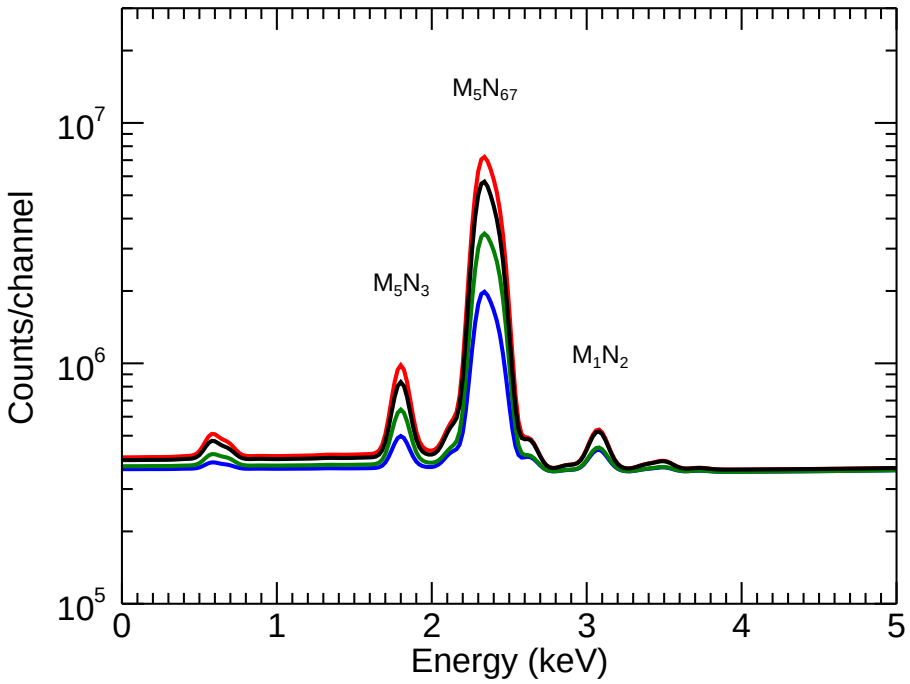

Figure 3.5: Partial spectrum of pure Pb, excited using an 18.0 keV beam. The blue spectrum was obtained excluding the cascade contributions, while the black and green curves correspond to cases in which the radiative and non-radiative contributions were alternatingly left out. The red spectrum includes both radiative and non-radiative contributions. The most intense M-lines are indicated.

Recently the *xraylib* library was extended to include the Compton broadening profiles of p_z, the momentum of the scattering electron calculated by Biggs et al.[31] and taken from the LSCAT extension of the EGS4 program[32]. These values are required when computing the energy loss of a photon after experiencing Compton scattering over an angle θ:

$$E_{i+1} = E_i \left(1 + \frac{E_i}{m_e c^2}(1 - \cos\theta) - \frac{2p_z}{m_e c} \sin\frac{\theta}{2}\right)^{-1} \tag{3.41}$$

The momentum p_z is usually selected from the Compton broadening profiles (which are essentially probability density functions) by means of a random number generator.

Access to these functions from the *xraylib* API is managed through a number of macros

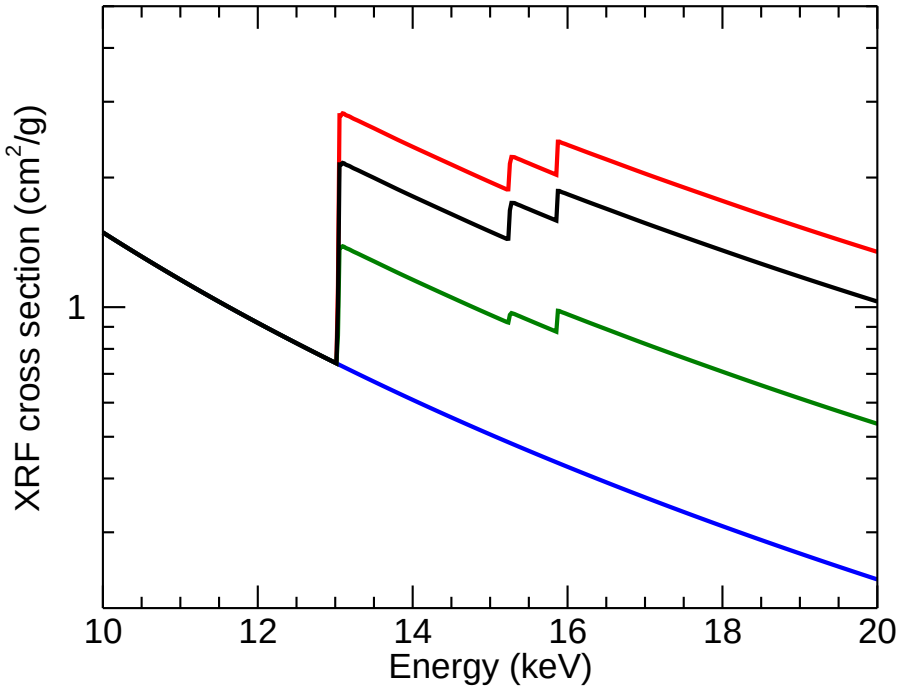

Figure 3.6: M_5N_7 cross section profiles of Pb, in the energy region around the L-edges. The blue curve was obtained disabling the cascade contributions, while the black and green curves refer to cases in which the radiative and non-radiative contributions were alternatingly left out. In the red curve both the radiative and non-radiative contributions are taken into account.

which allow for the extraction of specific information, such as a particular XRF line or atomic shell. A number of examples can be found in our earlier work[13]. However, care should be taken when using the macros related to the XRF lines. Despite the longstanding recommendation by the International Union of Pure and Applied Chemistry (IUPAC) to designate an XRF line based on the atomic levels involved in the transition (e.g. $K - L_3$), the Siegbahn notation is still widely used in X-ray spectroscopy. This notation (e.g. $K_{\alpha 1}$), which classifies lines on the basis of their relative intensities, is very often used in a way that overlapping lines are referred to using a single notation: e.g. K_α corresponds to both $K_{\alpha 1}$ and $K_{\alpha 2}$. Another example concerns the L_β line which actually indicates about twenty individual lines. This situation has an impact on how several functions from the *xraylib* API are used: Firstly, when retrieving an XRF cross section for a line group, the

Table 3.2: XRF cross sections ($\frac{cm^2}{g}$) of selected Pb lines, excited at 18.0 keV and obtained with or without the contribution of radiative and/or non-radiative cascades

XRF-line	No cascade	Radiative cascade	Non-radiative cascade	Full cascade
$L_3M_5(L_{\alpha 1})$	13.0962	13.0962	13.5537	13.5537
$L_2M_4(L_{\beta 1})$	8.59949	8.59949	8.59949	8.59949
$L_3N_5(L_{\beta 2})$	2.51998	2.51998	2.60801	2.60801
$L_1M_3(L_{\beta 3})$	0.679464	0.679464	0.679464	0.679464
$M_5N_7(M_{\alpha 1})$	0.309951	0.708079	1.35452	1.76536
$M_5N_6(M_{\alpha 2})$	0.0211526	0.0483228	0.0924393	0.120477
M_5N3	0.0223024	0.0509495	0.0974642	0.127025
M_1N2	0.00618514	0.00764419	0.00982103	0.0113192

function must return the sum of the XRF cross sections of all lines belonging to that group. Secondly, a problem arises when calling the XRF line energy of a line group. One solution is returning a (weighted) average of the individual line energies. In the case of elements with a high atomic number, however, this would result in a line energy that would be absent from a real experimental spectrum (e.g. Pb $K-L_2$: 72.8045 keV, $K-L_3$: 74.9693). Thirdly, in the case of transition probabilities, it makes no sense to request e.g. this value for L_β since it corresponds with several lines, originating from the L_1, L_2 and L_3 shells! These issues were circumvented at an earlier stage by defining 4 Siegbahn macros KA_LINE, KB_LINE, LA_LINE and LB_LINE which correspond to $K_{\alpha 1}+K_{\alpha 2}$, $K_{\beta 1}+K_{\beta 2}$, $L_{\alpha 1}$ and $L_{\beta 1}$, respectively. These 4 macros were accompanied by a large number of IUPAC macros, each associated with an individual line. Recent *xraylib* versions have, however, been augmented with about 45 new Siegbahn macros retrieving individual XRF lines[33]. Their usage will resolve entirely the above mentioned issues entirely. The original 4 Siegbahn macros are kept for backward compatibility but their usage is deprecated. When invoking functions with these macros, the returned values will be valid for the complete line group, which means that they will in some cases be different from older *xraylib* versions. The list of all the available Siegbahn macros is presented in Table 3.3.

Table 3.3: Overview of the Siegbahn macros accessible through *xraylib*, along with their IUPAC macro counterpart and the transition they represent.

Siegbahn macro	IUPAC macro	Transition
KA1_LINE	KL3_LINE	$K - L_3$
KA2_LINE	KL2_LINE	$K - L_2$
KB1_LINE	KM3_LINE	$K - M_3$
KB2_LINE	KN3_LINE	$K - N_3$
KB3_LINE	KM2_LINE	$K - M_2$
KB4_LINE	KN5_LINE	$K - N_5$
KB5_LINE	KM5_LINE	$K - M_5$
LA1_LINE	L3M5_LINE	$L_3 - M_5$
LA2_LINE	L3M4_LINE	$L_3 - M_4$
LB1_LINE	L2M4_LINE	$L_2 - M_4$
LB2_LINE	L3N5_LINE	$L_3 - N_5$
LB3_LINE	L1M3_LINE	$L_1 - M_3$
LB4_LINE	L1M2_LINE	$L_1 - M_2$
LB5_LINE	L3O45_LINE	$L_3 - O_{45}$
LB6_LINE	L3N1_LINE	$L_3 - N_1$
LB7_LINE	L3O1_LINE	$L_3 - O_1$
LB9_LINE	L1M5_LINE	$L_1 - M_5$
LB10_LINE	L1M4_LINE	$L_1 - M_4$
LB15_LINE	L3N4_LINE	$L_3 - N_4$
LB17_LINE	L2M3_LINE	$L_2 - M_3$
LG1_LINE	L2N4_LINE	$L_2 - N_4$
LG2_LINE	L1N2_LINE	$L_1 - N_2$
LG3_LINE	L1N3_LINE	$L_1 - N_3$
LG4_LINE	L1O3_LINE	$L_1 - O_3$
LG5_LINE	L2N1_LINE	$L_2 - N_1$
LG6_LINE	L2O4_LINE	$L_2 - O_4$
LG8_LINE	L2O1_LINE	$L_2 - O_1$
LE_LINE	L2M1_LINE	$L_2 - M_1$
LL_LINE	L3M1_LINE	$L_3 - M_1$
LS_LINE	L3M3_LINE	$L_3 - M_3$
LT_LINE	L3M2_LINE	$L_3 - M_2$

Table 3.3: Overview of the Siegbahn macros accessible through *xraylib*, along with their IUPAC macro counterpart and the transition they represent. (continued)

Siegbahn macro	IUPAC macro	Transition
LU_LINE	L3N6_LINE	$L_3 - N_6$
LV_LINE	L2N6_LINE	$L_2 - N_6$
MA1_LINE	M5N7_LINE	$M_5 - N_7$
MA2_LINE	M5N6_LINE	$M_6 - N_6$
MB_LINE	M4N6_LINE	$M_4 - N_6$
MG_LINE	M3N5_LINE	$M_3 - N_5$

3.2.6 Compound parser and related functions

A compound parser function was integrated into *xraylib* that returns a structure containing an array of the elements of the chemical formula (as atomic numbers), as well as arrays containing the weight and atomic fractions. The parser supports the use of brackets when dealing with formulas containing multiply repeated functional groups (e.g. $Al_2(SO_4)_3$). Due to the internal use of a recursive function to parse the elements of a functional group, there is no limit to the nesting depth when defining these groups. The compound parser has been used to define a number of functions to return cross sections for a given compound instead of an element. These functions can be recognized by the "_CP" suffix appended to their names. Another application of the parser lies within the two functions that calculate the real and imaginary part of the refractive index n of a given compound. Assuming n is written as $n = 1 - \delta - i\beta$ with:

$$\delta = \frac{h^2 e^2}{E^2 2\pi m_e} \sum_a \frac{N_A}{A} \rho \phi'_a \tag{3.42}$$

$$\beta = \frac{hc}{4\pi E}\mu = \frac{h^2 e^2}{E^2 2\pi m_e} \sum_a \frac{N_A}{A} \rho \phi''_a \tag{3.43}$$

and ϕ'_a and ϕ''_a being the real and imaginary parts of the anomalous dispersion correction, respectively.

3.3 Discussion

The core *xraylib* library is written in ANSI C89, implying that it can be compiled and run on virtually any architecture. While earlier releases included only a shell script that allowed for compilation and installation on Linux, installation support has been widely extended in the most recent versions. This has been accomplished by transitioning to a GNU Autotools (autoconf, automake and libtool) based procedure. The major advantage of this approach is immediate support on all UNIX and UNIX-like platforms. Using the combined strength of MSYS and MINGW32, the authors produced a working version for the Win32 platform. An installer was developed for Windows using the Nullsoft Scriptable Install System (NSIS), as well as rpm packages for Linux distributions such as Fedora, Red Hat, Scientific Linux and CentOS. Through MacPorts, it is possible for Mac OS X users to download, compile and install *xraylib* in a very convenient way.

The authors have also developed several interfaces to other popular programming languages: *xraylib* can be called directly from C++ and Objective-C, while bindings were written for Fortran 2003, IDL, Perl, Python, .NET and Java. Bindings for Matlab and Ruby are under development.

The *xraylib* package also contains a command-line utility, implemented as a Python script, that allows to query the underlying databases.

The source code is delivered with the physical data tabulated in a number of ASCII files. Most of these files have an intuitive layout and can be adjusted easily by the user. Other files, such as those containing the cross sectional data, have a fixed layout and should not be modified directly. If necessary, these files can be adapted using a number of IDL scripts which are included in the package. The datafiles are hardcoded into the library during the compilation. This involves a bootstrapping stage during which the physical data are written to a (huge) C source file that is compiled into the final library. This avoids the need to load the data files at runtime, and improves performance. Special care was taken to ensure that the functions from *xraylib* are thread-safe: it is possible to use them safely in multithreaded software using OpenMP, POSIX threads or the Windows multithreading API.

It is important to note that the datasets were taken over from their authors in their original form. This implies that in some cases the values returned by the API are less than trustworthy and should be considered as informative only. An example of this includes the

Coster-Kronig transition probabilities of the M-shells. The authors keep, however, track of relevant new databases that are publicly released, and may replace some of the existing databases in *xraylib* if they are deemed to be more accurate. *xraylib* is released under a BSD license and can be downloaded from `http://github.com/tschoonj/xraylib`.

Bibliography

[1] B. Beckhoff, Reference-free X-ray spectrometry based on metrology using synchrotron radiation, J. Anal. At. Spectrom. 23 (2008) 845–853.

[2] M. Lepy, M. Mantler, B. Beckhoff, International initiative on x-ray fundamental parameters, `http://exsa.pytalhost.net/news/?page_id=13`, 2008.

[3] J. Campbell, X-Ray Energies: Transition Probabilities, Fluorescence and Coster-Kronig Probabilities, Technical Report, Guelph-Waterloo Physics Institute, University of Guelph, 2010.

[4] P. Caussin, A Comparison of Five Available X ray Absorption Tables, Technical Report, Bruker-AXS, 2010.

[5] M. Berger, J. Hubbell, S. Seltzer, J. Chang, J. Coursey, R. Sukumar, D. Zucker, K. Olsen, XCOM: Photon cross section database, `http://www.nist.gov/pml/data/xcom/index.cfm`, 1987.

[6] P. Bandyopadhyay, C. Segre, MUCAL, `http://www.csrri.iit.edu/mucal.html`, 2005.

[7] J. Hubbell, W. Veigele, E. Briggs, R. Brown, D. Cromer, R. Howerton, Atomic form factors, incoherent scattering functions and photon scattering cross sections, J. Phys. Chem. Ref. Data 4 (1975) 471–538.

[8] J. Hubbell, I. Overbo, Relativistic atomic form-factors and photon coherent scattering cross-sections, J. Phys. Chem. Ref. Data 8 (1979) 69–105.

[9] J. Scofield, Theoretical Photoionization Cross Sections from 1 to 1500 keV, Technical Report UCRL-51326, Lawrence Livermore National Laboratory, 1973.

[10] W. McMaster, N. Del Grande, J. Mallett, J. Hubbell, Compilation of X-ray cross sections, Technical Report UCRL-50174, Lawrence Livermore National Laboratory, 1969.

[11] M. Krause, Atomic radiative and radiationless yields for K-shells and L-shells, J. Phys. Chem. Ref. Data 8 (1979) 307–327.

[12] W. Elam, B. Ravel, J. Sieber, A new atomic database for X-ray spectroscopic calculations, Radiat. Phys. Chem. 63 (2002) 121–128.

[13] A. Brunetti, M. Sanchez del Rio, B. Golosio, A. Simionovici, A. Somogyi, A library for X-ray-matter interaction cross sections for X-ray fluorescence applications, Spectrochim. Acta Part B 59 (2004) 1725–1731.

[14] L. Kissel, RTAB: the Rayleigh scattering database, Radiat. Phys. Chem. 59 (2000) 185–200.

[15] D. Sokaras, M. Mueller, M. Kolbe, B. Beckhoff, C. Zarkadas, A. G. Karydas, Resonant Raman scattering of polarized and unpolarized x-ray radiation from Mg, Al, and Si, Phys. Rev. A 81 (2010).

[16] D. Cullen, J. Hubbell, L. Kissel, EPDL97: The Evaluated Photon Library, Technical Report UCRL-50400 Vol. 6 Rev. 5, Lawrence Livermore National Laboratory Report, 1997.

[17] J. Sherman, The theoretical derivation of fluorescent X-ray intensities from mixtures, Spectrochim. Acta (1955) 283–306.

[18] L. Vincze, K. Janssens, F. Adams, A general Monte-Carlo simulation of Energy-Dispersive X-ray-Fluorescence Spectrometers .1. Unpolarized radiation, Homogeneous samples, Spectrochim. Acta Part B 48 (1993) 553–573.

[19] L. Vincze, K. Janssens, F. Adams, M. Rivers, K. W. Jones, A general Monte Carlo simulation of ED-XRF spectrometers. II: Polarized monochromatic radiation, homegeneous samples, Spectrochim. Acta Part B 50 (1995) 127–147.

[20] U. Bottigli, A. Brunetti, B. Golosio, P. Oliva, S. Stumbo, L. Vincze, P. Randaccio, P. Bleuet, A. Simionovici, A. Somogyi, Voxel-based Monte Carlo simulation of X-ray

imaging and spectroscopy experiments, Spectrochim. Acta Part B 59 (2004) 1747–1754.

[21] M. Chen, B. Crasemann, H. Mark, Relativistic M-shell radiationless transitions, Phys. Rev. A 21 (1980) 449–453.

[22] M. Chen, B. Crasemann, H. Mark, Radiationless transitions to atomic $M_{1,2,3}$ shells - Results of relativistic theory, Phys. Rev. A 27 (1983) 2989–2994.

[23] M. H. Chen, B. Crasemann, Relativistic Radiationless Transition Probabilities for Atomic K- and L-shells, At. Data Nucl. Data Tables 24 (1979) 13–37.

[24] W. Bambynek, C. Swift, B. Crasemann, H.-U. Freund, P. V. Rao, R. Price, H. Mark, R. Fink, X-Ray-fluorescence yields, Auger, and Coster-Kronig transition probabilities, Rev. Mod. Phys. 44 (1972) 716–813.

[25] F. Larkins, Semiempirical Auger-electron energies for elements $10 \leq Z \leq 100$, At. Data Nucl. Data Tables 20 (1977) 311–387.

[26] J. Scofield, Exchange corrections of K X-ray emission rates, Phys. Rev. A 9 (1974) 1041–1049.

[27] J. Scofield, Relativistic Hartree-Slater values for K and L X-ray emission rates, At. Data Nucl. Data Tables 14 (1974) 121–137.

[28] C. Bhalla, Radiative transition probabilities for vacancies in M sub-shells, J. Phys. B, At., Mol. Opt. Phys. 3 (1970) 916–924.

[29] J. Campbell, T. Papp, Widths of the atomic K-$N7$ levels, At. Data Nucl. Data Tables 77 (2001) 1–56.

[30] J. E. Fernandez, V. Scot, Self-enhancement effects on XRF K-lines due to natural width, X-Ray Spectrom. 38 (2009) 175–181.

[31] F. Biggs, L. Mendelsohn, J. Mann, Hartree-Fock Compton profiles for the elements, At. Data Nucl. Data Tables 16 (1975) 201.

[32] Y. Namito, S. Ban, H. Hirayama, Implementation of the Doppler broadening of a Compton-scattered photon into the EGS4 code, Nucl. Instrum. Methods Phys. Res., Sect. A 349 (1994) 489–494.

[33] R. Jenkins, R. Manne, R. Robin, C. Senemaud, Nomenclature, Symbols, Units and their Usage in Spectrochemical Analysis. VIII. Nomenclature system for X-ray spectroscopy - (Recommendations 1991), Pure Appl. Chem. 63 (1991) 735–746.

Chapter 4

Fundamental parameter based quantification algorithm for confocal nano X-ray fluorescence analysis

4.1 Introduction

X-ray fluorescence (XRF) has been used in analytical chemistry for several decades. Due to improvements in focusing optics and X-ray sources, a new branch has been formed that allows for the elemental imaging of samples at the (sub)micrometer spatial resolution level. Over the last ten years, a new variant called confocal micro-XRF has been developed that further reduces the probing volume by the mounting of a polycapillary half-lens in front of the detector. This has allowed for the characterization of a wide range of biological, geological, archaeometric samples[1–7]. In combination with a synchrotron radiation (SR) X-ray microbeam, it is possible to achieve absolute detection limits at the fg level, with a potential lateral resolution level of around 100 nm[8].

While imaging using confocal micro-XRF is a rather straightforward technique, the quantification of the spectral data remains challenging. Traditionally, XRF spectra have been quantified using empirical calibration (for bulk samples), Monte Carlo simulations[9,10] and the fundamental parameter method[11,12]. However, due to the energy dependent transmission properties of the polycapillary lens, these methods require modifications to ensure their compatibility with confocal micro-XRF. Several authors have already identified possible quantification pitfalls such as the mathematical description of the confocal volume[13]

and the treatment of secondary effects[14]. In this chapter we will present a methodology that can be used to quantify confocal micro-XRF data, along with a procedure to estimate the errors that accompany the results.

As an application of this methodology, we will discuss quantification results obtained from cometary dust particles, that were returned to Earth with National Aeronautical and Space Administration's (NASA) Stardust mission from comet 81P/Wild 2. Comet 81P/Wild 2 is a Jupiter family comet that was gravitationally forced into its current orbit in 1974 after a close encounter with Jupiter and is thought to have originated in the Kuiper Belt. The comet is made up of relict material from the solar nebula and is believed to have not been (strongly) changed since, e.g. by thermal metamorphism or hydrous alteration. NASA's Stardust spacecraft was designed to collect and bring comet coma particles from Comet 81P/Wild2 to Earth, as well as interstellar grains After a journey of 7 years in space, the Sample Return Capsule returned to Earth on January 15, 2006. The successful recovery of the Sample Return Capsule initiated an extensive study of this unique extraterrestrial material using various microanalytical and nanoanalytical techniques[4,8,15–17]. In order to facilitate the capture of the dust particles, NASA equipped the spacecraft with aerogel collectors, a silica based solid that has a porous, foamlike structure which is approximately 1000 times less dense than glass.. The relative speed between spacecraft and comet 81P/Wild2 during the flyby through the comet coma was ~ 6.1 km/s[18]. During capture, cometary particles entering the aerogel were stopped within a distance of typically a few hundred micrometers, creating carrot- and bulbous-shaped tracks inside the aerogel[16,19]. As the terminal particles of such impact tracks are typically only a few micrometers in size, a submicrometer spatial resolution is needed to study, e.g., the variation of elemental composition within the individual comet coma particles. The impact track studied was received inside a keystone which is a piece of dissected aerogel. The preparation was performed following the technique developed by Westphal et al[20]. The keystone analyzed in this example was extracted from cell C2012 and contained a carrot-shaped impact track (Track 110) with an end particle (terminal particle, TP) and several fragments along the wall of the track. The impact track has a total length of approximately 180 μm (Fig. 4.1). The use of the confocal optics, in conjunction with the exciting X-ray nano-beam (200-400 nm) allowed the local analysis of the TP, while effectively eliminating the impurity XRF signals originating from the aerogel collector.

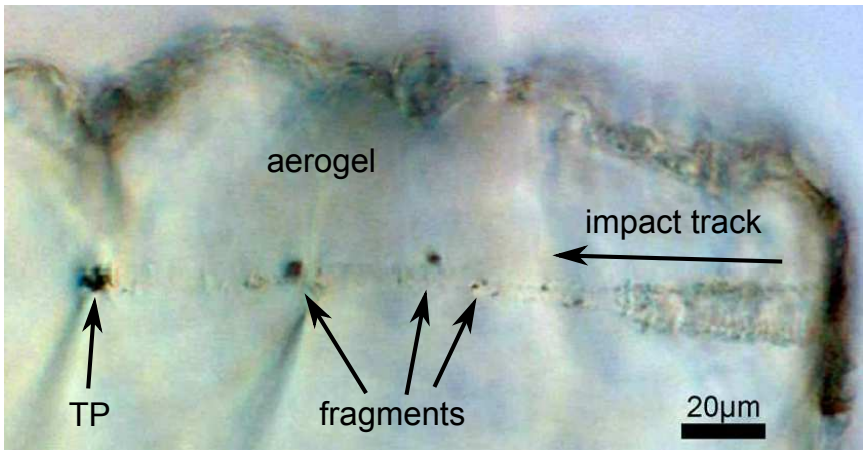

Figure 4.1: Stardust impact track 110 [C2012, 0, 100, 0, 0] with a total length of approx. 180 μm and a well defined TP at its end and several larger ($> 1\mu m$) and smaller fragments along the wall of the track.

4.2 Experimental

The entire impact track 110 was analyzed with SR induced XRF at the European Synchrotron Radiation Facility (ESRF) in Grenoble (France). The set-up was installed at the nano-focussing beamline ID13 that has an 18 mm period in-vacuum undulator X-ray source and is equipped with a liquid N_2 cooled Si(111) double crystal monochromator. The excitation energy of 12.7 keV combined with the detection in air allowed for the collection of elements between Si and Se for the K-lines and up to Pb for the L-lines. The incident beam size obtained was 300 $\times$ 1000 nm^2 with a flux of 9.7 $\times$ 10^{10} ph/s using two Be pre-focusing lenses or 300 $\times$ 300 nm^2 with one pre-focusing Be-lens at a lower flux of 3.9 $\times$ 10^9 ph/s. The fluorescence radiation was simultaneously collected in a confocal and a conventional detection mode with an energy-dispersive Si(Li) detector and a Vortex Si drift detector placed in a 90° geometry in the plane of linear polarization to reduce background signals. The working distance of the polycapillary half lens was only a few mm (< 2 mm) and the acceptance full width at half maximum (FWHM) in the direction perpendicular to the capillary was measured with a vertical detector scan over a 100 μm thick National Institute of Standards and Technology (NIST) standard reference material (SRM) 613 sample to be approximately 19 μm for Fe-K_α. This value was subsequently used to calculate the acceptance FWHM corresponding with the other XRF lines assuming

an inverse proportional relation between FWHM and line energy. A clear advantage of the confocal detection model is that it strongly reduces the fluorescence signal produced by the aerogel and its contaminants. For information on sample preparation and measurement strategies, the reader is referred to Schmitz et al[4].

4.3 Theory

4.3.1 Introduction

The equations we developed for the quantification of confocal nano-XRF data are based on the emission-transmission method[21] that establishes a relation between the K_α net-line intensity of an element i, $I_{i,K\alpha}$, and its corresponding weight fraction w_i for samples consisting of a single layer that are irradiated with a monochromatic beam (see Fig. 4.2):

$$I_{i,K\alpha} = I_0 G w_i Q_{i,K\alpha} \rho T \left(\frac{1 - \exp(-\chi\rho T)}{\chi\rho T} \right) \tag{4.1}$$

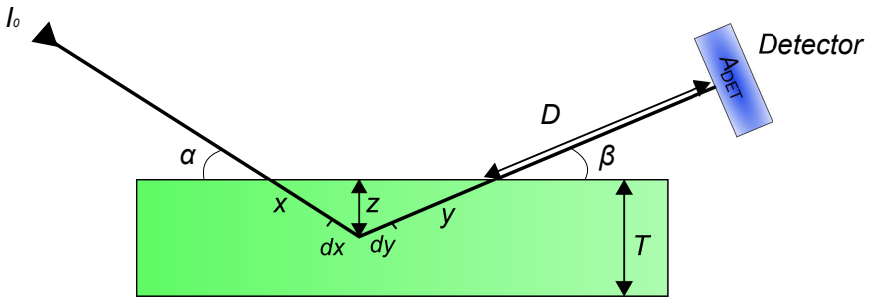

Figure 4.2: Schematic representation of the emission-transmission method, a classic method used for the quantification of XRF datasets of intermediate-thickness samples

Here I_0 is the beam intensity, G is a geometry factor determined by the characteristics of the detector and its position with respect to the beam, $Q_{i,K\alpha}$ is the XRF production cross-section and ρ and T are respectively the density and thickness of the sample. It should be noted that although Eq. (4.1) and all subsequent equations are derived for K_α radiation, similar equations may be derived for any other XRF line or group of XRF lines. Of special importance is the factor $\left(\frac{1 - \exp(-\chi\rho T)}{\chi\rho T} \right)$ which will correct for the absorption of both the impinging beam and the produced fluorescence radiation. The factor χ is calculated as:

$$\chi = \frac{\sum_{k=1}^{n} w_k \mu_{k,0}}{\sin \alpha} + \frac{\sum_{k=1}^{n} w_k \mu_{k,1}}{\sin \beta} \tag{4.2}$$

χ is determined both by the experimental setup through the angles α and β, as well as by the mass attenuation coefficients μ of all the elements in the samples for both the energy of the exciting beam and the K_α fluorescence energy of element i. The definition of χ reveals that the solution of this system of equations for all elements i must be solved in an iterative manner, unless the absorption can be ignored (thin/light sample). The emission-transmission equation can be easily extended for situations where the exciting and/or fluorescence photons need to cross additional layers by adding exponential Lambert-Beer terms which will correct for the additional absorption. This allows for example to take into account absorption and transmission effects in detectors. One should also be aware of the limitations of the emission-transmission equation: it ignores secondary effects such as fluorescence enhancement, which in some cases can have a considerable impact on the quantification results. Solutions for this issue can be found throughout the literature[22,23] but will not be considered in our work.

Eq. (4.1) can be used for the quantification of a sample in combination with a SRM measurement by observing the ratio of the emission-transmission equations of both:

$$\frac{I_{i,K\alpha}^{(u)}}{I_{i,K\alpha}^{(s)}} = \frac{I_0^{(u)} G w_i^{(u)} Q_{i,K\alpha} \rho^{(u)} T^{(u)} A_{i,corr}^{(u)}}{I_0^{(s)} G w_i^{(s)} Q_{i,K\alpha} \rho^{(s)} T^{(s)} A_{i,corr}^{(s)}} \tag{4.3}$$

with (u) and (s) referring to the unknown sample and the standard reference material respectively. The absorption correction factor $A_{i,corr}$ stands for:

$$A_{i,corr} = \left(\frac{1 - \exp(-\chi \rho T)}{\chi \rho T} \right) \tag{4.4}$$

Eq. (4.3) can be further simplified since the geometrical factor G and the XRF production cross-sections $Q_{i,K\alpha}$ are identical in denominator and numerator:

$$\frac{I_{i,K\alpha}^{(u)}}{I_{i,K\alpha}^{(s)}} = \frac{I_0^{(u)} w_i^{(u)} \rho^{(u)} T^{(u)} A_{i,corr}^{(u)}}{I_0^{(s)} w_i^{(s)} \rho^{(s)} T^{(s)} A_{i,corr}^{(s)}} \tag{4.5}$$

This approach has the great advantage of reducing the uncertainty on the final result as these XRF cross sections very often have considerable errors. This problem is known to be more serious for L-lines and M-lines than for K-lines[24]. Eq. (4.5) implies that a solution

can only be obtained for elements that are present in both standard reference material and unknown. This suggests to make use of standard reference materials that contain as many elements as possible, however, this is very often not a desirable solution. For instance, the NIST standard reference materials 610 to 613 contain up to sixty-one trace elements and four major elements, leading to considerable overlap in the resulting XRF spectra and thus, less reliable net-line intensities $I^{(s)}_{i,K\alpha}$ [25]. Therefore, we have used an SRM containing fewer elements and calculate the experimental elemental yields Y_i, defined as:

$$Y_{i,exp} = \frac{I^{(s)}_{i,K\alpha}}{I^{(s)}_0 w^{(s)}_i \rho^{(s)} T^{(s)} A^{(s)}_{i,corr}} = GQ_{i,K\alpha} \tag{4.6}$$

These yields $Y_{i,exp}$ were subsequently subjected to a procedure resulting in interpolated yield values for the elements present in the standard reference material as well as some that are absent in the SRM. The different steps in this calibration procedure are as follows:

1. Perform a weighted linear least squares polynomial fit of the experimental yields versus atomic number. The order of the polynomials used was three or four. The weights were set to the standard deviations on the experimental yields values as calculated with standard error propagation calculations, taking into account the standard deviation of net-line intensity, certified concentrations and errors of density and thickness.

2. Determine the new elemental yields $Y_{i,fit}$ for the elements present in the standard and those missing by interpolation.

3. In combination with an error estimation procedure (detailed in section 4.3.6), one obtains an accurate description of the distribution of these new elemental yields $Y_{i,fit}$

The interpolation scheme in the second step is only performed when two criteria are satisfied: at least four experimental yields are available and, if the difference between the atomic numbers of two consecutive elements present in the SRM is not larger than three. If these conditions were not met, the experimental yields $Y_{i,exp}$ were used instead. The conditions are imposed to assure the reliability of the fit of the experimental yields by requiring a minimum number of yields to be considered and by avoiding the use of yields of elements that are isolated from the main group. Taking these considerations into account, Eq. (4.5) transforms into:

$$w_i^{(u)} = \frac{I_{i,K\alpha}^{(u)}}{Y_i I_0^{(u)} \rho^{(u)} T^{(u)} A_{i,corr}^{(u)}} \tag{4.7}$$

with Y_i corresponding with either the experimental elemental yields or the interpolated elemental yields obtained according to the aformentioned two criteria.

We have taken Eq. (4.7) as a starting point for our derivations and combined it with the unique properties of the confocal setup to come up with new equations which will be discussed in the following sections.

4.3.2 An SRM based fundamental parameter model

The emission-transmission equation (Eq. (4.1)) assumes that samples are described as (a stack of) infinitely long parallel layers with a fixed thickness. While this may be appropriate and sufficient for the analysis of bulk samples, it is useful to make use of a more comprehensive model to describe samples that diverge significantly from the emission-transmission model. We have developed a new way to model samples cross sections using geometrical shapes such as rectangles and ellipses. An example can be found in Fig. 4.3 in which a situation is described where an ellipse shaped layer of interest is surrounded by two rectangular shaped layers. It is possible for the user to rotate the geometrical shapes to allow for the description of even more complicated models. In this modified form of the emission-transmission equation, it is assumed that the detector is positioned under an angle of 90° with respect to the incoming beam.

Obviously this new model implies considerable mathematical modifications to the emission-transmission equation. We have solved this problem by partitioning the layer of interest along the beampath in a large number (typically several thousands) of narrow intervals Δx_j, in which we individually apply a modified form of the emission-transmission equation, and afterwards sum up the individual contributions of all these intervals.

Consider the interval Δx_j. The procedure can be broken down into three steps:

1. Calculate the intensity of the incoming beam that reaches an interval Δx_j. This takes into account the absorption contributions from the layers that are traversed before the layer of interest as well as the contributions from the intervals Δx_1 to

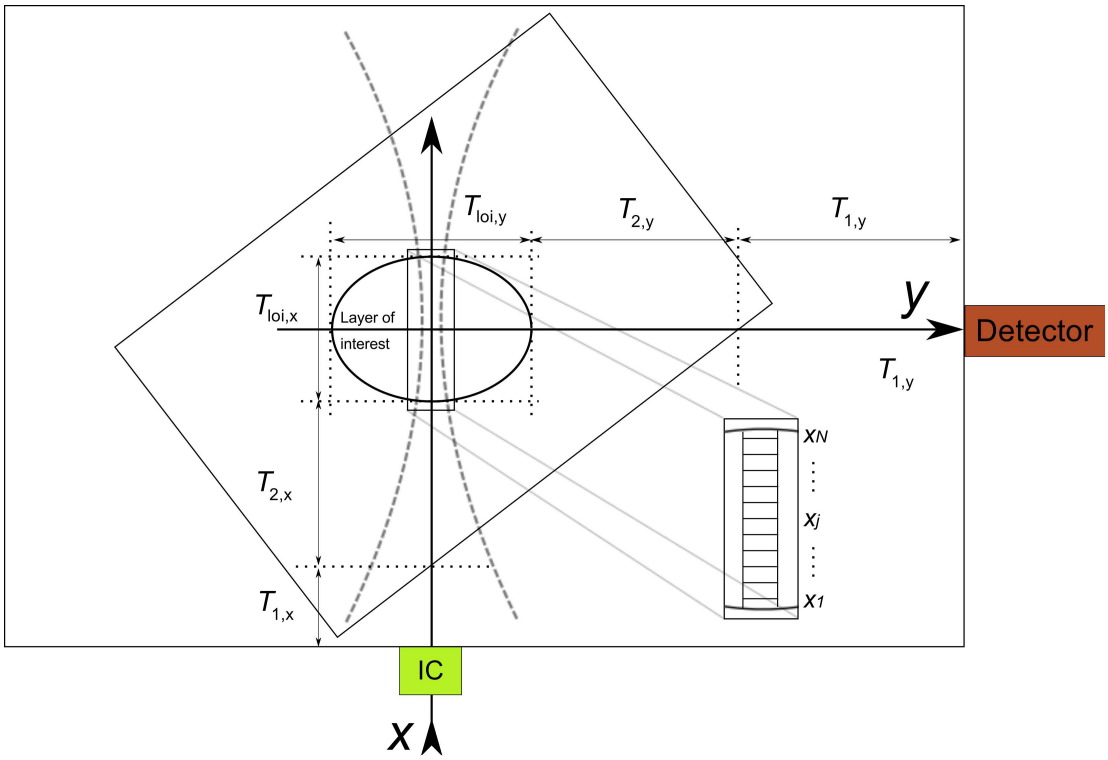

Figure 4.3: Schematic representation of an example descriptive model consisting of two rectangles and an ellipse (layer of interest). A very similar situation was used to model the Stardust samples: an ellipse (circle) is used to describe the particle, while the surrounding aerogel and air layers are represented by rectangles.

Δx_{j-1} within the layer of interest. Mathematically:

$$\mathrm{abs}^{X}_{\Delta x_j} = I_0 \left(\prod_{k=1}^{nlay-1} \exp\left(-\mu_{k,0}\rho_k T_{k,x}\right) \right) \exp\left(-\mu_{nlay,0}\rho_{nlay}(x_j - x_1)\right) \tag{4.8}$$

with $nlay$ the total number of layers ($1 \ldots nlay$, with $nlay$ corresponding to the layer of interest) and $T_{k,x}$ the thickness of the k-th layer along the beam-axis.

2. Integrate the generated K_α fluorescence intensity of element i in Δx_j:

$$\mathrm{fluo}_{\Delta x_j} = \int_{x_j}^{x_{j+1}} \rho_{nlay} w_{i,nlay} Q_{i,K\alpha} \exp\left(-\mu_{nlay,0}\rho_{nlay} x\right) dx \tag{4.9}$$

$$= \frac{w_{i,nlay} Q_{i,K\alpha}}{\mu_{nlay,0}} \left[\exp\left(-\mu_{nlay,0}\rho_{nlay} x_j\right) - \exp\left(-\mu_{nlay,0}\rho_{nlay} x_{j+1}\right) \right] \tag{4.10}$$

3. Calculate the attenuation that will be experienced by the fluorescence intensity produced in Δx_j before reaching the detector, including the absorption by the layer of interest and the other layers in the model:

$$\mathrm{abs}^{Y}_{\Delta x_j} = \prod_{k=1}^{nlay} \exp\left(-\mu_{k,1}\rho_k T_{k,y,j}\right) \tag{4.11}$$

with $T_{k,y,j}$ the thickness of the k-th layer along the detector-axis experienced by photons produced in interval Δx_j.

The sum for all intervals N of the product of Eqs. (4.8) and (4.11) and Item 2 and a geometry factor G yields an equation for the K_α net-line intensity of element i:

$$I_{i,K\alpha} = G\sum_{j=1}^{N}\left[\mathrm{abs}^{X}_{\Delta x_j}\mathrm{fluo}_{\Delta x_j}\mathrm{abs}^{Y}_{\Delta x_j}\right] \tag{4.12}$$

$$= I_0 G\frac{w_{i,nlay}Q_{i,K\alpha}}{\mu_{nlay,0}}\sum_{j=1}^{N}\left[\left(\prod_{k=1}^{nlay-1}\exp\left(-\mu_{k,0}\rho_k T_{k,x}\right)\right)\right.$$
$$\left[\exp\left(-\mu_{nlay,0}\rho_{nlay}x_j\right)-\exp\left(-\mu_{nlay,0}\rho_{nlay}x_{j+1}\right)\right] \tag{4.13}$$
$$\left.\exp\left(-\mu_{nlay,0}\rho_{nlay}(x_j-x_1)\right)\left(\prod_{k=1}^{nlay}\exp\left(-\mu_{k,1}\rho_k T_{k,y,j}\right)\right)\right]$$

Considering the similarity with Eq. (4.1), one can devise a new expression for the absorption correction factor:

$$A_{i,corr} = \frac{1}{\mu_{nlay,0}\rho_{nlay}T_{nlay,x}}\sum_{j=1}^{N}\left[\left(\prod_{k=1}^{nlay-1}\exp\left(-\mu_{k,0}\rho_k T_{k,x}\right)\right)\right.$$
$$\left[\exp\left(-\mu_{nlay,0}\rho_{nlay}x_j\right)-\exp\left(-\mu_{nlay,0}\rho_{nlay}x_{j+1}\right)\right]$$
$$\left.\exp\left(-\mu_{nlay,0}\rho_{nlay}(x_j-x_1)\right)\left(\prod_{k=1}^{nlay}\exp\left(-\mu_{k,1}\rho_k T_{k,y,j}\right)\right)\right] \tag{4.14}$$

An equation similar to Eq. (4.11) can also be derived, based on the same model, for polychromatic X-ray beams. Assuming that the excitation spectrum is described using N_e discrete intervals ΔE_l, each with a corresponding intensity I_0^l, one obtains:

$$I_{i,K\alpha} = G\sum_{j=1}^{N}\sum_{l=1}^{N_e}\left[\mathrm{abs}^{l,X}_{\Delta x_j}\mathrm{fluo}^{l}_{\Delta x_j}\mathrm{abs}^{Y}_{\Delta x_j}\right] \tag{4.15}$$

$$\begin{aligned} = Gw_{i,nlay}\sum_{j=1}^{N}\Bigg[\left(\prod_{k=1}^{nlay}\exp\left(-\mu_{k,1}\rho_k T_{k,y,j}\right)\right)\sum_{l=1}^{N_e}\Bigg(\frac{I_0^l Q^l_{i,K\alpha}}{\mu^l_{nlay,0}} \\ \left[\exp\left(-\mu^l_{nlay,0}\rho_{nlay}x_j\right)-\exp\left(-\mu^l_{nlay,0}\rho_{nlay}x_{j+1}\right)\right] \\ \exp\left(-\mu^l_{nlay,0}\rho_{nlay}(x_j-x_1)\right)\left(\prod_{k=1}^{nlay-1}\exp\left(-\mu^l_{k,0}\rho_k T_{k,x}\right)\right)\Bigg)\Bigg] \end{aligned} \tag{4.16}$$

In practice, we chose not to use Eqs. (4.11) and (4.14) directly, but instead prefer a standard based quantification method as was demonstrated in section 4.3.1 through Eqs. (4.5) and (4.7). This leads to the following expression for the monochromatic case (after simplification):

$$\frac{I^{(u)}_{i,K\alpha}}{I^{(s)}_{i,K\alpha}} = \frac{\sum_{j=1}^{N}\left[\mathrm{abs}^{X}_{\Delta x_j}\mathrm{fluo}_{\Delta x_j}\mathrm{abs}^{Y}_{\Delta x_j}\right]^{(u)}}{\sum_{j=1}^{N}\left[\mathrm{abs}^{X}_{\Delta x_j}\mathrm{fluo}_{\Delta x_j}\mathrm{abs}^{Y}_{\Delta x_j}\right]^{(s)}} \tag{4.17}$$

This equation is subsequently transformed into an expression containing elemental yields, that are obtained either directly from experimental yields or through interpolation of experimental yields. In fact, this new equation is identical to Eq. (4.7), although with a different expression for the absorption correction term $A^{(u)}_{i,corr}$, which is now given by Eq. (4.14) instead of Eq. (4.4).

4.3.3 Confocal X-ray fluorescence

The typical setup of a confocal X-ray fluorescence experiment is obtained by the mounting of a polycapillary half-lens in front of an energy dispersive detector (see Fig. 4.4). This is accomplished in such a way that the focus of the incoming beam coincides with the focus of the detector polycapillary half-lens. The focusing properties of the polycapillary are achieved through a bundle of several hundred thousands of narrow bent parallel glass fibers that are oriented towards the same focal point. These fibers transport X-ray photons through repeated total external reflections, provided they have entered under an angle that is smaller than their critical angle of total reflection θ_C. Since this angle depends on the energy of the photon[2], both transmission efficiency and the confocal volume defined by

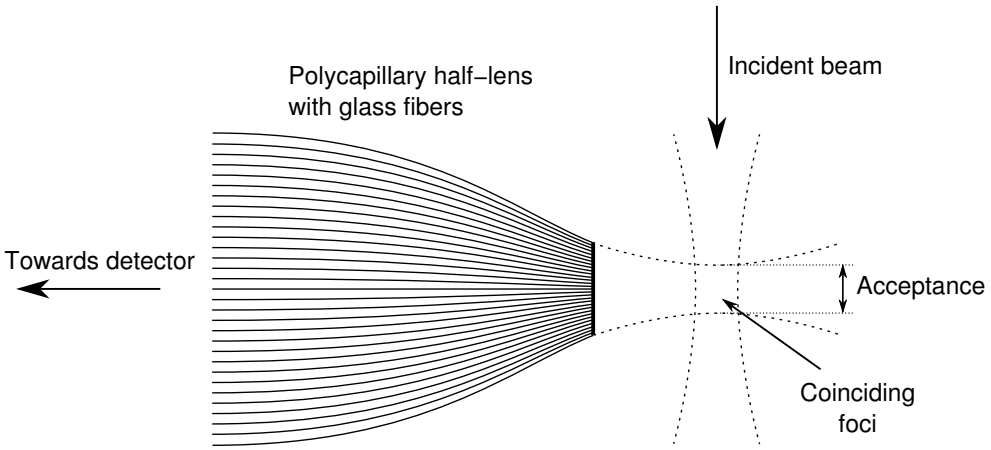

Figure 4.4: Schematic representation of a confocal setup

the intersection of the foci, will also be energy dependent. Because the polycapillary acceptance, defined as the FWHM of the detection volume measured along the beam axis in the plane formed by the X-ray beam and the detector , is approximately inverse proportional to the energy of the photons, the dimensions of the confocal volumes will be equally determined by the energy of the X-ray fluorescence photons. For the exciting beam, several focusing options such as CRL lenses[26], Fresnel zone plates[4], Kirkpatrick-Baez mirrors and polycapillaries[2] can be used.

4.3.4 Confocal nano X-ray fluorescence quantification

The model that has been described in Section 4.3.2 is useful for all conventional X-ray fluorescence techniques. It cannot be used for confocal XRF: Eq. (4.11) assumes that every interval Δx_j will have an identical contribution to the spectrum recorded by the detector. The polycapillary halflens that has been mounted in front of the detector however, voids this assumption. Malzer and Kanngiesser (2005) presented a mathematical model that describes the characteristics of the confocal volume in the case of a confocal setup obtained using a polycapillary in the excitation path[13]. Since we assume however, that the focussing is done using a technique that produces a beam that is very small compared to the acceptance of the polycapillary halflens, a 1-dimensional model of the confocal detection can be used. In our model for confocal nano XRF, we assume that the intensity weight distribution of the detected photons follows a Gaussian distribution with the FWHM equal

to the acceptance around the detector axis. The validity of this model was demonstrated by Wolff et al[27]. The absorption correction is, as before, calculated over the entire length of the layer of interest, but the contribution of every interval Δx_j will be scaled with a factor equal to the ratio of the difference of the cumulative distribution functions of the corresponding normal distribution calculated at the start and end of the interval, and the length of the interval $(x_{j+1} - x_j)$ and with the height of the probability density function scaled to one (see Fig. 4.5):

$$\begin{aligned} \text{scale}_{x_j} &= \text{FWHM}_{acc}\sqrt{\frac{\pi}{4\ln 2}}\left(\frac{\Phi\left(\frac{(x_{j+1}-x_{center})2\sqrt{2\ln 2}}{\text{FWHM}_{acc}}\right)-\Phi\left(\frac{(x_j-x_{center})2\sqrt{2\ln 2}}{\text{FWHM}_{acc}}\right)}{(x_{j+1}-x_j)\times 1}\right) \quad (4.18)\\ &= \frac{\text{FWHM}_{acc}}{2}\sqrt{\frac{\pi}{4\ln 2}}\left(\frac{\text{erf}\left(\frac{(x_{j+1}-x_{center})2\sqrt{\ln 2}}{\text{FWHM}_{acc}}\right)-\text{erf}\left(\frac{(x_j-x_{center})2\sqrt{\ln 2}}{\text{FWHM}_{acc}}\right)}{(x_{j+1}-x_j)}\right) \quad (4.19)\end{aligned}$$

Here x_{center} corresponds with the intersection of the excitation axis and the detector channel axis.

Using this scale factor one obtains, after multiplication with Eq. (4.11), and the energy-dependent transmission efficiency $\nu_{i,K\alpha}$, an expression that produces the net-line intensity $I_{i,K\alpha}$ recorded by the detector in confocal mode using monochromatic excitation:

$$\begin{aligned} I_{i,K\alpha} = \;& G\sum_{j=1}^{N}\left[\text{abs}^0_{\Delta x_j}\text{fluo}_{\Delta x_j}\text{abs}^1_{\Delta x_j}\text{scale}_{x_j}\right]\nu_{i,K\alpha} \\ = \;& I_0 G\frac{w_{i,nlay}Q_{i,K\alpha}}{\mu_{nlay,0}}\frac{\text{FWHM}_{acc}}{2}\sqrt{\frac{\pi}{4\ln 2}}\sum_{j=1}^{N}\Bigg[\prod_{k=1}^{nlay-1}\exp\left(-\mu_{k,0}\rho_k T_{k,x}\right) \\ & \left[\exp\left(-\mu_{nlay,0}\rho_{nlay}x_j\right)-\exp\left(-\mu_{nlay,0}\rho_{nlay}x_{j+1}\right)\right] \\ & \exp\left(-\mu_{nlay,0}\rho_{nlay}(x_j-x_1)\right)\prod_{k=1}^{nlay}\exp\left(-\mu_{k,1}\rho_k T_{k,y,j}\right) \\ & \left(\frac{\text{erf}\left((x_{j+1}-x_{center})2\sqrt{\ln 2}\,\text{FWHM}_{acc}^{-1}\right)-\text{erf}\left((x_j-x_{center})2\sqrt{\ln 2}\,\text{FWHM}_{acc}^{-1}\right)}{(x_{j+1}-x_j)}\right)\Bigg]\nu_{i,K\alpha} \end{aligned} \quad (4.20)$$

Since we prefer to use a standard based quantification procedure, we obtain

$$\frac{I^{(u)}_{i,K\alpha}}{I^{(s)}_{i,K\alpha}} = \frac{\sum_{j=1}^{N}\left[\text{abs}^X_{\Delta x_j}\text{fluo}_{\Delta x_j}\text{abs}^Y_{\Delta x_j}\text{scale}_{x_j}\right]^{(u)}}{\sum_{j=1}^{N}\left[\text{abs}^X_{\Delta x_j}\text{fluo}_{\Delta x_j}\text{abs}^Y_{\Delta x_j}\text{scale}_{x_j}\right]^{(s)}} \quad (4.21)$$

This equation was used further on in the examples. Remark that the above equations require access to several fundamental parameters such as cross-sections (photoelectric effect,

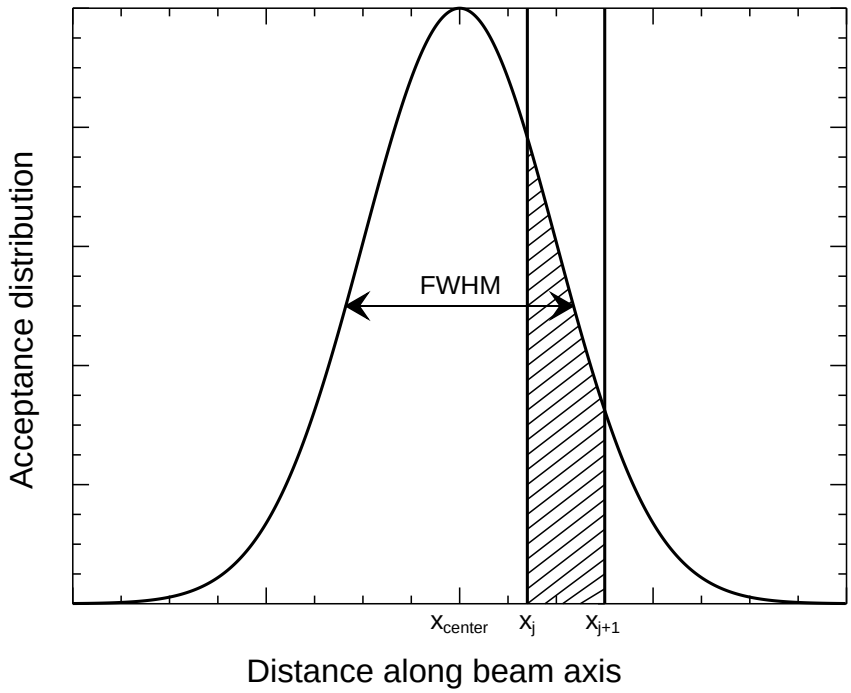

Figure 4.5: Schematic representation of the scale factor for confocal XRF quantification: the factor is calculated as the ratio of the shaded surface and the area of the rectangle enclosed by x_j and x_{j+1}

Rayleigh, Compton), XRF line energies, absorption edge energies etc. For this purpose, we made use of *xraylib*, a library for X-ray–matter interaction cross-sections for XRF applications[24,28] (see Chapter 3).

4.3.5 Depth estimation of the confocal volume

Our quantification model for confocal XRF requires the user to determine the depth of the confocal volume within the layer of interest. This is needed for an accurate calculation of the self-absorption effects: positioning the confocal volume deeper translates into a smaller absorption correction factor. We have estimated the depth of the confocal volume d (see Fig. 4.6), defined as the distance from the center of the confocal volume to the surface of the SRM along the axis of the detector polycapillary, using a simplified version of the fundamental parameter equation for confocal XRF (assuming that $\alpha = \beta = 45°$) that was

deduced for both K_α and K_β photons, based on Eq. (4.1):

$$I_{i,K\alpha} = I_0 G w_i Q_{i,K\alpha} \rho T_{acc,K\alpha} \frac{\sqrt{2}}{2} A_{corr,K\alpha} \tag{4.22}$$

with $T_{acc,K\alpha}$ equal to the (energy-dependent) acceptance (FWHM) of the polycapillary halflens.

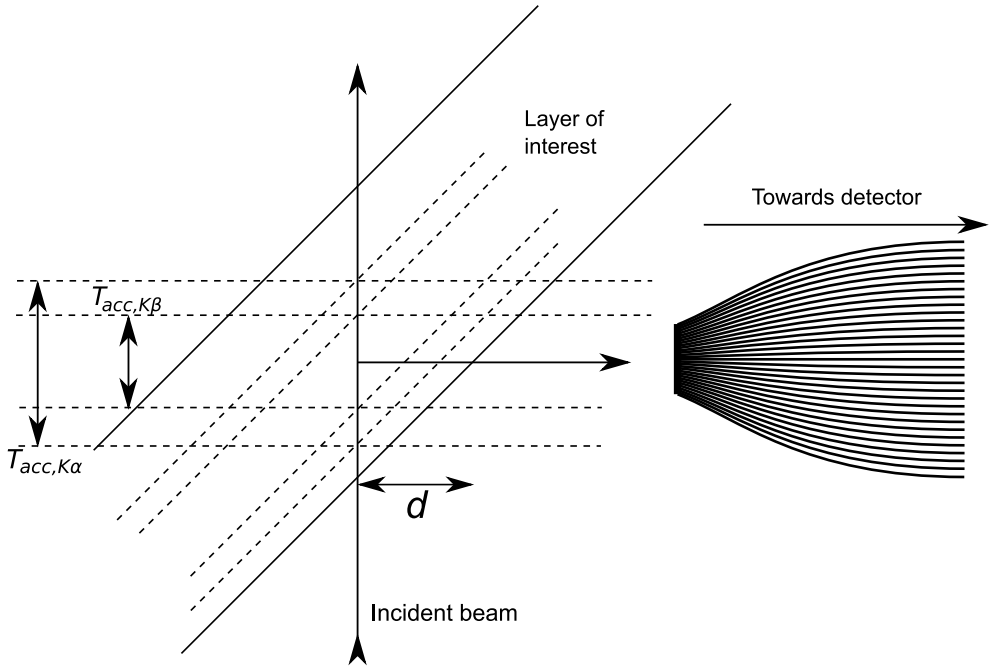

Figure 4.6: Schematic representation of depth estimation model

According to the situation depicted in Fig. 4.6, terms need to be added to correct for absorption of the incoming beam before the confocal volume, and for absorption by the fluorescence photons outside the confocal volume. Combined with terms that correct for the absorption in additional layers and the detector efficiency $\varepsilon_{i,K\alpha}$, one obtains:

$$\begin{aligned} I_{i,K\alpha} = I_0 G w_i Q_{i,K\alpha} \rho_{loi} T_{acc,K\alpha} \frac{\sqrt{2}}{2} A_{corr,K\alpha} \\ \exp\left(-\mu_{0,loi}\rho_{loi}\left(d - \frac{T_{acc,K\alpha}}{2}\right)\right) \exp\left(-\mu_{1,loi,K\alpha}\rho_{loi}\left(d - \frac{T_{acc,K\alpha}}{2}\right)\right) \\ \prod_{j=1}^{nlay} \exp\left(-\mu_{0,j}\rho_j T_j\right) \prod_{k=1}^{nlay} \exp\left(-\mu_{1,k,K\alpha}\rho_k T_k\right) \varepsilon_{i,K\alpha} \end{aligned} \tag{4.23}$$

and similar for the K_β intensity:

$$I_{i,K\beta} = I_0 G w_i Q_{i,K\beta} \rho_{loi} T_{acc,K\beta} \frac{\sqrt{2}}{2} A_{corr,K\beta} \exp\left(-\mu_{0,loi}\rho_{loi}\left(d - \frac{T_{acc,K\beta}}{2}\right)\right) \exp\left(-\mu_{1,loi,K\beta}\rho_{loi}\left(d - \frac{T_{acc,K\beta}}{2}\right)\right) \prod_{j=1}^{nlay} \exp\left(-\mu_{0,j}\rho_j T_j\right) \prod_{k=1}^{nlay} \exp\left(-\mu_{1,k,K\beta}\rho_k T_k\right) \varepsilon_{i,K\beta} \quad (4.24)$$

In both these equations (4.23) and (4.24), the variable d is of interest, which corresponds to the depth of the confocal volume within the layer of interest. An expression for d can be obtained by observing the ratio of these two equations while cancelling out several terms in numerator and denominator:

$$\frac{I_{i,K\alpha}}{I_{i,K\beta}} = \frac{Q_{i,K\alpha} T_{acc,K\alpha} A_{corr,K\alpha} \exp\left(\mu_{0,loi}\rho_{loi}\frac{T_{acc,K\alpha}}{2}\right)}{Q_{i,K\beta} T_{acc,K\beta} A_{corr,K\beta} \exp\left(\mu_{0,loi}\rho_{loi}\frac{T_{acc,K\beta}}{2}\right)} \times \frac{\exp\left(-\mu_{1,loi,K\alpha}\rho_{loi}\left(d - \frac{T_{acc,K\alpha}}{2}\right)\right)}{\exp\left(-\mu_{1,loi,K\beta}\rho_{loi}\left(d - \frac{T_{acc,K\beta}}{2}\right)\right)} \times \frac{\prod_{k=1}^{nlay} \exp\left(-\mu_{1,k,K\alpha}\rho_k T_k\right) \varepsilon_{i,K\alpha}}{\prod_{k=1}^{nlay} \exp\left(-\mu_{1,k,K\beta}\rho_k T_k\right) \varepsilon_{i,K\beta}} \quad (4.25)$$

which can be rewritten as:

$$d = \frac{\ln\left(\frac{I_{i,K\alpha}}{I_{i,K\beta}}\right) + \ln\left(\frac{p_{i,K\beta}}{p_{i,K\alpha}}\right) + \ln\left(\frac{T_{acc,K\beta}}{T_{acc,K\alpha}}\right) + \ln\left(\frac{A_{corr,K\beta}}{A_{corr,K\alpha}}\right)}{\rho_{loi}\left(\mu_{1,loi,K\beta} - \mu_{1,loi,K\alpha}\right)} + \frac{\left(\mu_{0,loi}\rho_{loi}\left(\frac{T_{acc,K\beta}}{2} - \frac{T_{acc,K\alpha}}{2}\right)\right) + \left(\rho_{loi}\left(\frac{\mu_{1,loi,K\beta}T_{acc,K\beta}}{2} - \frac{\mu_{1,loi,K\alpha}T_{acc,K\alpha}}{2}\right)\right)}{\rho_{loi}\left(\mu_{1,loi,K\beta} - \mu_{1,loi,K\alpha}\right)} + \frac{\sum_{k=1}^{nlay}\left(\rho_k T_k\left(\mu_{1,k,K\alpha} - \mu_{1,k,K\beta}\right)\right) + \ln\left(\frac{\varepsilon_{i,K\beta}}{\varepsilon_{i,K\alpha}}\right)}{\rho_{loi}\left(\mu_{1,loi,K\beta} - \mu_{1,loi,K\alpha}\right)} \quad (4.26)$$

In this equation we replaced the XRF production cross-sections $Q_{i,K\alpha}$ and $Q_{i,K\beta}$ respectively with the radiative rates $p_{i,K\alpha}$ and $p_{i,K\beta}$, which is valid considering the relations:

$$\begin{aligned} Q_{i,K\alpha} &= \sigma_{i,K}\omega_{i,K}p_{i,K\alpha} \\ Q_{i,K\beta} &= \sigma_{i,K}\omega_{i,K}p_{i,K\beta} \end{aligned} \tag{4.27}$$

Here $\sigma_{i,K}$ and $\omega_{i,K}v$ represent the partial photoelectric effect cross-section for the K shell of element i, and the fluorescence yield for the K shell of element i.
This method is based on two simplifications: it ignores the energy-dependent transmission efficiency of the polycapillary, as well as the Gaussian acceptance of the polycapillary. For this reason, the depth was included into our Monte Carlo based error estimation scheme (see next section), by varying this parameter using a uniform distribution assuming our result has a 10 % error. An alternative method for the depth estimation of the confocal volume is based on a depth scan over the surface of the SRM and may produce a more accurate estimate[13,29].

4.3.6 Error estimation

Taking into account that Eq. (4.21) is solved in an iterative manner, it is possible to rewrite the equation symbolically as:

$$w_i^{(u)} = f\left(I_{i,K\alpha}^{(u)}, I_{i,K\alpha}^{(s)}, w_i^{(s)}, \rho_j^{(u)}, \rho_j^{(s)}, T_j^{(u)}, T_j^{(s)}, \ldots\right) \tag{4.28}$$

Assuming that the errors and standard deviations of all these parameters were known, it remains an exceedingly difficult task to obtain an analytical solution based on the error propagation formulas that would yield the error estimate of $w_i^{(u)}$. Therefore, a different approach for the error estimation was devised that is essentially a brute-force Monte Carlo method. Based on the use of a random number generator, new values of the experimental parameters based on their original mean and their associated measurement errors or standard deviations are determined. A uniform distribution was used for the densities and layer thicknesses, while for the weight fractions of the SRM Gaussian distributions were used. In the case of the net-line intensities we used a different approach: every channel of the originally recorded spectra was varied using a Poisson distribution with λ equal to the measured counts in the experimental spectrum. The newly produced spectrum was subsequently processed using a software package in order to extract the net-line intensities, in this case AXIL[30]. The use of the software package has the advantage that the variation due to the fitting routine will also be taken into account in the error estimation. This pro-

cedure was performed tens of thousands of times (typically 100000) yielding a distribution of the results. The specific error estimation protocol differs for yields and quantification values, and is represented in Figs. 4.7 and 4.8, respectively.

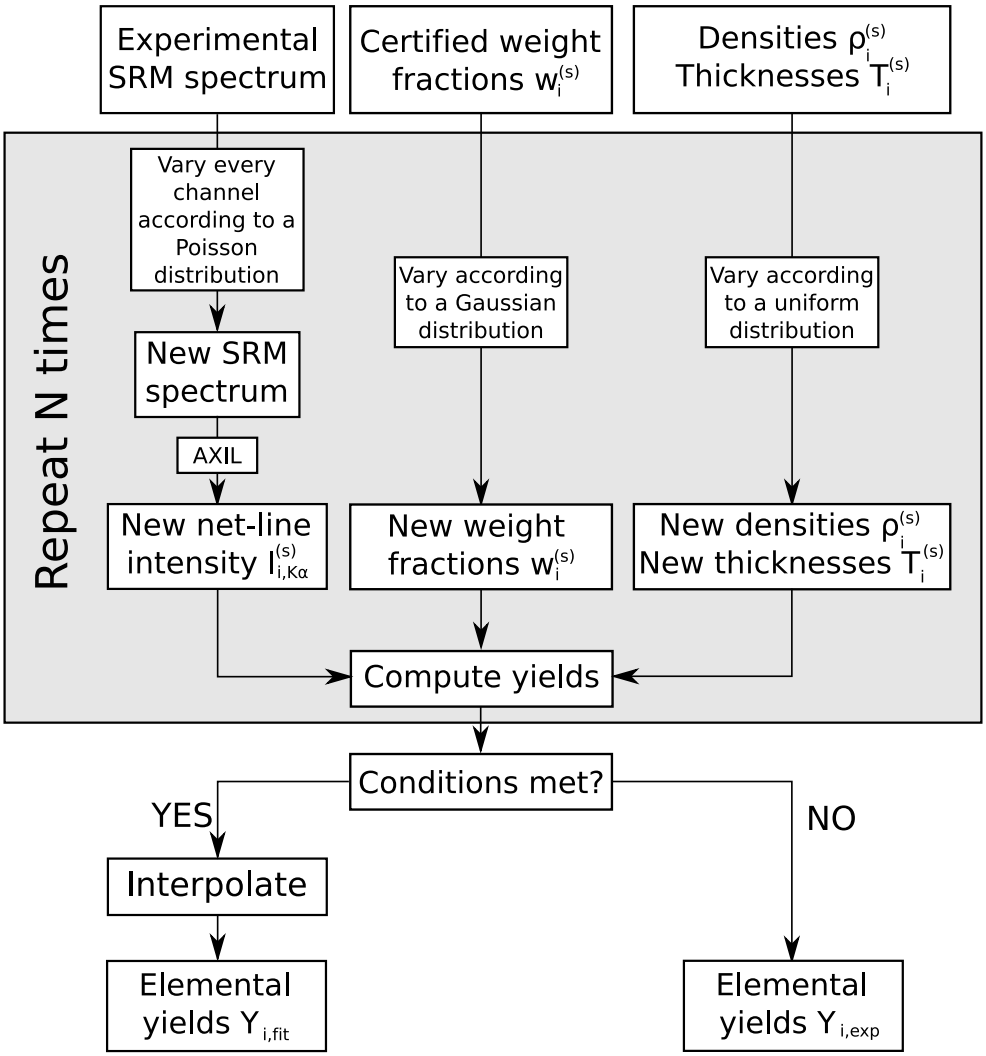

Figure 4.7: Schematic representation of the error estimation method used for the calculation of the elemental yields.

Critical in this approach was the use of a reliable pseudorandom number generator. We used the acclaimed Mersenne twister[31], implemented in the GNU Scientific Library[32]. Since the error estimation was carried out using multithreaded software, precautions were taken to ensure that each thread had its own random number generator instance and its own unique seed. The seeds themselves were obtained by reading from the random device

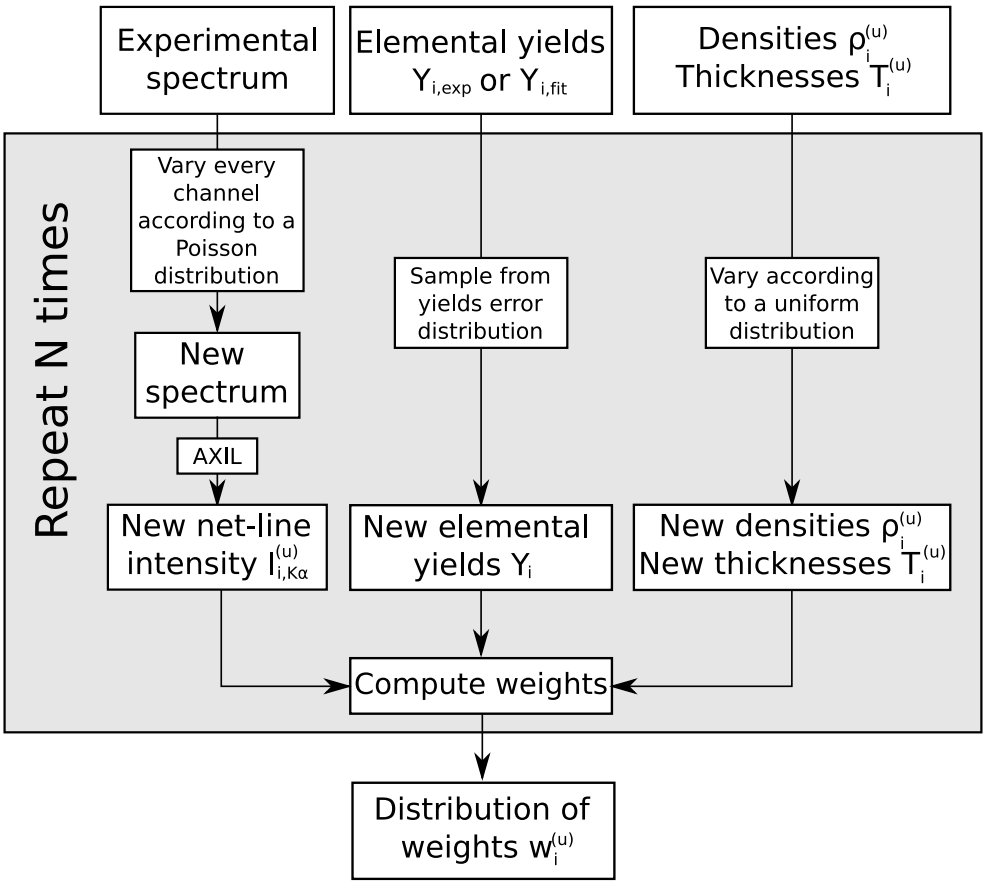

Figure 4.8: Schematic representation of the error estimation method for quantification.

`/dev/random` of a Linux workstation that collects environmental noise from device drivers (mouse and keyboard input), network traffic etc.

4.4 Results

In this section we will demonstrate some results that were obtained using the proposed methodology.

4.4.1 Elemental yields

The presented quantification procedure is based on the use of a standard reference material. In this particular example we made use of a 93 μm thick sample of the geological glass standard ATHO-G with certified elemental concentrations as the reference material[25]. A line scan of 11 points with a stepsize of 1 μm along the vertical axis was performed with 30 s real time per point, and the resulting normalized sum spectrum (see Fig. 4.9) was used to determine the elemental yields. A line scan was preferred over a single point measurement in order to avoid local inhomogeneity problems. The position of the standard within the horizontal plane was selected for optimal total count rate. Using Eq. (4.26) we obtained a depth d of 27.3 μm for the confocal volume based on the Ca-K_α XRF line. The sample did not allow for the calculation of the depth based on other elements: it can be seen in Fig. 4.9 that only the Ca XRF lines offer the high count rate, least overlap and the low energy that are required for sufficient contrast. For the normalization itself, we took into account the dead time of the detector as well as the reduction of the incident beam intensity over time using the readout of a mini-ionization chamber that was positioned into the beam just in front of the sample. The yields are not expressed in function of the ring current, since the exact correlation between mini-ionization readout and ring current was not stored during the experiment. This has however no impact on the quantification results. The experimental elemental yields are summarized in Table 4.1 and visualized in Fig. 4.10. In the case of the K_α lines, we used a third order polynomial while discarding Si (due to its separation from the main group of elemental yields) and Ni (due to its high relative standard deviation, caused by the high uncertainty of the certified concentration) from the further yields calculations. Since only two L_α lines were measured, no interpolation was performed on the corresponding elemental yields.

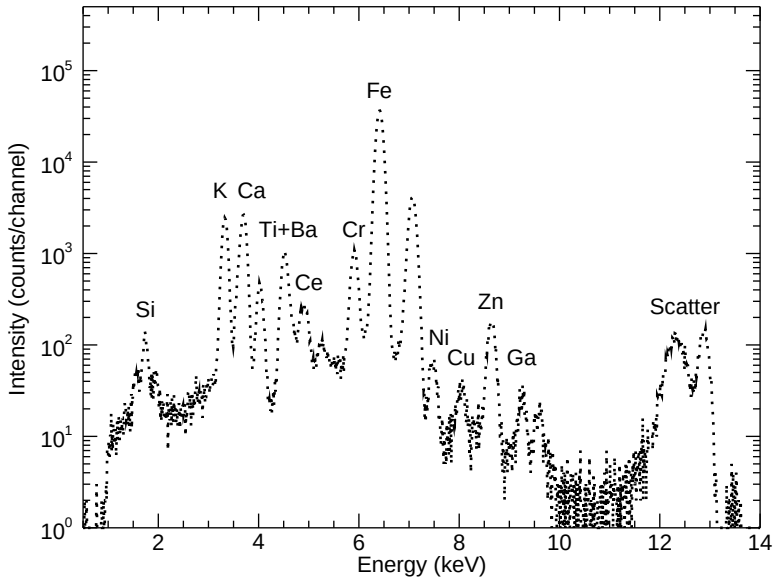

Figure 4.9: Normalized sum spectrum of a line scan performed on the ATHO-G geological glass reference material[25].

Table 4.1: Experimental yields of ATHO-G standard (counts*cm^2/s/g)

Element	Linetype	Elemental Yield	Standard deviation
Si	K_α	1.671	0.090
K	K_α	18.175	0.743
Ca	K_α	25.952	1.057
Ti	K_α	51.470	2.334
Mn	K_α	67.456	2.812
Fe	K_α	76.949	3.403
Ni	K_α	93.611	23.905
Cu	K_α	68.531	6.528
Zn	K_α	78.065	5.630
Ga	K_α	67.512	5.294
Ba	L_α	5.500	0.541
Ce	L_α	28.404	2.373

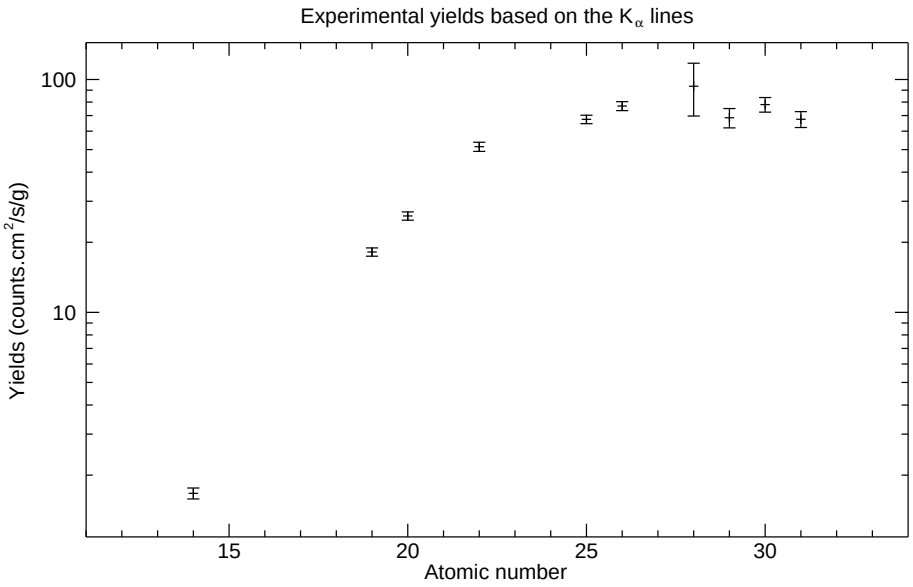

Figure 4.10: Experimental yields of ATHO-G standard (K_α lines only)

After applying our interpolation procedure on the experimental yields, combined with full error estimation using 50000 Monte Carlo simulations, we obtained the yields presented in Table 4.2.

The corresponding Monte Carlo based distribution histograms for the elemental yields of Ca, Cr, Fe and Zn are presented in Fig. 4.11. From these histograms, it can be seen that the shape of the curve varies considerably from Gaussian to almost uniform. This can be explained by the fact that these histograms are in fact convolutions of uniform (density, thickness), normal (weights of the elements in the SRM) and Poisson distributions (spectra). Depending on which relative standard deviation or error dominates, the corresponding distribution will have the most profound impact on the appearance of the histogram.

4.4.2 Quantification of STARDUST particles

The broad overview map (Fig. 4.12, stepsize = 1 μm, RT = 0.5 s, scanned area: 180 $\times$ 20 μm^2) of impact track 110 yields a terminal particle and at least four sub-particles along the track which have been characterized and localized by their Ca, Ti, Fe, Ni and

Table 4.2: Interpolated Monte Carlo based yields of ATHO-G standard (counts*cm^2/s/g)

Element	Linetype	Elemental Yield	Standard deviation
K	K_α	18.142	1.661
Ca	K_α	27.278	2.284
Sc	K_α	37.781	2.988
Ti	K_α	48.595	3.483
V	K_α	58.543	3.609
Cr	K_α	66.643	3.508
Mn	K_α	72.312	3.579
Fe	K_α	75.431	4.025
Co	K_α	76.275	4.553
Ni	K_α	75.384	4.766
Cu	K_α	73.429	4.526
Zn	K_α	71.117	4.238
Ga	K_α	69.155	5.208
Ba	L_α	5.449	1.654
Ce	L_α	28.976	2.859

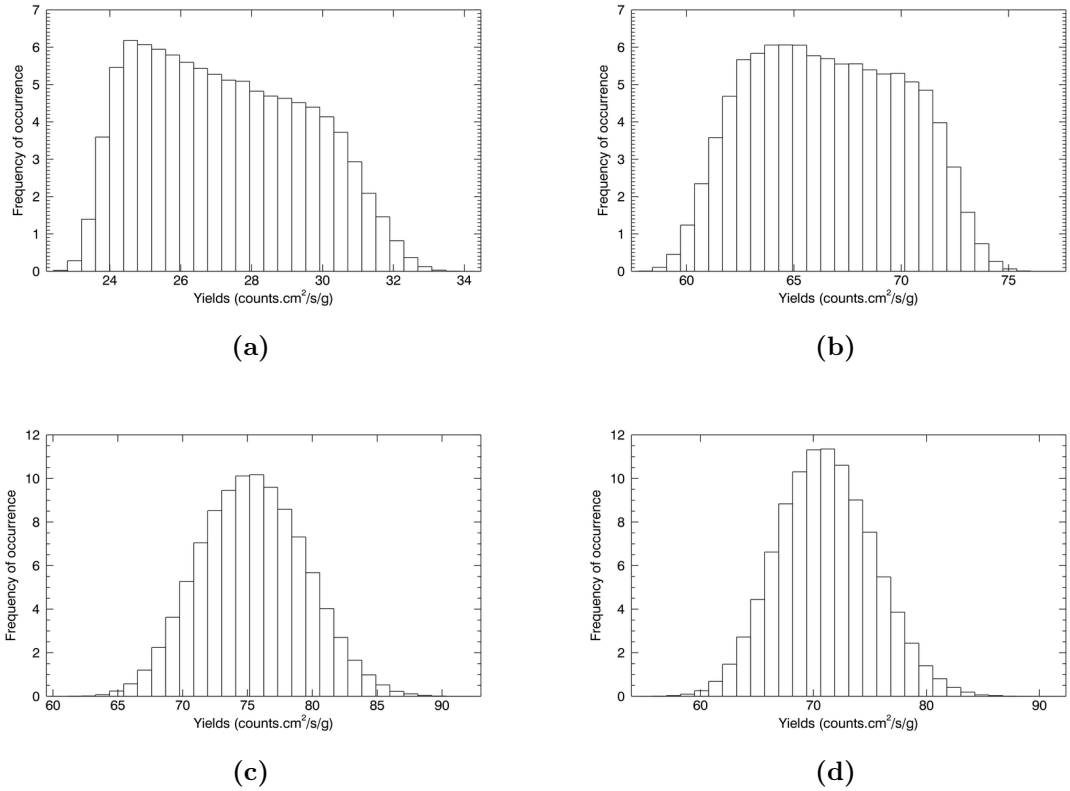

Figure 4.11: Monte Carlo based elemental yields distributions for Ca(a), Cr(b), Fe(c) and Zn(d)

Mn content. We identified two Fe, Ni-rich fragments and a single Ti-rich particle, but the most interesting observation are two Ca and Ti-rich grains (the TP and a particle along the track) at the end of the impact track, which also show some local enrichment in Fe and Ni.

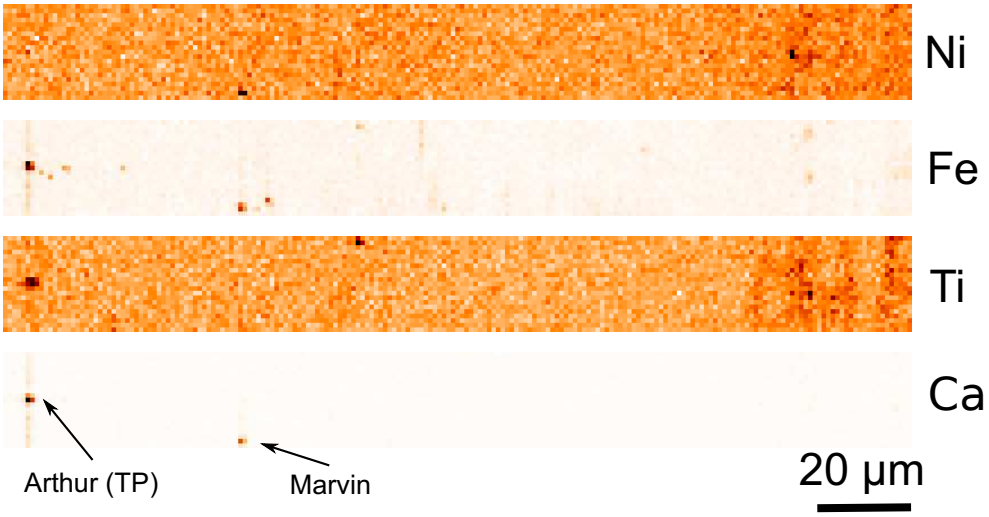

Figure 4.12: 2D conventional XRF maps of the entire impact track 110 [C2012, 0, 100, 0, 0] for the elements Ca, Ti, Fe and Ni (all Ka-lines). The terminal particle Arthur (far left) is characterized by elevated Ca, Ti, Fe and Ni concentrations. The grain Marvin can be recognized by elevated Ca, Ti and Fe signals. Along the track there are some more fragments enriched in Fe and Ni. One fragment shows only Ti signal. The entrance of the impact track is located at the far right.

The quantification model requires an accurate description of the dimensions, density and matrix composition of the layer that will be quantified. This is particularly important for very thin layers since the weight fractions are, under these conditions, inverse proportional to the product of the thickness and density. The dimensions of the particles were estimated using high resolution confocal elemental mappings, as shown in Fig. 4.13. These elemental mappings demonstrate that the particles are inhomogeneous, indicating that the quantification results to follow are merely representative for the measurement points (hot spots). We obtained a size of 2.0 μm for the terminal particle (TP,Arthur) and 1.5 μm for the particle fragment (Marvin[1]). We assumed during the error estimation that these sizes carried with them an uncertainty of 0.25 μm. Since the density could not be deduced

[1]Particle names from The Hitchhikers Guide to the Galaxy by Douglas Adams.

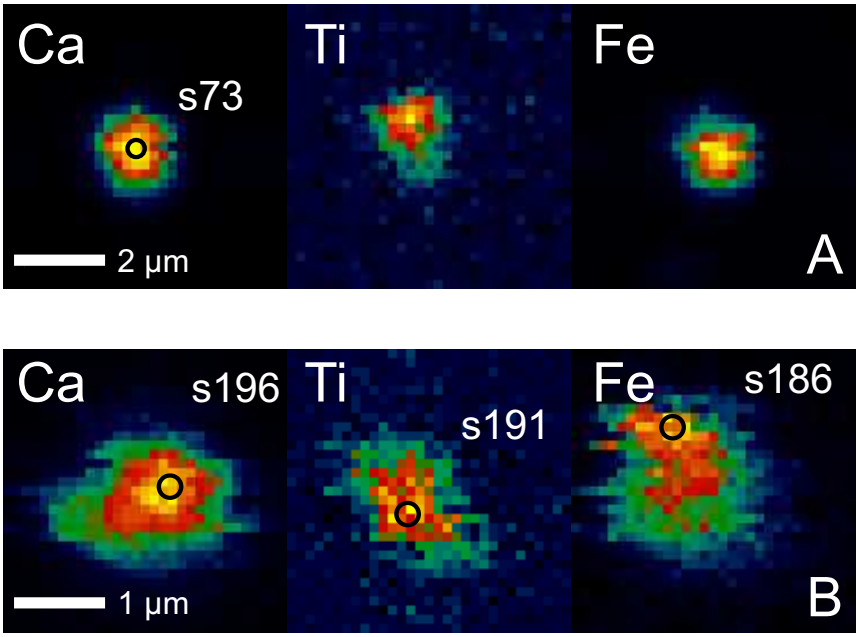

Figure 4.13: Confocal 2D XRF maps for the TP Arthur (A, 31 x 0.2 μm x 31 x 0.2 μm, 5 s real time) and for the grain Marvin (B, 31 x 0.1 μm x 31 x 0.1 μm, 5 s real time) for the elements Ca, Ti, Fe and Ni. The circles indicate the spot measurement positions (not to scale).

from the experimental data or obtained using another analytical technique, we assumed the density to correspond with that of silicates such as olivine: 3.5 ± 0.5 g/cm^3. Due to the fact that the quantification is solved in an iterative way, one has to define a starting matrix that will be used for the initial absorption correction, and which will be updated in further iterations as we calculate new weight fractions. For this purpose, quartz (SiO_2) was used. Considering the very small dimensions of the particles, it is obvious that the absorption correction has little or no influence on the results. The dimensions of the aerogel layer in which the particle is embedded ($100 \pm 20 \mu$m), were estimated using an optical image of the keystone. The quantification results of seven point measurements (300 s real time) are listed in Tables 4.3 and 4.4. The error estimation histograms of several elements are shown in Fig. 4.15, while the spectra of s73 (Arthur) and s191 (Marvin) are depicted in Fig. 4.14. The weight fractions of the matrix elements Si and O should be considered as to correspond not only to these two elements but also to those elements whose concentrations could not be determined, in particular elements such as Mg and Al, that were not detected with XRF but whose presence is likely based on other observations of similar particles. As can be seen from Fig. 4.14, the collected spectra include XRF lines of Se and S whose quantification results are not covered in Tables 4.3 and 4.4. In the case of the former element, this is due to the fact that it is a well-known contaminant of the aerogel (in addition to Pt and Au), meaning that the signal did not originate from the particle (layer of interest). S could not be quantified since there was no corresponding elemental yield available. It should be noted that the quantification of such low Z elements is particularly unreliable due to the strong absorption of the low energy XRF photons. Concerning the appearance of the histograms, the same remarks that were mentioned in the previous section apply here. For the geological interpretation and implications of these results, the reader is referred to Schmitz et al[4].

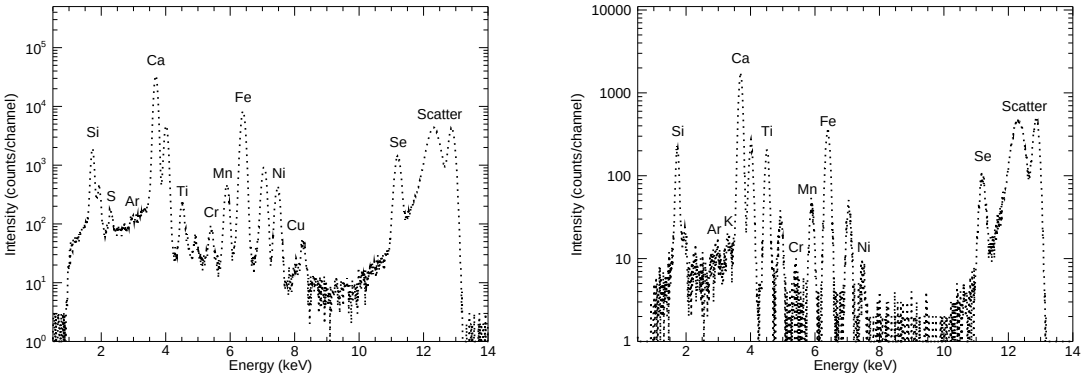

(a) s73 **(b)** s191

Figure 4.14: Spectra of confocal XRF point measurements on the TP Arthur (s73) and the grain Marvin (s191)

Table 4.3: Concentrations with standard deviations obtained for the terminal particle Arthur (data in wt.% except for asterisks representing data in ppm). Si and O are included due to the chosen starting matrix. nd = not detected

	Arthur concentrations			
	s66	s67	s68	s73
K	nd	nd	nd	nd
Ca	0.20 ± 0.03	0.35 ± 0.05	0.30 ± 0.04	42.0 ± 5.6
Ti	nd	nd	17* ± 8*	0.11 ± 0.02
Cr	nd	nd	14* ± 5*	275* ± 36*
Mn	nd	nd	nd	0.16 ± 0.02
Fe	62* ± 9*	171* ± 22*	109* ± 14*	3.0 ± 0.4
Ni	8* ± 3*	9* ± 4*	5* ± 3*	0.1 ± 0.02
Cu	18* ± 4*	11* ± 4*	11* ± 3*	30* ± 7*
Si	45.9 ± 0.01	45.8 ± 0.02	45.9 ± 0.02	25.1 ± 2.7
O	53.9 ± 0.02	53.8 ± 0.03	53.8 ± 0.02	29.5 ± 3.2

Table 4.4: Concentrations with standard deviations obtained for the grain Marvin (data in wt.% except for asterisks representing data in ppm). Si and O are included due to the chosen starting matrix. nd = not detected

	Marvin concentrations		
	s186	s191	s196
K	384* ± 129*	0.32 ± 0.06	nd
Ca	2.5 ± 0.4	19.8 ± 3.0	20.5 ± 3.1
Ti	465* ± 94*	1.1 ± 0.2	1.0 ± 0.2
Cr	34* ± 21*	61* ± 22*	nd
Mn	427* ± 75*	0.14 ± 0.02	0.12 ± 0.02
Fe	1.9 ± 0.3	1.1 ± 0.2	1.1 ± 0.2
Ni	384* ± 68*	138* ± 32*	57* ± 14*
Cu	nd	nd	nd
Si	43.9 ± 0.3	35.6 ± 1.5	35.5 ± 1.5
O	51.5 ± 0.3	41.8 ± 1.8	41.7 ± 1.8

4.5 Discussion and conclusions

A new method for the quantification of confocal micro/nano XRF data was derived based on the fundamental parameter method. It requires the measurement of a standard reference material and adapts the emission-transmission equation to take into account the specific properties of the polycapillary. We have demonstrated the usefulness of this method by applying it on confocal nano-XRF data that was collected from cometary dust particles at the ID13 beamline of the ESRF. Since the quantification model requires a reliable estimate of the position of the confocal volume within the layer of interest, we have developed a technique to obtain this parameter by examining the ratio of the K_α and K_β fluorescence of an element, taking advantage of the fact that the K_α radiation is prone to more absorption than the K_β radiation. For the error estimation of the quantification results, we have used a brute-force Monte Carlo based approach that involves the variation of the input parameters according to their errors and standard deviations using a random number generator.

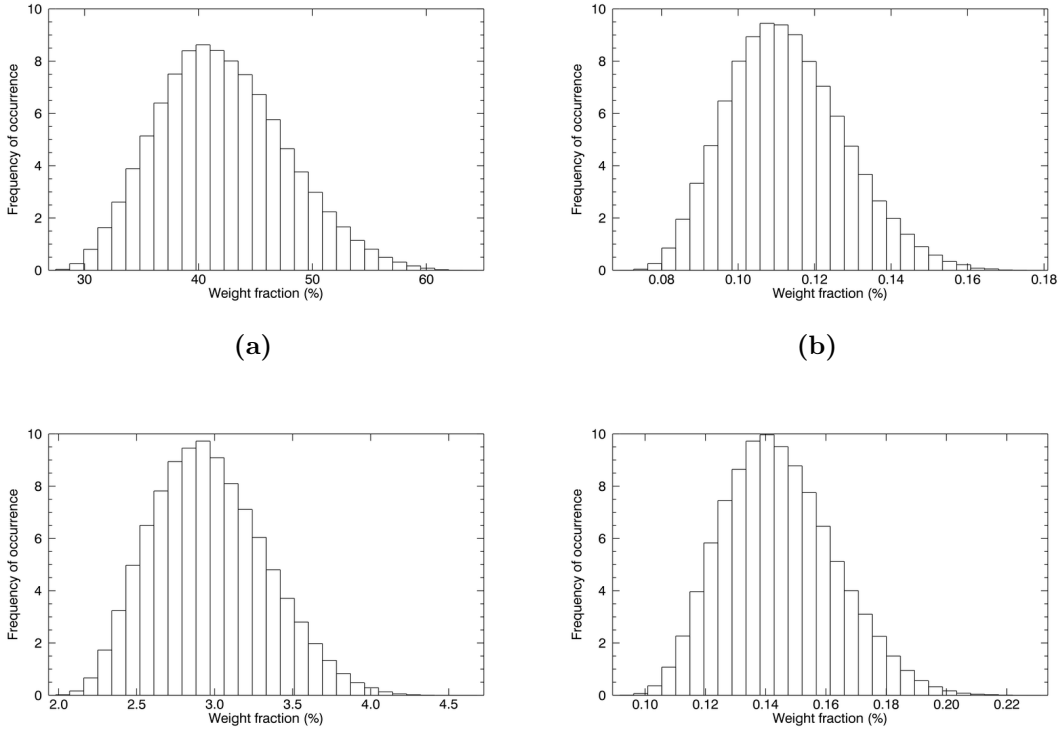

Figure 4.15: Monte Carlo based elemental yields distributions for Ca(a), Ti(b), Fe(c) and Ni(d) for s73 of the Arthur terminal particle. All numbers are in wt%.

Bibliography

[1] F. Brenker, L. Vincze, B. Vekemans, L. Nasdala, T. Stachel, C. Vollmer, M. Kersten, A. Somogyi, F. Adams, W. Joswig, J. Harris, Detection of a Ca-rich lithology in the Earth's deep (> 300 km) convecting mantle, Earth Planet. Sci. Lett. 236 (2005) 579–587.

[2] B. De Samber, G. Silversmit, K. De Schamphelaere, R. Evens, T. Schoonjans, B. Vekemans, C. Janssen, B. Masschaele, L. Van Hoorebeke, I. Szaloki, F. Vanhaecke, K. Rickers, G. Falkenberg, L. Vincze, Element-to-tissue correlation in biological samples determined by three-dimensional X-ray imaging methods, J. Anal. At. Spectrom. 25 (2010) 544–553.

[3] V. G. Mihucz, G. Silversmit, I. Szaloki, B. De Samber, T. Schoonjans, E. Tatar,

L. Vincze, I. Virag, J. Yao, G. Zaray, Removal of some elements from washed and cooked rice studied by inductively coupled plasma mass spectrometry and synchrotron based confocal micro-X-ray fluorescence, Food Chem. 121 (2010) 290–297.

[4] S. Schmitz, F. E. Brenker, T. Schoonjans, B. Vekemans, G. Silversmit, L. Vincze, M. Burghammer, C. Riekel, In situ identification of a CAI candidate in 81P/Wild 2 cometary dust by confocal high resolution synchrotron X-ray fluorescence, Geochim. Cosmochim. Acta 73 (2009) 5483–5492.

[5] Z. Smit, K. Janssens, K. Proost, I. Langus, Confocal mu-XRF depth analysis of paint layers, Nucl. Instrum. Methods Phys. Res., Sect. B 219 (2004) 35–40.

[6] L. Vincze, B. Vekemans, F. Brenker, G. Falkenberg, K. Rickers, A. Somogyi, M. Kersten, F. Adams, Three-Dimensional Trace Element Analysis by Confocal X-ray Microfluorescence Imaging, Anal. Chem. 76 (2004) 6786–6791.

[7] B. Kanngiesser, I. Mantouvalou, W. Malzer, T. Wolff, O. Hahn, Non-destructive, depth resolved investigation of corrosion layers of historical glass objects by 3D Micro X-ray fluorescence analysis, J. Anal. At. Spectrom. 23 (2008) 814–819.

[8] G. Silversmit, B. Vekemans, F. E. Brenker, S. Schmitz, M. Burghammer, C. Riekel, L. Vincze, X-ray Fluorescence Nanotomography on Cometary Matter from Comet 81P/Wild2 Returned by Stardust, Anal. Chem. 81 (2009) 6107–6112.

[9] L. Vincze, K. Janssens, B. Vekemans, F. Adams, Monte Carlo simulation of X-ray fluorescence spectra: Part 4. Photon scattering at high X-ray energies, Spectrochim. Acta Part B 54 (1999) 1711–1722.

[10] U. Bottigli, A. Brunetti, B. Golosio, P. Oliva, S. Stumbo, L. Vincze, P. Randaccio, P. Bleuet, A. Simionovici, A. Somogyi, Voxel-based Monte Carlo simulation of X-ray imaging and spectroscopy experiments, Spectrochim. Acta Part B 59 (2004) 1747–1754.

[11] F. Brenker, C. Vollmer, L. Vincze, B. Vekemans, A. Szymanski, K. Janssens, I. Szaloki, L. Nasdala, W. Joswig, F. Kaminsky, Carbonates from the lower part of transition zone or even the lower mantle, Earth Planet. Sci. Lett. 260 (2007) 1–9.

[12] I. Szaloki, D. G. Lewis, C. A. Bennett, A. Kilic, Application of the fundamental parameter method to the in vivo x-ray fluorescence analysis of Pt, Phys. Med. Biol. 44 (1999) 1245–1255.

[13] W. Malzer, B. Kanngiesser, A model for the confocal volume of 3D micro X-ray fluorescence spectrometer, Spectrochim. Acta Part B 60 (2005) 1334–1341.

[14] D. Sokaras, A.-G. Karydas, Secondary fluorescence enhancement in confocal x-ray microscopy analysis, Anal. Chem. 81 (2009) 4946–4954.

[15] D. S. Burnett, NASA Returns Rocks from a Comet, Science 314 (2006) 1709–1710.

[16] D. Brownlee, P. Tsou, J. Aleon, C. Alexander, T. Araki, S. Bajt, G. Baratta, R. Bastien, P. Bland, P. Bleuet, J. Borg, J. Bradley, A. Brearley, F. Brenker, S. Brennan, J. Bridges, N. Browning, J. Brucato, E. Bullock, M. Burchell, H. Busemann, A. Butterworth, M. Chaussidon, A. Cheuvront, M. Chi, M. Cintala, B. Clark, S. Clemett, G. Cody, L. Colangeli, G. Cooper, P. Cordier, C. Daghlian, Z. Dai, L. D'Hendecourt, Z. Djouadi, G. Dominguez, T. Duxbury, J. Dworkin, D. Ebel, T. Economou, S. Fakra, S. Fairey, S. Fallon, G. Ferrini, T. Ferroir, H. Fleckenstein, C. Floss, G. Flynn, I. Franchi, M. Fries, Z. Gainsforth, J. Gallien, M. Genge, M. Gilles, P. Gillet, J. Gilmour, D. Glavin, M. Gounelle, M. Grady, G. Graham, P. Grant, S. Green, F. Grossemy, L. Grossman, J. Grossman, Y. Guan, K. Hagiya, R. Harvey, P. Heck, G. Herzog, P. Hoppe, F. Horz, J. Huth, I. Hutcheon, K. Ignatyev, H. Ishii, M. Ito, D. Jacob, C. Jacobsen, S. Jacobsen, S. Jones, D. Joswiak, A. Jurewicz, A. Kearsley, L. Keller, H. Khodja, A. Kilcoyne, J. Kissel, A. Krot, F. Langenhorst, A. Lanzirotti, L. Le, L. Leshin, J. Leitner, L. Lemelle, H. Leroux, M. Liu, K. Luening, I. Lyon, G. MacPherson, M. Marcus, K. Marhas, B. Marty, G. Matrajt, K. McKeegan, A. Meibom, V. Mennella, K. Messenger, S. Messenger, T. Mikouchi, S. Mostefaoui, T. Nakamura, T. Nakano, M. Newville, L. Nittler, I. Ohnishi, K. Ohsumi, K. Okudaira, D. Papanastassiou, R. Palma, M. Palumbo, R. Pepin, D. Perkins, M. Perronnet, P. Pianetta, W. Rao, F. Rietmeijer, F. Robert, D. Rost, A. Rotundi, R. Ryan, S. Sandford, C. Schwandt, T. See, D. Schlutter, J. Sheffield-Parker, A. Simionovici, S. Simon, I. Sitnitsky, C. Snead, M. Spencer, F. Stadermann, A. Steele, T. Stephan, R. Stroud, J. Susini, S. Sutton, Y. Suzuki, M. Taheri, S. Taylor, N. Teslich, K. Tomeoka, N. Tomioka, A. Toppani, J. Trigo-Rodriguez, D. Troadec, A. Tsuchiyama, A. Tuz-

zolino, T. Tyliszczak, K. Uesugi, M. Velbel, J. Vellenga, E. Vicenzi, L. Vincze, J. Warren, I. Weber, M. Weisberg, A. Westphal, S. Wirick, D. Wooden, B. Wopenka, P. Wozniakiewicz, I. Wright, H. Yabuta, H. Yano, E. Young, R. Zare, T. Zega, K. Ziegler, L. Zimmerman, E. Zinner, M. Zolensky, Comet 81P/Wild2 Under a Microscope, Science 314 (2006) 1711–1716.

[17] G. Flynn, P. Bleuet, J. Borg, J. Bradley, F. Brenker, S. Brennan, J. Bridges, D. Brownlee, E. Bullock, M. Burghammer, B. Clark, Z. Dai, C. Daghlian, Z. Djouadi, S. Fakra, T. Ferroir, C. Floss, I. Franchi, Z. Gainsforth, J. Gallien, P. Gillet, P. Grant, G. Graham, S. Green, F. Grossemy, P. Heck, G. Herzog, P. Hoppe, F. Horz, J. Huth, K. Ignatyev, H. Ishii, K. Janssens, D. Joswiak, A. Kearsley, H. Khodja, A. Lanzirotti, J. Leitner, L. Lemelle, H. Leroux, K. Luening, G. MacPherson, K. Marhas, M. Marcus, G. Matrajt, T. Nakamura, K. Nakamura-Messenger, T. Nakano, M. Newville, D. Papanastassiou, P. Pianetta, W. Rao, C. Riekel, F. Rietmeijer, D. Rost, C. Schwandt, T. See, J. Sheffield-Parker, A. Simionovici, I. Sitnitsky, C. Snead, F. Stadermann, T. Stephan, R. Stroud, J. Susini, Y. Suzuki, S. Sutton, S. Taylor, N. Teslich, D. Troadec, P. Tsou, A. Tsuchiyama, K. Uesugi, B. Vekemans, E. Vicenzi, L. Vincze, A. Westphal, P. Wozniakiewicz, E. Zinner, M. Zolensky, Elemental Compositions of Comet 81P/Wild 2 Samples Collected by Stardust, Science 314 (2006) 1731–1735.

[18] F. Hoerz, R. Bastien, J. Borg, J. P. Bradley, J. C. Bridges, D. E. Brownlee, M. J. Burchell, M. Chi, M. J. Cintala, Z. R. Dai, Z. Djouadi, G. Dominguez, T. E. Economou, S. A. J. Fairey, C. Floss, I. A. Franchi, G. A. Graham, S. F. Green, P. Heck, P. Hoppe, J. Huth, H. Ishii, A. T. Kearsley, J. Kissel, J. Leitner, H. Leroux, K. Marhas, K. Messenger, C. S. Schwandt, T. H. See, C. Snead, F. J. Stadermann, T. Stephan, R. Stroud, N. Teslich, J. M. Trigo-Rodriguez, A. J. Tuzzolino, D. Troadec, P. Tsou, J. Warren, A. Westphal, P. Wozniakiewicz, I. Wright, E. Zinner, Impact features on Stardust: Implications for comet 81P/Wild 2 dust, Science 314 (2006) 1716–1719.

[19] P. Tsou, D. Brownlee, S. Sandford, F. Horz, M. Zolensky, Wild 2 and interstellar sample collection and earth return, J. Geophys. Res. 108 (2003).

[20] A. Westphal, C. Snead, A. Butterworth, G. Graham, J. Bradley, S. Bajt, P. Grant, G. Bench, S. Brennan, P. Pianetta, Aerogel keystones: Extraction of complete hy-

pervelocity impact events from aerogel collectors, Meteoritics & Planetary Science 39 (2004) 1375–1386.

[21] A. Markowicz, R. Van Grieken, Quantification in XRF Analysis of Intermediate-Thickness Samples, in: R. Van Grieken, A. Markowicz (Eds.), Handbook of X-ray Spectrometry, CRC Press, 2nd edition, 2001.

[22] P. Van Dyck, S. Török, R. Van Grieken, Enhancement effect in X-ray fluorescence analysis of environmental samples of medium thickness, Anal. Chem. 58 (1986) 1761–1766.

[23] M. Mantler, Quantitative Analysis, in: B. Beckhoff, B. Kanngiesser, N. Langhoff, R. Wedell, H. Wolff (Eds.), Handbook of Practical X-Ray Fluorescence Analysis, Springer, 2006.

[24] A. Brunetti, M. Sanchez del Rio, B. Golosio, A. Simionovici, A. Somogyi, A library for X-ray-matter interaction cross sections for X-ray fluorescence applications, Spectrochim. Acta Part B 59 (2004) 1725–1731.

[25] K. Jochum, D. Dingwell, A. Rocholl, B. Stoll, A. Hofmann, S. Becker, A. Besmehn, D. Bessette, H. Dietze, P. Dulski, J. Erzinger, E. Hellebrand, P. Hoppe, I. Horn, K. Janssens, G. Jenner, M. Klein, W. McDonough, M. Maetz, K. Mezger, C. Munker, I. Nikogosian, C. Pickhardt, I. Raczek, D. Rhede, H. Seufert, S. Simakin, A. Sobolev, B. Spettel, S. Straub, L. Vincze, A. Wallianos, G. Weckwerth, S. Weyer, D. Wolf, M. Zimmer, The preparation and preliminary characterisation of eight geological MPI-DING reference glasses for in-site microanalysis, Geostandard Newslett. 24 (2000) 87–133.

[26] B. Vekemans, L. Vincze, F. Brenker, F. Adams, Processing of three-dimensional microscopic x-ray fluorescence data, J. Anal. At. Spectrom. 19 (2004) 1302–1308.

[27] T. Wolff, I. Mantouvalou, W. Malzer, J. Nissen, D. Berger, I. Zizak, D. Sokaras, A. Karydas, N. Grlj, P. Pelicon, R. Schuetz, M. Zitnik, B. Kanngiesser, Performance of a polycapillary halflens as focussing and collecting optic-a comparison, J. Anal. At. Spectrom. 24 (2009) 669–675.

[28] T. Schoonjans, A. Brunetti, B. Golosio, M. Sanchez del Rio, V. A. Solé, C. Ferrero, L. Vincze, The xraylib library for X-ray—matter interactions. Recent developments, Spectrochim. Acta Part B (2011). In press, doi:10.1016/j.sab.2011.09.011.

[29] I. Mantouvalou, W. Malzer, I. Schaumann, L. Lühl, R. Dargel, C. Vogt, B. Kanngiesser, Reconstruction of thickness and composition of stratified materials by means of 3D micro X-ray fluorescence spectroscopy, Anal. Chem. 80 (2008) 819–826.

[30] B. Vekemans, K. Janssens, L. Vincze, F. Adams, P. Van Espen, Analysis of X-Ray-Spectra by Iterative Least-Squares (AXIL) - New Developments, X-Ray Spectrom. 23 (1994) 278–285.

[31] M. Matsumoto, T. Nishimura, Mersenne twister: a 623-dimensionally equidistributed uniform pseudorandom number generator, ACM Trans. Modelling Comput. Simulation 8 (1998) 3–30.

[32] M. Galassi, J. Davies, J. Theiler, B. Gough, G. Jungman, P. Alken, M. Booth, F. Rossi, GNU Scientific Library Reference Manual, Network Theory Ltd., third edition, 2009.

Chapter 5

A general Monte Carlo simulation of energy-dispersive X-ray fluorescence spectrometers – forward methodology

5.1 Introduction

Energy dispersive X-ray fluorescence (ED-XRF) has been widely used for non-destructive elemental analysis for several decades. The applications are numerous and can be found throughout biological, geological and archaeometric research, attributable to the qualitative and quantitative material information it yields on bulk, micrometer and, since recently, nanometer level. It is therefore not surprising that the prediction of the complete spectral response of ED-XRF spectrometers, carried out by means of Monte Carlo simulations of photon–matter interactions, has been given considerable attention. The main advantage of the use of Monte Carlo simulations revolves around their ability to take into account all physical phenomena that occur during the lifetime of a photon. The only requirement is the availability of the necessary probability density functions that govern the occurrence of the phenomena. Possible applications of Monte Carlo codes include the optimization of the design of future ED-XRF setups, the prediction of elemental yields and the quantitative analysis of XRF datasets. Traditionally, ED-XRF quantification is performed by

means of empirical calibration which requiring the preparation and measurement of a series of samples which have to be very similar to the unknown samples, or by means of the fundamental parameter (FP) method which establishes a relation between the elemental net-line intensities and their concentrations in the sample. The exact relations are usually not straightforward, depending on the variant of ED-XRF that was used, and often do not take into account higher order interactions such as enhancement (by fluorescent or scattered photons) which may lead to considerable errors. Since Monte Carlo simulations typically take into account these higher order interactions, they may serve as a superior quantification tool when used as an inverse method in which a certain composition is simulated and adapted iteratively until the simulated spectrum converges towards an experimental curve.

Several authors have already published codes that perform Monte Carlo simulations of photon–matter interactions, usually tailored to a specific application such as 3D(confocal)-μXRF or XRF-tomography[1–4]. In this chapter we present our latest advances in the development of a general purpose Monte Carlo simulation code for ED-XRF spectrometers, based on the previous work of Vincze et al[5–8]. The samples that can be treated with our code are assumed to be composed of a stack of parallel homogeneous layers. All geometries and excitation types are supported, allowing for the simulation of X-ray tube and synchrotron radiation sources, as well as radio-isotope excited systems. Several computational optimizations were introduced in order to increase the efficiency of the code, most notably through variance reduction and multithreading. The code was validated by comparison with experimental data acquired at a synchrotron facility. Through this comparison, the importance of the features that were added to the code such as the simulation of M-lines, cascade effects and pile-up, is demonstrated.

5.2 Comparison with similar Monte Carlo codes

Although many of the features such as the simulation of cascade effects (atomic relaxation) and M-line emission are not unique to our code as they are covered to some extent by some popular MC simulation packages, most of these so-called general purpose tools simulate a wide range of particle types in a broad energy range, and are therefore not as optimized as the dedicated simulation code for ED-XRF spectrometers operating through the simulation of photons in a relatively narrow energy range (1-100 keV) presented in this chapter. Such

packages most often allow for the use of (for our purpose unnecessarily) complex sample and detector geometries, rendering the incorporation of efficient variance reduction techniques impossible, thereby decreasing the computational efficiency dramatically. Their usability, therefore, is marginal for the point of view of quantitative elemental analysis. In the following section the most important Monte Carlo models will be discussed, with a focus on their capabilities concerning the simulation of X-ray fluorescence phenomena.

5.2.1 Geant4

Originating at the Conseil Européen pour la Recherche Nucléaire (CERN), Geant4 is an object-oriented toolkit for the simulation of particle–matter interactions[9], covering electromagnetic, hadronic and optical processes for a large set of long-lived particles, materials and elements. Initially developed for the simulation of high-energy particles as they pass through matter, by the introduction of so-called low energy extension packages it has become usable for the simulation of photoelectric effect, Compton and Rayleigh scattering. The work of Guatelli et al.[10] has led to the incorporation of atomic relaxation into the code, allowing for the simulation of cascade effects. A validation against NIST experimental data was published by the same authors[11]. Since Geant4 comes as a general purpose toolbox, the users are expected to generate their own code (in C++), through the exported interfaces. This requires the user to write program in order to model a specific problem.

5.2.2 MCNP

MCNP and its extension MCNPX are general-purpose Monte Carlo N-Particle codes allowing for the simulation of neutrons, photons and electrons using a general three-dimensional geometry with time-dependent, continuous energy distributions[12]. Development of the code is performed at the Los Alamos National Laboratory (LANL, Los Alamos, NM, USA). Applications include finding numerical solutions to problems associated with nuclear shielding, criticality safety, nuclear safeguards, detector design and analysis, nuclear well logging, health physics, medical physics, aerospace, and more[12]. Written in Fortran 77 and C, the software package is highly portable and can be compiled with support for multithreading (OpenMP, see Section 2.4.2) and distributed memory multiprocessing (MPI).

The usage of the MCNP code for ED-XRF applications has been demonstrated by Trojek et

al.[13], who have compared simulated XRF output with the results of analytical calculations and experiments. Their examination however did not include a verification of the atomic relaxation processes, which are also supported by the code.

5.2.3 PENELOPE

The PENELOPE package, developed at the University of Barcelona, targeted initially the Monte Carlo simulation of relativistic electron and positron transport in matter[14]. It is widely used for medical applications, with a focus on dosimetry and radiotherapy. Updates to the code resulted in a general-purpose Monte Carlo code system for the simulation of coupled electron and photon transport[15]. Support for the simulation of M-lines and atomic relaxation processes was added in 2005[16].

5.3 Experimental

The algorithms that will be discussed in the next sections were verified by comparing the simulated spectral response of a number of standard reference materials (SRM) purchased from the National Institute of Standards and Technology (NIST), with experimental data recorded at the beamline L of the HASYLAB synchrotron facility (Hamburg, Germany). The SRMs were chosen specifically to demonstrate the innovative characteristics of the code with a focus on the cascade effects. The samples were irradiated using an unfocused beam of which the dimensions were reduced by means of slits. The monochromaticy of the beam was achieved through a multilayer monochromator with a 1% energy bandwidth. Considering the rather large bandwidth, the Monte Carlo simulations were performed assuming that the excitation spectrum consists of a number of intervals (26) whose weights and energies are calculated from a Gaussian distribution centered around the mean excitation energy. This approach is necessary to ensure that the scatter peaks are simulated properly: their widths in the experimental data are not merely determined by the detector response function, but rather by the monochromator energy bandwidth. Since the beam intensity itself was not accurately known, it was estimated through the Monte Carlo simulation by comparing the intensity of the strongest fluorescence line from the experimental data and the simulated spectrum. The degree of polarization was calculated using the procedure of Vincze et al.[6]. Essentially one simulates the spectrum two times: once assuming a 100% horizontally

polarized X-ray beam, and once assuming a 100% vertically polarized beam. Out of these simulations, one obtains the scatter peak intensities $S_{\parallel}$ and $S_{\perp}$ which, combined with the experimental scatter intensity, yield the degree of polarization P:

$$P = \frac{2S_P - S_{\parallel} - S_{\perp}}{S_{\parallel} - S_{\perp}} \tag{5.1}$$

Obviously, this procedure is only relevant when the spectra exhibit a clearly defined scatter peak. The fluorescence radiation was collected with a Vortex silicon drift detector (Si crystal thickness = 350 μm, 50 mm^2 active detector area), equipped with a conical collimator (1 cm height, 2 mm opening diameter), positioned at 2.1 cm from the sample surface. In order not to overload the detector, the beam intensity was reduced by positioning a 1 mm Al absorber in the beam path.

5.4 Technical details

The simulation software is written using a combination of the C and Fortran 2003 programming languages. The former was mainly used to facilitate the input/output operations, while the latter's strength was exploited in the sections of the code focusing on the numerical computations. Advantage was taken of modern programming techniques such as OpenMP and POSIX threads to ensure that the executables would run using as many cores as the host can provide. Furthermore, MPI commands were added to enable clustered computing, effectively distributing the task over a number of networked computers, thereby paving the way for deployment on supercomputers. Extensive use was made of the GNU Scientific Library[17] through the Fortran 2003 bindings[18]. Of particular interest is the random number generation application programming interface (API), which includes the Mersenne twister algorithm[19] that was subsequently used in our software. Due to multithreaded nature of the Monte Carlo code, care was taken to ensure that each thread has its own high quality random seed, thereby producing independent streams of random numbers. This was accomplished on the Mac OS X and Linux platforms by gathering 64-bit unsigned integers from the random device `/dev/random`, produced by collecting environmental noise from device drivers, network traffic and other sources. Since the random device is sometimes quite slow producing these seeds, especially on systems with little user input, a UNIX daemon was written that periodically (typically every second) will try to

collect a seed and, upon success, store it internally in a pool. Upon request by the Monte Carlo executable, the daemon will transfer the required number of seeds to the executable using interprocess communication. Since the Windows platform does not come with a similar random device, the seeds are on this platform produced using an algorithm based on the process identification number, user identification number and the current time.
The physical data that is required for the simulation includes cross sections, fluorescence yields, radiative and non-radiative rates, absorption edge energies, fluorescence line energies etc., and is obtained from the *xraylib* library discussed in Chapter 3 . Part of the required data is precalculated in form of inverse cumulative distribution functions, which are stored in a hierarchical data format container (HDF5), and can be modified by the user[20]. Additional HDF5 files are used to store the (collimated) solid angles necessary for the variance reduction calculations, as well as for the escape peak ratios that are required for convoluting the spectrum with the detector response function. The input and output files are encoded in the extensible markup language (XML) and are handled through the *libxml2* library. The input files are created through a graphical user interface (GUI) written using the GIMP Toolkit (GTK+). Optionally, the output files can be converted into other formats such as ASCII (SPE format) and CSV as well as into an HTML file containing a detailed overview of the results. The different experimental conditions, X-ray source properties and sample conditions that can be manipulated using the GUI are summarized in Table 5.1.

5.5 Outline of the basic Monte Carlo formalism

A Monte Carlo code, simulates the fate of individual photons, i.e. photon-matter interactions, from the moment where they impinge on the sample with a given direction and energy to the point where they are either absorbed by a sample atom or emerge from the sample and are possibly detected, instead of attempting to model the underlying macroscopic phenomena such as as absorption, scattering, fluorescence, non-radiative transitions and higher order effects. The photon trajectories are modelled as consisting of a number of straight steps, as is illustrated in Fig. 5.1.
The length of the steps S_i is chosen from an exponential distribution that is determined by

Table 5.1: Input parameters of the Monte Carlo simulation software

General	Number of photons per discrete line	
	Number of photons per energy interval	
	Maximum number of sample interactions	n_{max}
Sample composition	Number of layers	n_l
	Composition (weight %), (n_i elements in layer i)	$w_{i,j}, i = 1 \dots n_l, j = 1 \dots n_i$
	Density	ρ_i
	Thickness	T_i
Geometry	X-ray source–sample distance	d_s
	Sample normal vector	$\boldsymbol{n_s}$
	Detector window position	$\boldsymbol{p_d}$
	Detector window normal vector	$\boldsymbol{n_d}$
	Active detector area	A_d
	Collimator height	C_h
	Collimator diameter	C_d
	Slits dimensions	s_x and s_y
X-ray source	Excitation continuum (n_c intervals)	E_j, I_j, p_j
	Excitation lines (n_l lines)	E_j, I_j, p_j
Absorbers	Excitation path	
	Detector path	
Detector	Type	Si(Li), Ge, SDD
	Measurement live time	t_m
	Gain	ΔE
	Zero	E_0
	Fano factor	F
	Electronic noise	ϵ_d
	Pulse width	τ
	Detector crystal composition	

the attenuation factors of the different elements composing the layers that the photon may encounter, and by the photon energy. The initial step $i = 0$ starts when the photon enters the sample along the original direction of the photon. In the laboratory coordinate system, the direction of propagation is described by two angles Θ_i (inclination) and Φ_i (azimuth). At the end of each step $\boldsymbol{r_i} = (x_i, y_i, z_i)$, an interaction with a particular type of sample atom with atomic number Z occurs. Three types of interactions are considered in the energy interval 1-100 keV: photoelectric effect (possibly) followed by X-ray fluorescence emission, elastic (Rayleigh) and inelastic (Compton) scattering. The likelihood of occurrence of these

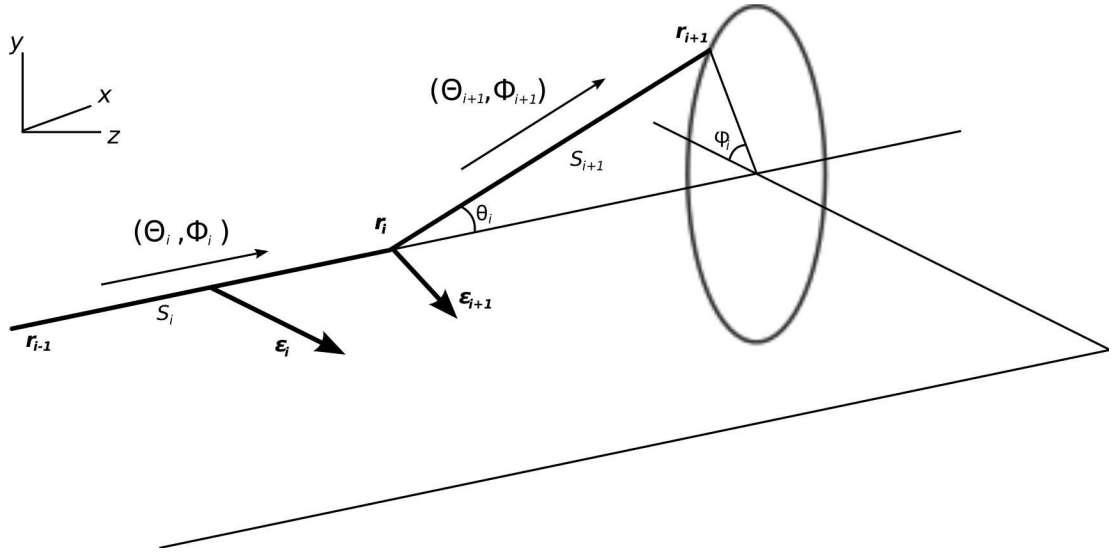

Figure 5.1: The basic step of a Monte Carlo simulation of photon–matter interactions: S_i is the distance between two subsequent interactions. As a result of the interaction at $\boldsymbol{r_i}$, photon direction, energy and electric field vector (Θ_i, Φ_i, E_i, $\boldsymbol{\epsilon_i}$) are changed.

these three interaction types, is determined by the ratio of their respective cross sections to the absorption coefficient: $\frac{\tau_Z}{\mu_Z}$, $\frac{\sigma_{R,Z}}{\mu_Z}$ and $\frac{\sigma_{C,Z}}{\mu_Z}$. The type of interaction will determine the change in direction, which is described by the polar (scattering) angle θ_i and azimuthal angle ϕ_i in the coordinate system attached to the photon, as shown in Fig. 5.1. If the photon is not absorbed, then the orientation $(\Theta_{i+1}, \Phi_{i+1})$ of the next segment of the photon trajectory (from $\boldsymbol{r_i}$ to $\boldsymbol{r_{i+1}}$) is calculated using the coordinate transformation:

$$\begin{bmatrix} \sin\Theta_{i+1}\cos\Phi_{i+1} \\ \sin\Theta_{i+1}\sin\Phi_{i+1} \\ \cos\Theta_{i+1} \end{bmatrix} = \begin{bmatrix} \cos\Theta_i\cos\Phi_i & -\sin\Phi_i & \sin\Theta_i\cos\Phi_i \\ \cos\Theta_i\sin\Phi_i & \cos\Phi_i & \sin\Theta_i\sin\Phi_i \\ -\sin\Theta_i & 0 & \cos\Theta_i \end{bmatrix} \begin{bmatrix} \sin\theta_i\cos\phi_i \\ \sin\theta_i\sin\phi_i \\ \cos\theta_i \end{bmatrix} \tag{5.2}$$

The new coordinates of the photon become at the next interaction point:

$$\begin{aligned} x_{i+1} &= x_i + S_{i+1}\sin\Theta_{i+1}\cos\Phi_{i+1} \\ y_{i+1} &= y_i + S_{i+1}\sin\Theta_{i+1}\sin\Phi_{i+1} \\ z_{i+1} &= z_i + S_{i+1}\cos\Theta_{i+1} \end{aligned} \tag{5.3}$$

The type of atom an interaction occurs with, the distance between two consecutive interactions and the type of interaction are randomly chosen using uniform random numbers

that select values from the relevant inverse cumulative distribution functions. When the photon is not absorbed at $\boldsymbol{r_{i+1}}$, and this location is still inside the simulated volume, the next step of the trajectory is calculated. In case the photon leaves the simulated volume, a subroutine will verify whether the current direction of the photon will make it intersect with the detector, without hitting the collimator (if present). If this condition is met, the final photon energy will be stored by the program. This is done by incrementing the content of the appropriate channel in a virtual multichannel analyzer (MCA) memory. After the simulation, the energy distribution of the photons is multiplied with terms that take into account the effect of the excitation and detection path absorbers (i.e. detector window and dead-layer), as well as the transmission of the detector crystal. In order to allow the comparison with actual experimental data, the distribution needs to be convoluted with the detector response function that takes into account peak broadening, fluorescence and Compton escape peaks, and pulse pile-up. A detailed description of the modeling of the different interactions that determine the fate of the photons along their trajectories is given in this section.

5.5.1 Selection of step length

The algorithm determining the step length of a photon trajectory is ultimately derived from the Bouguer-Lambert-Beer equation that establishes the rate of attenuation of an X-ray beam according to the properties of the matter it crosses through:

$$\frac{I}{I_0} = \exp\left(-\rho\mu S_{max}\right) \tag{5.4}$$

where $\frac{I}{I_0}$ is the ratio of the intensities of the outgoing (I) and incoming (I_0) radiation, μ the absorption coefficient, ρ the density of the material and S_{max} the linear extent of the material along the photon direction $\boldsymbol{k}_0$. The absorption coefficient and density are assumed to be constant everywhere in the layer of matter. The probability $F(S)$ of an interaction occurring within a distance $(0, S)$ along the direction $\boldsymbol{k}_0$ of a photon propagating in this layer is given by:

$$F(S) = 1 - \exp\left(-\rho\mu S\right) \tag{5.5}$$

The inverse cumulative distribution function $F^{-1}(R)$ converts the uniform distribution of a random number $0 \leq R < 1$ into the desired distribution for the distance S between two

subsequent interactions of a photon travelling along the direction $\boldsymbol{k}_0$. If R is greater than $1 - \exp(-\rho\mu S_{max})$, then the photon will not experience an interaction in the layer and is assumed to leave the sample. However, if not, the step length S of the photon can be calculated as:

$$S = -\frac{\ln(1-R)}{\mu\rho} \equiv -\frac{\ln(R)}{\mu\rho} \tag{5.6}$$

The situation becomes more complicated when the simulated system is composed of several layers, such as a stratified material or any sample that is being irradiated while being placed under an atmosphere (e.g. air, inert gas). In this case, the selection of the distance S between two subsequent events corresponding to a given random number R is done in a two-step procedure: first, the largest index m, counted starting from the current layer, is found for which the following inequality still holds:

$$R \leq \prod_{i=1}^{m-1} \exp\left(-\mu_i \rho_i S_{max}^i\right) \left(1 - \exp\left(-\mu_m \rho_m S_{max}^m\right)\right) \tag{5.7}$$

secondly, the actual step length S is then calculated as:

$$S = -\frac{\ln\left(\dfrac{1-R}{\prod_{i=1}^{m-1} \exp\left(-\mu_i \rho_i S_{max}^i\right)}\right)}{\mu_m \rho_m} + \sum_{i=1}^{m-1} S_{max}^i \tag{5.8}$$

The calculated distances depend on the current position of a photon as well as on its direction and energy, implying that the step length cannot be precalculated, but needs instead to be determined online for each simulated photon and after each interaction of a trajectory, making this step computationally rather expensive.

5.5.2 Selection of atom type

Assuming the photon did not leave the system after the calculation of its step length, the next stage is to determine with which kind of atom the photon interacted in its last collision. This needs to occur before the selection of the interaction type, since the photoelectric effect and scattering cross sections are element dependent.

If the current layer i contains n_i different atomic elements Z_j^i, each with a weight fraction w_j^i, then an interaction with an atom of the k-th element Z_k^i is chosen by means of a uniform random number R in such a a manner that the following equation holds:

$$\sum_{l=1}^{k} w_l^i m_l^i \leq R < \sum_{l=1}^{k+1} w_l^i m_l^i \tag{5.9}$$

with:

$$m_l^i = \frac{\mu_l^i}{\sum_{m=1}^{n_i} w_m^i \mu_m^i} \tag{5.10}$$

The correction of the composition weights using the absorption terms from Eq. (5.10) is required due to the different interaction probabilities of the different elements.

5.5.3 Selection of interaction type

The Monte Carlo simulation allows only for interactions in the energy range 1-100 keV. In this range, only photoelectric effect, Rayleigh and Compton scattering occur. The cross sections associated with these phenomena are denoted as τ_Z, σ_{RZ} and σ_{CZ} respectively, and their sum is equal to the absorption coefficient μ_Z. The interaction type is chosen according to:

$$\begin{cases} 0 \leq R < \dfrac{\tau_Z}{\mu_Z} & \text{photoelectric effect} \\ \dfrac{\tau_Z}{\mu_Z} \leq R < \dfrac{\tau_Z + \sigma_{RZ}}{\mu_Z} & \text{Rayleigh scattering} \\ \dfrac{\tau_Z + \sigma_{RZ}}{\mu_Z} \leq R < 1 & \text{Compton scattering} \end{cases} \tag{5.11}$$

5.5.4 Photoelectric effect: subshell selection

If the photoelectric effect was selected by the random number generator as an interaction type, the next selection concerns the particular (sub)shell that experienced the photoelectric effect. Depending upon the atom species and the excitation energy, up to 9 shells are taken into account by the simulation code (Z subscripts are dropped for clarity):

$$\begin{cases} 0 \leq R < \dfrac{\tau_K}{\tau} & \text{K shell} \\ \dfrac{\tau_K}{\tau} \leq R < \dfrac{\tau_K + \tau_{L1}}{\tau} & \text{L}_1 \text{ shell} \\ \dfrac{\tau_K + \tau_{L1}}{\tau} \leq R < \dfrac{\tau_K + \tau_{L1} + \tau_{L2}}{\tau} & \text{L}_2 \text{ shell} \\ \dfrac{\tau_K + \tau_{L1} + \tau_{L2}}{\tau} \leq R < \dfrac{\tau_K + \tau_{L1} + \tau_{L2} + \tau_{L3}}{\tau} & \text{L}_3 \text{ shell} \\ \dfrac{\tau_K + \tau_{L1} + \tau_{L2} + \tau_{L3}}{\tau} \leq R < \dfrac{\sum_{i=K}^{L3} \tau_i + \tau_{M1}}{\tau} & \text{M}_1 \text{ shell} \\ \dfrac{\sum_{i=K}^{L3} \tau_i + \tau_{M1}}{\tau} \leq R < \dfrac{\sum_{i=K}^{M1} \tau_i + \tau_{M2}}{\tau} & \text{M}_2 \text{ shell} \\ \dfrac{\sum_{i=K}^{M1} \tau_i + \tau_{M2}}{\tau} \leq R < \dfrac{\sum_{i=K}^{M2} \tau_i + \tau_{M3}}{\tau} & \text{M}_3 \text{ shell} \\ \dfrac{\sum_{i=K}^{M2} \tau_i + \tau_{M3}}{\tau} \leq R < \dfrac{\sum_{i=K}^{M3} \tau_i + \tau_{M4}}{\tau} & \text{M}_4 \text{ shell} \\ \dfrac{\sum_{i=K}^{M3} \tau_i + \tau_{M4}}{\tau} \leq R < \dfrac{\sum_{i=K}^{M4} \tau_i + \tau_{M5}}{\tau} & \text{M}_5 \text{ shell} \end{cases} \tag{5.12}$$

where τ_i is the partial photoelectric effect cross section referring to the element Z and an excitation energy E. It is possible, in particular for high Z elements, that a higher shell than those considered here was excited (e.g. N). If this case were to happen, the photon is assumed to be absorbed completely by the atom and its trajectory would be terminated since such photons possess very low energies. Only K, L and M lines are considered in this work.

5.5.5 Photoelectric effect: selection of transition type

Assuming an appropriate (sub)shell was selected in the previous step, the next stage in the algorithm will determine the nature of the transition necessary to relax the excited atom. A radiative transition resulst in a fluorescence line being emitted, while a radiationless transition produces an Auger electron. The quantity used to express the likelihood of fluorescence emission is called *fluorescence yield* (ω) and is defined as the number of photons emitted when vacancies in the shell are filled, divided by the number of primary vacancies in the shell[21]. This definition implies however, that the fluorescence yields are already corrected for any Coster-Kronig transitions that may have occurred before the actual radiative transition. Therefore, these fluorescence yields cannot be used if the Monte Carlo simulation has to decide by itself whether or not Coster-Kronig transitions effectively have taken place. In this case coefficients ν_i^X are needed to represent the total number of

characteristic X-shell X-rays (not necessarily from the radiative filling of a vacancy in the X_i-subshell) per primary vacancy in the X_i subshell. These coefficients can be calculated from the fluorescence yields and the Coster-Kronig transition probabilities as follows[21]:

$$
\begin{aligned}
\nu^K &= \omega_K \\
\nu_1^L &= \omega_1^L + f_{12}^L\omega_2^L + (f_{13}^L + f_{12}^L f_{23}^L)\omega_3^L \\
\nu_2^L &= \omega_2^L + f_{23}^L\omega_3^L \\
\nu_3^L &= \omega_3^L \\
\nu_1^M &= \omega_1^M + f_{12}^M\omega_2^M + (f_{13}^M + f_{12}^M f_{23}^M)\omega_3^M \\
&\quad +(f_{14}^M + f_{13}^M f_{34}^M + f_{12}^M f_{24}^M + f_{12}^M f_{23}^M f_{34}^M)\omega_4^M \\
&\quad\quad +(f_{15}^M + f_{14}^M f_{45}^M + f_{13}^M f_{35}^M + f_{12}^M f_{25}^M \\
&\quad\quad\quad +f_{13}^M f_{34}^M f_{45}^M + f_{12}^M f_{24}^M f_{45}^M + f_{12}^M f_{23}^M f_{35}^M + f_{12}^M f_{23}^M f_{34}^M f_{45}^M)\omega_5^M \\
\nu_2^M &= \omega_2^M + f_{23}^M\omega_3^M + (f_{24}^M f + f_{23}^M f_{34}^M)\omega_4^M \\
&\quad +(f_{25}^M + f_{24}^M f_{45}^M + f_{23}^M f_{35}^M + f_{23}^M f_{34}^M f_{45}^M)\omega_5^M \\
\nu_3^M &= \omega_3^M + f_{34}^M\omega_4^M + (f_{35}^M + f_{34}^M f_{45}^M)\omega_5^M \\
\nu_4^M &= \omega_4^M + f_{45}^M\omega_5^M \\
\nu_5^M &= \omega_5^M
\end{aligned}
\tag{5.13}
$$

where the f symbols represent the Coster-Kronig transition probabilities. The decision concerning the transition type is made by comparing the coefficient of the excited shell, ν_i^X, with a uniformly distributed random number $0 \leq R < 1$. If R is less than the coefficient ν_i^X, the transition is considered to be radiative and will result in the emission of a characteristic fluorescence line. If this condition is not met, then the atom will relax through a non-radiative transition that will trigger the emission of a characteristic Auger electron. Although Auger electrons, as well as photoelectrons and Compton electrons, may lead to the generation of additional photons in the sample through Bremsstrahlung and impact ionization, that in turn could lead to more fluorescence events, this effect is usually very small and will be ignored in this work. The new vacancies created by the electron transitions and the Auger effect lead to additional transitions since the atom is still in an unstable state (although more stable than compared to its state right after the initial ionization). This phenomenon, called the cascade effect, is included in the simulation algorithm and will be discussed in a later section.

5.5.6 X-ray fluorescence

If the Monte Carlo algorithm selects a photon that will experience a radiative transition, as a consequence the next step implies the determination of the shells that will be involved in this process. At this point it is still possible that the primary vacancy created by the photoelectric effect, will shift to a different subshell in the case of L- and M-shell excitation (Coster-Kronig transition). The likelihood of such a transition is governed by the Coster-Kronig transition probabilities and is shown in Figs. 5.2 and 5.3.

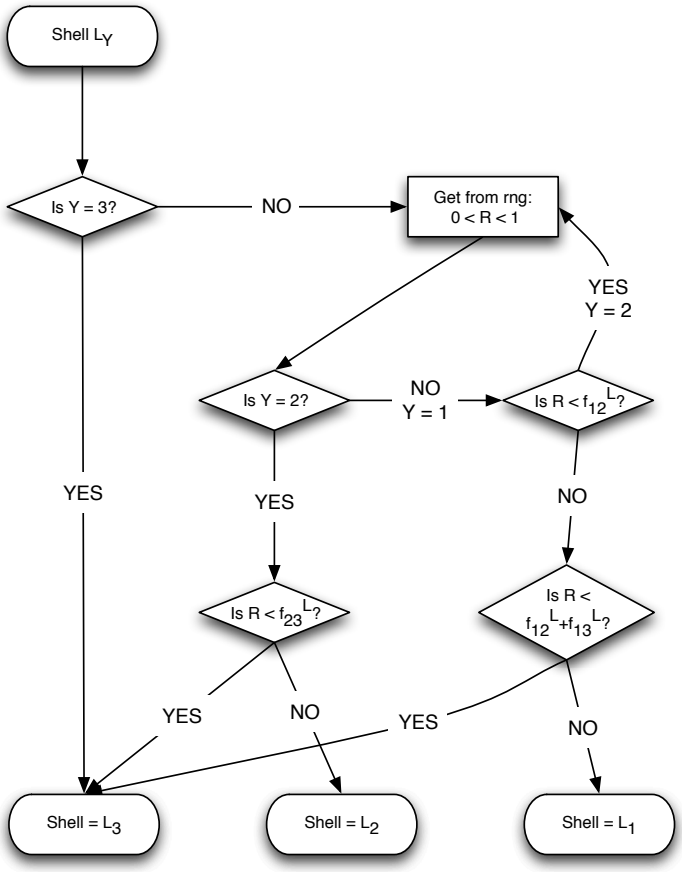

Figure 5.2: Flowchart describing the algorithm used to determine the eventual shell that will participate in the transition, assuming that an initial excitation of one of the L subshells has occurred

The second shell involved in the transition is selected from the radiative emission rates of the excited atom, which ultimately determine the energy of the produced fluorescence line.

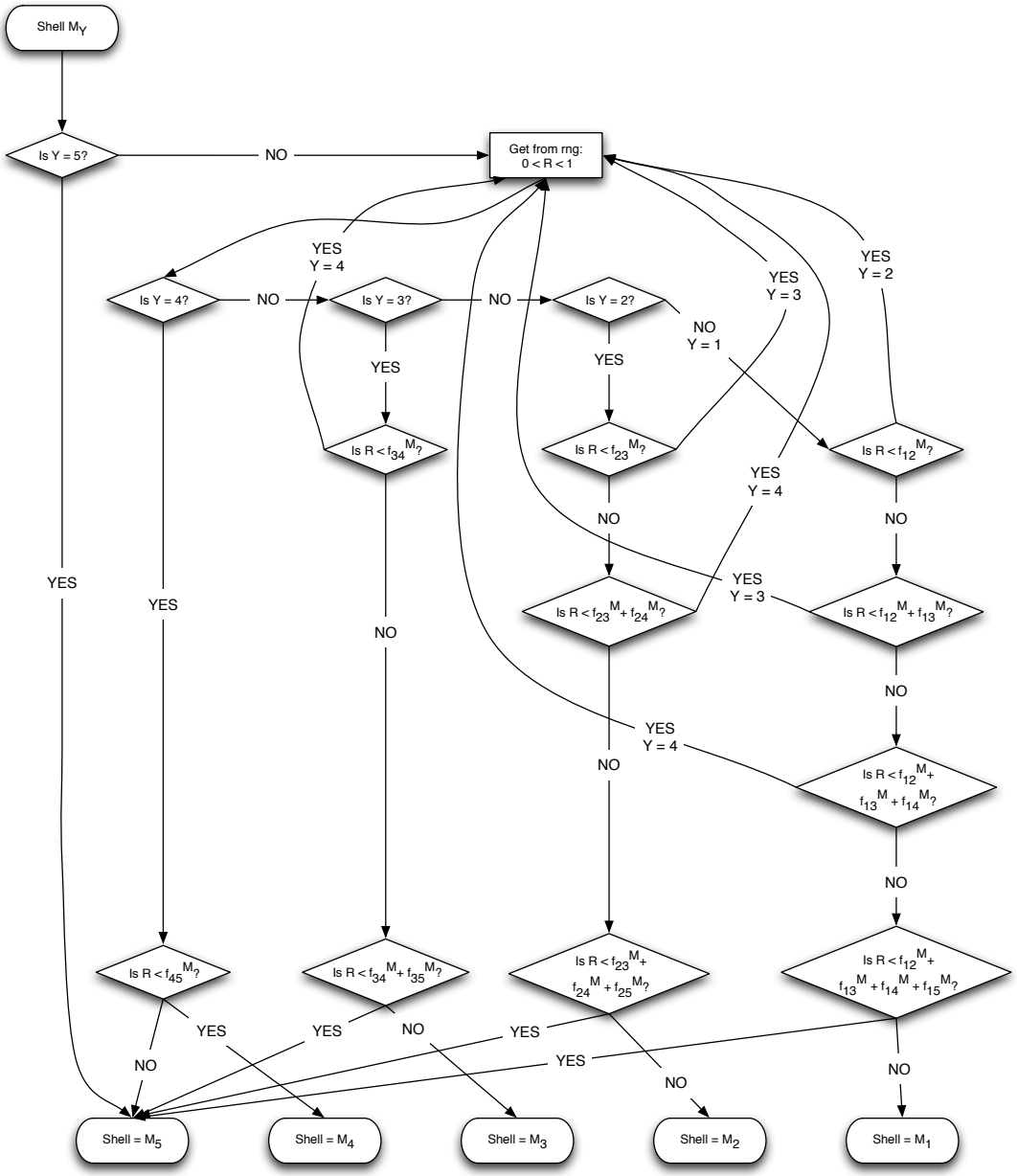

Figure 5.3: Flowchart describing the algorithm used to determine the eventual shell that will participate in the transition, assuming that an initial excitation of one of the M subshells has occurred

The selection occurs again through the generation of a random number $0 \leq R < 1$. For the K-shell transitions, the selection process is represented in the following equation:

$$\text{line} = \begin{cases} KL_2: & 0 \leq R < p_{KL2} \\ KL_3: & p_{KL2} \leq R < p_{KL2} + p_{KL3} \\ KM_2: & p_{KL2} + p_{KL3} \leq R < p_{KL2} + p_{KL3} + p_{KM2} \\ KM_3: & p_{KL2} + p_{KL3} + p_{KM2} \leq R < p_{KL2} + p_{KL3} + p_{KM2} + p_{KM3} \\ \ldots & \end{cases} \tag{5.14}$$

with p_X corresponding to the radiative emission rates of line X. Similar equations can be derived for the L- and M- subshells. Up to 320 K-,L-, and M-lines are taken into account for each element of the periodic table.
It is worth noting the absence of the KL_1 transition in Eq. (5.14). This transition is not accounted for owing to its multipole nature and its subsequent extreme weakness.
After the selection of the linetype and the corresponding energy, the new direction of the photon is calculated taking into account the isotropic nature of the fluorescence production:

$$\begin{aligned} \theta_i &= \arccos(2R - 1) \\ \phi_i &= 2\pi R \end{aligned} \tag{5.15}$$

where R has the aforementioned meaning.

5.5.7 Cascade effect

A single cascade event may lead to a two photon process: if the precursory transition type is radiative, and if the fluorescence yield selection step is favorable, then a second fluorescence photon is being produced. An example of such a process looks as follows:

1. Initial K-shell excitation
2. A radiative transition produces a KL_3 photon and a vacancy in the L_3 shell
3. The fluorescence yield of the L_3 shell is favorable, leading to a new radiative transition L_3M_5
4. The vacancy created in the M_5 shell is giving rise to a new secondary cascade event

In this case, the code will create an additional photon (offspring) which will be considered by the program as any other photon. Note that it is possible that the second shell may

first relax by means of a Coster-Kronig transition, before the radiative transition takes place (e.g. KL_2 and L_3M_5 photons). Alternatively, if the initial excitation leads to a non-radiative relaxation of the photon, the atom will be in a state characterized by two vacancies due to the emission of the Auger electron. These two vacancies will in turn be subject to transitions and thereby, depending on the fluorescence yields of the shells, result in the production of 0, 1 or 2 fluorescence photons. In order to determine which combination of electron vacancies is created after the initial non-radiative transition, a selection is made based on the non-radiative emission rates a_{X-YZ}, where X is the initially excited shell and Y and Z correspond to the shells with vacancies. The algorithm for the selection is analogue to the one employed in Eq. (5.14). An example of a non-radiative cascade effect is given below:

1. Initial K-shell excitation
2. A non-radiative transition produces vacancies in the L_2 and L_3 shells
3. L_2 results in a non-radiative transition and L_3 in radiative one
4. The three vacancies will give rise to subsequent cascade events

Here, the same remark applies to the Coster-Kronig transitions as in the case of radiative cascade events. Our implementation of the cascade effect takes into account only the primary event: secondary events produce lines that originate in shells differing by at least two principal quantum numbers from the initially excited shell, and it is very unlikely for current energy dispersive X-ray fluorescence spectrometers to produce spectra containing K-, L- and M-lines of the same element.

5.5.8 Scattering interactions

In the preceding paragraphs which describe the fluorescence production, the electric field vector that is associated with the simulated photon, was not mentioned. However, when investigating the scattering interactions of the photons, this vector becomes of the utmost importance, since it will determine the azimuthal scattering direction. This is only true, however, when dealing with polarized radiation: otherwise the azimuthal scattering angle is chosen randomly in the interval $[0, 2\pi]$. The accurate simulation of the scattering interactions becomes obvious when comparing spectra obtained using an X-ray tube (producing

unpolarized radiation) and synchrotron radiation (producing highly polarized radiation). In the former case, the intensity of the Rayleigh and Compton scatter peaks will be far more intense, and thus leading to considerable higher spectral background.

Generally speaking, in order to accurately model the change in direction of a photon after a scattering event, one needs to employ the appropriate differential scattering cross sections $\frac{d\sigma}{d\Omega}$ which characterize the angular distribution of the scattered photons. In the following, the coordinate system is chosen in such a way that the photon (with a propagation vector $\boldsymbol{k_0}$) travels along the Z-axis prior to the interaction and its electric field vector $\boldsymbol{\epsilon_0}$ is parallel to the X-axis. After the interaction, the new direction of the photon is characterized by the propagation vector $\boldsymbol{k_1}$ and the electric field vector $\boldsymbol{\epsilon_1}$. The expressions for the Rayleigh and Compton differential cross sections are given by:

$$\begin{aligned}\frac{d\sigma_R(\theta,\phi,E)}{d\Omega} &= \frac{d\sigma_T(\theta,\phi)}{d\Omega}F^2(x,Z) \\ &= r_e^2\left(1-\sin^2\theta\sin^2\phi\right)F^2(x,Z) \qquad (5.16)\\ \frac{d\sigma_C(\theta,\phi,E)}{d\Omega} &= \frac{d\sigma_{KN}(\theta,\phi,E)}{d\Omega}S(x,Z) \\ &= \frac{r_e^2}{2}\left(\frac{K}{K_0}\right)^2\left(\frac{K}{K_0}+\frac{K_0}{K}-2\sin^2\theta\cos^2\phi\right)S(x,Z) \qquad (5.17)\end{aligned}$$

where $\frac{d\sigma_T(\theta,\phi)}{d\Omega}$ denotes the Thompson and $\frac{d\sigma_{KN}(\theta,\phi,E)}{d\Omega}$ the Klein-Nishina differential cross sections. $F(x,Z)$ and $S(x,Z)$ are the atomic form factor and the incoherent scattering function respectively, $x(\mathring{A}^{-1}) = \sin\left(\frac{\theta}{2}\right)\frac{E}{12.4}$ is the momentum transfer function of the photon and r_e is the classical electron radius. The quantity $\frac{K_0}{K}$ is determined by the scattering angle θ and is equal to the ratio of the photon energy E before and after the Compton scattering event:

$$\frac{K_0}{K} = 1+\frac{E}{m_ec^2}(1-\cos\theta) \qquad (5.18)$$

with m_e being the rest mass of the electron and c is the speed of light in vacuo. The energy loss of the photon can be calculated from the scattering angle θ according to:

$$E_{i+1} = E_i\left(\frac{K_0}{K}-\frac{2p_z}{m_ec}\sin\frac{\theta}{2}\right)^{-1} \qquad (5.19)$$

The second term in Eq. (5.19) refers to the contribution of the momentum p_z of the scattering electron to the energy transfer during the interaction and is calculated as:

$$p_z = q\frac{m_e e^2}{2\epsilon_0 h} \tag{5.20}$$

where q is the reduced momentum of the scattering electron, ϵ_0 the vacuum permittivity, e the electron charge and h Planck's constant.

The probability that a photon is scattered within a finite solid angle defined by the angles $(\theta, \theta + d\theta; \phi, \phi + d\phi)$ can be calculated by means of the following equation:

$$p(\theta, \theta + d\theta, \phi, \phi + d\phi, E) = f(\theta, \phi, E)d\theta d\phi = \frac{1}{\sigma(E)}\frac{d\sigma}{d\Omega}(\theta, \phi, E)\sin\theta d\theta d\phi \tag{5.21}$$

with $f(\theta, \phi, E)$ being the probability density function of this event at energy E. The integration of Eq. (5.21) over ϕ in the interval $[0, 2\pi]$ gives the probability that the scattered photon can be found in a spherical section Γ comprised in $(\theta, \theta + d\theta)$:

$$f(\theta, E)d\theta = \frac{1}{\sigma(E)}\left[\int_0^{2\pi}\frac{d\sigma}{d\Omega}(\theta, \phi, E)d\phi\right]\sin\theta d\theta = \frac{2\pi}{\sigma(E)}\left(\frac{d\sigma}{d\Omega}\right)_U(\theta, E)\sin\theta d\theta \tag{5.22}$$

where $\left(\frac{d\sigma}{d\Omega}\right)_U$ is the differential cross sections for unpolarized incident radiation:

$$\begin{array}{rcl}\left(\frac{d\sigma_R}{d\Omega}\right)_U(\theta, E) & = & \frac{r_e^2}{2}\left(1 + \cos^2\theta\right)F^2(x, Z) \\ \left(\frac{d\sigma_C}{d\Omega}\right)_U(\theta, E) & = & \frac{r_e^2}{2}\left(\frac{K}{K_0}\right)^2\left(\frac{K}{K_0} + \frac{K_0}{K} - \sin^2\theta\right)S(x, Z)\end{array} \tag{5.23}$$

From Eq. (5.22) one can calculate the corresponding cumulative distribution function:

$$F_E(\theta) = \frac{2\pi}{\sigma(E)}\int_0^{\theta}\frac{d\sigma}{d\Omega}(\nu, E)\sin\nu d\nu \tag{5.24}$$

Inversion of Eq. (5.24), allows obtaining the scattering angle θ, when evaluated for a uniform random number $0 \leq R < 1$:

$$\theta = F_E^{-1}(R) \tag{5.25}$$

The calculation of the inverse cumulative distribution function F_E^{-1}, which depends on the atomic number Z, the initial photon energy E and the scattering angle θ, is not straightforward however: direct inversion is not possible analytically, but can be done numerically

since it is a monotonically increasing function. Our approach consists in the precalculation at regular intervals of the function $\theta(R, E)$ for all atomic elements separately. Typically 2000 and 200 intervals are considered in the R and E dimensions, respectively, totalling 400000 points per surface. These values need to be calculated only once for each element (both for coherent and incoherent scattering) and are read into the computer memory at runtime. These datasets are stored in an HDF5 file and can be modified by the user if necessary. Fig. 5.4 shows the inverse cumulative distribution surfaces of the Rayleigh and Compton scattering functions on an Fe atom.

During the run, the simulation will request function values $\theta(R, E)$ which will not correspond to the precalculated grid points. The necessary values will be calculated by means of a bilinear interpolation scheme: if the values of R and E are such that the closest precalculated values are E_- and E_+, respectively R_- and R_+, the interpolated value of the scattering angle $\theta_{int}(R, E)$ is approximated using:

$$\theta_{int}(R, E) = c_1\theta(R_-, E_-) + c_2\theta(R_+, E_-) + c_3\theta(R_-, E_+) + c_4\theta(R_+, E_+) \tag{5.26}$$

with the coefficients c_i defined as:

$$\begin{aligned} c_1 &= \frac{(R_+ - R)(E_+ - E)}{(R_+ - R_-)(E_+ - E_-)} \\ c_2 &= \frac{(R - R_-)(E_+ - E)}{(R_+ - R_-)(E_+ - E_-)} \\ c_3 &= \frac{(R_+ - R)(E - E_-)}{(R_+ - R_-)(E_+ - E_-)} \\ c_4 &= \frac{(R - R_-)(E - E_-)}{(R_+ - R_-)(E_+ - E_-)} \end{aligned} \tag{5.27}$$

The error introduced by this interpolation scheme has been shown to be small (less than 2%) [5], and to be of the same order as the uncertainty on a number of atomic properties, such as mass absorption coefficients, making it an acceptable solution.

The determination of the azimuthal angle ϕ at a specific scattering angle θ occurs ultimately through the probability density function:

$$f_\theta(\phi) = \frac{d\sigma}{d\Omega}(\theta, \phi, E) \left[\int_0^{2\pi} \frac{d\sigma}{d\Omega}(\theta, \phi, E) d\phi\right]^{-1} \tag{5.28}$$

Substituting the Rayleigh and Compton differential cross sections given by Eqs. (5.16) and (5.17), into Eq. (5.28) leads to:

$$f_\theta(\phi) = \frac{1}{2\pi}\left[1 - \frac{\sin^2(\theta)}{B(\theta)}\cos(2\phi)\right] \tag{5.29}$$

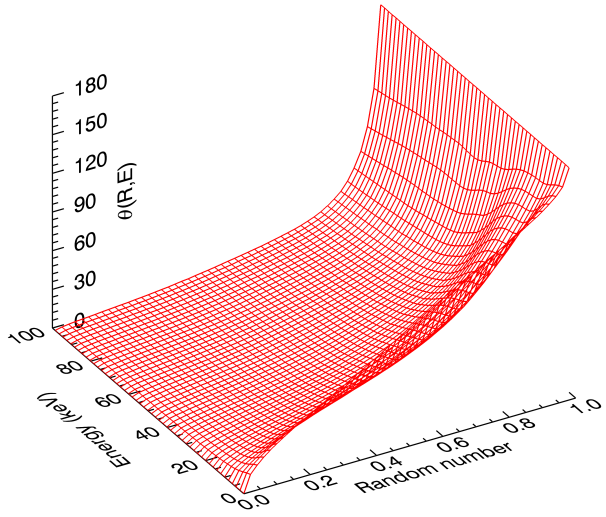

(a) Rayleigh scattering

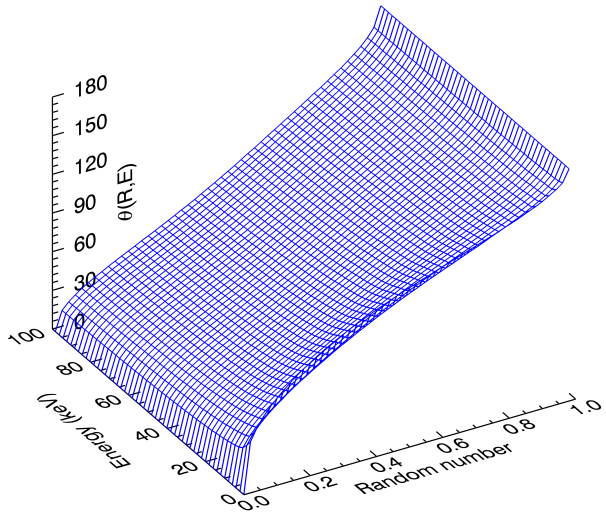

(b) Compton scattering

Figure 5.4: The $\theta(R, E)$ surfaces in the energy range 0-100 keV for Rayleigh (a) and Compton (b) scattering from an Fe atom

where the function $B(\theta)$ is given by:

$$B(\theta) = \begin{cases} 2 - \sin^2\theta & \text{Rayleigh scattering} \\ \frac{K}{K_0} + \frac{K_0}{K} - \sin^2\theta & \text{Compton scattering} \end{cases} \tag{5.30}$$

Eq. (5.30) reveals that $f_\theta(\phi)$ is energy-dependent only if Compton scattering occurs: if the ratio $\frac{K}{K_0}$ approaches unity, the expression reduces to the Rayleigh scattering formula. The last equation points out one of the advantages of X-rays with a high degree of linear polarization: assuming that detection occurs perpendicularly to the incoming beam and within the horizontal plane, the detected Compton and Rayleigh signals will be minimal ($\theta = 90°, \phi = 0°$ or $180°$). The probability that the azimuthal angle after the scattering interaction will be in the interval $[0, \phi]$ is given by the cumulative distribution function $F_\theta(\phi)$ defined as:

$$F_\theta(\phi) = \int_0^\phi f_\theta(\phi) d\phi = \frac{1}{2\pi}\left[\phi - \frac{\sin^2\theta}{2B(\theta)}\sin(2\phi)\right] \tag{5.31}$$

Like the selection of the scattering angle θ, the azimuthal angle ϕ is selected from the inverse cumulative distribution function $F_\theta^{-1}(R)$ through a uniform random number $0 \leq R < 1$. Since this function too cannot be solved analytically, a precalculated grid of azimuthal angles is stored in the aforementioned HDF5 file that will be loaded in the host's memory at runtime. Fig. 5.5 shows the inverse cumulative distribution function $F_\theta^{-1}(R)$ for Rayleigh scattering. After the scattering event, the electric field vector of the photon is assumed to be along the projection of $\boldsymbol{\epsilon_0}$ on the plane perpendicular to the new direction of propagation $\boldsymbol{k_1}$ of the photon. Under this condition the components of $\boldsymbol{\epsilon_1}$ can be written as:

$$\boldsymbol{\epsilon_1} = \frac{\epsilon_1}{\sqrt{1 - \sin^2\theta\cos^2\phi}} \begin{bmatrix} 1 - \sin^2\theta\cos^2\phi \\ -\sin^2\theta\sin\phi\cos\phi \\ -\sin\theta\cos\theta\cos\phi \end{bmatrix} \tag{5.32}$$

5.5.9 Escape peaks

After running the Monte Carlo simulation, the detected photons are stored in a virtual multichannel analyzer. This essentially corresponds to a situation in which one would have performed the experiment with an ideal detector. In a real system however, several artifacts and distortions are introduced in the recorded spectrum due to the physical limitations of

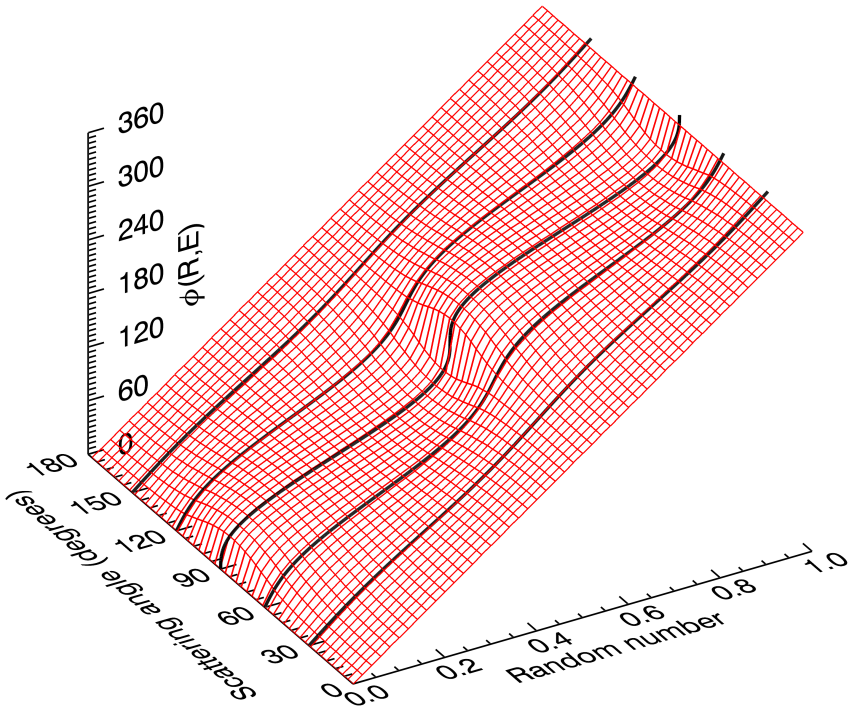

Figure 5.5: The inverse cumulative distribution function $F_\theta^{-1}(R)$ for Rayleigh scattering.

the detector and its associated electronics. The first of these detector effects that is taken into account by the software concerns the detector escape peaks. These lines appear as a result of the possibility that the secondary photons which are created in the detector crystal after either Compton scattering or photoionization with subsequent fluorescence may leave the detector through the window or through the back of the detector. If the photons in the detector originated from fluorescence processes, lines will then emerge in the spectrum at positions corresponding to the energy of the incoming photon minus the energy of the fluorescence lines of the detector crystal material. Otherwise, when the incoming photons experience Compton scattering upon interaction with the detector crystal, the escaping photons may take on energies ranging from 0 keV to the original energy of the photon minus $E_0(1 + \frac{2E_0}{m_e c^2})^{-1}$. However, assuming that the incoming photon impinged on the detector perpendicularly to its surface, it is far more likely to observe Compton

escape at scattering angles either close to 0° (leaving through the backside of the crystal) or close to 180° (leaving through the front window). This is because these photons have the shortest pathways on their way out of the crystal and are thus the most unlikely to become absorbed. The occurrence of escape peaks depends hence strongly on both the energy of the incoming photons and on the composition of the crystal, density and thickness. In order to have the software capable of modeling escape peaks of any kind of detector, a generalized algorithm was implemented in the package. Unlike other authors who suggest an analytical solution for the fluorescence escape peaks[22,23], our solution produces the escape ratios simultaneously for both fluorescence and Compton scattering, by applying a modified version of the Monte Carlo algorithm that has been discussed so far. Essentially, for a large number of different incoming energies, a large quantity of photons will be simulated while impinging the detector perpendicularly which is modeled as a layer with thickness and composition defined by the user. After the simulation of each photon, the program will verify if it interacted at all and if this happened through either photoionization or Compton effect, the photon's weight is scored in a matrix at position corresponding to its initial and final energy. The final computational step involves the normalization of this matrix by the number of simulated photons, thereby obtaining the required escape ratios. Since this procedure is typically (very) slow and depends only on the composition, density and thickness of the detector crystal, the escape ratios are calculated only once and stored in an HDF5 file. Whenever the simulation of an XRF spectrum is requested, the program will query this file for the escape ratios corresponding to the detector crystal defined within the simulation input file. Only if the ratios are not found, they will be calculated. The ratios will be applied to the spectrum by subtracting the count rate in a particular channel i with the sum of the ratios of all the possible escape lines multiplied by the count rate of i, while increasing at the same time the count rate of the channels of the escape lines with the appropriate escape ratio multiplied with the original count rate of channel i. The escape ratios for a silicon drift detector and a germanium detector are shown in Figs. 5.6 and 5.7.

5.5.10 Pulse pile-up

Another artifact that is commonly found in experimental data, involves so-called pulse pile-up. This effect results in the appearance of additional lines in the spectrum, at energy

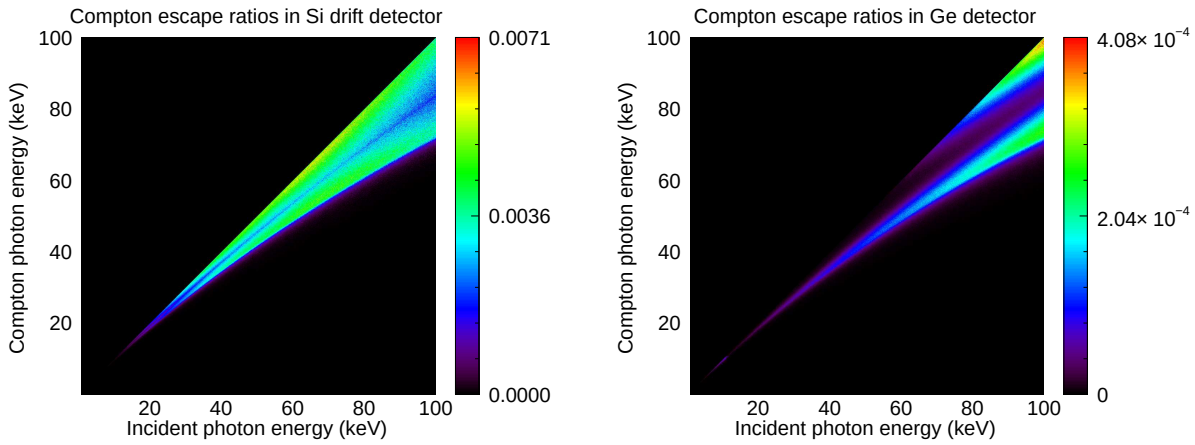

(a) Silicon drift detector

(b) Germanium detector

Figure 5.6: Compton escape ratios for a silicon drift detector (crystal thickness = 350 μm) and a germanium detector (crystal thickness = 5 mm). Before these ratios are applied to the unconvoluted spectrum, they must be multiplied by the ratio of the detector gain and the interval length of the output energies (in this case 0.1 keV).

values corresponding to the sum of the original photon energies. Its occurrence can be explained by the fact that the electronics equipment of the detector (amplifier etc.) needs a certain amount of time, i.e. the pulse width, to process an incoming pulse (photon). If two or more photons were to enter the detector system during this time frame, then the sum of the pulses would be detected instead of the separate pulses. In order to simulate this effect we use a modified version of the algorithm proposed by Gardner and Lee[24], consisting of a Monte Carlo method that exploits the exponential pulse interval distribution. Let N_t be the total number of counts detected during the measurement live time t_m and $h(E)$ the true probability density function of pulse-height energy E, which can be calculated by normalizing the input spectrum (assumed to be already corrected for escape peaks). In order to simulate the pulse piled-up total counts in the time t_m and the pulse-height distribution one samples N_t pulse events by first choosing a leading pulse size from $h(E)$ through a random number generator. Next, an interval is chosen between this pulse and the next one from the interval distribution given by:

$$f(\Delta t) = \lambda \exp(-\lambda \Delta t) \tag{5.33}$$

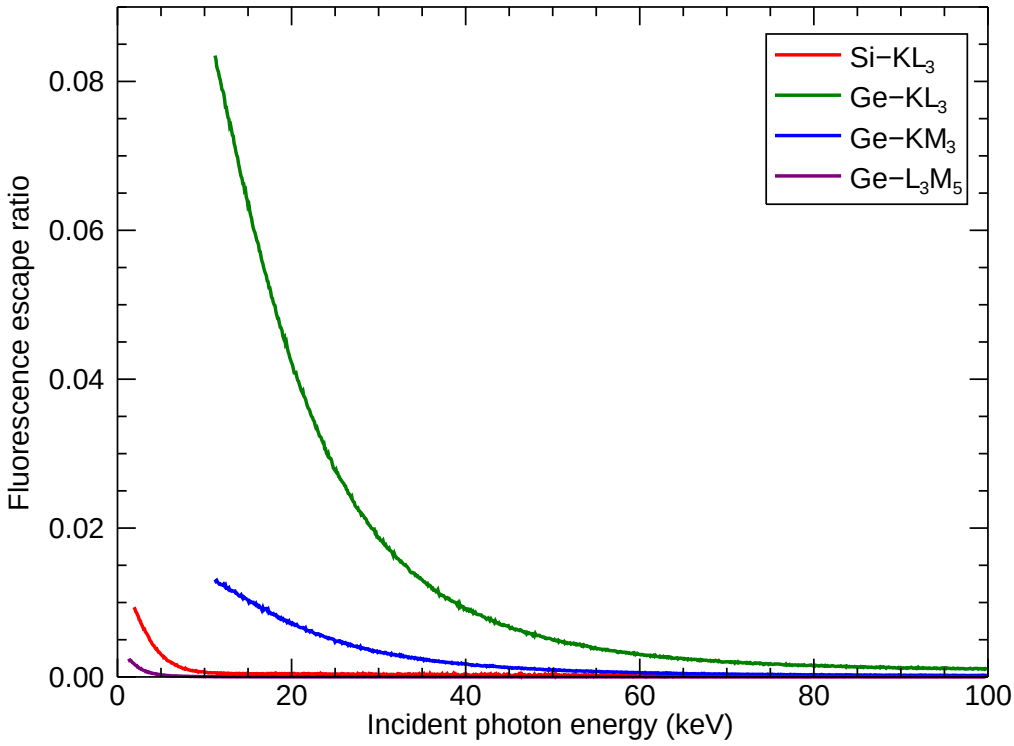

Figure 5.7: Fluorescence escape ratios of some selected lines for a silicon drift detector and a germanium detector.

with Δt being the time interval and λ the true counting rate $\frac{N_t}{t_m}$. The time intervals are chosen randomly by using the cumulative distribution function obtained by integrating Eq. (5.33) from 0 to Δt:

$$F(\Delta t) = \int_0^{\Delta t} f(x)dx = 1 - \exp(-\lambda \Delta t) \tag{5.34}$$

By means of a uniform random number $0 \leq R < 1$, one can select the required interval from the inverse of Eq. (5.34):

$$\Delta t = -\frac{1}{\lambda} \ln(1 - R) \tag{5.35}$$

Afterwards the first piled-up pulse is chosen from $h(E)$, etc., until the interval between pulses is larger than the pulse width τ. When this occurs, the pulse train being generated

is terminated and the sum of the energies of the pulses is recorded in the pulse-piled up spectrum. This differs from the original approach by Gardner and Lee: they assumed a Gaussian-shaped pulse corresponding with analog pulse processing equipment, while the digital equipment that was used during the experiments allowed for a simple summation of the pulses. The calculation time necessary for the pulse pile-up correction is typically about a few seconds. The magnitude of the pulse pile-up effect can be seen in Fig. 5.8, which shows the relationship between flux and the occurrence of pile-up peaks in the spectrum.

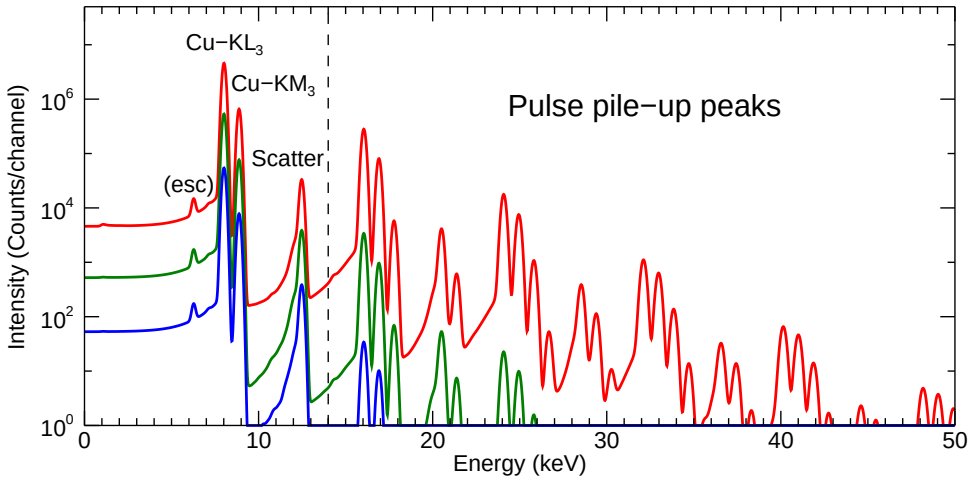

Figure 5.8: Monte Carlo simulation of an infinitely thick Cu sample irradiated with a 12.5 keV beam for 10 seconds at different fluxes: 4×10^{10} $\frac{photons}{s}$(red), 4×10^{9} $\frac{photons}{s}$(green), 4×10^{8} $\frac{photons}{s}$(blue).

After applying the escape peak and pulse pile-up corrections, the spectrum is convoluted with the detector response function thereby yielding the requested spectrum. The current implementation defaults to using the equations proposed by He et al[23]. It is however possible to modify the code and use a customized response function, appropriate for a particular detector. Such functions can be modelled for example by using the method discussed by Scholze and Procop[25].

5.6 Code optimization

Although the algorithms that were discussed in the preceding section are correct, they usually require a very large number of photons in order to simulate a stable spectrum. In fact, to simulate even the weakest lines correctly, one has to simulate a number of photons that is of the same order of magnitude as the flux times the live time. This can be attributed to the fact that the brute force implementation is inherently inefficient: if the sample is e.g. a very thin polymer film irradiated with a high-energy X-ray beam then a large number of the simulated photons will never interact with the sample but propagate through it, instead. A second problem involves the fluorescent yields of low Z elements: since these have low yields, a large amount of photons which managed to excite the K-shell will not lead to fluorescence, but will be lost since the cascade effect may only produce very low energy photons that will be discarded. Even the produced fluorescence photons that succeed in escaping the sample still have a very low chance of ever reaching the detector depending on the detector position, its orientation, its active area and the optional collimator. These issues were resolved in the code by adding a number of optimization steps which will be discussed in the following section.

5.6.1 Selection of the step length

Section 5.5.1 discusses the algorithm used to obtain the step length of a photon in the sample. The proposed equations allow a photon to leave the sample and, unless it hits the detector, to become useless for the purposes simulation. Our solution consists of forcing the photon to remain (and interact) within the sample until it has reached the maximum number of interactions, after which it is terminated. This is accomplished by introducing the term P_{abs} in Eq. (5.8), valid when dealing with samples consisting of a single layer:

$$S = \frac{\ln(1 - RP_{abs})}{\mu\rho} \quad \text{with} \quad P_{abs} = 1 - \exp(-\mu\rho S_{max}) \tag{5.36}$$

This condition will always produce a step length S between 0 and S_{max} for $0 \leq R < 1$, with R a uniformly distributed random number. The original weight factor of the photon has to be multiplied with P_{abs} in order to account for the escaped fraction of the beam. If the photon has to travel through n layers before leaving the sample, each medium can be indexed by an integer between 1 and n according to its order of appearance, as the photon

intersects the boundaries between the media. The selection of a distance S between two subsequent events corresponding to a given R can be made in two steps: first, the largest index m is found, for which the following inequality still holds:

$$\sum_{i=1}^{m} \mu_i S_i < -\ln(1 - RP_{abs}) \quad \text{with} \quad P_{abs} = 1 - \exp\left(-\sum_{i=1}^{n} \mu_i S_i\right) \tag{5.37}$$

Secondly, s is calculated according to:

$$S = \sum_{i=1}^{m} \left(1 - \frac{\mu_i}{\mu_{m+1}}\right) S_i - \frac{1}{\mu_{m+1}} \ln(1 - RP_{abs}), \tag{5.38}$$

i.e. the distance run by the photon in the sample.

5.6.2 Variance reduction

Since the photons are no longer allowed to leave the sample, it has now become impossible for them to reach the detector if this is positioned outside the layers of the system (e.g. in vacuum). This is remedied through the introduction of variance reduction techniques which greatly improve the overall efficiency of the code. Essentially, the same basic formalism is followed as described in Section 5.5, including the simulation of higher order events. Without that the trajectory of a particular photon is terminated, at each interaction point $\boldsymbol{r_i}$, the probability P of every possible pathway for that photon to travel from its current location to a point p_d on the detector surface (assuming no other interactions along the way) is calculated. The point $\boldsymbol{p_d}$ is selected randomly on the detector surface using the following equations, which assume a detector-based coordinate system with the Z-axis along the detector surface normal vector:

$$\begin{aligned} p_{d,x} &= \cos(2\pi R_1)\sqrt{R_2}\frac{D_{det}}{2} \\ p_{d,y} &= \sin(2\pi R_1)\sqrt{R_2}\frac{D_{det}}{2} \\ p_{d,z} &= 0 \end{aligned} \tag{5.39}$$

with R_1 and R_2 being uniform random numbers in the interval $[0, 1]$ and D_{det} the diameter of the detector active surface. Each pathway consists of (i) a "conversion" process during which the direction of the photon is altered in order for it to travel towards the selected point on the detector surface and (ii) the path the photon must travel to finally reach the detector. Three types of conversions are considered for each atomic element in the current

layer: Rayleigh scattering, Compton scattering and photoionization with subsequent fluorescence. Depending on the number of characteristic lines the atom under consideration may produce, a great many conversion possibilities can exist. In the case of a multielement sample, the various types of conversion may occur with different atomic species. Accordingly, a considerable number of different pathways from the current position $\boldsymbol{r_i}$ to the detector must be considered. As an example, consider the conversion processes that can occur in a $PbSO_4$ matrix irradiated with a 20 keV X-ray source. All three elements will give rise to Rayleigh and Compton scattering leading to six different conversion processes. The L- and M-shells of Pb can be excited at this energy and will lead to the emission of 128 fluorescence lines and as many conversion processes. In the energy region considered in our code (> 1 keV), S has 4 characteristic lines and O has none. This adds up to a total of 138 different conversion processes.

In general, the probability P_{cZ} of a pathway involving an interaction with a sample atom of type Z and a conversion of type c can be written as:

$$P_{cZ} = P_{cZ}^{conv} \times P_{cZ}^{dir} \times P_{cZ}^{esc} \tag{5.40}$$

with P_{cZ}^{conv}, P_{cZ}^{dir} and P_{cZ}^{esc} being the probability for the particular conversion to occur, the probability of the photon to change its direction over a scattering angle θ_i and an azimuthal angle ϕ_i, and the probability to escape from the sample when it is travelling towards the detector, respectively. If c refers to a fluorescent-type of conversion (producing a photon with energy E_f), the three probabilities can be calculated as follows:

$$\begin{aligned} P_{cZ}^{conv}(E_i) &= w_Z \frac{Q_Z^l(E_i)}{\mu(E_i)} \\ P_{cZ}^{dir} &= \frac{\Omega_{Det}}{4\pi} \\ P_{cZ}^{esc}(E_f, \theta_i, \phi_i) &= \exp\left(-\sum_{j=1}^{m} \mu_j(E_f)\rho_j S_j\right) \end{aligned} \tag{5.41}$$

where w_Z is the weight fraction of element Z in the current layer, Q_Z^l is the XRF production cross section of element Z for a line l at an excitation energy E_i, and Ω_{Det} is the solid angle subtended by the detector area at $\boldsymbol{r_i}$. The XRF production cross section expression can be, depending on the line l, quite long (especially when the cascade effects are taken into accounts) and will not be treated here. An overview of the expressions can be found in Schoonjans et al[26].

For a scatter-type conversion process, the probabilities can be written as follows:

$$\begin{aligned} P_{cZ}^{conv}(E_i) &= w_Z \frac{\sigma_{cZ}(E_i)}{\mu(E_i)} \\ P_{cZ}^{dir}(E_i, \theta_i, \phi_i) &= \frac{\Omega_{Det}}{\sigma_{cZ}(E_i)} \frac{d\sigma_{cZ}(\theta_i, \phi_i, E_i)}{d\Omega} \\ P_{cZ}^{esc}(E, \theta_i, \phi_i) &= \exp\left(-\sum_{j=1}^{m} \mu_j(E)\rho_j S_j\right) \end{aligned} \tag{5.42}$$

with $\frac{d\sigma_{cZ}(\theta_i,\phi_i,E_i)}{d\Omega}$ being either the Rayleigh or the Compton differential cross sections for polarized radiation (see Eqs. (5.16) and (5.17)). In the case of Compton scattering the final energy of the photon is calculated according to Eq. (5.19).

During the simulation of a photon trajectory and prior to simulating the next interaction on the trajectory, the probabilities of all possible pathways are calculated as explained above. These pathways with probability P can be thought of as "fractional photons" traveling towards the detector with weight equal to P. The impact of each fractional photon is recorded by adding the weight P to the contents of the appropriate channel of the virtual MCA. Afterwards, the next step in the current photon's trajectory is calculated.

5.6.3 Detector solid angle

The detector solid angle Ω_{Det} depends on the position $\boldsymbol{r_i}$, the detector active area and the (optional) collimator, implying that the value will be different for every photon during the simulation. The calculation of this solid angle is not straightforward, except for the trivial case when $\boldsymbol{r_i}$ is located on the detector axis in which case:

$$\Omega_{Det} = 2\pi(1 - \cos\alpha) \tag{5.43}$$

with α being the acceptance angle of the cone defined by the vertex $\boldsymbol{r_i}$ and the detector active area as the base. If a conical collimator is present and $\boldsymbol{r_i}$ is situated outside the collimator cone, then the base of solid angle cone corresponds to the opening of the collimator. Since a generalized analytical expression of the detector solid angle for an arbitrary position and arbitrary collimator does not exist, a numerical approach has to be employed. Our solution consists of a Monte Carlo simulation that estimates the detector solid angle by simulating a large number of photons within the smallest right cone that encompasses the true detector solid angle cone. Since the solid angle Ω_{Det}^R of this right cone can be easily calculated using Eq. (5.43), the required solid angle can then be estimated by multiplying Ω_{Det}^R with the ratio of the number of photons that hit the detector base to the total number

of simulated photons. Due to the circular symmetry of the detector and collimator, one can precalculate the detector solid angles for a two-dimensional grid defined by the distance of the interaction point to the detector center and by the slope of the line connecting these two points. The maximum distance that will be used in the grid is calculated based on the sample-detector distance and the thickness of the different layers. Two examples of such solid angle grids as calculated by the code, are presented in Fig. 5.9.

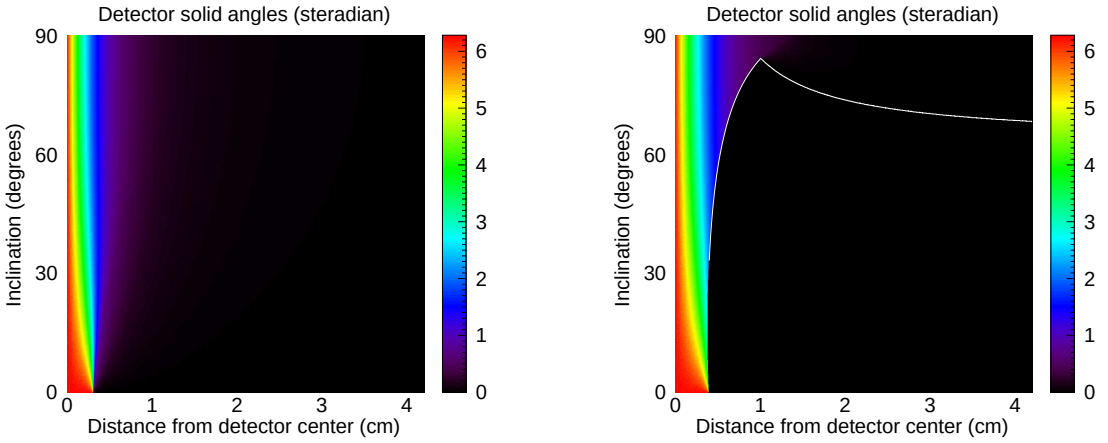

(a) Uncollimated detector

(b) Collimated detector

Figure 5.9: Solid angles grids for two different detector systems. (a) case of a detector with an active area of 30 mm^2. (b) case of a detector with an active area of 50 mm^2 and a collimator with a height of 1 cm and an opening diameter of 2 mm. The white line in (b) marks where the solid angles are defined, i.e. the positions from where the photons may reach the detector.

5.6.4 Fluorescence yield

In the brute force algorithm, a large amount of photons is terminated prematurely when the transition type is selected. This can be attributed to the fluorescence yield, which determines the number of shell excitations that effectively lead to fluorescence production. However, when no fluorescence is produced, an Auger electron is created which leads to a non-radiative cascade effect, possibly producing fluorescence radiation. Any fluorescence radiation produced in this manner always originates from at least one shell lower than the one that was originally excited and is therefore only important when dealing with high Z

elements, since the cascade photons have an energy considerably lower than the exciting photon. The code terminates photons when their energy is lower than a certain threshold (default setting is 1 keV), resulting in the elimination of a potentially tremendous number of photons. This was countered in the code by multiplying the weight of the photon by the fluorescence yield of the excited shell, instead of selecting the transition type. In order to still accommodate for the simulation of cascade events, the XRF production cross section equations were modified in order to take these effects into account, and can be found in Section 3.2.3.

A flowchart describing the algorithm of the optimized Monte Carlo model for ED-XRF spectrometers can be found in Fig. 5.10.

5.7 Results and discussion

5.7.1 Stainless steel NIST SRM 1155

Fig. 5.11 shows both the experimental and simulated spectra of the stainless steel standard NIST SRM 1155. The experiment was performed using a 16 keV beam with dimensions 10×10 μm^2 over 300 s real time. The degree of polarization was estimated to be around 91.5 %. Overall there is good agreement between both spectra. The pile-up peaks of the most intense XRF lines (Fe, Cr, Ni) were simulated assuming a pulse width of 2.03×10^{-7} s. Since the pulse width cannot be easily correlated to the detector setup parameters, it was estimated using a trial and error approach. The stainless steel sample is particularly interesting since it clearly shows the importance of higher order effects, which can be simulated since the algorithm allows for the photons to have multiple interactions per trajectory. Indeed, significant enhancement effects are occurring in the second and third interactions, as can be seen from Table 5.2: Ni lines may excite the Fe K-shell (and to a lesser extent, the Cr K-shell) leading to additional Fe XRF production. Furthermore, Fe lines may excite the Cr K-shell leading to additional Cr XRF production. The magnitude of the enhancement effect is due to the favorable XRF cross sections of the fluorescence photons compared to those from the incoming beam. This proves the usefulness of Monte Carlo quantification methods compared to fundamental-parameter-based methods. Since the latter typically do not take into account higher order effects, in this case they would produce unreliable results for Cr, and to a lesser extent, Fe.

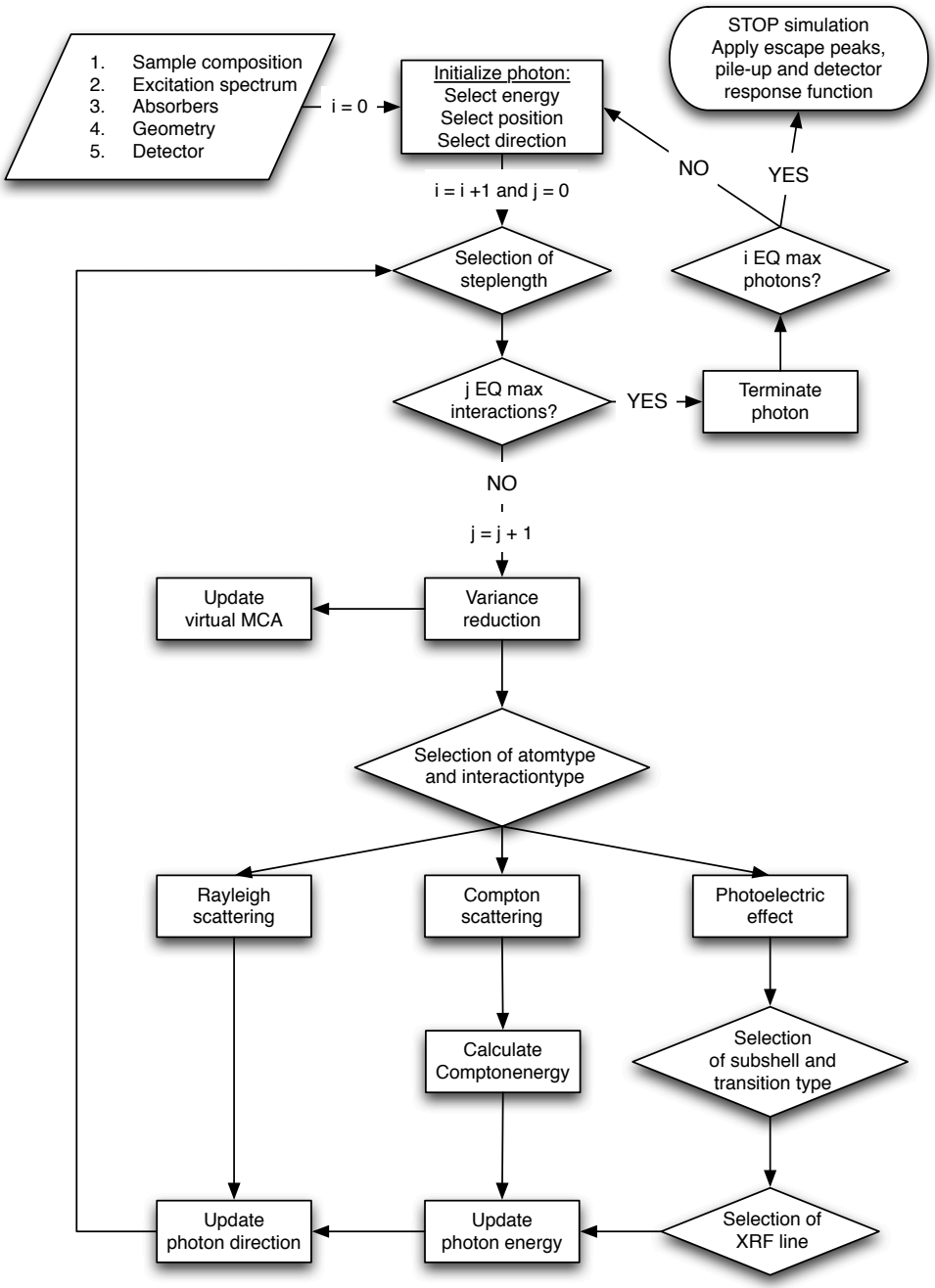

Figure 5.10: Flowchart describing the algorithm of the optimized Monte Carlo model for ED-XRF spectrometers. i refers to the index of the current photon and j refers to the number of interactions the current photon has experienced.

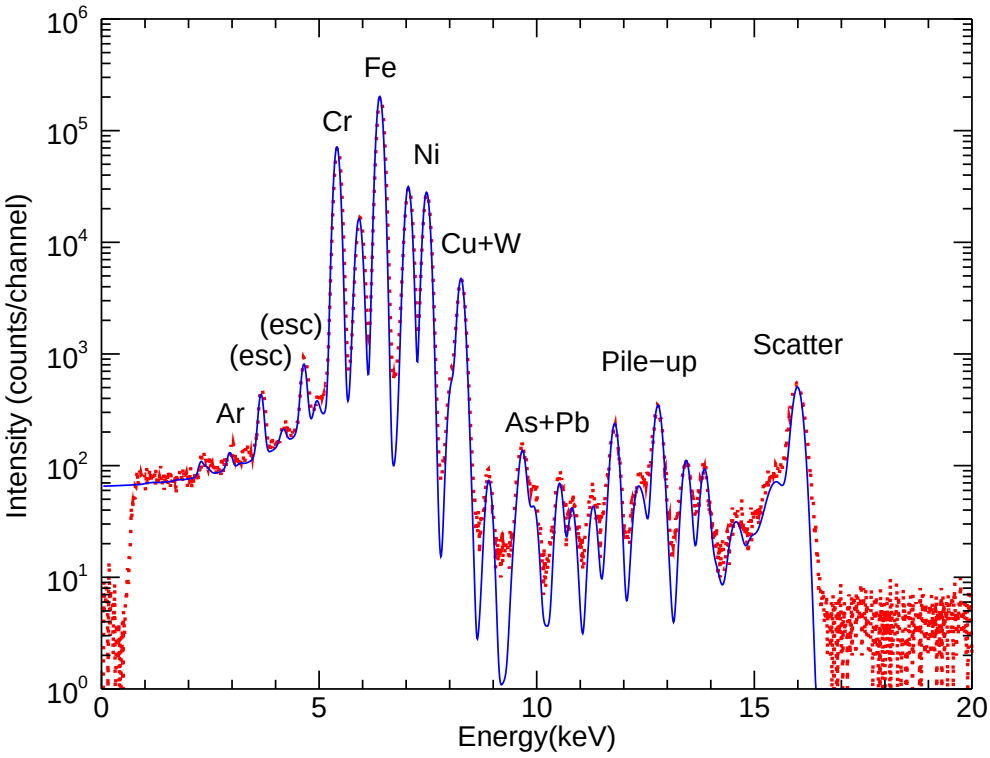

Figure 5.11: Experimental (red) and simulated (blue) spectra of NIST SRM 1155.

5.7.2 Pb-base bearing metal NIST SRM 1132

The simulation of the Pb-base baring metal NIST SRM 1132 allowed for the validation of the cascade effect algorithms (Fig. 5.12). The experimental data was acquired with a 10×10 μm^2 16 keV beam for 1500 s real time. Irradiation at 16 keV triggers the excitation of the three Pb L-shells and the five Pb M-shells and will give rise to the corresponding XRF lines in the spectrum. The intensity of the M-lines however, is primarily determined by the cascade effects from the L to the M shells. Since the code allows for the disabling of radiative and non-radiative cascade contributions independently, the quantitative study of each effect becomes feasible.

Fig. 5.13 shows the low energy region of the simulated and experimental data, as well as the simulated spectra obtained when disabling radiative, non-radiative and both cascade effects respectively. It can be seen that the simulation overestimates the Pb M-line intensity by

Table 5.2: Simulated number of photons reaching the detector after n interactions when irradiating NIST SRM 1155. The Fe signal receives considerable contributions from primary Ni fluorescence photons, while the Cr signal receives strong contributions from primary Fe fluorescence and from secondary Ni fluorescence.

n	Cr-KL_3	Cr-KM_3	Fe-KL_3	Fe-KM_3	Ni-KL_3	Ni-KM_3
1	394407	62019	1855990	295450	289772	49014
2	246726	40058	116944	19113	1823	334
3	17960	2983	1586	268	22	4
4	444	75	23	4	0	0

about 30 %, which can be attributed to the large uncertainties for the fluorescence yields of the Pb L-lines, the radiative rates of both Pb L- and Pb M-lines, and the non-radiative rates of the Auger transitions. Despite this considerable difference, it is however clear that the cascade effect is very strong and should not be ignored. This can be seen from the intensities of some selected Pb M-lines in Table 5.3. The overwhelming contribution of the non-radiative cascade effect can be explained by the low fluorescence yields of the Pb L-shells.

5.7.3 Multicomponent glass NIST SRM 1412

The third sample that was used to validate the code is the multicomponent glass NIST SRM 1412, displayed in Fig. 5.14. The experimental data was acquired by irradiating the 3.2 mm thick sample using a beam with a cross section of 60×60 μm^2 at 16.034 keV

Table 5.3: Simulated intensities of some selected Pb M-lines, obtained with or without considering the contribution of radiative and/or non-radiative cascades

XRF-line	No cascade	Radiative cascade	Non-radiative cascade	Full cascade
$M_5N_7(M_{\alpha 1})$	2839	5340	9345	11880
$M_5N_6(M_{\alpha 2})$	192	361	633	804
M_5N_3	64	124	220	278
M_1N_2	35	43	52	59

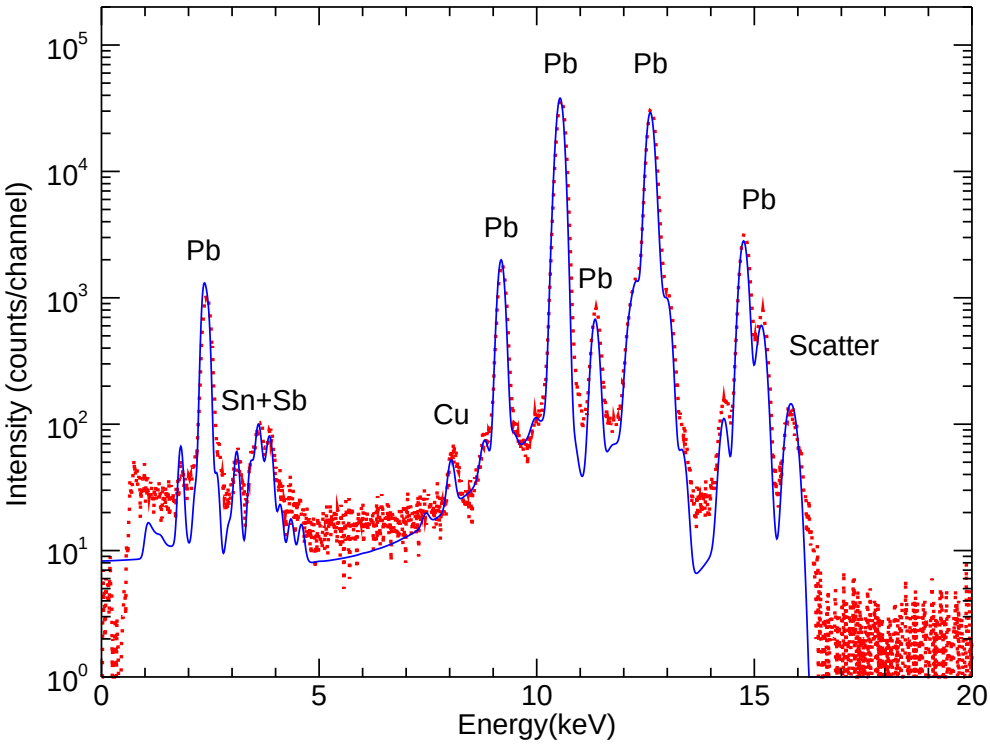

Figure 5.12: Experimental (red) and simulated (blue) spectra of NIST SRM 1132.

for 1500 s real time. Since this standard contains Sr, which has a K-shell edge energy of 16.1046 keV, only the fraction of the Gaussian excitation profile above this energy is deemed to be capable of causing excitation. The mean value of the excitation profile had to be calculated very precisely (eV level) since even small variations would cause a large shift in the Sr K intensities.

5.7.4 In foil

In order to investigate the K to L cascade effect, a 0.1 mm In foil (Goodfellow) was measured at 29 keV for 1500 s real time. Both the experimental and simulated spectra are reported in Fig. 5.15. The small peak situated on the left of the In KL_3 is due to scattering caused by the In foil that was considerably dented. In the energy region from 8 to 12 keV several weak lines can be seen in the experimental spectrum which were caused by photon

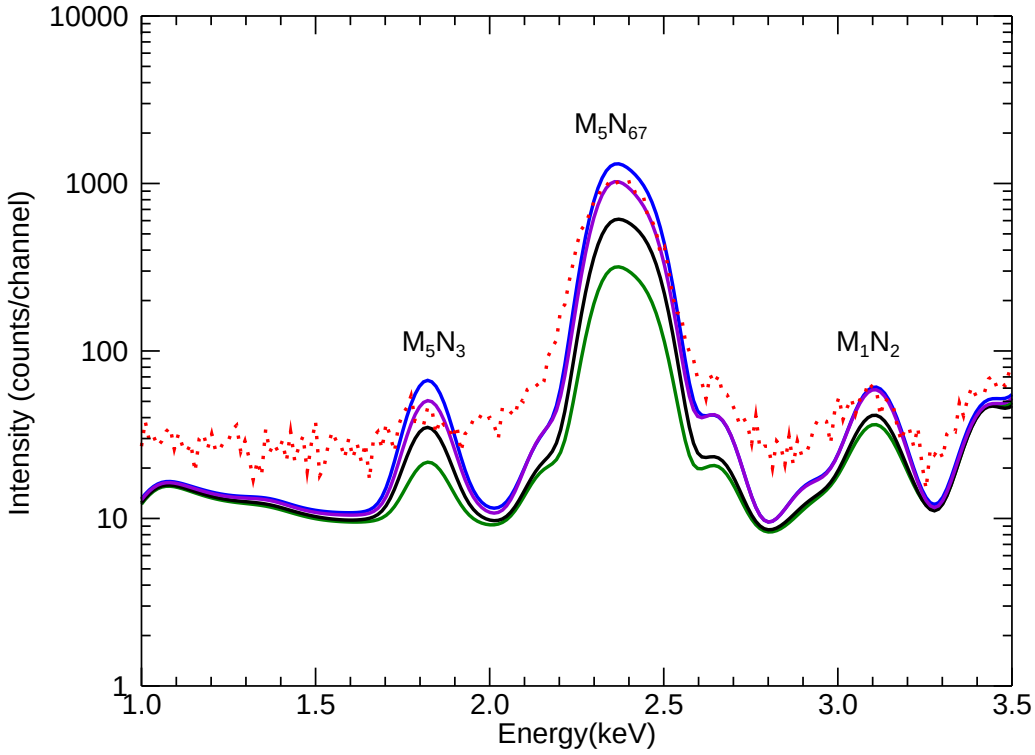

Figure 5.13: Pb-*M* lines of NIST SRM 1132 detail featuring experimental data (red dots), simulation with full cascade (blue), simulation without cascade (green), simulation with radiative cascade (black) and simulation with non-radiative cascade (violet)

interactions with the collimator that contained Ta and Pb. These interactions were not taken into account by the simulation. The In L-lines are situated on the top of the large Compton escape peak caused by the high energy photons impinging on the detector. As can be seen in Fig. 5.16, there is very good agreement between simulation and experiment concerning the L-lines. Again, it is clear that the cascade effects are considerable and should not be neglected. In this case, the largest cascade contributions are due to In K radiative transitions. This can be attributed to the high fluorescence yield of the In K shell (84.8 %). The line intensities of the most important In L lines are tabulated in Table 5.4. It can be seen that the L_1 lines receive no contribution from the radiative cascades, which is due to the absence of In KL_1 transitions (multipole type). This causes the line ratio

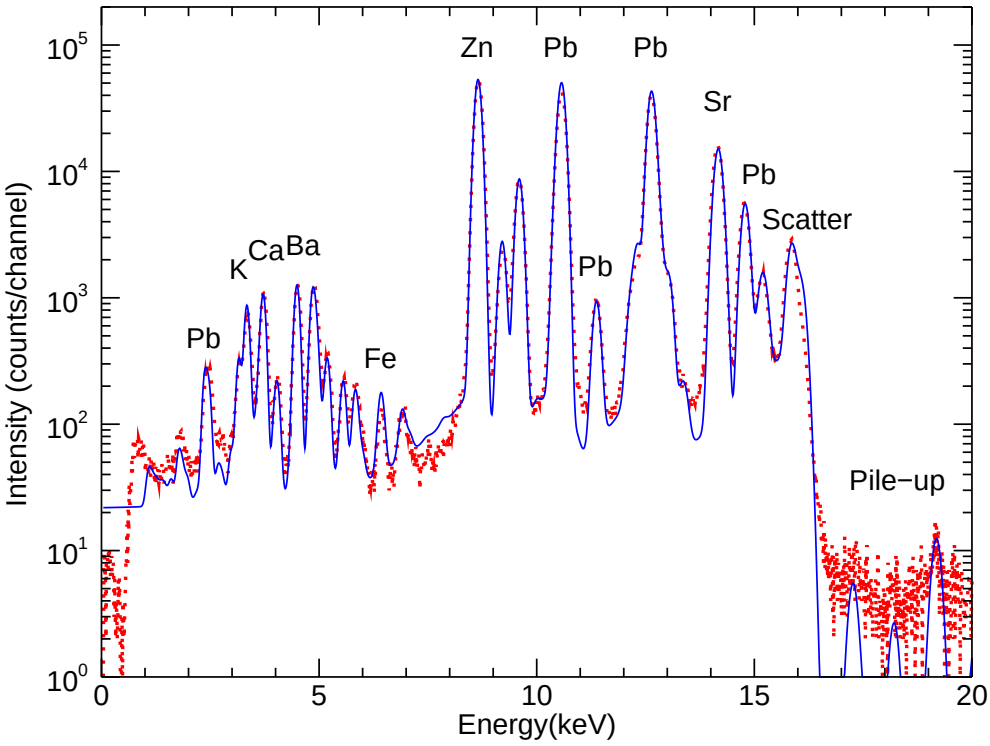

Figure 5.14: Experimental (red) and simulated (blue) spectra of NIST SRM 1412.

to change: the L_3M_{45} lines become considerably more intense if compared to the second highest peak, which is made up of the overlapping L_1M_3 and L_2M_4 lines.

5.8 Conclusions

In this chapter, a Monte Carlo simulation procedure aimed at the prediction of the spectral response of a general ED-XRF spectrometer is described. Essentially, it constitutes a major overhaul of the work of Vincze et al.[5–8]. A number of new features such as the simulation of M-lines, cascade effects and pulse pile-up were introduced, and a new set of physical constants (cross-sections, fluorescence/Coster-Kronig yields, transition probabilities etc.) was implemented. The validation of the new features was performed by verifying the code predictions on a number of standard reference materials. Future work will focus

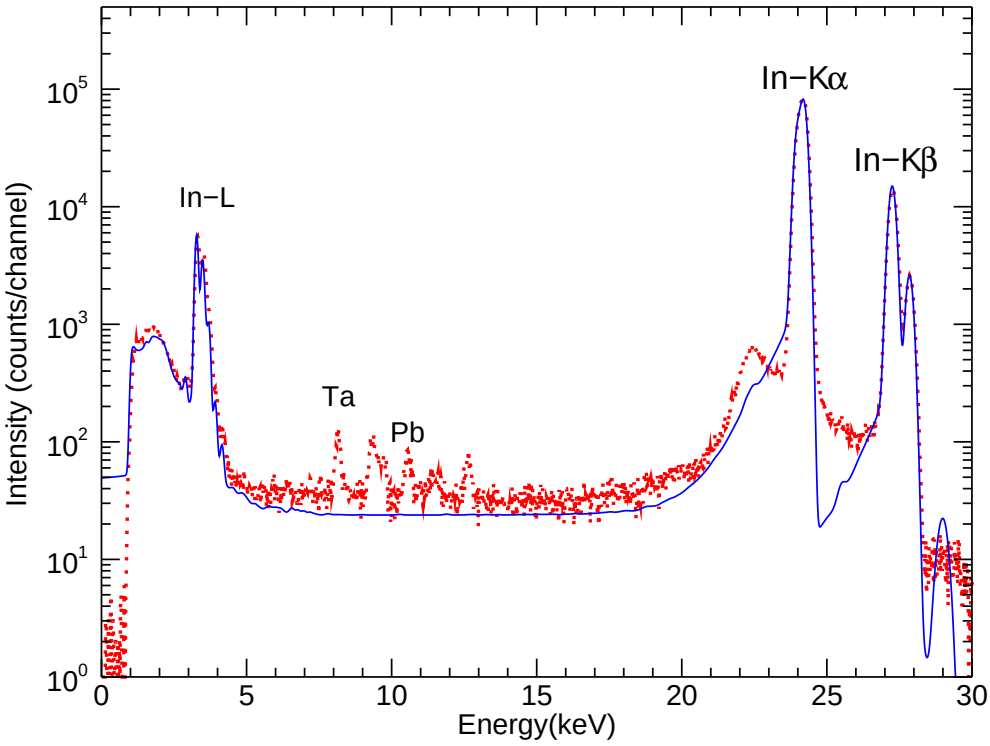

Figure 5.15: Experimental (red) and simulated (blue) spectra of an In foil.

on the modeling of the detector response function and on the incorporation of electron-matter interactions, which are necessary for the simulation of Bremsstrahlung and impact-ionization. In the next chapter, the possibility of using the code in an inverse way will be discussed, turning it in an efficient tool for the quantification of ED-XRF datasets. The *XMI-MSIM* package is released under the GNU General Public License and can be obtained freely from `http://github.com/tschoonj/xmimsim`.

Bibliography

[1] M. Czyzycki, D. Wegrzynek, P. Wrobel, A. Lankosz, Monte carlo simulation code for confocal 3D micro-beam X-ray fluorescence analysis of stratified materials, X-Ray Spectrom. 40 (2011) 88–95.

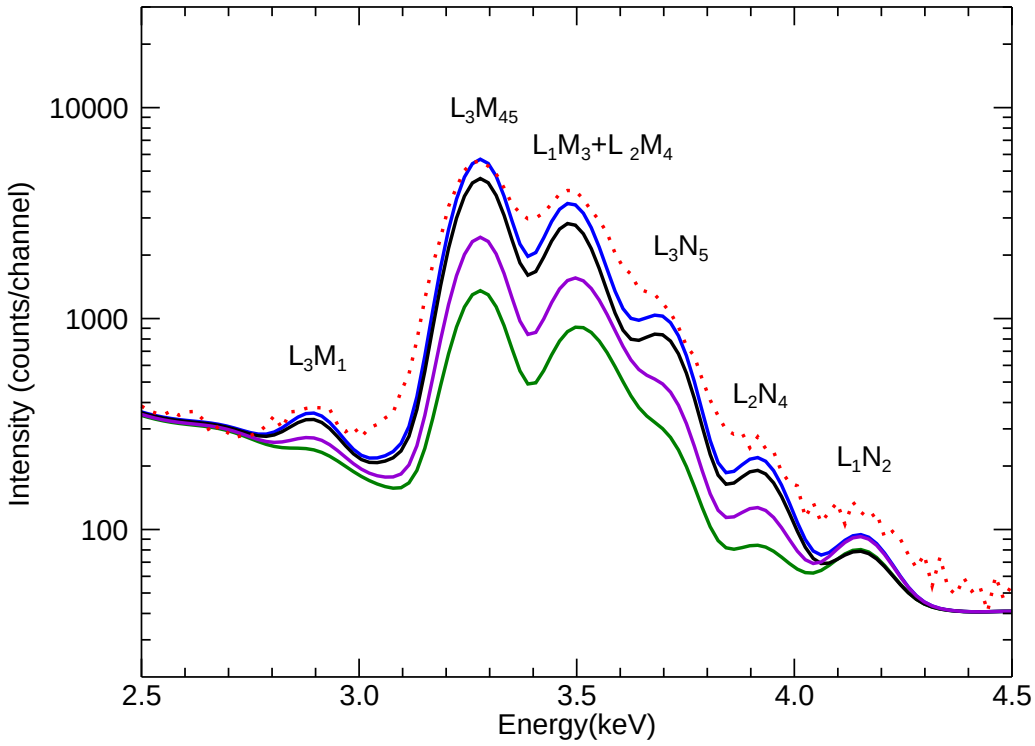

Figure 5.16: In L lines of In foil detail featuring experimental data (red dots), simulation with full cascade (blue), simulation without cascade (green), simulation with radiative cascade (black) and simulation with non-radiative cascade (violet)

[2] V. Scot, J. E. Fernandez, L. Vincze, K. Janssens, 3D extension of the Monte Carlo code MCSHAPE for photon-matter interactions in heterogeneous media, Nucl. Instrum. Methods Phys. Res., Sect. B 263 (2007) 204–208.

[3] J. E. Fernandez, V. Scot, Self-enhancement effects on XRF K-lines due to natural width, X-Ray Spectrom. 38 (2009) 175–181.

[4] U. Bottigli, A. Brunetti, B. Golosio, P. Oliva, S. Stumbo, L. Vincze, P. Randaccio, P. Bleuet, A. Simionovici, A. Somogyi, Voxel-based Monte Carlo simulation of X-ray imaging and spectroscopy experiments, Spectrochim. Acta Part B 59 (2004) 1747–1754.

Table 5.4: Simulated intensities of some selected In L-lines, obtained with or without considering the contribution of radiative and/or non-radiative cascades

XRF-line	No cascade	Radiative cascade	Non-radiative cascade	Full cascade
L_3M_5	9541	34394	13024	42632
L_2M_4	4984	22050	10070	27141
L_3N_5	1612	5722	2972	7084
L_1M_3	2347	2342	3287	3282
L_2N_4	265	1217	550	1502
L_3M_1	253	924	476	1147
L_1N_2	105	105	150	149

[5] L. Vincze, K. Janssens, F. Adams, A general Monte-Carlo simulation of Energy-Dispersive X-ray-Fluorescence Spectrometers .1. Unpolarized radiation, Homogeneous samples, Spectrochim. Acta Part B 48 (1993) 553–573.

[6] L. Vincze, K. Janssens, F. Adams, M. Rivers, K. W. Jones, A general Monte Carlo simulation of ED-XRF spectrometers. II: Polarized monochromatic radiation, homegeneous samples, Spectrochim. Acta Part B 50 (1995) 127–147.

[7] L. Vincze, K. Janssens, F. Adams, K. W. Jones, A general Monte Carlo simulation of energy-dispersive X-ray fluorescence spectrometers. Part 3. Polarized polychromatic radiation, homogeneous samples, Spectrochim. Acta Part B 50 (1995) 1481–1500.

[8] L. Vincze, K. Janssens, B. Vekemans, F. Adams, Monte Carlo simulation of X-ray fluorescence spectra: Part 4. Photon scattering at high X-ray energies, Spectrochim. Acta Part B 54 (1999) 1711–1722.

[9] S. Agostinelli, J. Allison, K. Amako, J. Apostolakis, H. Araujo, P. Arce, M. Asai, D. Axen, S. Banerjee, G. Barrand, F. Behner, L. Bellagamba, J. Boudreau, L. Broglia, A. Brunengo, H. Burkhardt, S. Chauvie, J. Chuma, R. Chytracek, G. Cooperman, G. Cosmo, P. Degtyarenko, A. Dell'Acqua, G. Depaola, D. Dietrich, R. Enami, A. Feliciello, C. Ferguson, H. Fesefeldt, G. Folger, F. Foppiano, A. Forti, S. Garelli, S. Giani, R. Giannitrapani, D. Gibin, J. Cadenas, I. Gonzalez, G. Abril, G. Greeniaus, W. Greiner, V. Grichine, A. Grossheim, S. Guatelli, P. Gumplinger, R. Hamatsu,

K. Hashimoto, H. Hasui, A. Heikkinen, A. Howard, V. Ivanchenko, A. Johnson, F. Jones, J. Kallenbach, N. Kanaya, M. Kawabata, Y. Kawabata, M. Kawaguti, S. Kelner, P. Kent, A. Kimura, T. Kodama, R. Kokoulin, M. Kossov, H. Kurashige, E. Lamanna, T. Lampen, V. Lara, V. Lefebure, F. Lei, M. Liendl, W. Lockman, F. Longo, S. Magni, M. Maire, E. Medernach, K. Minamimoto, P. de Freitas, Y. Morita, K. Murakami, M. Nagamatu, R. Nartallo, P. Nieminen, T. Nishimura, K. Ohtsubo, M. Okamura, S. O'Neale, Y. Oohata, K. Paech, J. Perl, A. Pfeiffer, M. Pia, F. Ranjard, A. Rybin, S. Sadilov, E. Di Salvo, G. Santin, T. Sasaki, N. Savvas, Y. Sawada, S. Scherer, S. Seil, V. Sirotenko, D. Smith, N. Starkov, H. Stoecker, J. Sulkimo, M. Takahata, S. Tanaka, E. Tcherniaev, E. Tehrani, M. Tropeano, P. Truscott, H. Uno, L. Urban, P. Urban, M. Verderi, A. Walkden, W. Wander, H. Weber, J. Wellisch, T. Wenaus, D. Williams, D. Wright, T. Yamada, H. Yoshida, D. Zschiesche, GEANT4–a simulation toolkit, Nucl. Instrum. Methods Phys. Res., Sect. A 506 (2003) 250–303.

[10] S. Guatelli, A. Mantero, B. Mascialino, P. Nieminen, M. G. Pia, Geant4 Atomic Relaxation, IEEE Trans. Nucl. Sci. 54 (2007) 585–593.

[11] S. Guatelli, A. Mantero, B. Mascialino, M. G. Pia, V. Zampichelli, Validation of Geant4 atomic relaxation against the NIST physical reference data, IEEE Trans. Nucl. Sci. 54 (2007) 594–603.

[12] J. Hendricks, K. Adams, T. Booth, J. Briesmeister, L. Carter, L. Cox, J. Favorite, R. Forster, G. McKinney, R. Prael, Present and future capabilities of MCNP, Appl. Radiat. Isot. 53 (2000) 857–861.

[13] T. Trojek, T. Cechak, Use of MCNP code in energy dispersive X-ray fluorescence, Nucl. Instrum. Methods Phys. Res., Sect. B 263 (2007) 72–75.

[14] J. Baro, J. Sempau, J. Fernandez-Varea, F. Salvat, PENELOPE - An algorithm for Monte-Carlo simulation of the penetration and energy-loss of electrons and positrons in matter, Nucl. Instrum. Methods Phys. Res., Sect. B 100 (1995) 31–46.

[15] J. Sempau, E. Acosta, J. Baro, J. FernandezVarea, F. Salvat, An algorithm for Monte Carlo simulation of coupled electron-photon transport, Nucl. Instrum. Methods Phys. Res., Sect. B 132 (1997) 377–390.

[16] X. Llovet, J. Fernandez-Varea, J. Sempau, F. Salvat, Monte Carlo simulation of X-ray emission using the general-purpose code PENELOPE, Surf. Interface Anal. 37 (2005) 1054–1058.

[17] M. Galassi, J. Davies, J. Theiler, B. Gough, G. Jungman, P. Alken, M. Booth, F. Rossi, GNU Scientific Library Reference Manual, Network Theory Ltd., third edition, 2009.

[18] R. Bader, A Fortran binding for the GNU Scientific Library, SIGPLAN Fortran Forum 26 (2007) 4–11.

[19] M. Matsumoto, T. Nishimura, Mersenne twister: a 623-dimensionally equidistributed uniform pseudorandom number generator, ACM Trans. Modelling Comput. Simulation 8 (1998) 3–30.

[20] The HDF Group, Hierarchical data format version 5, `http://www.hdfgroup.org/HDF5`, 2000-2011.

[21] W. Bambynek, C. Swift, B. Crasemann, H.-U. Freund, P. V. Rao, R. Price, H. Mark, R. Fink, X-Ray-fluorescence yields, Auger, and Coster-Kronig transition probabilities, Rev. Mod. Phys. 44 (1972) 716–813.

[22] S. Reed, N. Ware, Escape peaks and internal fluorescence in X-ray spectra recorded with lithium drifted silicon detectors, Journal of Physics E-Scientific Instruments 5 (1972) 582–584.

[23] T. He, R. Gardner, K. Verghese, An improved Si(Li) detector response function, Nucl. Instrum. Methods Phys. Res., Sect. A 299 (1990) 354–366.

[24] R. Gardner, S. Lee, Monte Carlo simulation of pulse pile up, Advanced X-ray Anal 41 (1999) 941–950.

[25] F. Scholze, M. Procop, Modelling the response function of energy dispersive X-ray spectrometers with silicon detectors, X-Ray Spectrom. 38 (2009) 312–321.

[26] T. Schoonjans, A. Brunetti, B. Golosio, M. Sanchez del Rio, V. A. Solé, C. Ferrero, L. Vincze, The xraylib library for X-ray—matter interactions. Recent developments, Spectrochim. Acta Part B (2011). In press, doi:10.1016/j.sab.2011.09.011.

Chapter 6

A general Monte Carlo simulation of energy-dispersive X-ray fluorescence spectrometers – Quantification through iterative simulations

6.1 Introduction

X-ray fluorescence (XRF) has been used for several decades for the analysis of samples coming from a wide range of sources such as archaeology, biology, medicine, art, outer space etc[1–7].These analyses may be performed using single point measurements or scans (one, two or three dimensional). Typically, such datasets are evaluated using dedicated software such as AXIL[8] or PyMca[9], which allow for the computation of the net-line intensity of the XRF peaks in the spectra. It is however not possible to obtain quantitative information directly from such measurements based on extracting the net-line intensities only. This is due to the fact that the fitting routines that produce the net-line intensities typically only take into account the detector peak broadening and detector artefacts such as escape peaks and pile-up, and ignore the physical processes that occur in the sample itself such as the XRF generation and its attenuation. However, these can be taken into account by applying the fundamental parameter method[10] (FPM) to the net-line intensities. This method relies on the relation between the net-line intensity of a particular XRF line (usually

K_α or L_α) of an element and its corresponding weight fraction. It takes into account the attenuation of incoming X-ray beam, the production of the fluorescence in the sample and the attenuation of the outgoing fluorescence photons as they propagate towards the detector. In its standard (reference-free) form, the FPM requires the availability of XRF production cross sections (see Chapter 3) and geometric parameters in order to perform the quantification. Often, their usage may be circumvented through the measurement of a standard reference material (SRM), whose net-line intensities will be compared to those of the specimen with unknown composition, thereby canceling out the XRF production cross section and geometric factor. The FPM introduces a number of simplifications which make the method unsuitable for the quantification of specific samples. Most importantly, the method ignores all higher order interactions, i.e. it does not take into account the fact that the fluorescence photons may interact in the sample and thereby give rise to additional fluorescence production. Extensions to the standard FPM that allow for second and third order interactions exist but make implementations considerably more complicated[11].

In this chapter, an alternative methodology to the quantification of XRF spectral data involving Monte Carlo simulations will be discussed. Monte Carlo algorithms have been used for several decades to predict the spectral response for (energy-dispersive) XRF spectrometers[12–17]. Their popularity can be explained by the fact that they have the potential to include essentially all physical phenomena that may occur during the complex trajectories of the photons. In order to apply Monte Carlo simulations as a quantification tool, they have to be applied in an 'inverse' manner using an iterative algorithm. We will present our implementation of such an algorithm, based on our recently developed Monte Carlo simulation tool for ED-XRF spectrometers[17], combined with a number of examples, demonstrating its usefulness. Our tool has been developed as a plug-in to PyMca[9], a popular open-source package for the analysis of ED-XRF spectra, in which it can be invoked as an alternative for the default FPM based quantification method.

6.2 Experimental

The quantification procedure that will be discussed in the next section was verified using spectral data recorded at the beamline L of the HASYLAB synchrotron facility (Hamburg, Germany) corresponding to a number of standard reference materials (SRM) purchased

from the National Institute of Standards and Technology (NIST) and well-characterized reference foils obtained from Goodfellow. The samples were irradiated using an unfocused beam of which the dimensions were reduced by means of slits. The monochromaticy of the beam was achieved through a multilayer monochromator with a 1% energy bandwidth. The fluorescence radiation was collected with a Vortex silicon drift detector (Si crystal thickness = 350 μm, 50 mm^2 active detector area), equipped with a conical collimator (1 cm height, 2 mm opening diameter), positioned at 2.1 cm from the sample surface. In order not to overload the detector, the beam intensity was reduced by positioning a 1 mm Al absorber in the beam path.

6.3 Algorithm description

6.3.1 Principle of the Monte Carlo simulation model

The quantification tool is driven by the invocation of a series of Monte Carlo algorithms that model photon–matter interactions, thereby simulating the fate of individual photons, from the point where they impinge on the sample with a certain direction energy and polarization to the point where they are either absorbed by the sample atom or emerge from the specimen, and are optionally detected. The trajectory of each photon is modeled as consisting of a number of straight steps. At the end of each step, an interaction with a particular type of sample atom occurs. The simulation operates in the 1 to 100 keV energy range in which three interaction types are considered: photoelectric effect, coherent (Rayleigh) and incoherent (Compton) scattering. Depending on the type of interaction, the energy and/or direction is changed. At the i-th interaction, the change in direction is described by the polar scattering angle θ_i and the azimuthal angle ϕ_i in the frame of reference attached to the photon. The selection of these angles is performed on the basis of pre-calculated inverse cumulative distribution functions that are based on the differential scattering cross sections. The atom type with which an interaction occurs, the distance between interactions and the type of interaction taking place are chosen by means of uniform random numbers, produced by a Mersenne twister random number generator. In order to increase the speed of the calculations as well as to decrease the noise level of the simulated spectra, variance reduction techniques were employed extensively. The model takes into account cascade effects, M-lines, detector pulse pile-up and escape peaks

(fluorescence and Compton). For a full description, see Chapter 5.

6.3.2 Quantification procedure

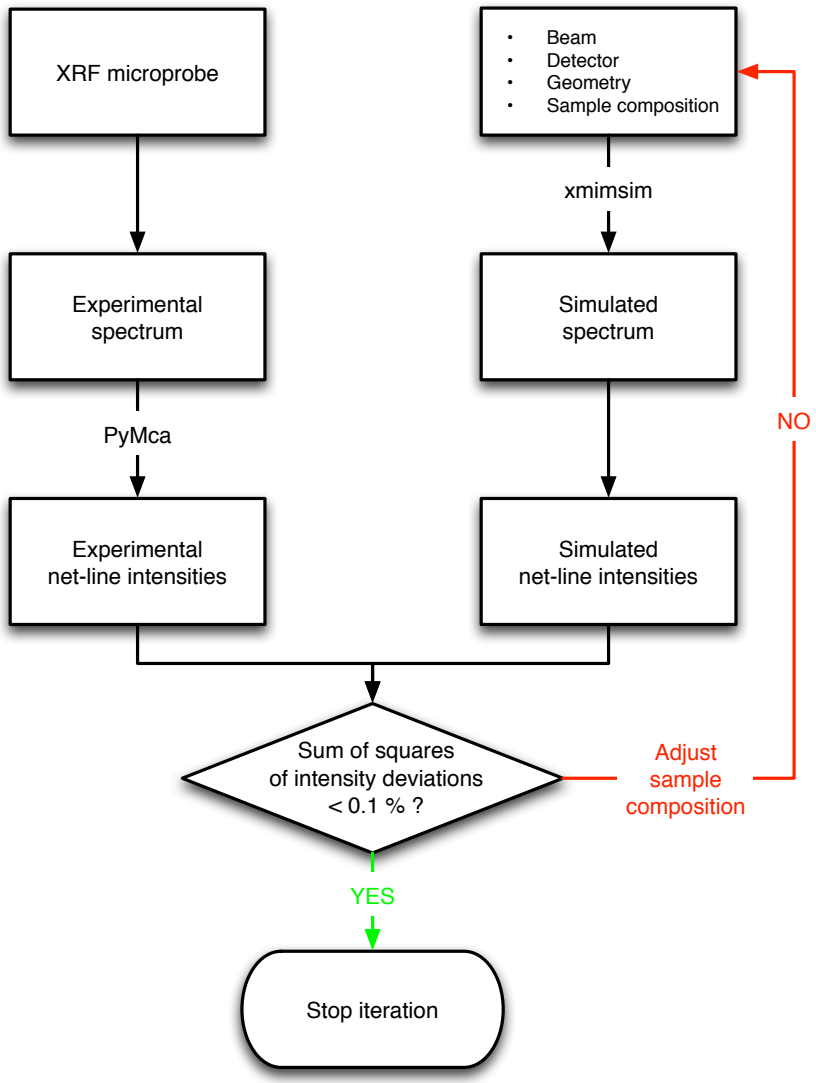

Figure 6.1: Flowchart describing the algorithm used in our inverse Monte Carlo simulation based quantification method.

The actual quantification procedure can be broken down into several distinct stages, as can be seen in Fig. 6.1. Firstly, the user sets up the fitting parameters using the 'Advanced Fitting' interface of PyMca. These include:

fitting parameters: fitting model, background algorithm, peak shape parameters etc.

detector parameters: gain, zero noise, Fano factor, pile-up factor, detector crystal.

source parameters: excitation spectrum (monochromatic or polychromatic), flux, live time

XRF line selection: XRF lines that will be considered by the fitting algorithm. Depending on the selected element, K-, L- and M-lines may be enabled for the fit. The user has the option to decide whether the ratio between line groups is fixed according to transition probabilities (K-lines) or XRF cross sections (L-lines) or allowed to vary.

X-ray attenuators: beamfilters, detector window, atmosphere, etc.

matrix composition: in many cases, the quantification will be performed on samples with a non-fluorescent matrix. The user is required to define the matrix composition (n_{loi} elements each with a weight $w_{i,loi}$) , density and thickness. This step is essential since it allows the Monte Carlo routines to correctly estimate the absorption. The sample may be composed of up to 10 layers, one of which (layer of interest) will be quantified while the other layers have constant compositions.

detector parameters: active area, distance between sample and detector.

Next, the spectrum is fitted according to these parameters yielding the net-line intensities I_j^{exp} that are required for comparison with their simulated counterparts. In the case of K-lines, the code uses the KL_2 and KL_3 lines while the L-lines are compared using the L_3M_4 and L_3M_5 lines. It must be noted at this point that the success of the quantification will be largely dependent on the quality of the fit. Poorly fitted peaks will lead to unreliable net-line intensities, which in turn will lead to incorrectly calculated concentrations, not just for those elements whose peaks were fitted improperly, but possibly (all) other elements as well. The output file that is created through this method, is further modified through an interface dealing with the additional information that is required by the Monte Carlo routine such as degree of linear polarization (important for the correct simulation of scatter peaks), beam size and profile, distance between source and sample. This file is then sent to the quantification executable which will first parse the output file and then determine which elements can be quantified by the program. This determination is performed based on three criteria:

1. The K_α or L_α intensity of the element under scrutiny has to be strictly positive.
2. The element cannot be part of the matrix composition.
3. The element cannot be part of any of the other layers in the system e.g. atmosphere.

In the initial simulation, the selected elements will be assigned a default elemental weight $w_j^{(0)}$ of 100 ppm, while the composition of the layer of interest will be adjusted according to the matrix composition in order for the sum of the weight fractions to be equal to 100 %. As output, the Monte Carlo simulation produces not just the spectrum, but also the net-line intensities $I_j^{(0)}$ of the different lines of the simulated elements. In turn, these intensities are used to adjust the current estimate of the elemental weights according to:

$$w_j^{(n)} = w_j^{(n-1)} \times \frac{I_j^{(exp)}}{I_j^{(n-1)}} \tag{6.1}$$

where $c_j^{(n)}$ is the n-th estimate of the weight fraction of element j. These estimates are subsequently used as input for a new iteration of the Monte Carlo simulation. The iterative algorithm stops when convergence is reached, i.e. when the sum of the squares of the intensity deviations drops below a certain threshold (default value is 0.1 %). If no convergence is reached after 100 iterations, the algorithm will exit with an error message. Such a situation may present itself when one or more of the input parameters were incorrectly defined, e.g. an underestimated X-ray beam flux. Care was taken to deal with situations where the sum of the quantifiable elements would exceed 100 %, which is possible when the major constituent elements are being quantified. Since the first iteration starts with a very low value, elements with a high actual weight fraction would see their current estimate increase by a very large factor, producing (unrealistically) high weight fractions. This can be explained by the fact that the major elements determine the self-absorption behavior of the analyzed specimen, which is strongly dependent on the weight fractions of these elements. We circumvented this issue through two interventions in the algorithm. Firstly, if the user performs within PyMca a FPM based quantification after the fit, then these results will be used as starting values for the elemental weight fractions instead of the low default value, leading to a more realistic initial representation of the actual sample. Since this will also reduce the number of iterations, convergence will be achieved faster thereby reducing the computational time. A second modification involves the introduction of safeguards in the code that monitor the evolution of the intensity ratio $\frac{I_j^{(exp)}}{I_j^{(n-1)}}$ with respect to

the weight fraction $w_j^{(n-1)}$. This allows the iterative process to adapt in a slow but stable manner to the increasing weight fractions of the major elements in between iterations.

Perhaps the most important parameter in the algorithm is the incident X-ray beam flux. Although essential to the quantification algorithm it is usually only approximately known. This is due to the fact that the flux is determined not only by the source (which may vary with time, e.g. synchrotron), but also by the optics of the system and the atmospheric absorption. It must, however, be known accurately since the fluorescence line intensities are linearly proportional to its value, leading to uncertainties propagating into the quantification results. A possible solution that can be applied in some cases has been implemented in our software, based on the Rayleigh scatter peak. If this peak is fitted by PyMca, then this intensity may be used to normalize the simulated spectra by varying the photon flux along with the weight fractions of the elements in the layer of interest. However, our experience has shown that great care has to be taken when applying this optional feature. First of all, the Rayleigh peak has to be clearly defined, meaning that there should be no overlap with the Compton scatter peak or fluorescence lines. In particular the Compton peak poses a problem here, since PyMca currently fits this peak as a mere Gaussian peak, thereby ignoring the typical wide shape of such peaks caused by a combination of Doppler broadening and multiple scattering[18]. This reduces the applicability of this method to experiments where a relatively high excitation energy was used (either monochromatic energy or discrete lines of an X-ray tube). Another issue arises when the exciting beam is monochromatized by a multilayer monochromator: such monochromators produce a pink beam with a relatively high bandwidth. As in the case of the Compton peaks, PyMca fits the Rayleigh peaks as Gaussians assuming their linewidth is determined merely by the detector resolution, thereby underestimating the intensity.

Although implemented in our code as an option, the authors recommend its use only in cases when the previously mentioned issues are not a concern. As a more general protocol, we advise the following procedure:

1. Measure a standard reference material (SRM) under the exact same conditions (geometry and excitation energy) as the unknown samples. Preference should be given to SRMs that produce a clearly defined Rayleigh scatter peak.

2. Use the forward Monte Carlo simulation tool to estimate the flux, and in the case of

polarized beams, the degree of linear polarization. The former can be accomplished by adapting the flux until the intensity of the most intense fluorescence line in the experimental spectrum corresponds to its simulated counterpart. The latter may be calculated using the method in Vincze et al.[16].

3. If the measurements of the unknown specimens occur at a different flux, e.g. due to the changing storage ring current, then the readout of an ionization chamber should be used to scale the flux to the correct value.

The weight fractions that are obtained this way may be verified by comparing the simulated spectrum with its experimental counterpart, thereby serving as a visual confirmation of the quantification results.

6.4 Results and discussion

In this section some results will be shown that were obtained using our Monte Carlo based quantification method. For each of the test samples from the validation set, results will be presented for 10 quantification runs, along with the average and standard deviation of the weight fraction of each element. The scatter based normalization feature was not enabled during the quantification procedure. In the Advanced Fitting dialog of PyMca, the following fit parameters were enabled for all examples:

- Fit Function: Mca Pseudo-Voigt
- Continuum type: Linear polynomial
- Escape peaks and Pile-up enabled
- Attenuators: atmosphere, Be detector window, Al beamfilter, Si detector crystal and matrix (composition depending on sample)
- Incoming and take-off angles set to 45° with respect to the sample normal vector

All quantifications were performed 10 times. The tables in the following sections contain the mean quantification values, along with standard deviation and relative standard deviation.

6.4.1 Multicomponent glass NIST SRM 1412

The first reference sample used to demonstrate our quantification procedure is the multicomponent glass NIST SRM 1412. The experimental data was acquired by irradiating the 3.2 mm thick sample using a beam with a cross section of 60×60 μm^2 at 16.034 keV for 1500 s real time. Since this standard contains Sr, which has a K-shell edge energy of 16.105 keV, only the fraction of the Gaussian excitation profile above this energy is able to excite the Sr K-shell. The mean value of the excitation profile had to be calculated very precisely (at the eV level) since even small variations would cause a large shift in the Sr K intensities. The specimen was assumed to have an initial matrix composition consisting of Si and O in a 1:3 ratio. Since the certificate of this SRM contains a number of elements

Table 6.1: Results of quantitative analysis of NIST SRM 1412 Multicomponent glass. Concentrations are given in weight %. Values in parentheses are for information only.

Element	Certified (%)	Calculated (%)	Standard deviation (%)	Rel. standard deviation (%)	d(%)
O	–	47.61	0.21	0.43	–
Si	19.81	27.83	0.11	0.38	40.5
K	3.44	3.26	0.016	0.49	-5.1
Ca	3.24	3.17	0.017	0.52	-2.0
Fe	(217) ppm	220 ppm	1 ppm	0.58	1.3
Zn	3.60	3.63	0.021	0.58	0.9
Sr	3.85	3.97	0.030	0.75	3.2
Cd	3.83	2.85	0.014	0.49	-25.7
Ba	4.18	4.27	0.023	0.55	2.0
Pb	4.08	3.38	0.023	0.68	-17.3

(Al, Mg, Na, Li, B) that were not detected, it is assumed that the final result of Si and O includes the weight fractions for these elements as well. The quantification results are summarized in Table 6.1, while the experimental spectrum is shown in Fig. 6.2, along with the PyMca fitted and simulated curves. Apart from the large deviation for Si, considerable differences with the NIST certified weight fractions can be seen for Pb and Cd. The deviation for Pb may be related to inaccurate XRF production cross sections for the Pb

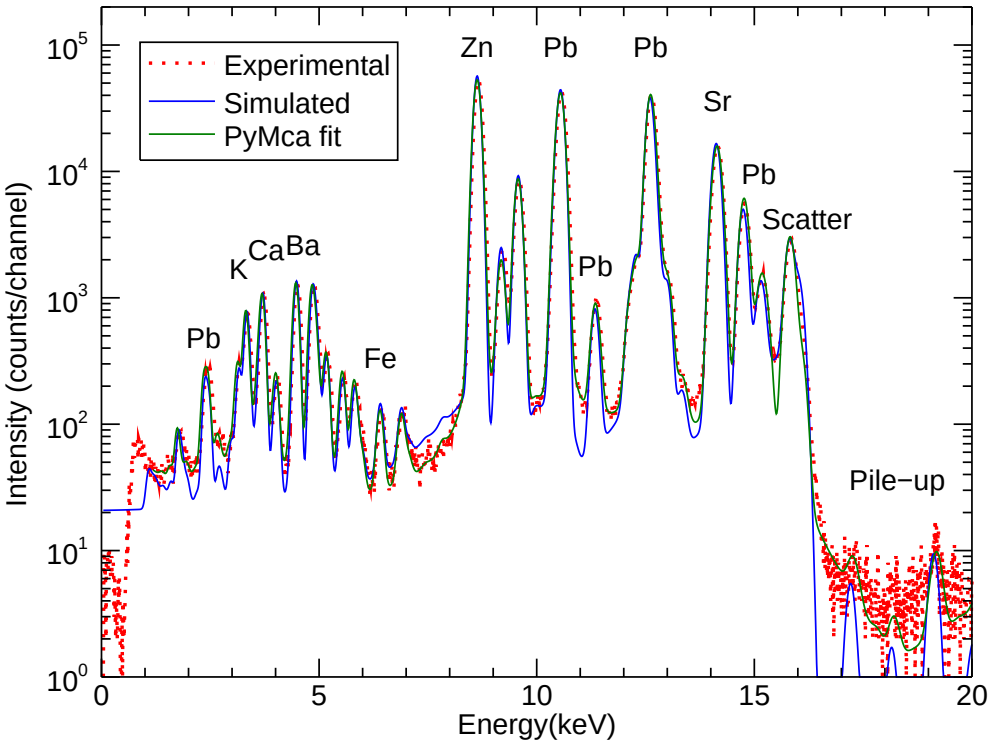

Figure 6.2: Experimental, fitted and simulated spectra of NIST SRM 1412 Multicomponent Glass.

L-lines, while in the case of Cd, the difference can be attributed to the weak intensity of the Cd L-lines, leading to an unreliable fit and thus, a poor quantification result for this particular element. This discrepancy may also be attributed to local inhomogeneities: since the measurement was performed on a single spot with a micro-beam, it is possible that the irradiated area corresponded with a zone depleted of Pb.

6.4.2 Stainless steel NIST SRM 1155

A second sample whose composition was examined concerns the stainless steel standard NIST SRM 1155. The experimental data was collected using a 16 keV beam with dimensions 10×10 μm^2 over 300 s real time. This particular sample is very well suited for demonstrating the advantages of an Monte Carlo based quantification method over tradi-

tional FPMs, since the detected line intensities of Cr and Fe are very strongly influenced by higher order interactions leading to enhancement of these lines, an effect usually ignored by the latter. In the previous chapter, we have demonstrated that up to 40 % of the Cr intensity is caused by enhancement effects from Fe and Ni K-lines. The quantification was performed assuming a Mo matrix which, according to the NIST certificate, is present at 2.26 weight % in the standard, but is not present in the spectrum because the excitation energy did not allow for the generation of Mo K-lines and because the Mo L-lines were too weak in intensity for proper detection. As in the case of SRM 1412, this standard too contains a number of elements, apart from Mo, that were not detected in the experiment, either because they were present in too low concentrations, because they had unfavorable XRF cross sections and/or because the produced XRF signal was absorbed before reaching the detector unit. These elements include: C, S, V, P, Si, Bi and N. The quantification

Table 6.2: Results of quantitative analysis of NIST SRM 1155 Stainless Steel. Concentrations are given in weight %. Values marked with † are not certified but reference only, while those values that are marked with ⋆ are informative only.

Element	Certified (%)	Calculated (%)	Standard deviation (%)	Rel. standard deviation (%)	d(%)
Cr	18.37	18.51	0.15	0.84	0.78
Mn	1.619	1.85	0.011	0.59	14.6
Fe	–	64.96	0.28	0.43	–
Co	0.109†	0.38	0.0015	0.41	248
Ni	12.35	12.07	0.082	0.68	-2.2
Cu	0.175	0.19	0.0012	0.61	9.9
As	107 ppm†	90 ppm	$<$ 1 ppm	0.49	-16.1
Mo	2.26†	1.88	0.44	23.28	-16.8
W	0.11⋆	0.13	8 ppm	0.66	16.5
Pb	10 ppm⋆	60 ppm	$<$ 1 ppm	0.49	502.5

results are summarized in Table 6.2, while the experimental spectrum is shown in Fig. 6.3, along with the PyMca fitted and simulated curves. Overall there is good agreement with the NIST certified and reference values except for the case of Co which can be explained by

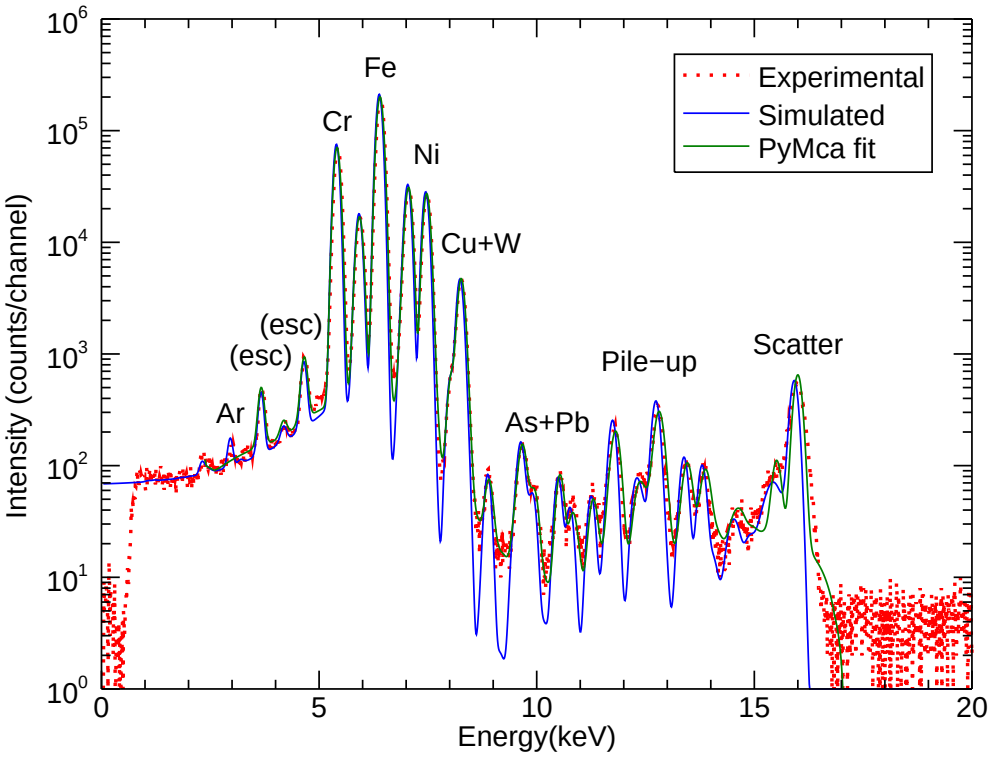

Figure 6.3: Experimental, fitted and simulated spectra of NIST SRM 1155 Stainless Steel.

the overlap of its lines with Fe KM_{23} and Ni KL_{23}, making a good fit virtually impossible, and by the large uncertainty (0.092 %) for this element, mentioned in the NIST certificate. The result of As is determined by the presence of Pb in the specimen: the overlap of the As KL_{23} and Pb L_3M_{45} lines strongly influences the fit of these lines and thus, their quantifications. The same statement applies to a lesser extent to the elements Cu and W.

6.4.3 Nickel silver Goodfellow

The final sample that will be discussed in this chapter concerns a so-called Nickel silver rod, purchased from Goodfellow. According to the manufacturer, this rod is composed of Cu (45 %), Zn (43 %), Ni (10 %) and Pb (2 %) with no uncertainties given. Because of this, the quantification of this specimen cannot be considered as a validation of our procedure, but should instead be seen as a typical practical application of it. As in the

previous case, considerable higher order interactions occur in this specimen: the Ni K-line production is enhanced by Zn K-lines and Cu KM_{23}, while the Cu K-lines are enhanced to a lesser extent by the Zn KM_{23} photons. The sample was irradiated under the same conditions as the NIST SRM 1155, except for the beam energy, which was tuned to 14 keV. The quantification results are summarized in Table 6.3, while the experimental spectrum

Table 6.3: Results of quantitative analysis of Nickel Silver rod, procured from Goodfellow. Concentrations are given in weight %. Values are informative only. The presence of Mn and Fe is not reported by the manufacturer.

Element	Certified (%)	Calculated (%)	Standard deviation (%)	Rel. standard deviation (%)	d(%)
Mn	–	0.19	4 ppm	0.002	–
Fe	–	0.17	3 ppm	0.002	–
Ni	10.0	10.12	0.03	0.003	1.20
Cu	45.0	46.57	0.05	0.001	3.48
Zn	43.0	41.66	0.06	0.001	-3.12
Pb	2.0	1.29	39 ppm	0.003	-35.31

is shown in Fig. 6.4, along with the PyMca fitted and simulated curves. Although Mo was used as matrix element, all quantifications finished without a remaining Mo weight fraction, indicating that the spectral response can be explained completely by the six quantified elements. From the results it can be seen that the rod contains two minor elements Fe and Mn, that are not reported by the manufacturer. The quantified weight fraction of Pb deviates significantly from the value presented by the manufacturer. This may be due either to a production error, or to a problem with the XRF cross sections of Pb L-lines, as was already encountered in the case of the NIST SRM 1412, or both.

6.5 Conclusions

In this chapter, we have demonstrated a quantification algorithm for ED-XRF data based on the application of Monte Carlo simulations in an inverse manner. Our implementation, which acts as a plug-in of the PyMca software package, offers the user an alternative

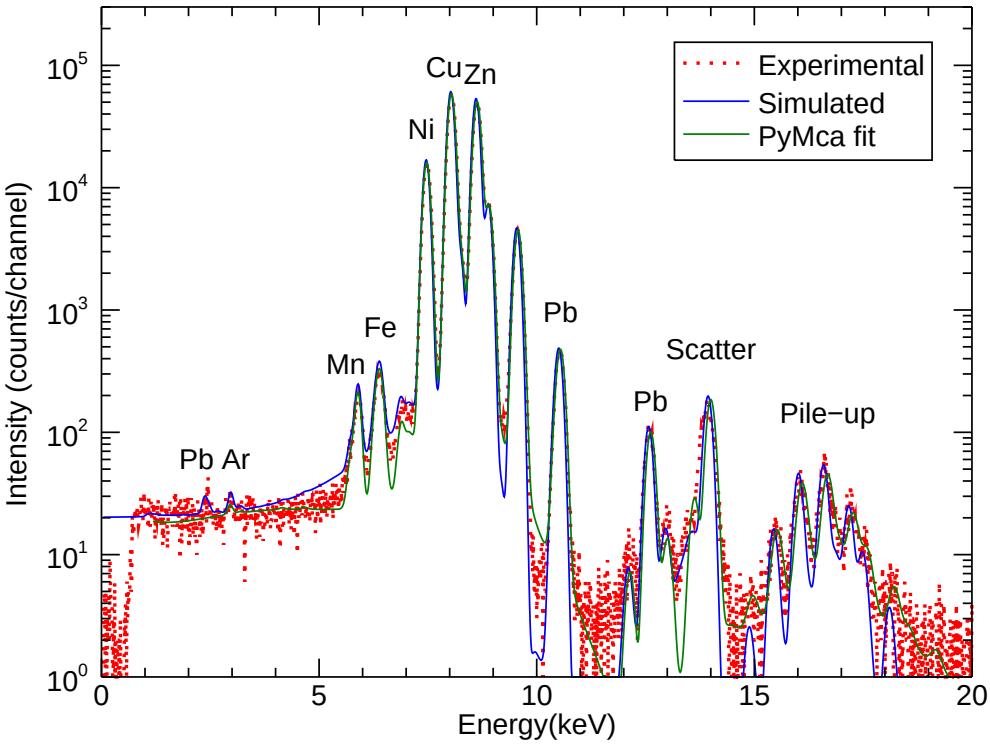

Figure 6.4: Experimental, fitted and simulated spectra of Goodfellow Nickel Silver rod.

to the commonly used FPM based methods. It was shown in our examples, that such methods cannot be used to quantify specimens that exhibit strong higher order effects. Another major advantage of our Monte Carlo based approach is the fact that it produces a simulated spectrum, including scatter peaks, which can be used for direct comparison with the experimental data, thereby serving as a visual confirmation of the success of the quantification.

Our tool has been implemented as part of the XMI MSIM package, using the ANSI C and Fortran 2003 programming languages. It can be downloaded freely from `http://github.com/tschoonj/xmimsim`, while PyMca can be obtained at `http://pymca.sourceforge.net`. Both software packages are released under the GNU General Public License.

Bibliography

[1] F. Brenker, L. Vincze, B. Vekemans, L. Nasdala, T. Stachel, C. Vollmer, M. Kersten, A. Somogyi, F. Adams, W. Joswig, J. Harris, Detection of a Ca-rich lithology in the Earth's deep (> 300 km) convecting mantle, Earth Planet. Sci. Lett. 236 (2005) 579–587.

[2] B. De Samber, G. Silversmit, K. De Schamphelaere, R. Evens, T. Schoonjans, B. Vekemans, C. Janssen, B. Masschaele, L. Van Hoorebeke, I. Szaloki, F. Vanhaecke, K. Rickers, G. Falkenberg, L. Vincze, Element-to-tissue correlation in biological samples determined by three-dimensional X-ray imaging methods, J. Anal. At. Spectrom. 25 (2010) 544–553.

[3] V. G. Mihucz, G. Silversmit, I. Szaloki, B. De Samber, T. Schoonjans, E. Tatar, L. Vincze, I. Virag, J. Yao, G. Zaray, Removal of some elements from washed and cooked rice studied by inductively coupled plasma mass spectrometry and synchrotron based confocal micro-X-ray fluorescence, Food Chem. 121 (2010) 290–297.

[4] S. Schmitz, F. E. Brenker, T. Schoonjans, B. Vekemans, G. Silversmit, L. Vincze, M. Burghammer, C. Riekel, In situ identification of a CAI candidate in 81P/Wild 2 cometary dust by confocal high resolution synchrotron X-ray fluorescence, Geochim. Cosmochim. Acta 73 (2009) 5483–5492.

[5] M. Alfeld, K. Janssens, J. Dik, W. de Nolf, G. van der Snickt, Optimization of mobile scanning macro-XRF systems for the in situ investigation of historical paintings, J. Anal. At. Spectrom. 26 (2011) 899–909.

[6] L. Vincze, B. Vekemans, F. Brenker, G. Falkenberg, K. Rickers, A. Somogyi, M. Kersten, F. Adams, Three-Dimensional Trace Element Analysis by Confocal X-ray Microfluorescence Imaging, Anal. Chem. 76 (2004) 6786–6791.

[7] B. Kanngiesser, I. Mantouvalou, W. Malzer, T. Wolff, O. Hahn, Non-destructive, depth resolved investigation of corrosion layers of historical glass objects by 3D Micro X-ray fluorescence analysis, J. Anal. At. Spectrom. 23 (2008) 814–819.

[8] B. Vekemans, K. Janssens, L. Vincze, F. Adams, P. Van Espen, Analysis of X-Ray-

Spectra by Iterative Least-Squares (AXIL) - New Developments, X-Ray Spectrom. 23 (1994) 278–285.

[9] V. A. Sole, E. Papillon, M. Cotte, P. Walter, J. Susini, A multiplatform code for the analysis of energy-dispersive X-ray fluorescence spectra, Spectrochim. Acta Part B 62 (2007) 63–68.

[10] J. Sherman, The theoretical derivation of fluorescent X-ray intensities from mixtures, Spectrochim. Acta (1955) 283–306.

[11] P. Van Dyck, S. Török, R. Van Grieken, Enhancement effect in X-ray fluorescence analysis of environmental samples of medium thickness, Anal. Chem. 58 (1986) 1761–1766.

[12] M. Czyzycki, D. Wegrzynek, P. Wrobel, A. Lankosz, Monte carlo simulation code for confocal 3D micro-beam X-ray fluorescence analysis of stratified materials, X-Ray Spectrom. 40 (2011) 88–95.

[13] V. Scot, J. E. Fernandez, L. Vincze, K. Janssens, 3D extension of the Monte Carlo code MCSHAPE for photon-matter interactions in heterogeneous media, Nucl. Instrum. Methods Phys. Res., Sect. B 263 (2007) 204–208.

[14] J. E. Fernandez, V. Scot, Self-enhancement effects on XRF K-lines due to natural width, X-Ray Spectrom. 38 (2009) 175–181.

[15] L. Vincze, K. Janssens, F. Adams, A general Monte-Carlo simulation of Energy-Dispersive X-ray-Fluorescence Spectrometers .1. Unpolarized radiation, Homogeneous samples, Spectrochim. Acta Part B 48 (1993) 553–573.

[16] L. Vincze, K. Janssens, F. Adams, M. Rivers, K. W. Jones, A general Monte Carlo simulation of ED-XRF spectrometers. II: Polarized monochromatic radiation, homegeneous samples, Spectrochim. Acta Part B 50 (1995) 127–147.

[17] T. Schoonjans, L. Vincze, V. A. Solé, M. Sanchez del Rio, P. Brondeel, G. Silversmit, K. Appel, C. Ferrero, A general Monte Carlo simulation of energy-dispersive X-ray fluorescence spectrometers – Part 5. Polarized radiation, stratified samples, cascade effects, M-lines, 2011. Submitted.

[18] M. Van Gysel, P. Lemberge, P. Van Espen, Description of Compton peaks in energy-dispersive x-ray fluorescence spectra, X-Ray Spectrom. 32 (2003) 139–147.

Chapter 7

Summary and conclusions

This work has focused on the development of quantification methods for X-ray fluorescence (XRF), a powerful tool for the chemical analysis of a wide variety of samples, at the bulk, micro and nano level. Two widely used methods were investigated in this dissertation: one focused on the use of the fundamental parameter method and another method using Monte Carlo simulations. Since both of these techniques rely extensively on a large set of physical parameters important for X-ray–matter interactions, such as interaction cross sections, line energies, edge energies, fluorescence yields etc., our work was initially directed towards finding a reliable and easy to use source of these parameters. Our search identified *xraylib*, a library written in ANSI C that provides convenient access to the aforementioned data as the most complete source of X-ray fundamental parameters. The development of this library, initially a collaboration between researchers of the University of Sassari (Sardinia, Italy) and the European Synchrotron Radiation Facility (ESRF, Grenoble, France), was continued by our group starting from 2008 and has resulted in about a dozen releases since. Numerous features were added in these releases, such as partial photoionization cross sections, Compton broadening profiles, cascade corrected XRF production cross sections, revised XRF line energies, M-shell Coster-Kronig transition probabilities, atomic level widths and more. On the software level, the installation script was rewritten enabling easy installations on all UNIX(-like) platforms, and in addition a software development kit was produced for the Windows platform. Furthermore, through the addition of language bindings for the Fortran 2003, IDL, Python, Perl, .NET and Java languages, the applicability of the library has been extended considerably.

The usefulness of the *xraylib* library was first exploited in our work on the fundamental parameter method. This method, relying on the relation between the net intensity of the XRF lines in a spectrum and the elemental concentrations, was adapted to accommodate the special case of confocal micro/nano XRF. Such a confocal XRF setup is obtained through the mounting of a polycapillary half-lens in front of the detector window, effectively reducing the probing volume and thereby enabling depth sensitive three-dimensional sample characterization. The required modifications for this particular technique are due to the specific characteristics of the polycapillary, such as its energy-dependent transmission efficiency and its energy-dependent acceptance. Our methodology for confocal XRF was applied to a unique dataset, obtained at the ID13 beamline of the ESRF from cometary dust particles returned by NASA's Stardust mission. The quantification of these spectra was combined with a thorough error estimation procedure, based on the use of Monte Carlo simulations, in which all parameters (spectra, weights, densities, thicknesses etc.) were varied according to their errors and standard deviations, leading to the generation of histograms of the error distributions.

Monte Carlo simulations were also used in the second quantification procedure that was studied in this work. Generally speaking, such simulations allow one to model a problem that is too complex to be solved in an analytical way, through random number generators and probability density functions that describe the different parameters of the system. In this case, Monte Carlo simulations were employed to model energy-dispersive XRF spectrometers. Based upon the work of Vincze et al., we have entirely rewritten the code base, called *XMI-MSIM*, in order to take advantage of recent computational advances such as multithreading and multiprocessing. The required physical datasets that are essential to the program were all updated through linking with *xraylib*, facilitating the incorporation of M-lines and cascade effects. Furthermore, the code was adapted to allow for the simulation of detectors equipped with conical or cylindrical collimators, as well as for the generation of fluorescence and Compton escape peaks for arbitrary detector crystals. The pile-up effect, which occurs sometimes in XRF spectra due to high countrates, is also simulated in order to make the simulations appear as realistic as possible, as was demonstrated using experimental data obtained at the micro-XRF beamline L of HASYLAB (Hamburg Synchrotron Laboratories, Germany).

Apart from using this Monte Carlo simulation tool in a forward manner, we have developed

a plug-in for *PyMca*, the leading open-source software package for XRF data analysis, that allows for the application of these simulations in an inverse, iterative manner, thereby producing an efficient XRF quantification tool. It was demonstrated that a Monte Carlo based quantification method has the potential of simulating all relevant interactions in a sample, therefore proving to be the superior method.

Our software packages are considered sufficiently stable and mature for public release as is proven by the fact that both *xraylib* and *XMI-MSIM* are now distributed through the open-source code repository `http://www.github.com/tschoonj`, were they can be freely downloaded. However, development of these packages is expected to continue in the future. Work on *xraylib* will be focused mainly on the incorporation of more reliable databases, possibly those that may be produced by the Fundamental Parameter Initiative. On a software level, we intend to develop language bindings for Matlab, Ruby and Lua (possibly more depending on user demand), as well as to implement a more robust error handling interface. Concerning *XMI-MSIM*, we plan on significantly improving the graphical user interface whose functionality at this point is limited to the generation of input files. Ideally, the complete manipulation of the simulation code would be handled through the interface in a convenient and clear manner. Apart from user interface improvements, we would like to extend the Monte Carlo code towards confocal XRF, implying that the specific characteristics of the detector channel polycapillary half-lens are taken into account, possibly using ray tracing techniques. Such an extension would permit to perform the quantification of confocal XRF spectral data, thereby theoretically offering a superior alternative over the fundamental parameter based approach.

Chapter 8

Samenvatting en conclusies

Dit werk was toegespitst op de ontwikkeling van kwantificatiemethodes voor X-straal fluorescentie spectroscopie (XRF), een krachtige en veelzijdige methode voor chemische analyse op macro-, micro- en nanoniveau. Twee veelvuldig gebruikte methodes werden bestudeerd in dit werk: de eerste was gericht op de fundamentele parameter methode, de tweede maakte daarentegen gebruik van Monte Carlo simulaties. Aangezien deze beide methodes afhangen van een aantal fysische grootheden die relevant zijn voor de studie van X-straal–materie interacties zoals werkzame doorsnedes, XRF lijn energieën, bindingsenergieën, fluorescentie opbrengsten etc., was ons werk initieel gericht op het vinden van een betrouwbare en eenvoudig te gebruiken bron van dergelijke grootheden. Onze zoektocht heeft geleid naar *xraylib*, een bibliotheek ontwikkeld in ANSI C die op eenvoudige wijze toegang verschaft tot deze parameters. De ontwikkeling van deze bibliotheek, gestart als een samenwerking tussen onderzoekers van de Universiteit van Sassari (Sardinië, Italië) en de *European Synchrotron Radiation Facility* (ESRF, Grenoble, Frankrijk), werd voortgezet door onze groep vanaf 2008 en heeft sindsdien geleid tot een dozijn software releases. Talrijke nieuwe elementen werden toegevoegd, zoals partiële photoionizatie werkzame doorsnedes, Compton verbredings profielen, XRF productie werkzame doorsnedes die gecorrigeerd zijn voor het cascade effect, herziene lijn energieën, M-schil Coster-Kronig transitie probabiliteiten, etc. De installatie procedure van het pakket werd vereenvoudigd voor zowel UNIX(-achtige) als Windows besturingssystemen. Daarenboven werd de toepasbaarheid van de bibliotheek vergroot door het toevoegen van *bindings* voor andere programmeertalen zoals Fortran 2003, IDL, Python, Perl, .NET en Java.

De *xraylib* bibliotheek werd in ons werk eerst toegepast met betrekking tot de fundamentele parameter methode. Deze methode, die gebruik maakt van het verband tussen de netto intensiteiten van de XRF lijnen in een spectrum en de element concentraties, werd aangepast om ingezet te kunnen worden in het bijzondere geval van confocale micro/nano XRF spectroscopie. Dergelijke confocale XRF opstellingen worden bekomen door het monteren van een polycapillaire half-lens voor het detector scherm, waardoor het geanalyseerde volume wordt verkleind en zodoende dieptegevoelige driedimensionale karakterisering mogelijk wordt. De modificaties die deze techniek mogelijk maken zijn te wijten aan de specifieke eigenschappen van het polycapillair, zoals de energie afhankelijke transmissie efficiëntie en de energie afhankelijke acceptantie. Onze methodologie voor confocale XRF spectroscopie werd toegepast op een unieke dataset die werd verkregen aan de ID13 bundellijn van het ESRF uit komeetstof deeltjes die naar de Aarde gebracht werden in het kader van NASA's Stardust missie. De kwantificatie van deze spectra werd gecombineerd met een grondige foutanalyse, gebaseerd op het gebruik van Monte Carlo simulaties, waarin alle parameters (spectra, gewichten, dichtheden, laagdiktes, etc.) gevarieerd werden naargelang hun standaardafwijkingen en fouten, wat geleid heeft tot histogrammen van de foutverdelingen.

Monte Carlo simulaties werden tevens gebruikt in de tweede kwantificatieprocedure die bestudeerd werd in dit werk. Dergelijke simulaties laten toe dat een probleem gemodelleerd wordt dat te complex is om analytisch opgelost te worden. Dit gebeurt door middel van generatoren van willekeurige getallen en de probabiliteit dichtheidsfuncties die de verschillende parameters van het systeem beschrijven. In dit geval werden Monte Carlo simulaties gebruikt ter modellering van energiedispersieve XRF spectrometers. De computercode van Vincze et al. werd volledig herschreven als het software pakket *XMI-MSIM*, zodat recente computationele technologieën zoals multithreading en multiprocessing konden gebruikt worden. De benodigde datasets met fysische grootheden werden bekomen door integratie van *xraylib*, waardoor M-lijnen en cascade effecten konden ingebouwd worden. Bovendien werd de code aangepast zodat ook detectoren die uitgerust zijn met conische of cilindrische collimators kunnen gesimuleerd worden, evenals het voorkomen van fluorescentie en Compton ontsnappingspieken voor arbitraire detectorkristallen. Het *pile-up* fenomeen, dat optreedt door hoge telfrequenties, werd eveneens gesimuleerd met de bedoeling de simulaties zo realistisch mogelijk te laten lijken, zoals aangetoond werd met behulp van experimentele data die bekomen werd aan de micro-XRF bundellijn L van HASYLAB

(Hamburgse Synchrotron Laboratoria, Duitsland).

Naast het aanwenden van deze Monte Carlo simulatie op een voorwaartse manier, werd er ook een plug-in ontwikkeld voor *PyMca*, het populaire opensourcesoftware pakket voor XRF dataverwerking, dat gericht is op de toepassing van deze simulaties op een inverse, iteratieve wijze, waardoor deze getransformeerd worden in een efficiënt XRF kwantificatie hulpmiddel. Er werd aangetoond dat een op Monte Carlo simulaties gebaseerde kwantificatie methode het potentieel heeft alle relevante interacties in een monster te simuleren, waardoor het de superieure methode wordt.

Zoals aangetoond door de distributie van zowel *xraylib* als *XMI-MSIM* via het open source code webplatform `http://www.github.com/tschoonj`, zijn onze softwarepakketten voldoende stabiel en volwassen voor een publieke release. De ontwikkeling ervan zal echter voortgezet worden in de toekomst. Verder werk omtrent *xraylib* zal voornamelijk gericht zijn op de introductie van meer betrouwbare databases, mogelijk deze die zullen vrijgegeven worden door het *Fundamental Parameter Initiative*. Op het softwareniveau plannen we vooral de foutenafhandeling te versterken, naast de introductie van *bindings* voor Matlab, Ruby en Lua (mogelijk meer afhankelijk van de vraag van gebruikers). Wat betreft *XMI-MSIM*, zal in de eerste plaats de functionaliteit van de grafische gebruikersinterface uitgebreid worden, aangezien deze momenteel beperkt is tot het genereren van invoerbestanden. Op termijn is het de bedoeling dat de volledige besturing van de simulatie code via deze gebruikersinterface zou verlopen, op een eenvoudige en duidelijke manier. Daarnaast zou de code uitgebreid worden met de mogelijkheid tot het simuleren van confocale XRF experimenten, wat impliceert dat de specifieke eigenschappen van de detector polycapillaire half-lens in rekening moeten gebracht worden, eventueel door middel van *ray tracing* technieken. Een dergelijke uitbreiding zou het mogelijk maken confocale XRF data te gaan kwantificeren, waardoor deze in theorie een superieur alternatief zou vormen voor de fundamentele parameter gebaseerde aanpak.

Appendix A

xraylib API summary

Table A.1: The functions offered by the *xraylib* API.

Category	Function prototype	Return value
Atomic data	float AtomicWeight(int Z)	Atomic weight
	float ElectronConfig(int Z, float E)	Electon configuration
Cross sections: (cm^2/g)	float CS_Total(int Z, float E)	Total cross section (photoionization + Rayleigh + Compton)
	float CS_Photo(int Z, float E)	Photoionization CS
	float CS_Photo_Total(int Z, float E)	Photoionization CS (Kissel)
	float CS_Photo_Partial(int Z, int shell, float E)	Partial photoionization CS
	float CS_Rayl(int Z, float E)	Rayleigh CS
	float CS_Compt(int Z, float E)	Compton CS
	float CS_KN(float E)	Klein-Nishina CS
Cross sections: (barns/atom)	float CSb_Total(int Z, float E)	Total cross section (photoionization + Rayleigh + Compton)
	float CSb_Photo(int Z, float E)	Photoionization CS
	float CSb_Photo_Total(int Z, float E)	Photoionization CS (Kissel)

Table A.1: The functions offered by the *xraylib* API (continued).

Category	Function prototype	Return value
	float CSb_Photo_Partial(int Z, int shell, float E)	Partial photoionization CS
	float CSb_Rayl(int Z, float E)	Rayleigh CS
	float CSb_Compt(int Z, float E)	Compton CS
XRF cross sections: (cm^2/g)	float CS_FluorLine(int Z, int line, float E)	Using jump approximation
	float CS_FluorLine_Kissel_Cascade(int Z, int line, float E)	Using partial PE CS and full cascade
	float CS_FluorLine_Kissel_-Nonradiative_Cascade(int Z, int line, float E)	Using partial PE CS and nonradiative cascade
	float CS_FluorLine_Kissel_-Radiative_Cascade(int Z, int line, float E)	Using partial PE CS and radiative cascade
	float CS_FluorLine_Kissel_-no_Cascade(int Z, int line, float E)	Using partial PE CS and no cascade
XRF cross sections: (barns/atom)	float CSb_FluorLine(int Z, int line, float E)	Using jump approximation
	float CSb_FluorLine_Kissel_-Cascade(int Z, int line, float E)	Using partial PE CS and full cascade
	float CSb_FluorLine_Kissel_-Nonradiative_Cascade(int Z, int line, float E)	Using partial PE CS and nonradiative cascade
	float CSb_FluorLine_Kissel_-Radiative_Cascade(int Z, int line, float E)	Using partial PE CS and radiative cascade
	float CSb_FluorLine_Kissel_-no_Cascade(int Z, int line, float E)	Using partial PE CS and no cascade

Table A.1: The functions offered by the *xraylib* API (continued).

Category	Function prototype	Return value
Differential unpolarized cross sections: (cm^2/g/sterad)	float DCS_Rayl(int Z, float E, float theta)	Rayleigh DCS
	float DCS_Compt(int Z, float E, float theta)	Compton DCS
	float DCS_Thoms(float theta)	Thomson DCS
	float DCS_KN(float E, float theta)	Klein-Nishina DCS
Differential polarized cross sections: (cm^2/g/sterad)	float DCSP_Rayl(int Z, float E, float theta, float phi)	Rayleigh DCSP
	float DCSP_Compt(int Z, float E, float theta, float phi)	Compton DCSP
	float DCSP_Thoms(float theta, float phi)	Thomson DCSP
	float DCSP_KN(float E, float theta, float phi)	Klein-Nishina DCSP
Compound cross sections: (cm^2/g)	float CS_Total_CP(const char compound[], float E)	Total cross section (photoionization + Rayleigh + Compton)
	float CS_Photo_CP(const char compound[], float E)	Photoionization CS
	float CS_Photo_Total_CP(const char compound[], float E)	Photoionization CS (Kissel)
	float CS_Photo_Partial_CP(const char compound[], int shell, float E)	Partial photoionization CS
	float CS_Rayl_CP(const char compound[], float E)	Rayleigh CS
	float CS_Compt_CP(const char compound[], float E)	Compton CS
	float DCS_Rayl_CP(const char compound[], float E, float theta)	Rayleigh DCS

Table A.1: The functions offered by the *xraylib* API (continued).

Category	Function prototype	Return value
	float DCS_Compt_CP(const char compound[], float E, float theta)	Compton DCS
	float DCSP_Rayl_CP(const char compound[], float E, float theta, float phi)	Rayleigh DCSP
	float DCSP_Compt_CP(const char compound[], float E, float theta, float phi)	Compton DCSP
Compound cross sections: (barns/atom)	float CSb_Total_CP(const char compound[], float E)	Total cross section (photoionization + Rayleigh + Compton)
	float CSb_Photo_CP(const char compound[], float E)	Photoionization CS
	float CSb_Photo_Total_CP(const char compound[], float E)	Photoionization CS (Kissel)
	float CSb_Photo_Partial_CP(const char compound[], int shell, float E)	Partial photoionization CS
	float CSb_Rayl_CP(const char compound[], float E)	Rayleigh CS
	float CSb_Compt_CP(const char compound[], float E)	Compton CS
	float DCSb_Rayl_CP(const char compound[], float E, float theta)	Rayleigh DCS
	float DCSb_Compt_CP(const char compound[], float E, float theta)	Compton DCS
	float DCSPb_Rayl_CP(const char compound[], float E, float theta, float phi)	Rayleigh DCSP

Table A.1: The functions offered by the *xraylib* API (continued).

Category	Function prototype	Return value
	float DCSPb_Compt_CP(const char compound[], float E, float theta, float phi)	Compton DCSP
Absorption edges and transition data	float EdgeEnergy(int Z, int shell)	Absorption edge energy
	float LineEnergy(int Z, int line)	Fluorescence line energy
	float FluorYield(int Z, int shell)	Fluorescence yield
	float JumpFactor(int Z, int shell)	Jump ratio
	float RadRate(int Z, int line)	Radiative transition probability
	float AugerRate(int Z, int electrons)	Auger transition probability
	float CosKronTransProb(int Z, int trans)	Coster-Kronig transition probability
	float AtomicLevelWidth(int Z, int shell)	Atomic level width
Scattering factors	float Fi(int Z, float E)	anomalous scattering factor ϕ'
	float Fii(int Z, float E)	anomalous scattering factor ϕ''
	float FF_Rayl(int Z, float q)	Rayleigh form factor
	float SF_Compt(int Z, float q)	Incoherent scattering function
	float MomentTransf(float E, float theta)	Momentum transfer
Compton broadening profiles	float ComptonProfile(int Z, float pz)	Full Compton profile
	float ComptonProfile_Partial(int Z, int shell, float pz)	Compton profile for single shell
Refractive indices	float Refractive_Index_Re(const char compound[], float E, float density)	Real part

Table A.1: The functions offered by the *xraylib* API (continued).

Category	Function prototype	Return value
	float Refractive_Index_Im(const char compound[], float E, float density)	Imaginary part
Miscellaneous	float ComptonEnergy(float E0, float theta)	Photon energy after Compton scattering
	int CompoundParser(const char compoundString[], struct compoundData *cd)	Compound string parser
	char * AtomicNumberToSymbol(int Z)	Returns chemical symbol corresponding with atomic number
	int SymbolToAtomicNumber(char *symbol)	Returns atomic number corresponding with chemical symbol

Appendix B

Publications and activities

B.1 List of (contributions to) Publications

B.1.1 A1 (ISI Web of Science – Science Citation Index)

1. T. Schoonjans, V.A. Solé, M. Sanchez del Rio, K. Ricker, L. Vincze, C. Ferrero, A general Monte Carlo simulation of energy-dispersive X-ray fluorescence spectrometers – Part 6. Quantification through inverse simulations, submitted.

2. T. Schoonjans, L. Vincze, V.A. Solé, M. Sanchez del Rio, P. Brondeel, G. Silversmit, K. Appel, C. Ferrero, A general Monte Carlo simulation of energy-dispersive X-ray fluorescence spectrometers – Part 5. Polarized radiation, stratified samples, cascade effects, M-lines, submitted.

3. T. Schoonjans, G. Silversmit, B. Vekemans, S. Schmitz, M. Burghammer, C. Riekel, F. E. Brenker, L. Vincze, Fundamental parameter based quantification algorithm for confocal nano X-ray fluorescence analysis, Spectrochim. Acta Part B, (2012), in press.

4. R. Evens, K. De Schamphelaere, B. De Samber, G. Silversmit, T. Schoonjans, B. Vekemans, L. Balcaen, F. Vanhaecke, I. Szalóki, K. Rickers, G. Falkenberg, L. Vincze and C. Janssen, Waterborne versus dietary zinc accumulation and toxicity in Daphnia magna: a synchrotron radiation based X-ray Fluorescence imaging approach, Environ. Sci. Technol., (2012), in press.

5. T. Schoonjans, A. Brunetti, B. Golosio, M. Sanchez del Rio, V.A. Solé, C. Ferrero, L. Vincze, The xraylib library for X-ray–matter interactions. Recent developments, Spectrochim. Acta Part B, (2011), in press.

6. G. Silversmit, B. Vekemans, K. Appel, S. Schmitz, T. Schoonjans, F.E. Brenker, F. Kaminsky, L. Vincze, Three-dimensional Fe speciation of an inclusion cloud within an ultradeep diamond by confocal μ-X-ray absorption near edge structure: Evidence for late stage overprint, Anal. Chem. 83 (2011).

7. G. Silversmit, B. Vekemans, S. Nikitenko, S. Schmitz, T. Schoonjans, F.E. Brenker, L. Vincze, Spatially resolved 3D micro-XANES by a confocal detection scheme, Phys. Chem. Chem. Phys. 12 (2010).

8. B. De Samber, G. Silversmit, K. De Schamphelaere, R. Evens, T. Schoonjans, B. Vekemans, C. Janssen, B. Masschaele, L. Van Hoorebeke, I. Szaloki, F. Vanhaecke, K. Rickers, G. Falkenberg, L. Vincze, Element-to-tissue correlation in biological samples determined by three-dimensional X-ray imaging methods, J. Anal. At. Spectrom. 25 (2010).

9. V.G. Mihucz, G. Silversmit, I. Szaloki, B. De Samber, T. Schoonjans, E. Tatar, L. Vincze, I. Virag, J. Yao, G. Zaray, Removal of some elements from washed and cooked rice studied by inductively coupled plasma mass spectrometry and synchrotron based confocal micro-X-ray fluorescence, Food Chem. 121 (2010).

10. B. De Samber, S. Vanblaere, R. Evens, K. De Schamphelaere, G. Wellenreuther, F. Ridoutt, G. Silversmit, T. Schoonjans, B. Vekemans, B. Masschaele, L. Van Hoorebeke, K. Rickers, G. Falkenberg, I. Szaloki, C. Janssen, L. Vincze, Dual detection X-ray fluorescence cryotomography and mapping on the model organism Daphnia magna, Powder Diffr. 25 (2010).

11. V. Cnudde, G. Silversmit, M. Boone, J. Dewanckele, B. De Samber, T. Schoonjans, D. Van Loo, Y. De Witte, M. Elburg, L. Vincze, L. Van Hoorebeke, P. Jacobs, Multi-disciplinary characterisation of a sandstone surface crust, Sci. Total Environ. 407 (2009).

12. S. Schmitz, F.E. Brenker, T. Schoonjans, B. Vekemans, G. Silversmit, L. Vincze, M. Burghammer, C. Riekel, In situ identification of a CAI candidate in 81P/Wild 2

cometary dust by confocal high resolution synchrotron X-ray fluorescence, Geochim. Cosmochim. Acta 73 (2009).

13. B. De Samber, R. Evens, K. De Schamphelaere, G. Silversmit, B. Masschaele, T. Schoonjans, B. Vekemans, C. Janssen, L. Van Hoorebeke, I. Szaloki, F. Vanhaecke, G. Falkenberg, L. Vincze, A combination of synchrotron and laboratory X-ray techniues for studying tissue-specific trace level metal distributions in Daphnia magna, J. Anal. At. Spectrom. 23 (2008).

14. A. Adriaens, K. De Wael, D. Bogaert, H. Buschop, T. Schoonjans, B. Vekemans, D. Depla, L. Vincze, Cobalt thin films on gold: A new reference material for the quantification of cobalt phthalocyanine and cobalt porphyrin modified gold electrodes with synchrotron radiation micro X-ray fluorescence spectroscopy, Spectrochim. Acta Part B 63 (2008).

B.1.2 P1 (ISI Web of Science – Conference Proceedings Citation Index - Science)

1. T. Schoonjans, A. Brunetti, B. Golosio, M. Sanchez del Rio, V.A. Solé, C. Ferrero, L. Vincze, The xraylib library for x-ray-matter interaction cross sections: new developments and applications, Proc. SPIE 8141, 814110 (2011)

B.1.3 C3 (Conference - meeting abstracts)

1. T. Schoonjans, V.A. Solé, M. Sanchez del Rio, C. Ferrero, L. Vincze. A general Monte-Carlo simulation of ED-XRF spectrometers. New developments. International Congress on X-Ray Optics and Microanalysis (ICXOM), Campinas, SP, Brazil, September 5-8th 2011 (poster presentation)

2. T. Schoonjans, A. Brunetti, B. Golosio, M. Sanchez del Rio, V.A. Solé, C. Ferrero and L. Vincze. The xraylib library for X-ray matter interaction cross sections: New developments and applications, SPIE Optics and Photonics, San Diego, CA, USA, August 21-25th 2011 (poster presentation)

3. L. Vincze, B. Vekemans, G. Silversmit, T. Schoonjans, S. Schmitz, M. Burghammer, C. Riekel, S. Schöder and F.E. Brenker. Submicron X-ray fluorescence imaging on

unique cometary matter returned by NASA's Stardust mission, European Conference on X-Ray Spectrometry, Figueira da Foz, Coimbra, Portugal, June 20-25th 2010 (oral presentation)

4. T. Schoonjans, M. Sanchez del Rio, A. Brunetti, B. Golosio, A. Simionovici, C. Ferrero and L. Vincze. The xraylib library for X-ray matter interaction cross sections: New developments, European Conference on X-Ray Spectrometry, Figueira da Foz, Coimbra, Portugal, June 20-25th 2010 (oral presentation)

5. I. Szaloki, B. De Samber, T. Schoonjans, B. Vekemans, V. Czhech, Gy. Zaray and L. Vincze. XRF microtomography and confocal imaging for the 2D/3D determination of toxic elements in biological samples, European Conference on X-Ray Spectrometry, Figueira da Foz, Coimbra, Portugal, June 20-25th 2010 (oral presentation)

6. B. De Samber, T. Schoonjans, B. Vekemans, G. Silversmit, D. Gholap, A. Izmer, R. Evens, K. De Schamphelaere, L. Van Hoorebeke, C. Janssen, F. Vanhaecke and L. Vincze. X-ray Microspectroscopic Imaging and Laser Ablation Inductively Coupled Plasma Mass Spectrometry for Metal Analysis in Biological Model Organisms, European Conference on X-Ray Spectrometry, Figueira da Foz, Coimbra, Portugal, June 20-25th 2010 (oral presentation)

7. G. Silversmit, B. Vekemans, T. Schoonjans, S. Schmitz, F.E. Brenker and L. Vincze. 3D confocal Fe-K XANES on inclusions in 'ultra-deep' diamonds, European Conference on X-Ray Spectrometry, Figueira da Foz, Coimbra, Portugal, June 20-25th 2010 (oral presentation)

8. L. Vincze, B. Vekemans, G. Silversmit, T. Schoonjans, S. Schmitz, M. Burghammer, C. Riekel, S. Schöder and F.E. Brenker. Three-dimensional synchrotron XRF methods applied to unique cometary matter returned by STARDUST, Summer school in the framework of the IAP NACHO network, Erice, Sicily, Italy, June 14-21st 2010 (oral presentation)

9. B. Vekemans, B. De Samber, T. Schoonjans, G. Silversmit, L. Vincze, R. Evens, K. De Schamphelaere, C. Janssen, B. Masschaele, L. Van Hoorebeke, S. Schmitz, F.E. Brenker, R. Tucoulou, P. Cloetens, M. Burghammer, J. Susini and C. Riekel. Polycapillary based confocal detection schemes for XRF micro- and nano-spectroscopy,

Denver X-ray Conference, Colorado Springs, CO, USA, July 27-31st 2009 (oral presentation)

10. T. Schoonjans, M. Sanchez del Rio, L. Vincze. The xraylib library for X-ray matter interaction cross-sections: New developments and applications, Denver X-ray Conference, Colorado Springs, CO, USA, July 27-31st 2009 (poster presentation - Best XRF poster award)

11. T. Schoonjans, B. Vekemans, G. Silversmit, L. Vincze, S. Schmitz and F.E. Brenker. Stardust Cometary Matter Analyzed by Synchrotron nano-XRF: New Results and Developments, Denver X-ray Conference, Colorado Springs, CO, USA, July 27-31st 2009 (oral presentation)

12. T. Schoonjans, B. Vekemans, G. Silversmit, L. Vincze, S. Schmitz and F.E. Brenker. Stardust Cometary Matter Analyzed by Synchrotron nano-XRF: New Results and Developments, Non-destructive Analysis of Cultural Heritage Objects PhD day, Université de Liège, July 2nd, 2009 (oral presentation)

13. B. De Samber, G. Silversmit, T. Schoonjans, R. Evens, K. De Schamphelaere, C. Janssen, L. Balcaen, F. Vanhaecke, B. Masschaele, L. Van Hoorebeke, B. Vekemans, G. Wellenreuther, K. Rickers, G. Falkenberg and L. Vincze. X-ray Fluorescence and Absorption Microtomography reveal Tissue Specific Distribution of Metals in Daphnia magna, SyNew Synchrotron and Neutron Workshop, Brussels Academy House, Brussels, Belgium, April 23th 2009 (oral presentation)

14. B. De Samber, R. Evens, K. De Schamphelaere, B. Masschaele, G. Silversmit, T. Schoonjans, B. Vekemans, L. Van Hoorebeke, F. Vanhaecke, C. Janssen, S. Bohic, G. Wellenreuther, K. Rickers, G. Falkenberg and L. Vincze. Laboratory and Synchrotron Radiation Micro and Nano X-ray Fluorescence, JST Symposium on 'Micro and Trace X-ray Analysis', Media Center, Osaka City University, Osaka, Japan, 12-14th February 2009 (oral presentation)

15. B. De Samber, T. Schoonjans, G. Silversmit, B. Vekemans, L. Vincze, R. Evens, K. De Schamphelaere, C. Janssen, B. Masschaele, L. Van Hoorebeke, S. Bohic, K. Rickers and G. Falkenberg. A Top-Down Approach using X-ray Imaging Techniques:

Instrumental Developments and Applications in Life Science, Denver X-ray Conference, Denver, CO, USA, August 4-8th 2008 (oral presentation)

16. B. Vekemans, T. Pisternick, T. Schoonjans, F.E. Brenker, A. Szymanski, W. De Nolf, K. Janssen, J. Harris, R. Tucoulou and L. Vincze. SR-XRF analysis of fluid-inclusions in cloudy diamonds from Koffiefontein, South-Africa, European Conference on X-Ray Spectrometry, Cavtat, Dubrovnik, Croatia, June 16-20th 2008 (oral presentation)

17. T. Schoonjans, B. Vekemans, G. Silversmit, S. Schmitz, F.E. Brenker and L. Vincze. Confocal XRF quantification procedures applied to the cometary matter returned by NASA's Stardust mission, European Conference on X-Ray Spectrometry, Cavtat, Dubrovnik, Croatia, June 16-20th 2008 (oral presentation)

18. B. De Samber, R. Evens, T. Schoonjans, G. Silversmit, B. Vekemans, K. De Schamphelaere, C. Janssen, B. Masschaele, L. Van Hoorebeke, K. Rickers, G. Falkenberg and L. Vincze. Three dimensional SR-confocal micro XRF combined with absorption microtomography on Daphnia magna: Instrumental developments and recent advances in dataprocessing, European Conference on X-Ray Spectrometry, Cavtat, Dubrovnik, Croatia, June 16-20th 2008 (oral presentation)

19. V. Mihucz, G. Silversmit, I. Szaloki, T. Schoonjans, E. Tatar, B. De Samber, L. Vincze, I. Virag, J. Yao and G. Zaray. Element removal from washed and cooked rice studied by SF-ICP-MS and synchrotron radiation based confocal micro-XRF, XIII Italian-Hungarian Symprosium on Spectrochemistry: environmental contamination and food safety, Bologna, Italy, April 20-24th, 2008 (oral presentation)

20. L. Vincze, B. Vekemans, G. Silversmit, T. Schoonjans, S. Schmitz, M. Burghammer, C. Riekel and F. Brenker. Synchrotron microanalysis of cometary particles, 8th EMAS Regional Workshop on Electron Probe Microanalysis of Materials Today, The Abdus Salam International Centre for Theoretical Physics, Trieste, Italy, April 19-22nd, 2008 (oral presentation)

21. T. Schoonjans, F.E. Brenker, S. Schmitz, G. Silversmit, B. De Samber, B. Vekemans, M. Burghammer, C. Riekel and L. Vincze. Nano-XRF study of cometary matter

returned by NASA's Stardust mission: a quantitative and qualitative approach, EUROanalysisXIV, Antwerp, Belgium, September 9-14th 2007 (poster presentation)

22. B. De Samber, G. Silversmit, T. Schoonjans, R. Evens, K. Deschamphelaere, B. Masschaele, C. Janssen, L. Van Hoorebeke, L. Balcaen, F. Vanhaecke, G. Falkenberg and L. Vincze. Studying tissue-specific distributions of metals in Daphna Magna using scanning X-ray fluorescence and absorption micro-tomography, EUROanalysisXIV, Antwerp, Belgium, September 9-14th 2007 (oral presentation)

23. L. Vincze, B. Vekemans, G. Silversmit, T. Schoonjans, S. Schmitz, M. Burghammer, C. Riekel and F.E. Brenker. Submicron X-ray fluorescence imaging on cometary matter returned by NASA's STARDUST mission, EUROanalysisXIV, Antwerp, Belgium, September 9-14th 2007 (oral presentation)

24. L. Vincze, B. Vekemans, G. Silversmit, T. Schoonjans, S. Schmitz, M. Burghammer, C. Riekel and F.E. Brenker. Three dimensional nano-XRF on cometary matter returned by NASA's STARDUST mission, Denver X-ray Conference, Colorado Springs, CO, USA, July 30 - August 3rd 2007 (oral presentation)

25. T. Schoonjans, F.E. Brenker, G. Silversmit, B. De Samber, B. Vekemans, M. Burghammer, C. Riekel and L. Vincze. Quantitative nano-XRF study of cometary matter returned by NASA's STARDUST mission, Symposium of the Faculty of Science, Ghent University, Ghent, Belgium, April 24th 2007 (poster presentation)

B.2 List of Attended Beamtimes

B.2.1 Hamburger Synchrotron Labor (HASYLAB), Hamburg, Germany

II-20052045 EC Characterization of electrochemically modified electrode surfaces using synchrotron radiation microbeam XRF and XANES. Project leaders: Prof. Dr. Laszlo Vincze and Prof. Dr. Annemie Adriaens.

1. July 24-28, 2006: Beamline L
2. June 18-22, 2007: Beamline L

3. September 5-10, 2007: Beamline L

II-20060097 EC Three-dimensional micro-XRF/XANES studies on metal toxicity in biological systems by tomographic methods. Project leaders: Prof. Dr. Imre Szaloki and Prof. Dr. Laszlo Vincze.

1. October 25-30, 2006: Beamline L
2. October 21-25, 2007: Beamline L

II-20070159 EC Development of three-dimensional XRF/XANES microanalysis using confocal detection mode for the non-destructive characterisation of inclusions in diamond. Project leader: Dr. Geert Silversmit.

1. October 1-8, 2007: Beamline L
2. November 19-25, 2008: Beamline L
3. March 10-17, 2009: Beamline L
4. October 16-22, 2009: Beamline L

I-20090058 EC Development of new and improvement techniques for the immobilization of redox enzymes onto electrodes. Project leaders: Prof. Dr. Laszlo Vincze and Prof. Dr. Annemie Adriaens.

1. November 27-December 1, 2009: Beamline L
2. July 3-6, 2010: Beamline L

I-20100035 EC Development of new and improvement techniques for the immobilization of redox enzymes onto electrodes. Project leaders: Prof. Dr. Laszlo Vincze and Prof. Dr. Annemie Adriaens.

1. November 12-16, 2010: Beamline L
2. June 10-14, 2011: Beamline L

B.2.2 European Synchrotron Radiation Facility (ESRF), Grenoble, France

EC70 In situ (sub)micro-fluorescence and -diffraction of mantle fluids and deep Earth high pressure phases trapped in diamond. Project leaders: Prof. Dr. Koen Janssens, Prof. Dr. Frank Brenker and Prof. Dr. Laszlo Vincze.

1. April 19-27, 2007: Beamline ID18F
2. November 14-19, 2007, Beamline ID22N
3. April 24-28, 2008: Beamline ID18F
4. October 1-8, 2008: Beamline ID18F
5. June 10-18, 2008: Beamline ID18F

EC337 Sub-micron XRF and XRD on interstellar grains sampled during NASAs Stardust mission. Project leaders: Prof. Dr. Frank Brenker and Prof. Dr. Laszlo Vincze.

1. November 11-17, 2008: Beamline ID13
2. February 24 - 1 March, 2010: Beamline ID13
3. July 13-18, 2010: Beamline ID13

MI937 Methodology and device for combined micro-analysis of extraterrestrial samples. Project leader: Prof. Dr. Alexandre Simionovici.

1. June 30-July 3, 2010: Beamline ID22